UNIVERSITY OF SÃO PAULO
SÃO CARLOS SCHOOL OF ENGINEERING

LEANDRO FALCÃO LOUREIRO REGO

DEVELOPMENT OF A PYLON BLOWING SYSTEM FOR A PUSHER PROPELLER CONFIGURATION WITH THE STUDY OF THE ASSOCIATED AERODYNAMIC AND AEROACOUSTIC PHENOMENA

São Carlos
2017

LEANDRO FALCÃO LOUREIRO REGO

DESENVOLVIMENTO DE UM SISTEMA DE SOPRO PARA UMA CONFIGURAÇÃO PILONE-HÉLICE PUSHER COM O ESTUDO DOS FENÔMENOS AERODINÂMICOS E AEROACÚSTICOS ASSOCIADOS

Dissertação apresentada à Escola de Engenharia de São Carlos, da Universidade de São Paulo, como requisito para a obtenção do Título de Mestre em Engenharia Mecânica.

Área de concentração: Aeronaves

Orientador: Prof. Tit. Fernando M. Catalano

ESTE EXEMPLAR TRATA-SE DA VERSÃO CORRIGIDA.
A VERSÃO ORIGINAL ENCONTRA-SE DISPONÍVEL JUNTO AO DEPARTAMENTO DE ENGENHARIA MECANICA DA EESC-USP

São Carlos
2017

Rego, Leandro Falcão Loureiro
R343d Development of a pylon blowing system for a pusher propeller configuration with the study of the associated aerodynamic and aeroacoustic phenomena / Leandro Falcão Loureiro Rego ; advisor Fernando M. Catalano. -- São Carlos, 2017.

Master (Thesis) - Graduate Program in Mechanical Engineering and Subject area in Aircrafts -- São Carlos School of Engineering, at University of São Paulo, 2017.

1. Pusher propeller. 2. Installation effects. 3. Wake deficit. 4. Propeller noise. 5. Pylon blowing. I. Title.

FOLHA DE JULGAMENTO

Candidato: Engenheiro **LEANDRO FALCÃO LOUREIRO REGO.**

Título da dissertação: "Desenvolvimento de um sistema de sopro para uma configuração *Pilone-Hélice Pusher* com o estudo dos fenômenos aerodinâmicos e aeroacústicos associados".

Data da defesa: 22/06/2017.

Comissão Julgadora:	**Resultado:**
Prof. Titular **Fernando Martini Catalano** **(Orientador)** (Escola de Engenharia de São Carlos/EESC)	APROVADO
Prof. Dr. **Roberto da Mota Girardi** (Instituto Tecnológico de Aeronáutica/ITA)	APROVADO
Prof. Dr. **Ulf Tomas Joakim Gronstedt** (Chalmers Tekniska Hogskola)	APROVADO

Coordenador do Programa de Pós-Graduação em Engenheira Mecânica:
Prof. Associado **Gherhardt Ribatski**

Presidente da Comissão de Pós-Graduação:
Prof. Associado **Luis Fernando Costa Alberto**

To my parents, Ronise and Fabio

ACKNOWLEDGEMENTS

I would like to thank the following people, without whom this work would not be possible:

- Prof. Fernando Catalano, my supervisor and my friend, for the invaluable help with his advices and for the great discussions throughout all the phases of this work. More than that, for always teaching me how to become a better engineer;

- Lourenço Tércio, my friend, who also helped me immensely with the experimental measurements and who taught me a lot about aeroacoustics;

- Osnan Faria, technician at the Laboratory of Aerodynamics and my friend, who helped me build the models for the wind tunnel tests with great quality;

- Eng. Udo Krause, my former supervisor at Airbus Operations, who first introduced me to the topic of this work;

- Elena Gonçalves, from the EESC-USP Library, who reviewed and spellchecked this work;

- Luiz Otávio, Fernanda Monteiro and Antônio Carlos Daud, my friends, for all the great talks and wonderful moments.

"When everything seems to be going against you, remember that the airplane takes off against the wind, not with it."

Henry Ford

ABSTRACT

REGO, L. F. L. **Development of a Pylon Blowing System for a Pusher Propeller Configuration with the Study of the Associated Aerodynamic and Aeroacoustic Phenomena**. 2017. 213p. Dissertation (Master of Science) – São Carlos School of Engineering, University of São Paulo, São Carlos, 2017.

This report contains the work performed for the development of a tangential blowing system, to be integrated to a pylon mounted with a propeller in pusher configuration. This model was built to represent a new configuration of turboprop aircraft, known as open rotor, which tends to be more fuel efficient than the current turbofan-powered ones. There is, however, one issue associated with the practical application of the open rotor, which is the high levels of noise emissions, especially from the propellers. Aside from the propeller self-noise, there is also an additional noise generation mechanism, which arises from the pylon wake impinging on disc, and is related to the occurrence of an unsteady loading component on the blades. This effect of the pylon wake on the propeller was assessed through wind tunnel tests, where measurements were carried out to provide a better understanding on the aerodynamic and aeroacoustic phenomena occurring in this type of configuration. Moreover, a potential solution was developed aiming to mitigate the installation effects on the propeller, based on the control of the flow around the pylon. A tangential blowing system was integrated to the pylon in order to reduce the boundary layer thickness near the trailing edge region and thus, reduce the intensity of the wake impinging on the propeller. The ultimate goal is then to reduce the noise penalty due to the presence of the upstream pylon and bring the propeller noise levels to those of an isolated configuration. The aerodynamic measurements, especially the flow mapping performed through hot-wire anemometry indicated a major reduction in the wake velocity deficit. Given some non-uniformity on the blowing outflow, the regions near the propeller hub were subjected to some overshooting, while the ones near the blades tips still had some remaining local velocity deficit. For some stations near the 60% blade radius, the wake was completely eliminated and the propeller inflow velocity profile was uniform. Unfortunately, it was not possible to control the blowing mass flow. Therefore, there is a specific free stream speed value, where the blowing provides the best results, which was found to be close to 16 m/s. The aeroacoustic measurements allowed for quantitative and qualitative analyses on the propeller noise emissions. It was found that the installation effects resulted in noise increases especially at the tones of the blade passage frequency and higher harmonics. For the blown configuration, significant noise reductions were achieved, especially at the tones of the higher harmonics of the BPF, despite some increase in broadband noise for higher frequencies. For some frequencies, the noise levels of the isolated configuration were achieved, as was originally intended. These results confirm the application of pylon blowing as an effective noise reduction solution for the pusher propeller configuration.

Keywords: Pusher propeller. Installation effects. Wake deficit. Propeller noise. Pylon blowing.

RESUMO

REGO, L. F. L. **Desenvolvimento de um Sistema de Sopro para uma Configuração Pilone-Hélice *Pusher* com o Estudo dos Fenômenos Aerodinâmicos e Aeroacústicos Associados**. 2017. 213p. Dissertação (Mestrado) – Escola de Engenharia de São Carlos, Universidade de São Paulo, São Carlos, 2017.

Este documento contém as atividades envolvidas no desenvolvimento de um sistema de sopro tangencial, a ser integrado a um pilone, montado a uma hélice em configuração *pusher*. Este modelo foi construído de modo a representar uma nova configuração de aeronaves turboélice, conhecida como *open rotor*, que tende a ser mais eficiente em termos de consumo de combustível, que os atuais aviões com motores *turbofan*. Entretanto, existe ainda um entrave à aplicação prática da tecnologia *open rotor*, relacionado aos níveis de emissão de ruído, especialmente das hélices. Além do ruído próprio da hélice, existe também um mecanismo adicional de geração de ruído, que provém da interação entre a esteira do pilone e a hélice, e está relacionado ao surgimento de uma componente transiente de carregamentos nas pás. Este efeito da interação da esteira do pilone com a hélice foi investigado através de ensaios em túnel de vento, com o objetivo de promover um melhor entendimento dos fenômenos aerodinâmicos e aeroacústicos, que ocorrem neste tipo de configuração. A seguir, uma possível solução foi desenvolvida, de modo a mitigar estes efeitos de instalação na hélice, baseada no controle do escoamento ao redor do pilone. Um sistema de sopro tangencial foi integrado ao pilone, com o objetivo de reduzir a espessura da camada limite na região do bordo de fuga e, consequentemente, diminuir a intensidade da esteira a montante da hélice. O objetivo principal é, então, eliminar ou reduzir a componente de ruído, proveniente dos efeitos de instalação, e trazer os níveis de ruído para valores próximos aos de uma hélice na configuração isolada. Os ensaios aerodinâmicos, especialmente o mapeamento do escoamento, com anemômetro de fio-quente indicaram uma grande redução no déficit de velocidades na esteira do pilone. Houve certa não-uniformidade no escoamento de saída do sopro, com regiões próximas à raiz da hélice com velocidade superior àquela do escoamento livre local, enquanto que próximo às pontas, ainda havia certo déficit de velocidades. Para algumas regiões, especialmente próximo aos 60% do raio da pá, a esteira foi completamente eliminada. Não foi possível, nos testes, controlar a vazão do sopro. Dessa forma, os resultados com a aplicação do sopro foram mais positivos para uma certa região de velocidades, próximas a 16 m/s. Os ensaios aeroacústicos permitiram análises quantitativas e qualitativas no ruído das hélices. Os efeitos de instalação tendem a produzir aumento de ruído, especialmente nos tons da frequência de passagem de pá, e seus harmônicos. Com o sopro atuante, grandes reduções de ruído foram obtidas, especialmente nos harmônicos superiores, apesar do aumento da componente de banda larga em altas frequências. Para algumas frequências, os níveis de ruído da hélice isolada foram obtidos, confirmando a aplicação do sopro em pilone, como mecanismo efetivo de redução de ruído em uma hélice *pusher*.

Palavras-chave: Hélice *pusher*. Efeitos de instalação. Déficit de velocidades na esteira. Ruído de hélices. Sopro em pilones.

LIST OF FIGURES

LIST OF TABLES

LIST OF ABBREVIATIONS AND ACRONYMS

IATA	International Air Transport Association
ICAO	International Civil Aviation Organization
NASA	National Aeronautics and Space Administration
TRL	Technology Readiness Level
LTO	Landing/Take-off
FAA	Federal Aviation Administration
ATP	Advanced Turboprop
DOC	Direct Operational Costs
UDF	Unducted Fan
CAEP	Committee on Aviation Environmental Protection
LAE	Laboratory of Aerodynamics (EESC-USP)

LIST OF SYMBOLS

B	Blade number
c	Pylon chord
C_P	Pressure coefficient
C_T	Thrust coefficient
D	Propeller diameter
f	Frequency
I	Integral wake velocity deficit
J	Advance ratio
k_1 / k_2	Yaw factors
m	Harmonic number
$\dot{m}$	Mass-flow
n	Rotational speed
n_{crit}	Amplification factor
OASPL	Overall sound pressure level
p	Atmospheric pressure
P_{ref}	Reference pressure
P_S	Static pressure
PSD	Power spectral density
q	Dynamic pressure
r	Propeller radial station
R	Universal gas constant
R	Propeller radius
SPL	Sound pressure level
T	Temperature
u	Local flow speed (x-direction)
U / V	Velocitites in probe coordinates
u_turb	Turbulence level (x-direction)
U_1 / U_2	Velocities in wire coordinates
U_{1cal} / U_{2cal}	Calibrated velocity
U_∞	Free stream speed

z^*	Mach radius position
α	Angle of attack
α_1 / α_2	Angles in wire coordinates
β	Blade pitch angle
γ	Ratio of specific heats
δ	Boundary layer thickness
δ^*	Boundary layer displacement thickness
η	Propeller efficiency
θ	Axial directivity angle
ρ	Density
Φ	Circumferential directivity angle
ω	Angular velocity

CONTENTS

1 INTRODUCTION

1 INTRODUCTION

The growth in the world air traffic has been demanding increasingly efficient aircraft, especially concerning fuel consumption. Depending on the mission, fuel expenses can reach from 25 to 35% of the direct operating costs for aircraft operation (IATA ECONOMIC BRIEFING, 2010). Therefore, higher fuel efficiencies would mean cost reductions for the aircraft operator and higher profit, due to increased payload capability.

In addition to the economic benefit, there is also the environmental aspect for reducing fuel consumption. The restrictions for CO_2 and NO_X emissions in the atmosphere are also becoming more stringent. In consequence, the design and operation of more efficient aircraft must also consider these restrictions, since they are already of great concern for several regulatory agencies.

In February 2016, ICAO issued new standard values for CO_2 emissions, to be adopted by the entire aeronautical sector. This new document determines a reduction of 4%, compared to current levels, on the emission levels for cruise flight. Depending on the aircraft's weight or category, this reduction can reach values up to 11% (INTERNATIONAL COUNCIL ON CLEAN TRANSPORTATION, 2016). On the table shown in Figure 1, the current emission metrics are displayed, according to the ICAO measurement criteria, and the targets for later years.

Figure 1 – Current values and targets for CO_2 emissions, according to each aircraft category

Aircraft category[1]	MTOM (tonnes)	Metric Value (kg/km)			% reduction	
		2015 worst	2015 average	2028 Target[2]	Worst aircraft	Average aircraft
Very large aircraft	>350	2.95	2.93	2.62	11%	10%
Twin aisle	120 - 350	1.88	1.70	1.75	7%	0%
Single aisle	60 - 120	0.94	0.91	0.86	9%	6%
Regional jets	13.5 - 60	0.71	0.69	0.68	3%	0%
Business jets	<60	0.64	0.56	0.61	6%	0%
Freighters	n/a	2.13	2.06	1.92	10%	7%
Average		1.59	1.49	1.46	8%	4%

[1] Example aircraft include VLA: A380, Twin Aisle: B-777, Single Aisle: A320, Regional Jet: Embraer E-190, Business Jet: Gulfstream G550, Freighter B777-F
[2] Assumes the same MTOMs in the 2015 sales mix. Actual required reductions will vary if the sales mix changes over time
[3] Also with less than 19 certified seats

Source – International Council on Clean Transportation (2016)

Those goals must then be approved by the aviation authorities of each country, so that afterwards they can become regulations and hence, mandatory. According to ICAO, new aircraft already applying for certification must meet these new standards by 2020, and aircraft already in production must do so by 2023, since they may require a supplemental type

certificate. As of 2028, all operating aircraft must be in conformity, so that they are allowed to be produced and operated (INTERNATIONAL CIVIL AVIATION ORGANIZATION, 2016).

Besides ICAO, other institutions have their own goals, concerning aircraft environmental impact. NASA, for example, has defined standards of pollutants and noise emissions that should have been achieved by 2015, with a progressive reduction until 2025, as shown in Figure 2. They estimated that these targets would be attained with the incorporation of technologies that, at that time, were in middle vales of TRL (4 to 6) (GUYNN et al., 2011).

Figure 2 – Targets for NO_X and noise emissions, and fuel burn for future aircraft, according to NASA

TECHNOLOGY BENEFITS*	TECHNOLOGY GENERATIONS (Technology Readiness Level = 4-6)		
	N+1 (2015)	N+2 (2020**)	N+3 (2025)
Noise (cum margin rel. to Stage 4)	-32 dB	-42 dB	-71 dB
LTO NOx Emissions (rel. to CAEP 6)	-60%	-75%	-80%
Cruise NOx Emissions (rel. to 2005 best in class)	-55%	-70%	-80%
Aircraft Fuel/Energy Consumption‡ (rel. to 2005 best in class)	-33%	-50%	-60%

* Projected benefits once technologies are matured and implemented by industry. Benefits vary by vehicle size and mission. N+1 and N+3 values are referenced to a 737-800 with CFM56-7B engines, N+2 values are referenced to a 777-200 with GE90 engines

** ERA's time-phased approach includes advancing "long-pole" technologies to TRL 6 by 2015

‡ CO_2 emission benefits dependent on life-cycle CO_{2e} per MJ for fuel and/or energy source used

Source – Guynn et al. (2011)

NASA names as "N+1" single-aisle, subsonic and civil aircrafts, that are capable of being more efficient than the current Boeing 737 and Airbus A320 families. The NO_X emission of those aircrafts must be 60% smaller and the fuel consumption 33% less. The other goal is related to noise, whose levels must have a 32 dB cumulative margin, relative to the Stage 4 of FAA Part 36 and ICAO's Chapter 4. Also according to NASA, the future goals (N+3) will not be achieved with only small changes to current airframe and engine configurations. New technologies will have to be incorporated and non-conventional aircraft still on research stages may have to be adopted (BERTON, 2012).

This concern with fuel consumption in the aeronautical sector is not current. One of the main events that boosted the search for more efficient engines was the Oil Crisis in 1973, which allowed for the development of several research programs on this topic all around the world. One of them was the *Advanced Turboprop* (ATP) by NASA, which considered the use of turboprop engines in the commercial aviation sector as a possible solution for the low propulsive efficiency of the aircraft. At that time, same as in the present, NASA envisioned the application of non-conventional technologies as a way to reach its goals.

1.1 TURBOPROPS VS. TURBOFANS

Turboprop engines display a higher propulsive efficiency, when compared to turbofans, due to the high bypass levels associated with the former. This effect can be demonstrated through the Actuator Disc Theory, according to which, a rotor, modelled by a two-dimensional disk, injects momentum in a flow passing through it and thus a reaction in the form of thrust is generated. By neglecting losses, and considering the flow as irrotational, the Bernoulli Equation can be applied at points upstream and/or downstream of the disc and the thrust produced will be equal to the increase in flow momentum. By defining the (ideal) propulsive efficiency of the disc as the ratio between the work produced and the total energy, the following equations can be obtained (HOUGHTON; CARPENTER, 2003).

$$T = \dot{m}(V_s - V) \qquad \text{Equation 1}$$

$$\eta = \frac{V}{\frac{1}{2}(V_S + V)} \qquad \text{Equation 2}$$

Source – Houghton and Carpenter (2003)

From the equations above, it is possible to conclude that the thrust will be a function of the mass flow through the disc ($\dot{m}$), the free stream speed (V) and the velocity in the slipstream (V_S), which also define the propulsive efficiency. Therefore, the maximum efficiency will be attained, when the acceleration imposed to the fluid is minimum, that is, $V_s/V \sim 1$. Nevertheless, in order to produce acceptable thrust levels, it is necessary for the mass flow to be high, which in turn means a larger disc cross-section and diameter (HOUGHTON; CARPENTER, 2003). Despite increasing the disc efficiency for a fixed amount of produced thrust, larger diameters also mean more weight and inertia, aside from being related to other rotor operation parameters, such as tip speed and advance ratio.

For turbofan engines, the bypass will be defined as the ratio between the cold jet, which passes through the fan, and the hot jet, which passes through the engine core. Therefore, in order to increase the turbofan propulsive efficiency, the fan diameter (equivalent to the actuator disc) must be increased. There are, however, constructive constraints related to the nacelle size, which means there must be a trade-off between efficiency and increased weight and drag. Presently, the most efficient turbofans used in civil aviation reach bypass ratios around 12, such as the Pratt & Whitney PW1100-JM, which equip the new Airbus A320neo aircraft (PRATT & WHITNEY PUREPOWER ENGINE FAMILY SPECS CHART, 2012).

Turboprops, on the other hand, can reach bypass ratios in the order of 50, and thus are the most efficient engine configurations, since a larger quantity of air is slightly accelerated.

Consequently, for this type of engine, the dependency on combustion for thrust generation will be much smaller than that of turbofans, and hence the fuel consumption will also be smaller, for the same operating condition. It is estimated that turboprops allow a 20% reduction in fuel burn, such as displayed in Figure 3 (TRENDS IN THERMAL AND PROPULSIVE EFFICIENCY, 2016).

Figure 3 – Fuel burn and bypass ratio comparison for different engine types

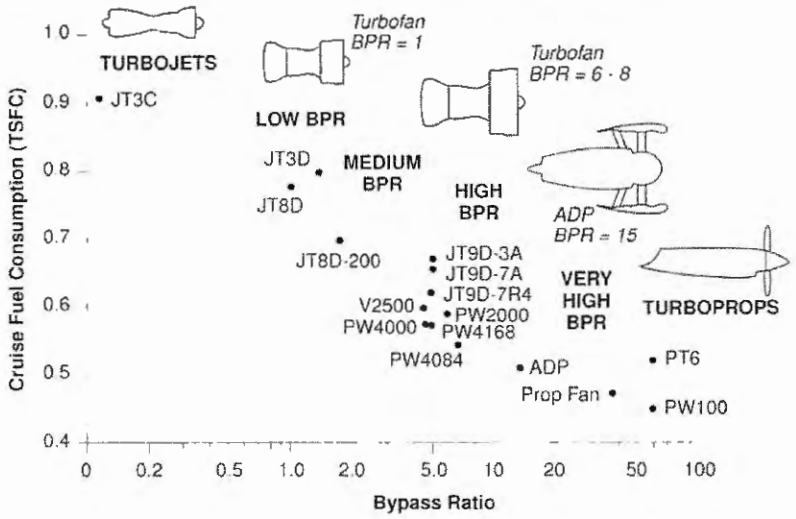

Source – Trends in Thermal and Propulsive Efficiency (2016)

Despite their higher propulsive efficiency, turboprop engines have a huge setback, which limits their application, especially in long-range commercial aviation. Due to the large rotor diameter, and the absence of a nacelle around the propeller, the flow speed at the blade tips will be much higher than at the hub. At that region, the flow can reach the transonic regime, in which the compressibility effects such as the formation of shock waves will highly affect the aerodynamic characteristics of the propeller and its performance. Moreover, load variations induced by shock waves can also cause structural problems and increased noise emission.

A study was carried out by Stack et al. (1950), in order to determine the performance degradation in propellers caused by compressibility effects. The results indicated that, for Mach numbers up to 0.85 at the blade tips, the propeller efficiency remains approximately constant. For higher tip Mach values, the efficiency tends to decrease almost linearly, with the rate depending on the blade pitch angle (β), and showed reductions of up to 15% at the highest tested speed values. This trend is illustrated in Figure 4.

Considering the compressibility effects, turboprop engines do not seem like a viable choice for medium/long range commercial aviation, since the aircraft at this category have cruise speeds around 900 km/h, or Mach 0.8 approximately. Since this is the free stream speed

around the aircraft, the flow around some blade sections, especially near the tip, would most likely be in transonic regimes, undergoing shock wave formations. Therefore, in order to avoid such problems, the operating conditions for propeller-powered aircraft have to be constrained to low/medium subsonic regime, which is usually applied for general and regional aviation categories.

Figure 4 – Effect of Mach number increase, up to transonic values, in the propeller efficiency

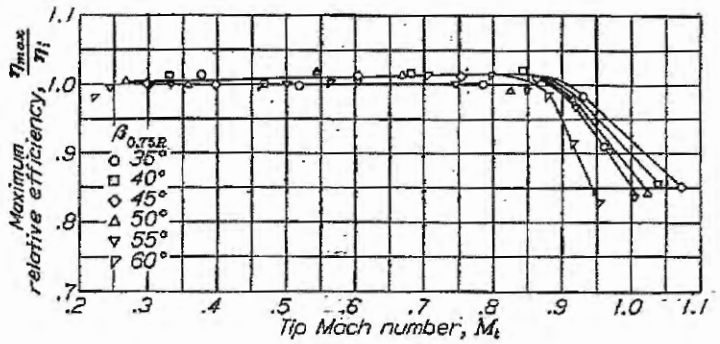

Source – Stack et al. (1950)

With the purpose of making turboprops viable for operation in medium range commercial aviation, and thus profit from all the benefits from this kind of engine (especially the reduced fuel burn), NASA had developed the *Advanced Turboprop* program. This program consisted in large efforts from many research centers to create a propeller configuration, with optimized bladed geometry, which allowed the usually higher propulsive efficiency from turboprops to be sustained, even for higher flight speeds. Thereby, the configuration presently known as *open rotor* was conceived.

1.2 OPEN ROTOR ENGINES

To ensure that the propeller kept its efficiency for higher Mach numbers, several modifications on the blades geometry were necessary. The researchers in the ATP program employed a complete makeover to the usual propeller design, by reducing the blades thickness, increasing the chord and adding sweep, especially near the tips. The disc diameter was also reduced and the number of blades increased to increase blade loading. Adjacent components, such as the spinner, were designed following the Area Rule. Owing to all these modifications, the objective of reducing the compressibility effects at the propeller was achieved and a new configuration, named *propfan*, was created (WHITLOW JR.; SIEVERS, 1984). This configuration is displayed in Figure 5, where the engine is installed in the aft-fuselage of a real aircraft (MD-80), and was used by GE for some of the ATP tests, with the name of *UnDucted Fan* (UDF).

Figure 5 – Unducted fan installed in a MD-80 aircraft

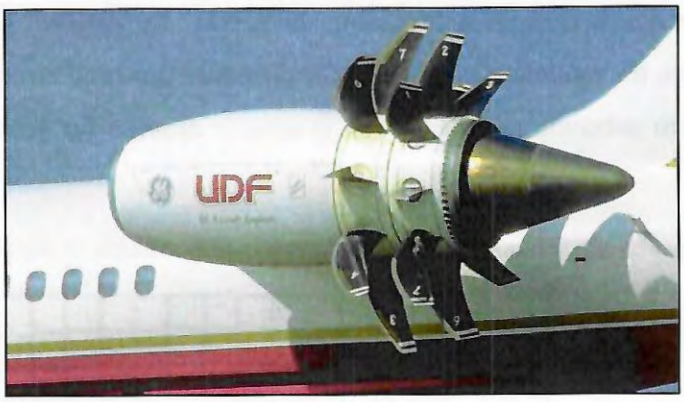

Source – Sustainable Skies (2016)

Presently, this configuration is known as *open rotor*, due to the absence of casing, and it is usually employed with a pair of counterrotating propellers, as shown in Figure 5. The second rotor was added, in order to avoid thrust losses due to the rotation effects in the slipstream, and so to ensure that the increase in momentum occurs only in the axial direction, as the flow passes through the discs (WHITLOW JR.; SIEVERS, 1984).

One of the main aspects considered during the development of the open rotor was the savings in fuel consumption. As a part of the ATP program, the Lockheed Company conducted investigations on the feasibility of this new configuration, with the ultimate goal of quantifying this parameter in terms of fuel savings and reduction in operational costs. For the analysis, two different aircraft configurations were considered, one equipped with a characteristic turbofan engine from that time (bypass ratio of 5.4), while the other was equipped with the open rotor. Parameters from actual aircraft were taken into account for this study, in which the weight, performance and even certification requirements were evaluated, aiming to perform an analysis as realistic as possible (REVELL; TULLIS, 1977).

Both aircraft had wing-mounted powerplants. So, owing to the higher noise generated by the open rotor, it was necessary to consider different acoustic treatment, in order to provide 48 dB of cabin noise reduction. This resulted in an increase of 3.3% in total weight, for this configuration. Even so, for different mission profiles, with varying range and cruise Mach, comparing both aircraft, it was found that the open rotor presented less fuel consumption than the turbofan, reaching savings of about 21%. These results were converted into Direct Operational Costs (*DOC*), by considering the fuel prices at that time. Comparing the performance of both aircraft, the open rotor provides a 10% reduction in the *DOC*, as shown in the Figure 6 charts (REVELL; TULLIS, 1977).

Figure 6 – Fuel burn and DOC comparison for open rotor- and turbofan-equipped aircraft

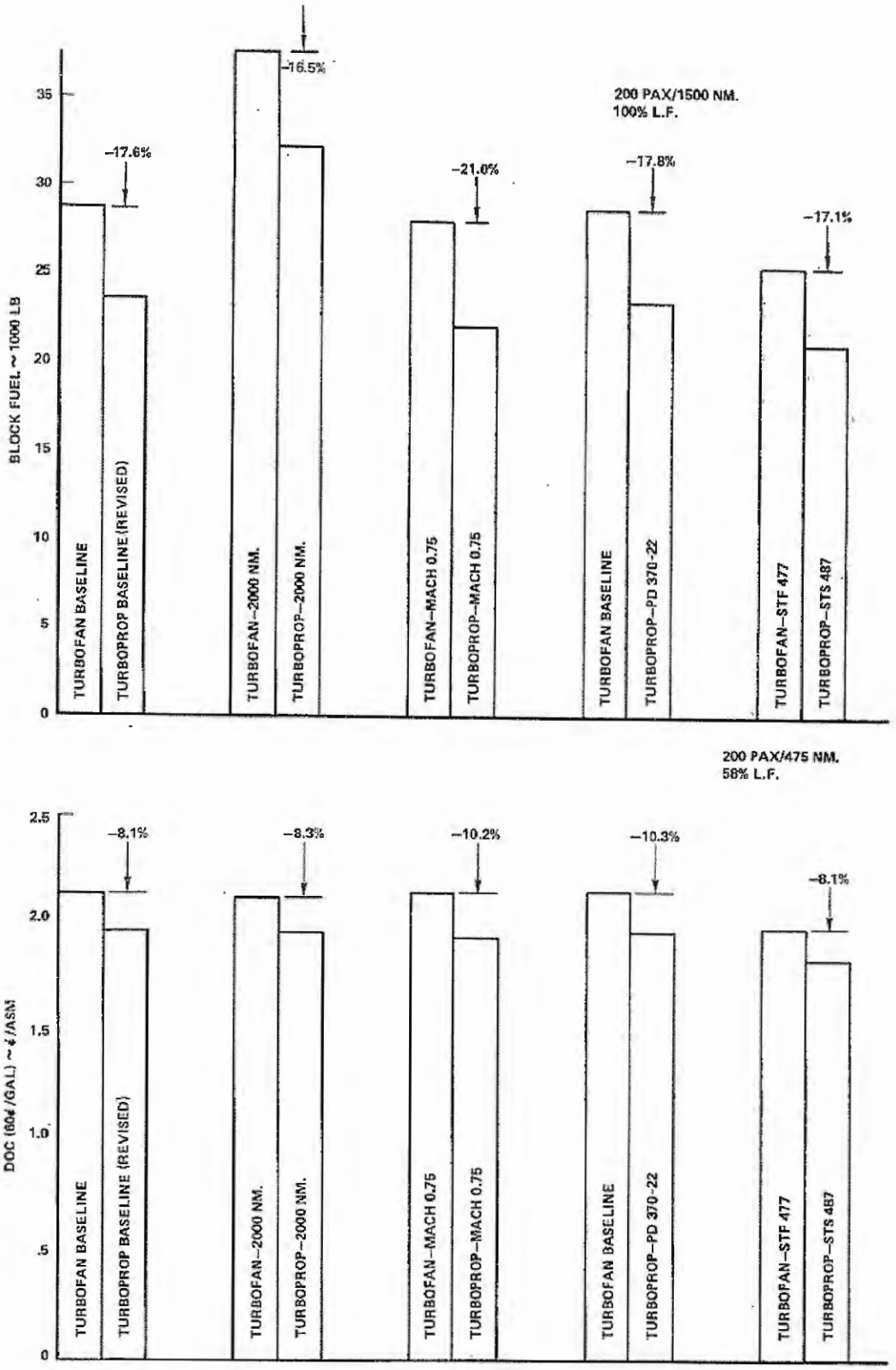

Source – Revell and Tullis (1977)

Based on the obtained data, it was possible to conclude that open rotor engines provide the best performance results for operations in short to medium ranges, in which the aircraft spends more time in lower speeds (condition of highest efficiency for the turboprop), or even for a longer range mission at a cruise Mach of 0.75 (REVELL; TULLIS, 1977).

Other important studies involving open rotors were conducted, in order to assess the best engine placement on an aircraft (wing or aft-fuselage mounted). Using aircraft design criteria, Mann and Stuart (1985) defined a group of parameters for a sensitivity analysis, such as performance and noise, among others. Aside from the position in the aircraft, the possibility for single rotors or a counterrotating pair, and tractor or pusher configurations was considered. According to the authors, the results indicated that the best configurations are wing-mounted tractor and aft-fuselage-mounted pusher (MANN; STUART, 1985).

In a subsequent study, Blythe and Smith (1985) assessed the characteristics for the two best open rotor engine placements previously described. For the analysis, the authors compared the characteristics of each configuration, by considering a regional aircraft, with capacity for 100 to 120 passengers. The results are included in Table 1.

Table 1 – Comparison between wing- and fuselage-mounted open rotors

	Wing Mounted	**Aft-Fuselage Mounted**
Wing Position	High Wing	High / Low Wing
Ideal Propeller Configuration	Counterrotating Tractor	Counterrotating Pusher
Propeller Flow	Uniform inflow, but for higher angles of attack there is an influence of the wing upwash	Interaction effects with the wing downwash or the pylon wake
Cabin Noise	Higher levels of cabin noise and more acoustic treatment is necessary	Lower levels of cabin noise
Trim Drag	No additional trim drag	Higher ground clearance gives rise to a trim drag component
Wing Flow	Interaction with the propeller slipstream	Possible benefits from the propeller inflow
Engine Number	2 or 4 (military application)	2 (possibly 3)

Source – Adapted from Blythe and Smith (1985)

For the wing-mounted configuration, it is required for the wing to be high mounted in the aircraft, so there is enough ground clearance for the propellers. A high clearance is also necessary for the fuselage-mounted, for the take-off condition, in which the rear part of the

aircraft is closer to the ground. For this case, since the engines must be placed in a higher position, the thrust line will not coincide with the wing, which generates a trim drag component (BLYTHE; SMITH, 1985).

Regarding the propeller flow quality, the tractor configuration would be more advantageous, since there will be no disturbance in the upstream flow, such as the pylon wake. However, the wing-mounted tractor has a setback, which becomes more evident for conditions of high angles of attack. The upwash generated at the wing leading edge will tend to change the flow direction, which will no longer be parallel to the propeller axis, as shown in Figure 7. This produces a non-axisymmetric inflow, causing the blade loading to change during a revolution, leading to vibrations and noise generation (METZGER, 1995).

Figure 7 – Propeller unsteady loading caused by wing upwash

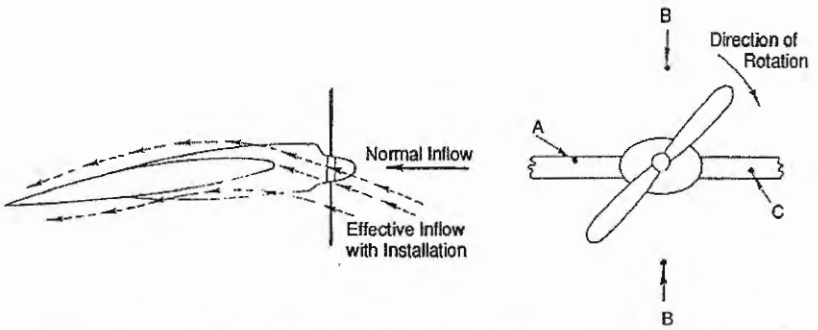

Blade Location	Velocity Vectors Rotation, V_{rot}; Inflow, V_{in}	Relative Velocity V_{rel}	Angle of Attack, α	Blade Loading
A	Blade Airfoil	Lowest	Lowest	Lowest
B	α, V_{rel}, V_{in}, V_{rot}	Average	Average	Average
C		Highest	Highest	Highest

Source – Metzger (1995)

Among the considered aspects, the biggest disadvantage for the wing-mounted configuration is the cabin noise, which would require more acoustic treatment for the aircraft, resulting in increased weight. The unsteady loads caused by the wing upwash, as previously mentioned, also contribute to noise generation. For the aft-fuselage-mounted pusher, the noise sources are placed as far as possible from the cabin (BLYTHE; SMITH, 1985). In terms of certification requirements, considering a rotor non-containment scenario, the pusher configuration is also better regarded, since the propeller is positioned relatively far from the passengers and primary wing structures.

From these studies regarding open rotor, it was verified that the noise produced by these engines is an important and decisive factor, which influences the aircraft design already at conceptual stages (engine placement). The absence of a casing around the propeller, despite being one of the major contributors for its high propulsive efficiency, is also one major issue, since there is no structure to act as noise shielding, as the nacelle works for the turbofan.

Therefore, noise is currently the greatest barrier for the practical application of this technology, especially for the commercial aviation sector. In the following section, the main noise sources in an open rotor configuration will be described, with a brief explanation of the noise generation mechanisms.

1.3 NOISE SOURCES IN OPEN ROTORS

For an open rotor configuration, each of the engine components will act as a noise source, such as the propeller (single rotor or counterrotating), the compressor, the turbine and the jet exhaust. Moreover, there are increased noise emissions resultant from the interaction between these components, for example the frontal rotor (R1) wake and tip vortices on the aft rotor (R2). For the pusher configuration, another important interaction effect occurs between the pylon wake and the downstream propeller. The effect of the angle of attack on the propeller can also be considered for noise generation, since it is directly related to the loading on the blades. There can also be an interaction effect between the propeller flow and the fuselage boundary layer, which tends to be thick at this region. These main noise sources are displayed in Figure 8 (HOFF, 1990).

Figure 8 – Noise sources in an open rotor configuration

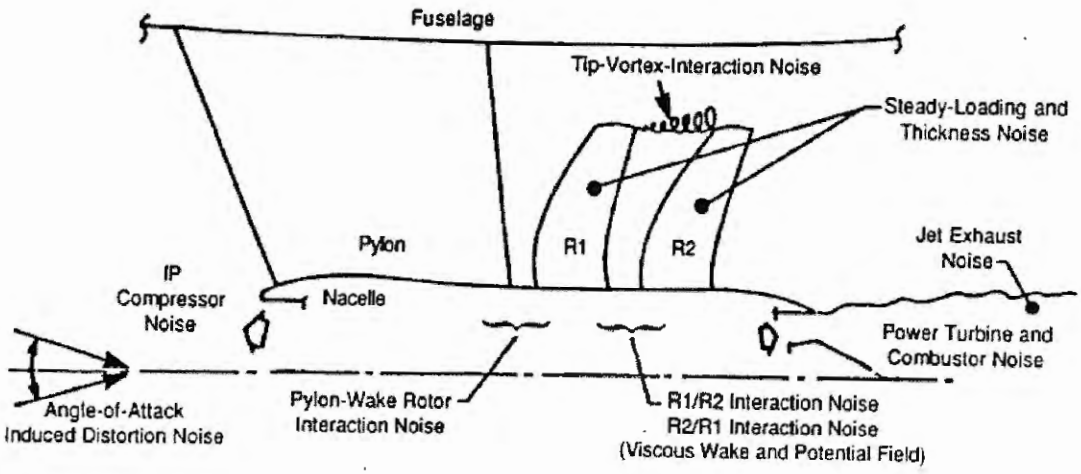

Source – Hoff (1990)

For an open rotor, the propeller is the dominant noise source, since it has no shielding barrier to counteract its high levels emissions. Propeller-generated noise has both tonal and broadband characteristics. In the noise spectrum, tones occur as peaks at specific frequency values, which tend to cause a higher discomfort in an observer, while the broadband extends in a wide frequency range. A typical propeller noise spectrum is displayed in Figure 9. The first tonal peak occurs at the blade passage frequency (BPF), which relates the blade number (B) and the propeller rotational velocity (ω, in radians per second), as described in Equation 3. The following tones will occur at each of the BPF harmonics (m) (MARTE; KURTZ, 1970).

Figure 9 – Typical propeller noise spectrum with tonal and broadband components

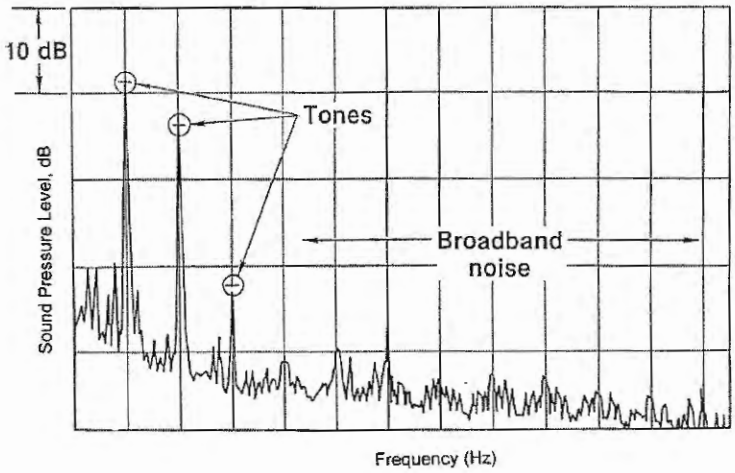

Source – Metzger (1995)

$$BPF = m * B * \omega/(2\pi)$$ Equation 3

Source – Marte and Kurtz (1970)

In terms of aeroacoustic analogy, the sound emitted from a propeller is composed by the three types of sources: monopoles, dipoles and quadrupoles. The monopole sources are related to the physical displacement of air caused by the blades (thickness noise), and has a tonal characteristic. The dipole sources are related to the aerodynamic loading produced on the blades, either steady or fluctuating (due to non-uniformities), and have a strong tonal characteristic. There are also dipoles related to vortex shedding, which increases the broadband noise. Finally, the quadrupole sources are related to the turbulence levels at the flow leaving the trailing edge, and are also responsible for the broadband noise (METZGER, 1995). These different noise generation mechanisms, with their respective characteristics are illustrated in Figure 10.

Figure 10 – Noise generation mechanisms in a rotor

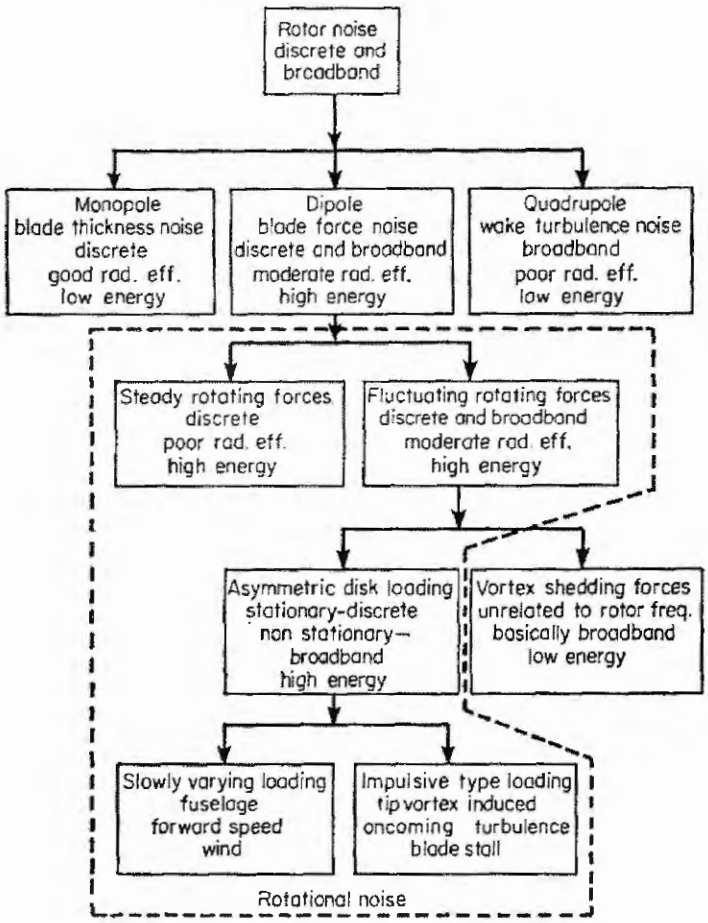

Source – Wright (1969)

These noise generation mechanisms can be affected by the interaction between the propeller and other components, like the fuselage, the pylon or even another rotor, for counterrotating configurations. For the latter, the full spectrum will have, aside from the tones at each rotor BPF and harmonics, tonal peaks at linear combinations of the two rotors frequencies, in the form of $m_1 B_1 \omega_1/(2\pi) + m_2 B_2 \omega_2/(2\pi)$, for example, where the subscripts 1 e 2 represent the fore and aft rotors, respectively (HANSON, 1985).

The interaction with other components, such as the pylon, are related to non-uniformities that will be part of the propeller inflow. The pylon wake, for example, produces a region of lower velocity at the inflow, which in turn induces fluctuations on the blade loads, as it passes this region. These variations occur in a harmonic fashion, and cause structural vibrations and noise increase (GENTRY JR.; BOOTH JR.; TAKALLU, 1990). This increase in noise is usually referred to as installation effects, which have been extensively studied, since the ATP Program. These effects can be regarded, in terms of noise spectra, as shown in Figure 11.

Figure 11 – Installation effects on open rotor noise spectra

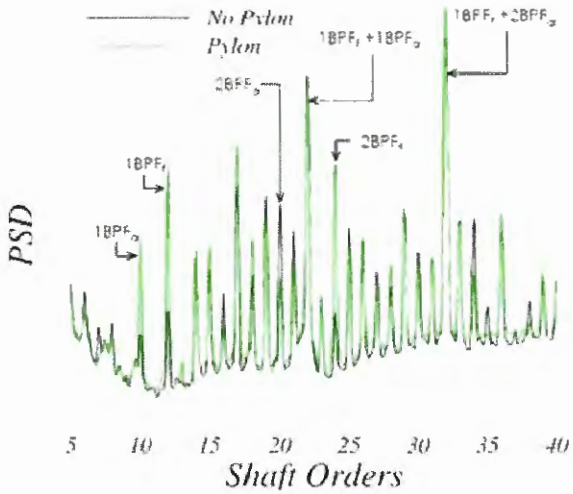

Source – Adapted from Envia (2010)

From Figure 11, it is possible to verify that these spectra are from a counterrotating configuration, with a different number of blades for each rotor, since there are two different peaks, corresponding to each rotor BPFs. The aft rotor has fewer blades and thus will have a lower blade passage frequency. The interaction tones are also shown as linear combinations of the each rotor frequencies, and have noise levels as high as or even higher than the single rotor tones (ENVIA, 2010).

When the pylon is introduced, the installation effects tend to increase the sound pressure level for the tones, especially for the frontal rotor, since it is affected directly by the pylon wake. The aft rotor peaks also show an increase, but to a lesser extent. The interaction tones, on the other hand, do not seem to be affected by the presence of the pylon. For the installed configuration, there is a change in the relative strength of sources, and the asymmetric disc loading in the frontal rotor tends to become the dominating one, as shown in the phased array measurements of Figure 12 (ENVIA, 2010).

Figure 12 – Phased array measurements indicating the unsteady loading as dominant noise source

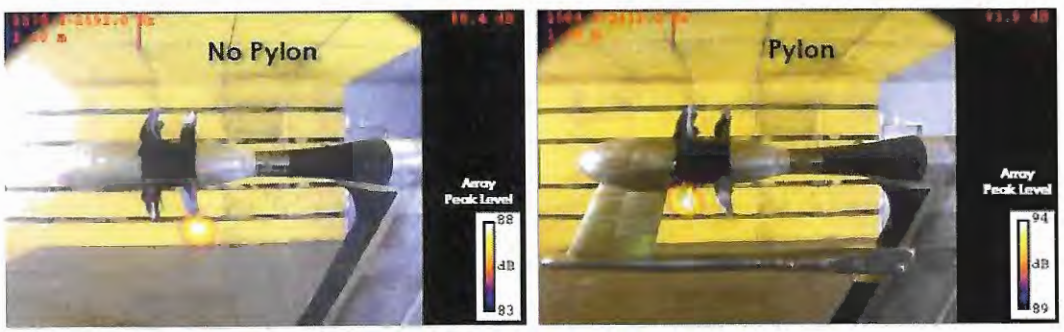

Source – Adapted from Envia (2010)

In the Section 2.1 of this work, the noise generation mechanisms in a propeller will be described with further details, focusing on the physical phenomena responsible for each mechanism and their particularities. The aerodynamic and aeroacoustic effects resultant from the interaction between the propeller and the wake from an upstream pylon will also be assessed. In this work, focus will be given only to the propeller noise, and the contribution of other components, such as the compressor, turbines and jet exhaust, to the total open rotor noise will not be evaluated.

1.4 GOALS AND REQUIREMENTS FOR NOISE REDUCTION

At the time of the first researches involving open rotors, there was already a concern with the noise levels emitted from this configuration. During the UDF tests, the goals of fuel burn reduction were reached, and there was still a positive margin, regarding the noise regulations of the time, which was the Chapter 3, from ICAO's Annex 16. An optimization of the configuration was not possible at the time, since there were not many tools available, capable of performing a trade-off between performance and aeroacoustic parameters. So, if further noise reductions were necessary, the configuration would have to be redesigned, with a consequent degradation of its performance, and its benefits from the commercial and environmental points of view (reduced fuel burn) would be lost (VAN ZANTE et al., 2014).

Nonetheless, instead of the noise regulations, the fall of fuel prices at the late 80s was the major contributor in halting the ATP program. Since then, very few studies were carried out on the topic until 2005, when there was a renewed interest on this configuration, due to its potential environmental benefits. However, the open rotor designed during the 80s is no longer capable of meeting the present levels of noise regulations. Since 2006, the Chapter 4 from Annex 16 was adopted as the new perceived noise regulation. The limits are defined based on measurements in three different references: flyover, sideline and approach. Each one has its particularities, as shown in Figure 13 (GUYNN et al., 2011):

Figure 13 – References for aircraft perceived noise measurements

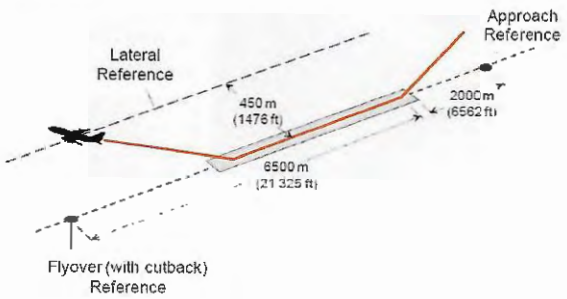

Source – Guynn et al. (2011)

During the certification tests, the aircraft noise levels must be measured for each of those references, and they must not exceed the established limits. There is also an overall limit, which the sum of the noise for those three references must also not exceed. For the Chapter 4, it was defined that the overall limit from Chapter 3, with a reduction of 10 EPNdB, would be used. Therefore, for aircraft that had noise levels close to the Chapter 3 limits, it was necessary a reduction of 10 dB, in order to meet the new requirements (AIRBUS FLIGHT OPERATIONS SUPPORT & LINE ASSISTANCE, 2003). The noise limits in EPNdB for each Chapter of Annex 16 are shown in Figure 14 (DICKSON, 2013).

Figure 14 – Noise regulations for each Chapter of Annex 16

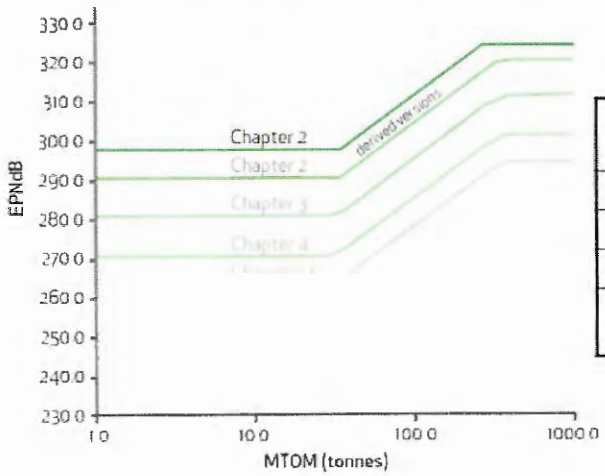

Chapter	Applicable Year	Cum Margin (EPNdB)
2	1972	Ch. 3 –-16
3	1978	0 (Ref)
4	2006	Ch. 3 +10
14	2017 & 2020	Ch. 3 +17 (Ch. 4 +7)

Source – Dickson (2013)

For certification purposes, the noise emitted from an aircraft is measured in EPNdB (Effective Perceived Noise Level in Decibels). This parameter was created in order to assess primarily the annoyance caused in an observer. It takes into account the human response to the spectral shape (tonal content), the noise intensity and the duration. The standard way to calculate this parameter is described in ICAO's Annex 16, since it is not possible to be measured directly (DEPITRE, 2006).

Recently, a further reduction of 7 EPNdB, relative to the Chapter 4 levels, was proposed, and should be adopted sometime between 2017 and 2020. These new limits will be incorporated to the Chapter 14 of Annex 16 (DICKSON, 2013). However, since it is still an ICAO resolution, it is necessary that the certifying authorities of each country adopt these propositions, so that they can be turned into actual certification requirements. Thus, aircraft manufacturers and operators will be given a time frame to adequate their fleet to the new imposed limits.

1.5 CURRENT STATUS OF THE OPEN ROTOR TECHNOLOGY

During the 70s and the 80s, since its conception in a time of extremely high fuel prices, the open rotor technology has been largely investigated. Experiments and simulations in several fields, including aerodynamic, structural, aeroelastic, and aeroacoustic were carried out, in order to completely assess this configuration and optimize is characteristics for the aircraft operational conditions at the time. Since the drop in oil prices, the researches in this field were abandoned and the configuration was frozen.

Presently, aiming to comply with the stringent environmental goals described in the previous sections of this work, stakeholders from all around the world resumed the open rotor researches. Their goal is to make the technology viable for commercial application in current generation aircraft. These new investigations now focus on the optimization of the geometries designed in the past, with the aid of the modern design and analysis tools, based on new design criteria, especially in regards to noise.

In 2011, a group of researchers from different institutions was given the task by ICAO to assess the possibility of noise reduction in new aircraft and engine concepts, including the open rotor. Economic and environmental parameters were also taken into account, so that goals could be defined, in order to put these noise reduction technologies into practice. Regarding the open rotor, the results obtained are shown in Figure 15.

Figure 15 – Open rotor technology development roadmap for application on current aircraft

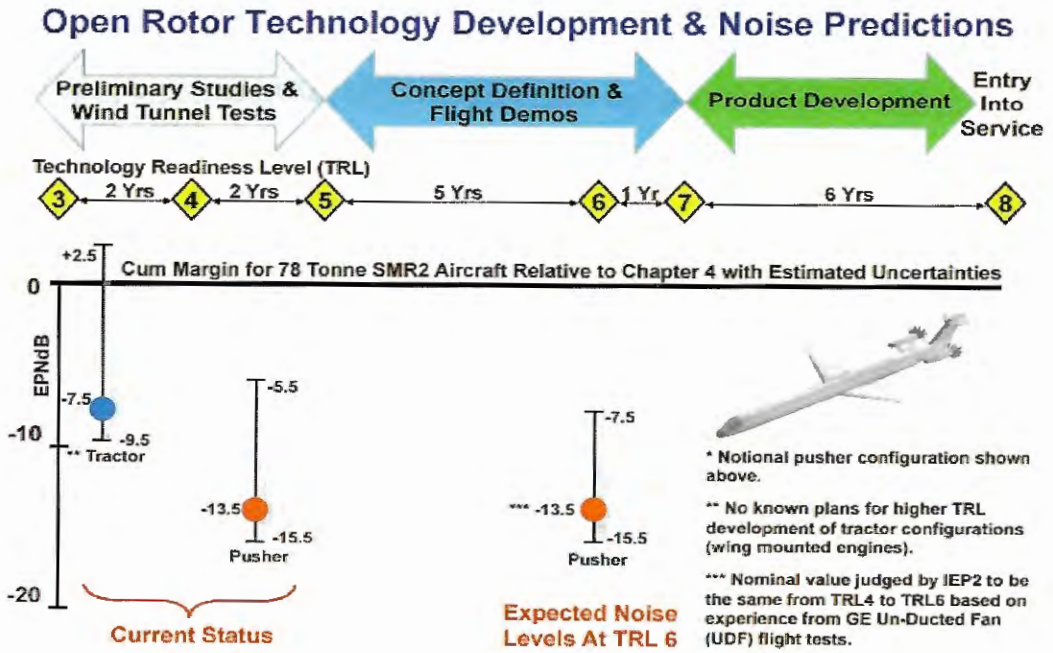

Source – Mongeau et al. (2013)

Initially, the emitted noise levels for the two main aircraft configurations with open rotor engines defined in the ATP program (wing-mounted tractor and aft-fuselage-mounted pusher) were compared, taking the Chapter 4 limits as reference. The results indicated that the pusher configuration presented a lower nominal noise emission than the tractor. For some of the conditions, the latter even surpassed the established limits. This high level of emitted noise is linked to the crossflow at the propeller, due to the wing upwash. Since the flow is not aligned with the propeller axis, the blades will undergo an asymmetric loading and thus generate noise (MONGEAU et al., 2013). These results rendered the tractor configuration inferior to the pusher, so that currently the most accepted concept for open rotor-equipped aircraft is the aft-fuselage-mounted engine configuration.

The main focus of current open rotor research is the field of aeroacoustics. The current numerical tools of CFD and CAA, which were unavailable during the course of the ATP program, are now the major contributors of these researches and are responsible for the advances that the open rotor technology has recently been through. These tools still require, however, experimental validation from aerodynamic and aeroacoustic wind tunnels and flight tests. Therefore, highly complex wind tunnel campaigns were conducted, by testing from full aircraft to high-fidelity open rotor components and subsystems. This combined effort from simulations and experiments has given rise to new open rotor configurations, with performance comparable or even better than the one obtained in the ATP, but now with much lower noise levels.

Using the blade design developed during the ATP as a starting point, many parameters of the open rotor geometry were changed. The blade number was set as 12 for the frontal rotor and 10 for the aft one. However, in order to reduce the blade loading and also the noise, the diameters of the rotors were increased in about 1 m. A clipping to the aft rotor was added, so it has a slightly reduced diameter. This was conceived as a way to mitigate the interaction noise due to the blade tip vortices. A variable pitch control system was also added to the model, which provided both performance and acoustic benefits (VAN ZANTE et al., 2014).

Through tests conducted by GE, the new developed configurations were compared with each other and with the past open rotor design. The chart in Figure 16 illustrates the cumulative margin to the perceived noise limits from Chapter 4, for each of the tested geometries. The red bar displays the noise for the best configuration developed during the UDF tests. The purple one consists in a modified blade design, created in the late 80s, in order to marginally reach the Chapter 4 levels (with consequent aerodynamic and performance degradation). The last two bars (blue and green) represent the new modified designs. The "GEN2A+B" configuration has

also further blade tip modifications to reduce the rotor-rotor interaction noise (VAN ZANTE et al., 2014).

Figure 16 – Noise levels for current and past open rotor configurations, compared to Chapter 4 limits

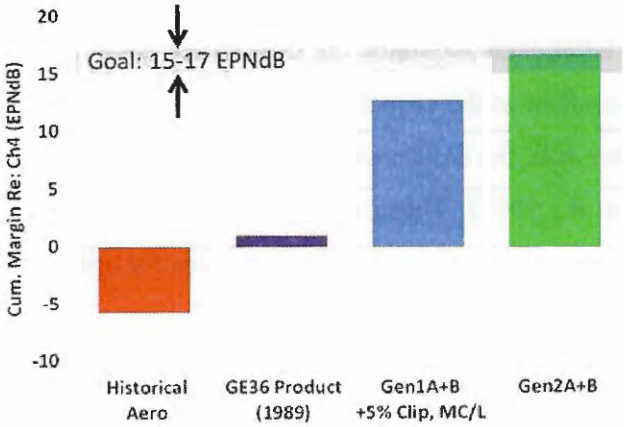

Source – Van Zante et al. (2014)

It can then be verified, by comparing the different versions, that the current open rotor designs have a 17 dB margin to the current levels established in the certification requirements (VAN ZANTE et al., 2014). This means a reduction of approximately 23 dB, compared to the ATP program configuration. Therefore, by considering the aeroacoustic design criteria, these new configurations are highly feasible for practical application.

The performance parameters of the new open rotor configurations were investigated by Hendricks et al. (2013) through modelling of the propulsive system, integrated to a chosen airframe of a single-aisle aircraft, with engines mounted on the aft-fuselage in a pusher configuration. This aircraft concept was picked based on the results obtained by Mongeau et al. (2013), as previously shown, as the most indicated open rotor configuration (with engine mounted on the aft-fuselage), especially for short and medium range missions. Therefore, the configuration analyzed in these tests is the same as the one illustrated in Figure 15. Again, the late 80s open rotor design was compared to the two new configurations. In these analyses, new airframe technologies, inexistent during the ATP program, were considered, such as new composite materials. The main evaluated parameters are shown in the charts of Figure 17 (HENDRICKS et al., 2013).

The empty weight reduction is related to the inclusion of the new composite materials to the aircraft structures, as well as to optimized aerodynamic surfaces. This reduction is counterbalanced by a necessary additional weight, due to the engine mount structures and cabin noise isolation. The net weight, however, shows the results are positive, and this means that an increase in payload can be obtained. The block fuel reduces approximately 40%, for the new

configurations, which translates in a higher efficiency and less operational costs. Moreover, the NO_X emission levels decreased about 75%, and now have an 83.2% margin, regarding the CAEP/6 requirements (HENDRICKS et al., 2013).

Figure 17 – Comparison of the performance and gas emission levels between current and past open rotor designs

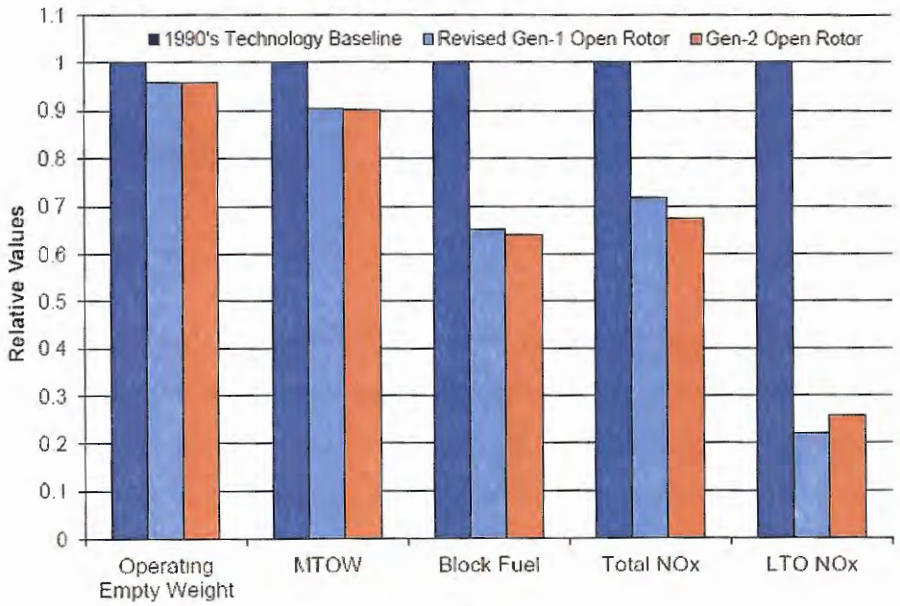

Source – Hendricks et al. (2013)

The investigations of the new open rotor configurations yielded very positive and encouraging results. The technology was brought to present standards and it has become once again the state-of-the-art in propulsive efficiency. Either from the performance, or from the aeroacoustic point of view, the new open rotor rises as a competitive configuration, with a large capability to comply with the future noise and emission requirements. This technology is currently at a medium TRL value, possibly 4 or 5, and several concept definitions and tests are still required before the entry into service. At this stage, the main research focus is to integrate the open rotor with the airframe and to develop its systems and subsystems, which highly increases the complexity of the analyses.

One of these subsystems, currently under intense research, is related to the application of a flow control mechanism on the pylon, in order to mitigate the installation effects of its wake in the propeller inflow. With this flow control, both aerodynamic and aeroacoustic benefits are expected, in regards to the complete elimination of the interaction noise, which was described in Section 1.3. One of the first works in this topic was conducted by Shivashankara, Johnson and Cuthbertson (1990), and consisted in a blowing system mounted in the pylon trailing edge, as show in Figure 18a, to fill the velocity deficit in the wake.

Figure 18 – a) Blowing system mounted in the pylon trailing edge b) SPL reduction for the blown configuration

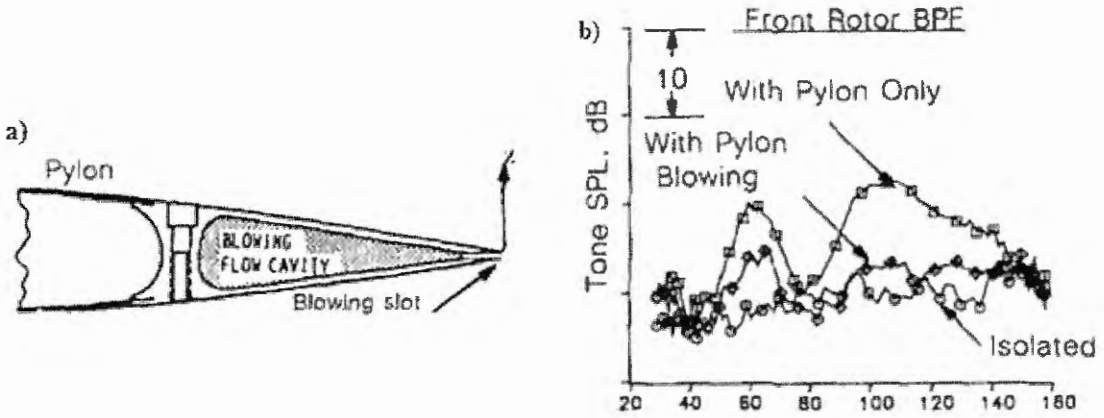

Source – Adapted from Shivashankara, Johnson and Cuthbertson (1990)

Initially the isolated propeller results were compared with the ones from the installed configuration. For the directivity analysis, the model with the pylon displayed higher sound pressure levels, especially at the BPF and harmonics, in nearly all directions. With the application of the blowing system, a great noise reduction was obtained for those frequencies, and the noise practically returned to the isolated levels, as shown in Figure 18b. Thus, the goal of eliminating the wake (or at least reducing its velocity deficit) was reached and a very large reduction of the interaction noise was obtained (SHIVASHANKARA; JOHNSON; CUTHBERTSON, 1990).

After this work was carried out in 1990, the use of pylon blowing was set aside for a long time, since the majority of the researches in open rotor was halted. However, with the renewed interest in this technology, the use of blowing was again considered as an interesting solution for the installation effects in a pusher propeller configuration. In recent years, there was some advancement in the development of this technology, with the focus of optimizing its characteristics, as so to reap the best aerodynamic and aeroacoustic results. These further assessments of pylon blowing will be discussed in Section 2.3 of this work.

1.6 OBJECTIVES OF THIS WORK

Based on the information presented in the previous sections, the current studies in open rotor are related to the practical application of this technology in aircraft and its issues, such as the installation effects for a pusher configuration. Solutions for these adverse effects have also been investigated, such as the application of flow control, specifically pylon blowing, with very encouraging results.

The main objective of this work is then to design a tangential blowing system and integrate it to a model pylon, aiming to mitigate the velocity deficit in the wake region and then reduce installation effects. With the use of pylon blowing, the propeller inflow will become more uniform and, consequently, the fluctuations on the blades loading will be reduced. Ultimately, the interaction noise component should also be reduced and the sound levels should remain as close as possible to the isolated configuration. In order to achieve the expected results, some intermediary goals have been defined:

- Conduct oriented studies, regarding propeller noise and the installation effects due to the presence of an upstream pylon. The previous investigations of the application of pylon blowing will also be studied, and their results will be used as guidance for the conduction of this work;
- Analyze, through wind tunnel tests, the effect of the pylon wake upstream of a pusher propeller, focusing on the phenomena of boundary layer separation and the wake properties from this aerodynamic surface. The interaction effects on the flow around the pylon due to the propeller inflow slipstream should also be verified;
- Design the blowing system, based on a configuration from the literature, also developed at the LAE, for a similar application. A high efficiency for the system, as well as the capacity for integration to the wind tunnel models must be assured;
- Conduct wind tunnel tests to assess the effect of the blowing on the flow at the pylon trailing edge region, aiming for total or partial elimination of the wake velocity deficit. Comparative aerodynamic and aeroacoustic measurements will allow for corroboration of the effectiveness of the blowing system;
- Take conclusions about the obtained results and about the feasibility of the blowing design developed in this work as a solution for the interaction noise problem.

2 LITERATURE REVIEW

2 LITERATURE REVIEW

According to the objectives of this work, the main studies regarding open rotor propeller noise will be described. Initially, this chapter will consider the general noise sources in propellers and their characteristics. Then, the aerodynamic and aeroacoustic effects resulting from the interaction between the pylon and a pusher propeller will explained. Finally, the application of pylon blowing as a flow control mechanism to reduce these installation effects will be evaluated, based on work already conducted in this topic.

2.1 PROPELLER NOISE

The sound produced by rotors, e.g. propellers, fans, turbines and so on, can be classified as self-noise or interaction noise. The former occurs from the steady flow over the blades themselves, while the latter is the result of the encounter between a rotating blade and a time-varying disturbance (BLAKE, 1986).

2.1.1 Propeller Self-Noise

Self-noise sources in propellers may be resultant from potential or viscous flow phenomena. The main potential noise source is called *Loading* or *Gutin Noise*, which is proportional to the steady loading produced on the blades and occurs at the multiples of the blade passage frequency (Equation 3). It results from the aerodynamic loading (thrust and torque) that, despite being steady for a frame of reference moving with the blades, has an unsteady behavior, when considering a fixed point in the acoustic medium, that has no rotation itself. This noise component is dependent on the Mach number, blade number and directivity (BLAKE, 1986).

The loads produced on a rotating blade will be generated from an also rotating pressure field, which will be regarded as an oscillating pressure (sound), considering a fixed point on the disc as reference. This oscillation will have a fixed frequency equal to the times the blade passes that specific point, or the blade passage frequency. The waveform of this oscillating pressure will be determined by the pressure distribution on the blades. This noise component can be represented as an array of stationary dipole sources in the rotor disc, activated at the blade passage (MARTE; KURTZ, 1970). These dipole sources will have a strength equal to the net loading produced by the blade (pressure difference between upper and lower surfaces) at each location (MCALPINE; KINGAN, 2012).

The other component of potential noise sources in rotors is the *Thickness Noise*, resultant from the displacement of an element of air in the disc, caused by the finite thickness

of the blade. By considering a fixed frame of reference, same as for the loading noise, this displacement will be equivalent to a periodic introduction and removal of mass at each element of air near the disc. The blade profile, incidence and speed will determine the rate of mass introduction or volume displacement, which can be expressed as a monopole source. This noise component becomes important at higher tip speeds, being generally smaller than the loading noise (MARTE; KURTZ, 1970).

To assess the noise from a propeller in the flowfield completely, quadrupole sound sources must also be considered, which represent the sound generated by the fluid flow around the blade. These sources, related to the Reynolds stress, are distributed throughout the volume exterior to the blade and, similarly to the dipoles distributed over the blade surface, are responsible for the generation of discrete-tone noise, due to the mean Reynolds stresses rotating in a circle (FFOWCS-WILLIAMS; HAWKINGS, 1969). In Goldstein's notation, the Ffowcs-Williams Equation for propeller tonal noise includes all noise generation mechanisms. This equation is shown in Figure 19.

Figure 19 – Self-noise generation mechanisms in a propeller

$$p'(\mathbf{x},t) = \underbrace{\int_{-\infty}^{\infty}\int_{S(\tau)} \rho_0 v_n \frac{D_0 G}{D\tau}\, dS(\mathbf{y})\, d\tau}_{\text{Thickness Noise}} + \underbrace{\int_{-\infty}^{\infty}\int_{S(\tau)} f_i \frac{\partial G}{\partial y_i}\, dS(\mathbf{y})\, d\tau}_{\text{Loading Noise}} + \underbrace{\int_{-\infty}^{\infty}\int_{V(\tau)} T_{ij} \frac{\partial^2 G}{\partial y_i \partial y_j}\, dy\, d\tau}_{\text{Quadrupole Noise}}$$

Source – Envia (2014)

These quadrupole sources are, however, significant only for transonic and supersonic tip Mach numbers, and, for low-speed cases, they can be removed from the modelling for simplification purposes (ENVIA, 2014). These sources are also not likely to generate significant broadband noise, since the flow induced around a blade is mainly laminar, with the wake as the only significant turbulent region. Thus, there will be only a small region of quadrupoles of randomly fluctuating strength, and its noise will be negligible compared to that produced by force fluctuations (FFOWCS-WILLIAMS; HAWKINGS, 1969).

The viscous noise sources are associated to different types of broadband noise generation mechanisms, all related to load fluctuations resulting from different phenomena, namely due to: the inflow turbulence, turbulent boundary layers passing the blade trailing edge, local stall, tip vortex formation, vortex shedding from laminar separation and vortex shedding from a blunt trailing edge (KNOWLES, 1987). The intensity of the broadband noise generated by these fluctuations will tend to have a dipole form of radiation and follow the sixth power law of the section velocity (FFOWCS-WILLIAMS; HAWKINGS, 1969).

The blade trailing edge noise will be produced due to the deformation of the turbulent boundary layer vortices, when passing through this region, in order to satisfy the Kutta condition (continuity between the static pressure on the upper and lower sides of the blade). The tip noise occurs due to the complex three-dimensional flow at this region, associated with the formation of vortices. The tip vortices may be a significant noise source, compared to the trailing edge, since the highest blade velocities are achieved at the rotor tip. Finally, regions of separated flow will produce a large amount of noise, due to their natural unsteady characteristics (NODÉ-LANGLOIS et al., 2014).

Numerical studies identified that the inflow turbulence was the dominant broadband component at low frequencies (below 1 kHz). Conversely, trailing edge and tip vortex noise were more significant for higher frequencies, when the inflow turbulence was weaker. The trailing edge noise was found to be more important for rotors with larger diameters and to increase slowly with the angle of attack, while tip vortex noise was more significant at higher angles of attack, for wide-chord rotors (KNOWLES, 1987).

2.1.2 Propeller Interaction Noise

The interaction noise in propellers is caused by circumferential non-uniformities in the inflow, due to the presence of another rotor or a stationary geometry upstream. These upstream components will have their own effect on the flow, such as the generation of downwash and/or a wake, which will translate as a velocity deficit on the downstream flow injected in the rotor. For the case with two rotor rows, the blade tip vortex and the rotating potential field of each rotor will also have major contributions to the propeller interaction noise (BLAKE, 1986).

There is a difference, however, between the acoustic and the aerodynamic interference between rotors, which is worth mentioning. For the former, the noise radiated by each row can be computed separately and the addition of the two noise fields can be constructive or destructive at specific points. The latter is the one that provokes unsteady loading on a rotor, due to a non-uniform flowfield produced by the other (HANSON, 1985). This unsteady loading, generating mostly noise of tonal characteristic, can be represented by dipole sources with periodic variation in strength, unlike the rotor-alone tones, represented by sources with strength independent from the position and time (MCALPINE; KINGAN, 2012).

For an open rotor engine, as shown in Figure 8, the main interaction noise sources occur from unsteady loads due to the effects of the rotors on each other, and an inflow velocity deficit, caused by the wake of the upstream pylon. The former will not be further detailed, since it is

not of great importance to the work of this project. The latter, which constitutes the core of this work, will be better described in the next sections.

2.1.3 Tonal and Broadband Propeller Noise

The different types of sources and their specific features will each have their contributions to the overall propeller noise. These contributions can sometimes be analyzed through sound spectra and directivity plots, for example, which provide a great deal of information on the propeller noise characteristics. The spectra will indicate the occurrence of tonal peaks, at the blade passage frequency and its harmonics, as well as the region of broadband dominance. In the directivity plots, the sound levels and the noise propagation for a specific frequency value can be evaluated, either in the longitudinal or in the circumferential direction.

A propeller sound spectrum will be composed by both tonal and broadband components. Parry, Kingan and Tester (2011) evaluated the effective contributions from each of these components to the overall propeller noise. An isolated (no installation effects) counterrotating open rotor rig was tested for zero angle of attack and operating conditions equivalent to take-off thrust. In order to verify the relative importance of each noise component, measurements with inflow microphones were carried out. A tone deletion technique with a moving median curve fitting was employed on the narrowband spectra, so that only the broadband noise would remain. The measured and tone deleted spectra are shown in Figure 20

Figure 20 – Narrowband and one-third octave isolated propeller spectra with tones deleted

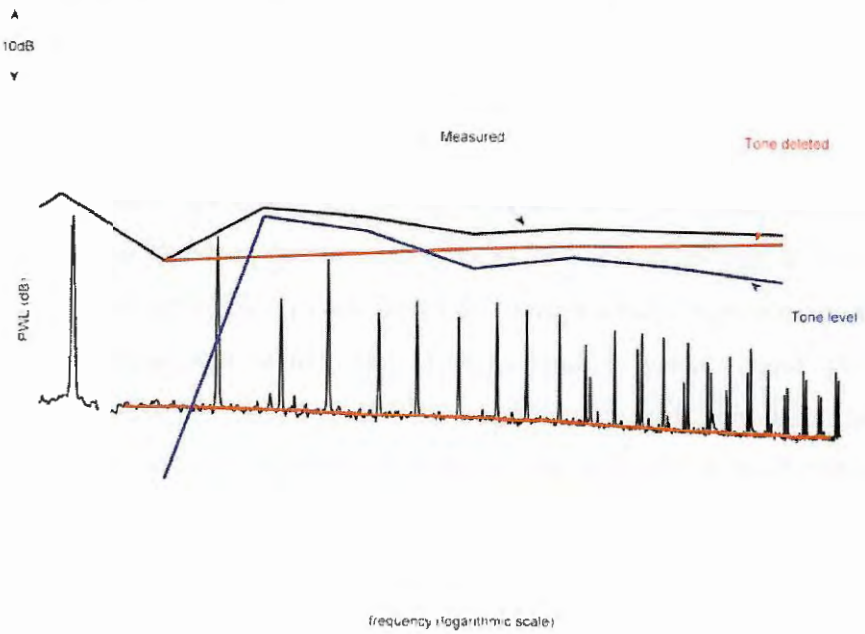

Source – Parry, Kingan and Tester (2011)

The black and red curves are the one-third octave measured spectrum and the tone deleted spectrum, respectively. The difference between them is the blue curve, which is the resultant tone level. Although there are no frequency values displayed in the chart, it is possible to verify that for very low values, the broadband noise is dominant. After the first BPF peak, which would occur for low to medium frequencies, there is a gap between the black and red curves, indicating a higher tonal noise. As the frequency increases even more, the tones levels start to decrease and the broadband is once again dominant (PARRY; KINGAN; TESTER, 2011).

The conclusion is that there is a frequency range, probably around the first harmonics of the BPF, where tonal noise is far greater. Outside this region, especially for higher frequencies, the broadband is the major noise source, since the higher BPF harmonics do not tend to have high sound pressure levels. This trend was also verified on the work conducted by Woodward (1987a) as shown in Figure 21. In this case, a single propeller was tested and the tonal peaks are visible up to the third harmonic, after which the broadband noise becomes more significant. A windmilling case was also evaluated, but no tonal peaks were found, since they likely have lower sound pressure levels than the wind tunnel background noise.

Figure 21 – Single-rotating propeller noise signature

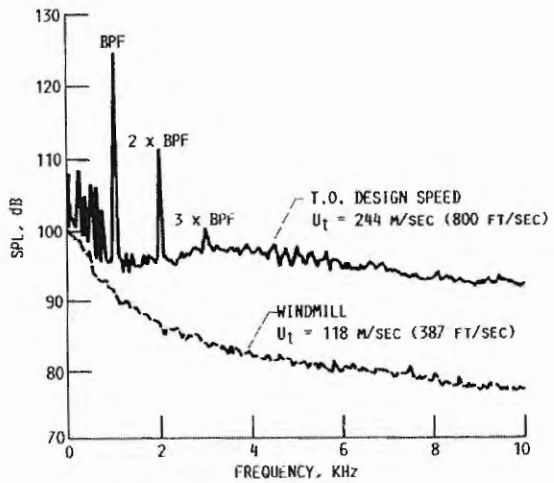

Source – Woodward (1987a)

For counterrotating propellers, the narrowband sound pressure spectra will have a similar behavior, but with a particularity. Aside from the rotor-alone tones for each propeller, there will be a noise component related to the interaction between them, as described in the previous sections. If the number of blades of each rotor are unmatched, new tonal peaks will arise at linear combinations of both rotors BPFs. The rotor-alone tones are more visible for lower frequencies (for higher frequencies, the broadband dominates), while the interaction

tones display high values of sound pressure for a wider frequency range, as shown in Figure 22 (WOODWARD, 1987b).

Figure 22 – Counterrotating propeller noise signature

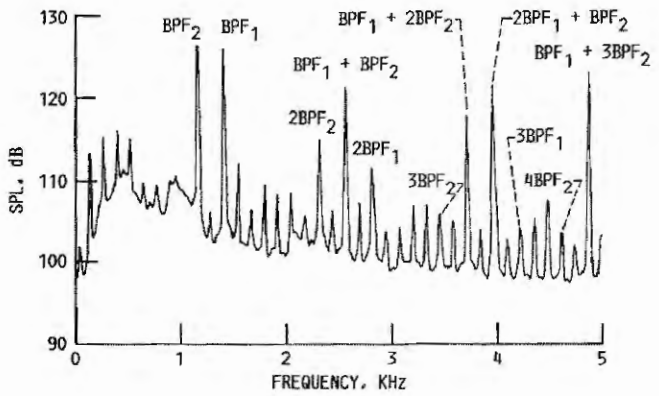

Source – Woodward (1987b)

The directivity of a propeller indicates in which directions there is more and less noise radiation. The usual convention states the propeller plane as $\theta = 90°$, with decreasing θ for the upstream direction, so that the propeller axis corresponds to 0° (180° for downstream). This parameter can be analyzed as the sound pressure level distribution over a range of θ angles, for a given frequency value, preferably the BPF and its harmonics, which provide the highest noise levels in the spectra. A propeller directivity curve for take-off condition, obtained by Woodward (1987a), is shown in Figure 23.

Figure 23 – Single propeller directivity for the blade passage frequency and its second harmonic

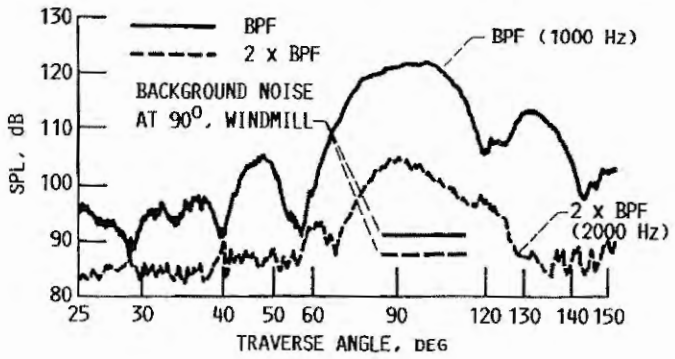

Source – Woodward (1987a)

The results indicate the maximum tone level occurs at the propeller plane, tending to decrease towards the axis (WOODWARD, 1987a). However, the downstream angles seem to have higher levels than the upstream region, indicating an asymmetric behavior. For the counter rotating case, the rotor-alone tones display the same behavior seen above, while the interaction

tones tend to be higher toward the propeller axis, as shown in Figure 24 (WOODWARD, 1987b).

Figure 24 – Counterrotating propeller directivity for both rotors BPFs and the first interaction tone

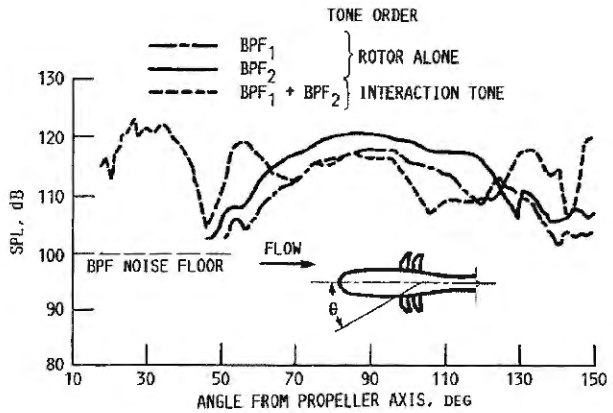

Source – Woodward (1987b)

2.1.4 Effects of Aerodynamic Parameters on Propeller Noise

The geometrical features of the propeller and the characteristics of the inflow will deeply influence its acoustic response. The effects of parameters, such as tip speed, pitch angle, RPM and the angle of attack, on the propeller noise were evaluated by Woodward (1987a), for a single-propeller rig. Increases in the tip speed and the blade pitch angle (β) tend to increase the sound pressure levels almost linearly, since the resulting blade loading is also higher, as shown in Figure 25.

Figure 25 – Sound pressure level with increasing tip speed and blade pitch angle

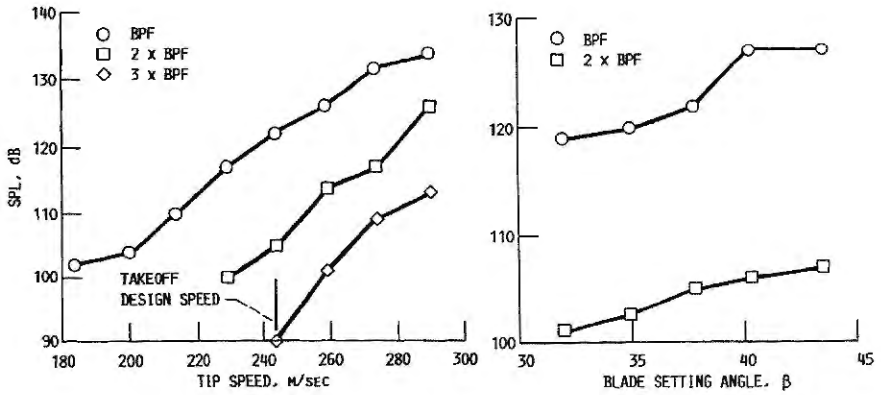

Source – Adapted from Woodward (1987a)

The angle of attack of the inflow also had a major influence on the noise emitted from the propeller. The left curves in Figure 26 represent the directivity plots for different α angles, which indicate that increasing the angle of attack of the propeller axis away from the

microphones tends to produce higher tonal levels, up to 10 dB, especially for $\theta = 90°$ and upstream. The opposite effect was verified, when the angle was increased toward the microphones. This can be explained by an increased effective angle of attack for the blade approaching the microphone (for positive α, which increases loading and noise). By looking at the curves on the right, it is possible to verify that the levels for the rotor-alone tones show a great dependence on the propeller axis angle of attack, with variations of up to 20 dB on the sound pressure level, while the interaction tones do not display this same trend (WOODWARD, 1987b).

Figure 26 – Single and counterrotating propellers directivity plots for different angles of attack

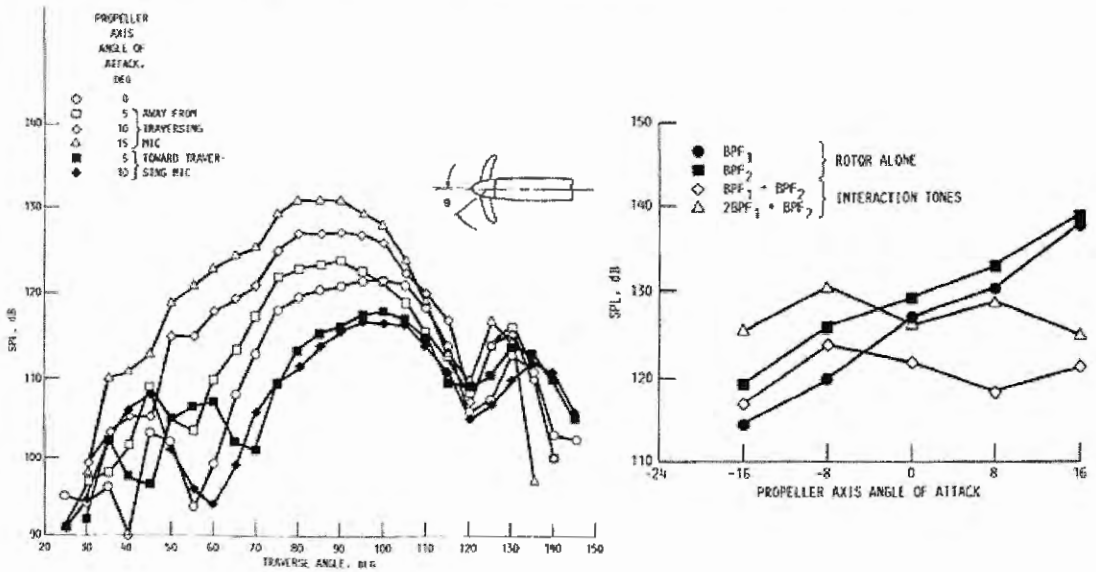

Source – Adapted from Woodward (1987b)

The effects from aerodynamic parameters on open rotor noise were also assessed by Elliott (2012). The rig used counter rotating propellers with 12 blades on the forward rotor and 10 blades on the aft, and the blade design was the same used in the late ATP tests, which is shown in Figure 27.

Figure 27 – Open rotor rig with historical baseline blades

Source – Elliott (2012)

The tested parameters included variations on the pitch angle, shaft speed and angle of attack. For the first analysis, two configurations were established and named take-off and approach, with the former having a higher pitch angle. The spectra in Figure 28 show the results for these two conditions for directivity angles of 141° and 45°, respectively.

Figure 28 – PSD spectra for two different blade pitch angles, for 141° and 45° of directivity, respectively

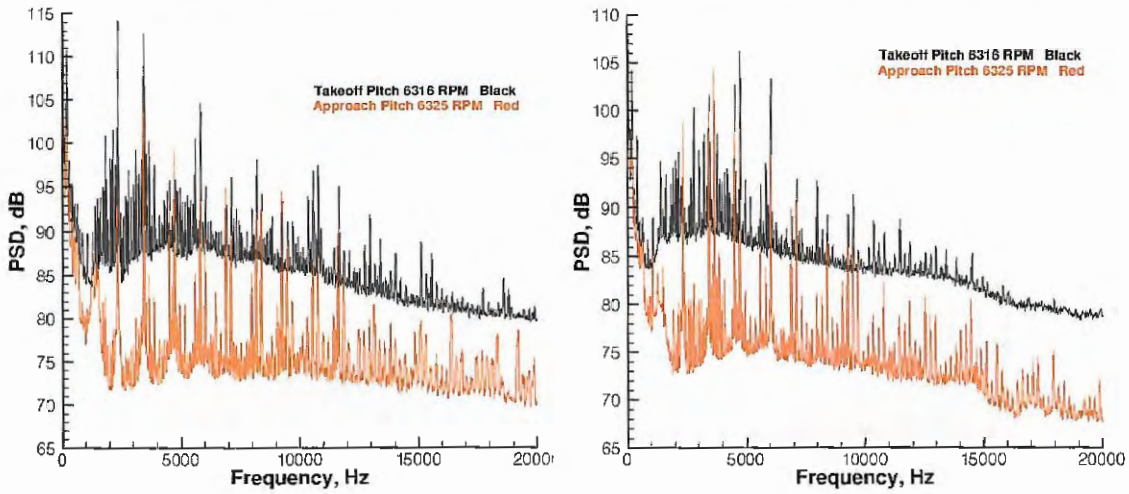

Source – Adapted from Elliott (2012)

The results show that, for both directivity angles, the configuration with take-off (higher) pitch display broadband noise about 13 dB more than the approach for the same shaft speed. However, for the latter, the relative tonal content (levels and number of peaks) is higher. The spectra in Figure 29 show the effect of changing the shaft speed, considering the take-off pitch condition, for the same two directivity angles. It is clear that increasing the rotation speed by 1000 RPM raises the broadband noise levels by approximately 10 dB (ELLIOTT, 2012).

Figure 29 – PSD spectra for different shaft speeds, for 141° and 45° of directivity, respectively

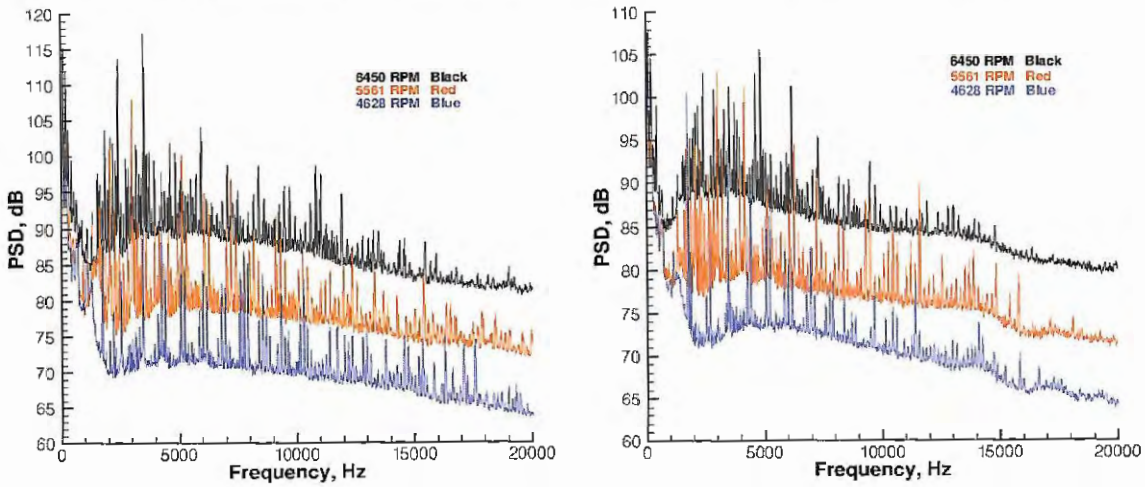

Source – Adapted from Elliott (2012)

An increase in the angle of attack, relative between the free stream and the propeller axis, was shown to have a small effect on the overall noise levels, as shown in Figure 30. For the broadband component, the spectrum for 3° is very close to the 0° condition, while the 8° spectrum shows an average increase of 3 dB approximately over the entire frequency range. For this condition, there is also an increase in tonal content, including higher levels for the already existent peaks and even the addition of new peaks (ELLIOTT, 2012).

Figure 30 – PSD Spectra for different angles of attack, for 141° and 45° of directivity, respectively

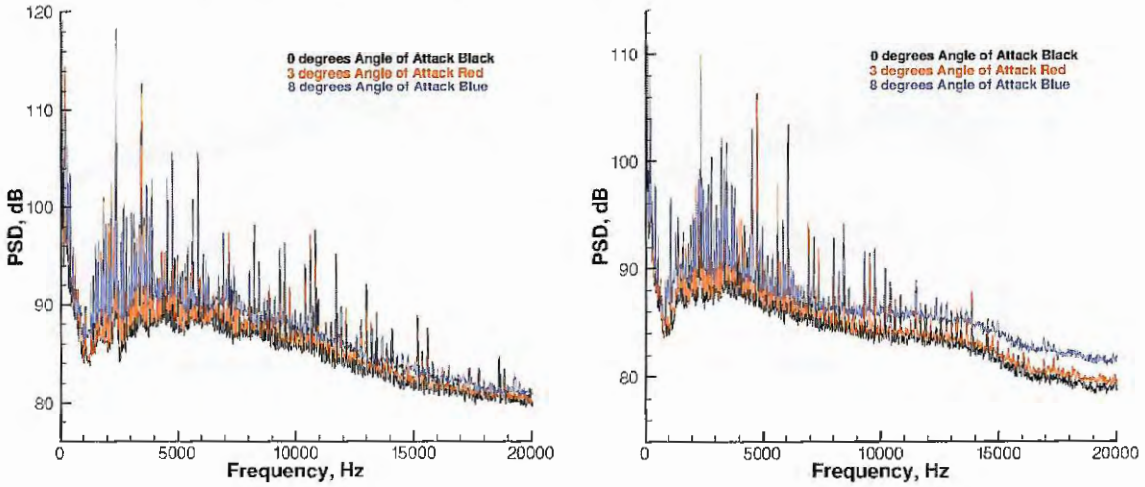

Source – Adapted from Elliott (2012)

2.2 PYLON-PUSHER PROPELLER INTERACTION

As explained in the previous sections, for a real open rotor configuration, there are noise components related to unsteady loadings, resulting from interaction between elements, such as rotor-rotor and rotor-pylon. In this chapter, the noise generation mechanism related to the latter will be described, with the associated aerodynamic phenomena and acoustic characteristics. The aerodynamic effect of the propeller inflow on the upstream pylon will also be assessed.

2.2.1 Aerodynamic Effects of the Pylon Wake on a Downstream Propeller

This type of interaction noise starts with the viscous flow around the pylon, specifically the boundary layer that, after being subjected to the adverse pressure gradient, will undergo separation at the trailing edge region, and the flow will turn into a wake. This wake is characterized by a section of low-speed flow, when compared to the free stream speed. Since the propeller is located downstream of the pylon, the wake will introduce non-uniformities to some parts of the propeller inflow velocity, as shown in Figure 31.

Figure 31 – Effect of the pylon wake on the propeller inflow velocity and blade angle of attack

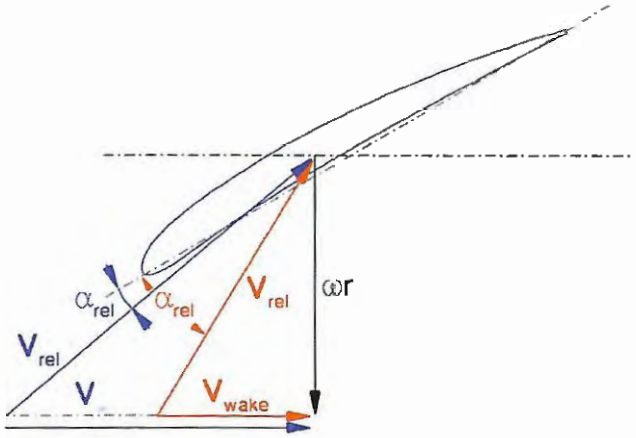

Source – Stuermer and Yin (2010)

The blue vectors demonstrate the behavior for an isolated propeller, where the free stream speed (V_∞) combined with the local rotational velocity (ωr) will generate a resultant velocity (V_{rel}) with a respective angle of attack (α_{rel}) to the local chord. Because the inflow speed is relatively high, the resultant angle of attack will be relatively small. However, if the inflow velocity is reduced, due to the wake produced by the pylon, for example, the resultant velocity will cause a much higher angle of attack to that blade section and thus locally increase the aerodynamic loading.

Stuermer and Yin (2010) evaluated, through numerical analyses, the variation of the blade angle of attack and the magnitude of the load fluctuations on the blades caused by the pylon wake, and the results are shown in Figure 32.

Figure 32 – Effective angle of attack and load fluctuations on the blades caused by the pylon wake

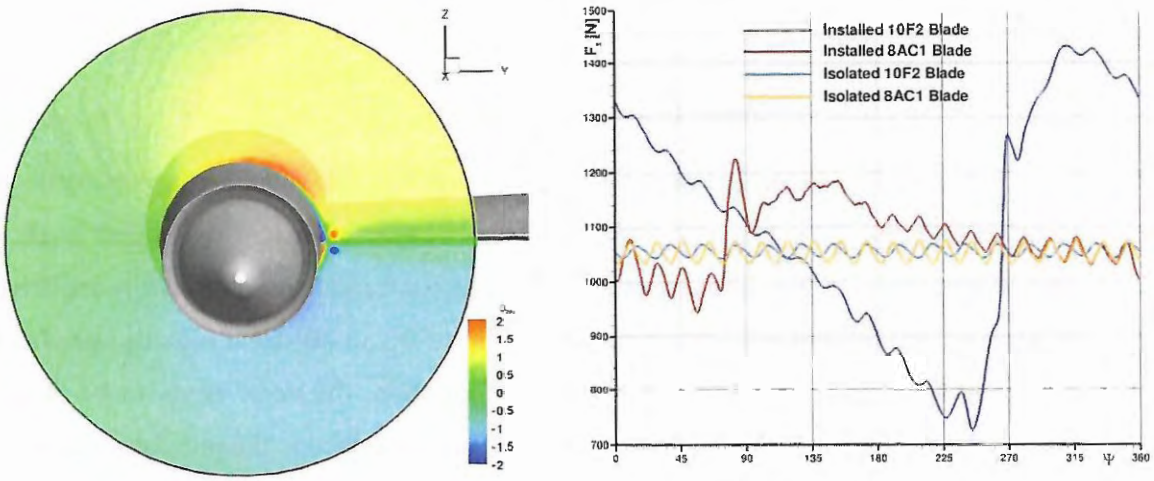

(a) Installation impact on blade effective angle of attack

(b) Reference blade thrust development

Source – Stuermer and Yin (2010)

The results from the simulations at cruise condition indicated that the velocity deficit caused by pylon wake could result in variations of up to 2° in the effective angle of attack (Figure 32a). This, in turn, would result in the trend displayed in Figure 32b, where the thrust force is compared for each rotor at isolated and installed configurations. For the isolated case, as shown by the light blue and orange curves respectively, the blade thrust shows an oscillating behavior around a constant mean level for both rotors, which is caused by rotor-rotor interactions. For the installed case, the thrust distribution changes drastically, especially for the front rotor (dark blue curve), due to the change in effective angle of attack. For the region near the pylon wake (~270°), there is a sudden increase in the force, as expected. For the aft rotor (red curve), the effect of pylon wake is much smaller, but can still be verified at ~90° (STUERMER; YIN, 2010).

This phenomenon will tend to occur in a rather small region (only the section affected by the pylon wake), while at the other positions, the blades will be subjected to the free stream conditions, with smaller angle of attack. Hence, the rotating blades will experience a sudden fluctuation in the aerodynamic forces, while passing through this region, providing an unsteady characteristic to the loading, consequently resulting in noise generation.

The fluctuation in the forces will occur every time a blade passes through the wake region, and thus will have a periodic nature. Given this behavior, the noise generated will have a tonal characteristic, with peaks occurring at the blade passage frequency and its harmonics. Therefore, by comparing the noise spectra from a pylon-pusher propeller configuration with the isolated condition, the sound pressure levels for the former would be much higher for the tonal peaks. Some effect on the broadband noise would also occur, mostly due to the turbulence from the pylon wake at the propeller inflow.

2.2.2 Pylon-Pusher Propeller Interaction Noise

Several studies have been carried out in order to assess the aeroacoustic effects of the interaction between pylon and propeller. Block (1986) evaluated the sound levels and the directivity of a propeller in the tractor and pusher configurations. The results are presented in Figure 33, in the form of color contours of noise levels in dB, for a high tip speed condition. These plots indicate that, for the tractor configuration, the noise tends to be larger in the propeller plane, which is in accordance to what was described in the previous sections. For the pusher configuration, however, there is a large noise component in the propeller axis, in the upstream direction, with levels up to 15 dB higher than the isolated case, distributed in

throughout the first four harmonics. In the propeller plane, the increase in noise ranges from 2 to 5 dB, and it occurred only for the first harmonic (BLOCK, 1986).

Figure 33 – OASPL contour for propeller in tractor and pusher configurations

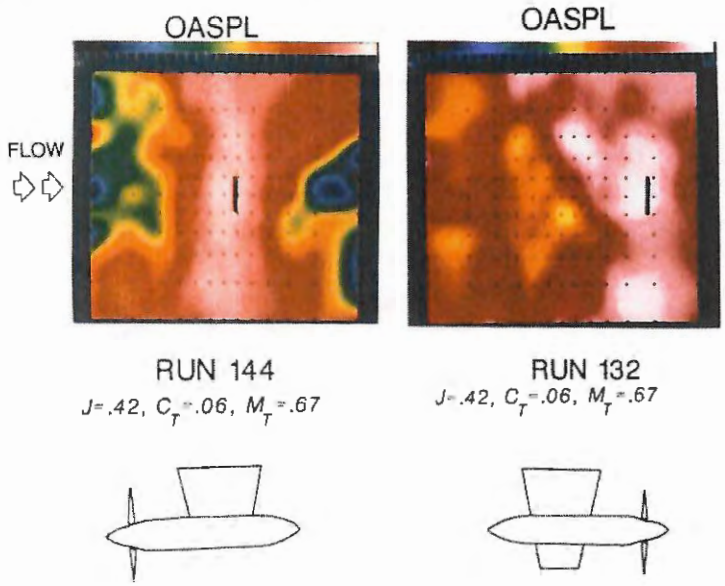

Source – Adapted from Block (1986)

Block and Gentry Jr. (1986) also conducted further tests to evaluate the increase in sound pressure level and the directivity for this installed configuration using a single-rotation propeller. The OASPL was measured for different axial (θ) and circumferential angles (Φ), as shown in Figure 34. As a convention, the propeller plane was set as $\theta = 90°$, with increasing value in the downstream direction. In addition, the line parallel to the pylon span was set as $\Phi = 0°$, increasing in the counterclockwise direction, looking upstream.

Figure 34 – Axial and circumferential angles for the installed configuration measurements

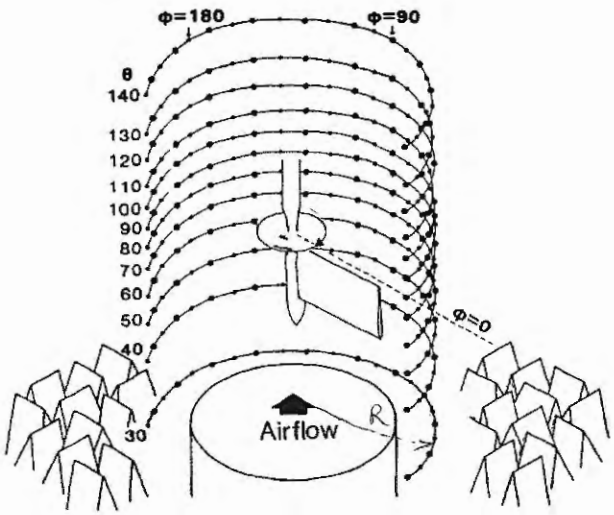

Source – Block and Gentry Jr. (1986)

For the charts displayed in Figure 35, the noise penalty plotted in the y-axis is the difference between the OASPL for the pusher and tractor configurations (installed and isolated, respectively). The charts contain the results for a four-bladed propeller with $\beta_{0.75} = 18.8°$ for different rotation speeds (BLOCK; GENTRY JR., 1986).

Figure 35 – Noise penalty for 4-bladed propeller in installed configuration

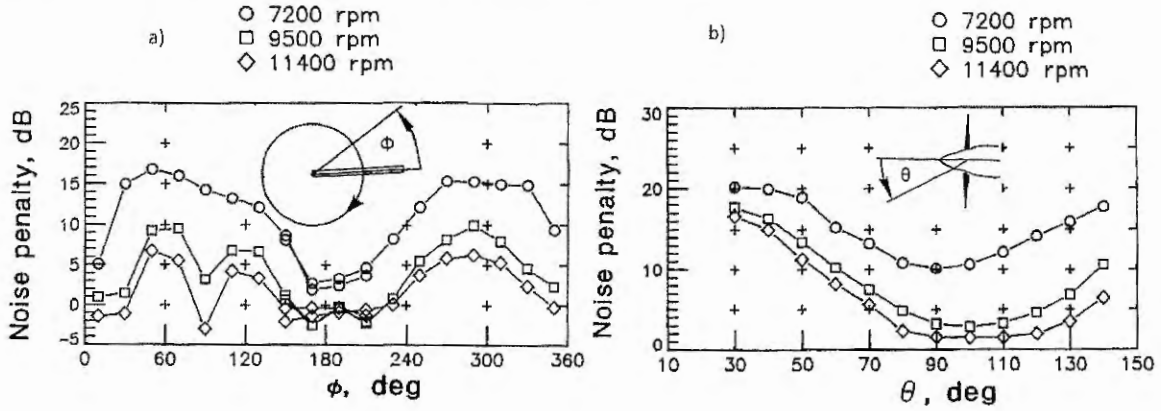

Source – Adapted from Block and Gentry Jr. (1986)

For the circumferential directivity (Figure 35a), the higher noise levels tend to occur at positions around $\Phi = 60°$ and $\Phi = 300°$, reaching up to 16 dB. The lower noise levels are found at $\Phi = 10°$ (possible position for the fuselage) and $\Phi = 180°$, with negative values, indicating that the pusher configuration is quieter at this region. This can be concluded, since the tractor propeller displays azimuthal symmetry, with the same sound levels for the entire circumference. The authors state that at $\Phi = 180°$, the noise signal undergoes a phase change. For the higher rotational speeds, there is also a sharp drop perpendicular to the pylon ($\Phi = 90°$), which could be result from the cancellation between the sound fields produced by the steadily and unsteadily loaded propeller blades (BLOCK; GENTRY JR., 1986).

For the axial directivity (Figure 35b), the noise penalties tend to have a minimum (between 2 and 11 dB, depending on the rotational speed) value at the propeller plane ($\theta = 90°$), with increasing levels toward the propeller axis, for both upstream and downstream directions, reaching a highest of 20 dB for $\theta = 30°$. The peak noise levels for the pusher configuration were approximately constant, irrespective of the axial angle of measurement. Moreover, as already shown in the previous sections, an isolated single propeller tends to display maximum noise levels at the propeller plane.

Therefore, the maximum noise penalties will in fact occur near the propeller axis and the minimum at the propeller plane. It was also possible to conclude that increasing the rotational speed decreased the noise penalty. This occurred due to the smaller effect of the

unsteady loading due to the pylon wake, for lower advance ratio conditions (high thrust), where the steady loading noise dominates (BLOCK; GENTRY JR., 1986).

In the same work, Block and Gentry Jr. (1986) also evaluated the effect of the pylon-to-propeller spacing. The previous directivity measurements were carried out for a distance between the pylon trailing edge and the propeller plane of about 10% of the pylon chord. The following results were obtained for a spacing equal to 30% of the pylon chord, and for this case, the noise penalty is considered as the difference between the levels for the two spacings, and is plotted against the circumferential and axial directivities in Figure 36.

Figure 36 – Noise penalty in the installed configuration for different pylon spacings

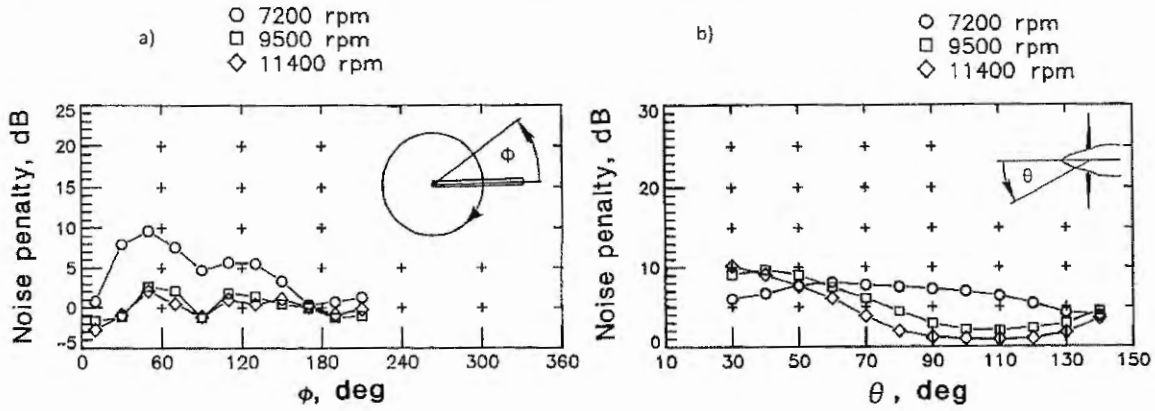

Source – Adapted from Block and Gentry Jr. (1986)

By moving the propeller plane further downstream from the pylon, the sound levels tend to decrease, almost reaching the isolated condition, which is indicated by the high noise penalty, especially near the propeller axis. For the lower rotational speed (7200 RPM), the noise penalty near the propeller plane is high, and by comparing with the previous results, the resultant noise is very close to the tractor condition. For the higher rotations, the noise penalty was already small for the previous results, so the improvement margin was short (BLOCK; GENTRY JR., 1986). Therefore, the results indicate that a higher spacing between pylon and propeller tend to reduce the interaction noise, since there is an additional length for the dissipation of the wake, before impinging on the propeller. It is then necessary to take the pylon-propeller spacing into account during the design of the aircraft powerplant, since it can greatly influence the noise penalties in this configuration.

In a more recent test campaign, Ricouard et al. (2010) assessed the main aeroacoustic characteristics of the installation effects on propeller noise. During the tests, the influence of many parameters were verified, such as tip speed, blade pitch, as well as pylon geometry and positioning. Initially, the measured acoustic spectra is shown in Figure 37.

Figure 37 – Noise spectra for counterrotating installed propellers

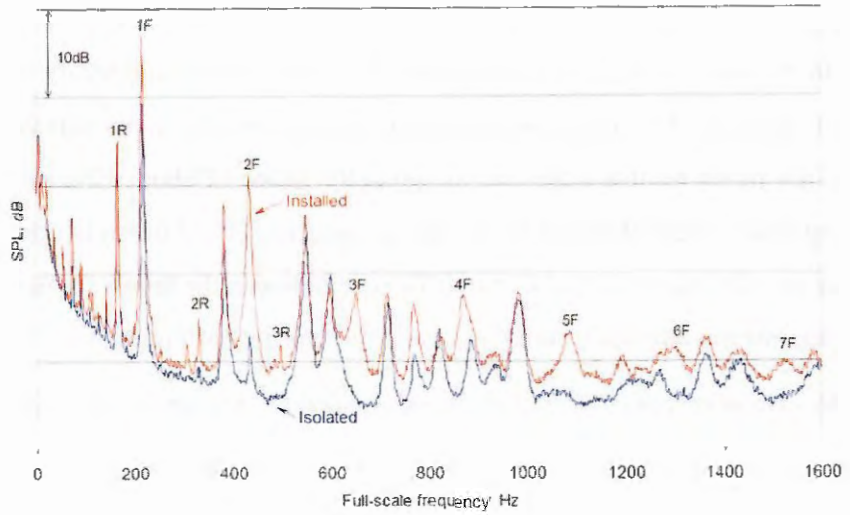

Source – Ricouard et al. (2010)

By comparing the isolated and the installed acoustic spectra from Figure 37, the increase in sound pressure level for the latter is visible throughout the entire frequency range, especially for the front rotor BPF and its harmonics. The tone at the BPF displays an increase of approximately 10 dB. However, the tone at the second harmonic is the one that displays the highest noise penalty, of approximately 16 dB, meanwhile the third one has now a clearly defined peak (RICOUARD et al., 2010).

The presence of the pylon upstream of the propeller has also given rise to higher BPF harmonics that were previously buried in broadband noise, for the isolated configuration. For the rear rotor, the effect is much less pronounced, but still noticeable. The interaction tones show also almost no variation. There is also a slight increase in broadband noise, shifting the entire curve upwards, likely due to the increased turbulence caused by the wake on the propeller inflow (RICOUARD et al., 2010).

The sensitivity of the acoustic characteristics to the propeller operating conditions was also evaluated. In the directivity curves shown in Figure 38a, the tip speed was increased, but with approximately the same thrust produced by the propeller. For the blade pitch analysis (Figure 38b), the goal was to compare different thrust values (RICOUARD et al., 2010).

For the isolated configuration, the directivity curves for both tip speed and thrust variation show a great dependence of the sound pressure level to these parameters. However, for the installed configuration, the variation with rotational speed and thrust was much less evident, which implies that, while the interaction noise dominates for all the tested cases, the pure propeller tones start to become more important for higher tip speeds and thrust. The installed curves, while also having a maximum at the propeller plane, also display higher noise

levels towards the propeller axis, especially in the downstream direction (RICOUARD et al., 2010). Changes to the pylon geometry and propeller spacing were also assessed, with the results shown in Figure 39, for the first two BPF harmonics.

Figure 38 – Directivity for the different tip speeds and pitch for the installed configuration

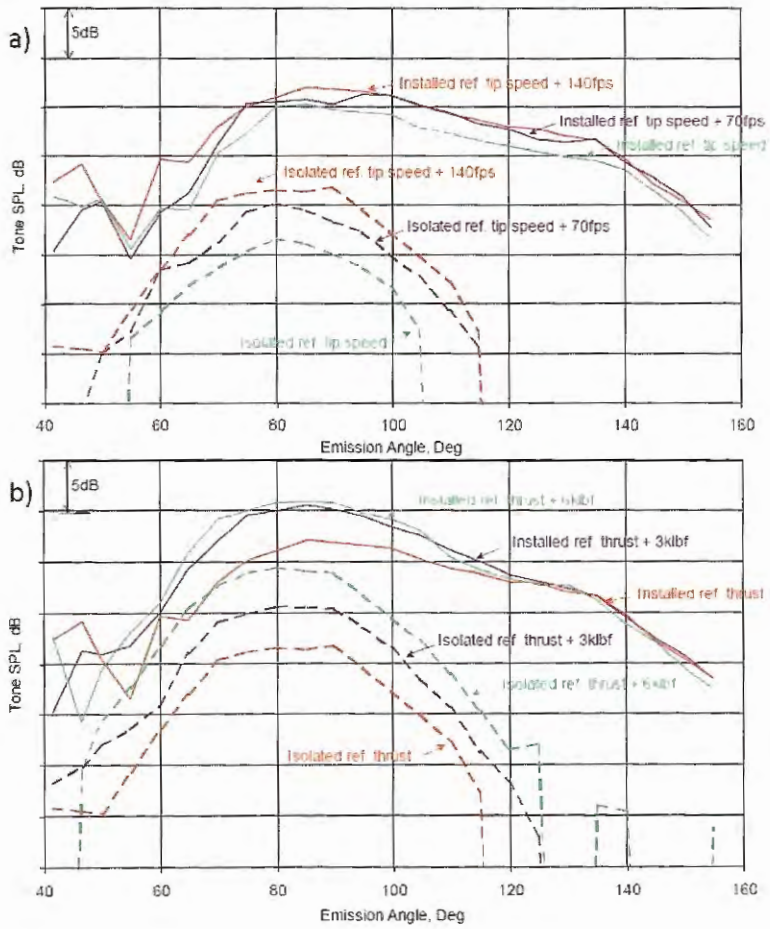

Source – Adapted from Ricouard et al. (2010)

Figure 39 – Directivity for the different pylon spacings and sweep angle

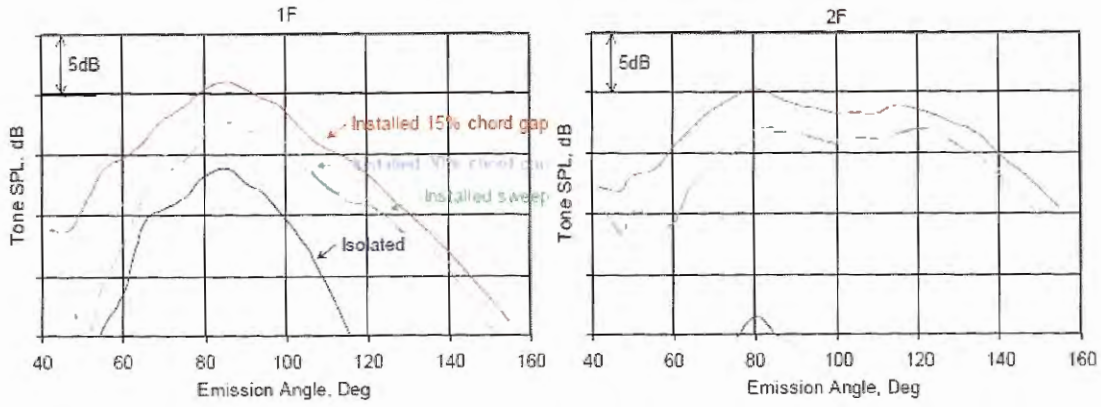

Source – Adapted from Ricouard et al. (2010)

The gap between the pylon trailing edge and the propeller was doubled (from 0.15c to 0.30c), which resulted in a noise reduction of 3 dB. A sweep angle was also included, in order to provide the same velocity deficit and thickness to the wake at different pylon stations. This has also shown benefits to the overall noise, and demonstrated the noise sensitivity to the wake characteristics (RICOUARD et al., 2010).

2.2.3 Propeller Inflow Effects on an Upstream Pylon

As described in the previous section, there are aerodynamic and aeroacoustic effects caused by the interaction between a propeller and an upstream placed pylon, specifically due to the influence of the pylon wake in the propeller inflow. However, this interaction does not affect only the propeller, but also the flow around the pylon. The changes normally induced by the propeller in the upstream flow behavior will also produce variations in the pylon aerodynamic characteristics and, consequently, its wake.

Concerning the pylon, or any aerodynamic surface, the effect of a downstream propeller inflow can be translated into induced velocities at numerous points of interest. These velocities can be decomposed into three vectors for each Cartesian direction (axial, vertical and transversal). By considering a vertical plane through the center of the propeller disc, the spanwise induced velocity will be zero, and the resultant components will behave as shown in Figure 40 (CATALANO, 1993).

Figure 40 – Induced velocities by the propeller inflow in an upstream aerodynamic surface

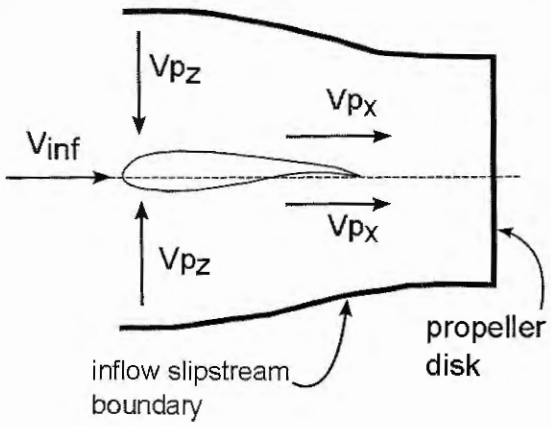

Source – Catalano (1993)

At the symmetry plane, the induced velocity will have an axial component (V_{px}), which is responsible for increasing the local flow speed; and a vertical component (V_{pz}), which in turn will change the local flow incidence. Outside of this plane, the transversal velocity component will induce a cross flow on the surface of the wing. These velocities and their effects can be

altered by changing the relative position between the propeller and the aerodynamic surface. For example, by moving the propeller in the axial direction, the intensity of the induced velocities will change, and, by moving it in the vertical direction, there will be an unbalance in the vertical induced velocities in the upper and lower surface, resulting in an increase or reduction of the flow incidence (CATALANO, 1993).

To evaluate the characteristics of these induced velocities and their effects on the flow around an upstream positioned wing; Catalano (1993) has carried out surface pressure measurements for different angles of attack and relative positions between the wing and the propeller. For these tests, natural transition was allowed to occur. The goal was to identify the main regions relating to boundary layer transition and separation, for low and high incidences (CATALANO, 1993).

Figure 41 – Effect of the propeller inflow on an upstream wing pressure distribution for $\alpha = 4.5°$ and $\alpha = 12.5°$

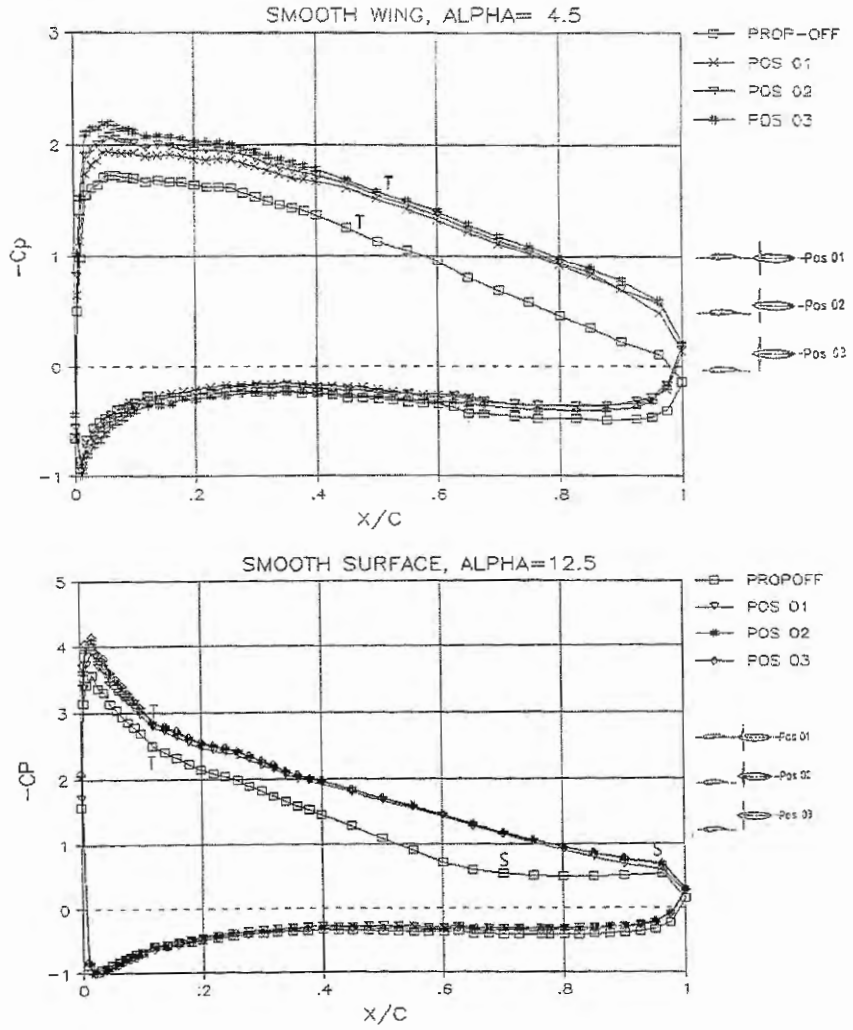

Source – Adapted from Catalano (1993)

For the $\alpha = 4.5°$ condition, shown in Figure 41a, there is a visible change in the transition region, that is moved downstream, for the case with operating propeller. This would translate into a slight reduction in skin-friction drag. The curves for the propeller positioned above the wing show only small differences to the aligned case, mostly in the form of a higher suction near the leading edge. For the $\alpha = 12.5°$ condition, there are no visible changes to transition. However, the region of separation moves much further downstream, from approximately 70% to 95% of the chord (CATALANO, 1993).

Given the effects of the propeller inflow on the pylon pressure distribution and boundary layer parameters, it will consequently alter the wake characteristics. Horne and Soderman (1988) conducted tests with a pitot-static probe to compare the wake of a vertical empennage with and without a downstream rotating propeller. The velocity deficit, considering the free stream speed, was measured for several points in the wake for both cases. The resultant wake profiles are shown in Figure 42. The results indicate an acceleration of the flow for the propeller-on case, shifting the curve downwards. However, the shape and width of the wake remain approximately the same (HORNE; SODERMAN, 1988).

Figure 42 – Velocity deficit in the wake for empennage with and without a downstream operating propeller

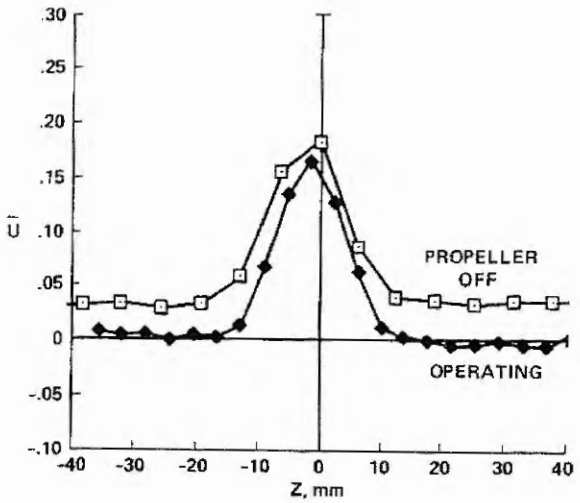

Source – Horne and Soderman (1988)

Horne and Soderman (1988) also measured the disturbances in the flow with a hot-wire anemometer at two positions, one outside and another inside the wake, in order to correlate the results with the propeller acoustic behavior. The spectrum of the data outside of the wake, as shown in Figure 43, shows periodic disturbances from the propeller, occurring at the blade passage frequency and its harmonics. Inside of the wake, the spectrum is practically broadband,

given the high turbulence levels at this region, though the first two tonal peaks are still visible (HORNE; SODERMAN, 1988).

Figure 43 – Velocity deficit in the wake for empennage with and without a downstream operating propeller

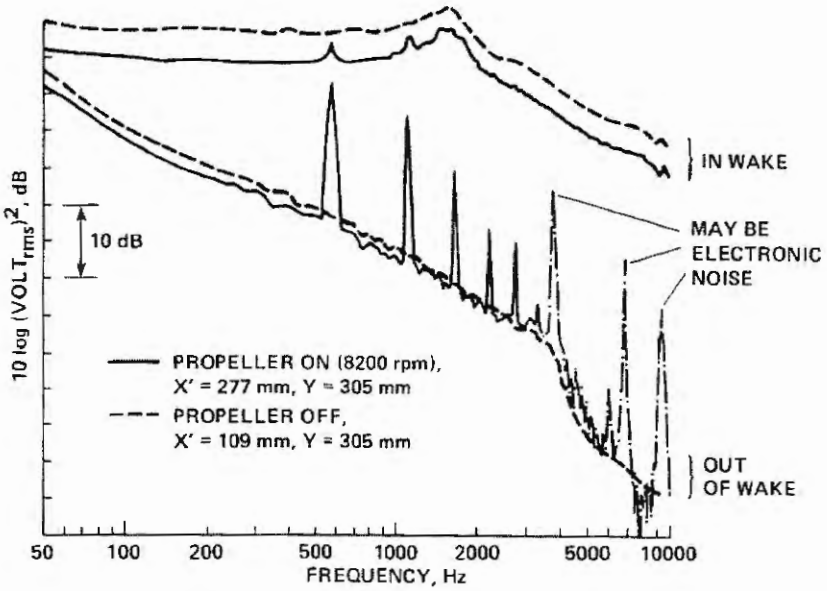

Source – Horne and Soderman (1988)

2.3 PYLON TANGENTIAL BLOWING

The interaction between the pylon wake and the propeller in a pusher configuration was described in the previous sections, along with the related aerodynamic and aeroacoustic issues (installation effects), especially the added noise. One of the proposed solutions for this problem, and the one that is currently regarded as the most viable for practical application, is the mitigation of the pylon wake through a flow control mechanism of pylon blowing. In this section, the blowing mechanism and the subsequent studies on its application on open rotor technology will be further described.

2.3.1 Flow Control through Pylon Tangential Blowing

The tangential blowing, proposed as a solution to mitigate the installation effects in the pusher propeller configuration, is a flow control method usually employed for boundary layer separation control. Separation is a phenomenon that occurs when the retarded flow particles in the boundary layer cannot penetrate too far in a region of adverse pressure gradient. This gradient, combined with the shear stresses from wall friction, will reduce the flow kinetic energy at this region until reverse flow occurs near the wall, and the boundary layer detaches

from it. At this region, there is considerable thickening of the boundary layer, in order to satisfy the continuity condition, which will translate into a strong wake and increased form drag (SCHLICHTING, 1979).

Numerous flow control methods were developed in order to avoid or delay boundary layer separation, and thus resulting in a potential drag reduction and lift enhancement. They can be classified into passive and active techniques. While the former is based on momentum transfer to the near-wall from other regions of the flow (e.g. vortex generators), with an associated parasitic drag, the latter requires an external source of energy, such as the propulsive system, to provide the required momentum (e.g. tangential blowing) (GAD-EL-HAK, 2000).

For the open rotor, the formation of the pylon wake can occur due to separation at the trailing edge or even at the upper/lower surfaces, for high angle of attack conditions. The wake is a region of reduced flow velocity, downstream of a body, formed from the boundary layers on the upper and lower surfaces that merge at the trailing edge. The velocity profile of this wake will change as it moves downstream, with an increase in cross-section and decrease of the mean velocity deficit, relative to the free stream speed. The usual behavior for a wake is shown in Figure 44 (HOUGHTON; CARPENTER, 2003).

Figure 44 – Velocity profiles for a wake downstream of a body

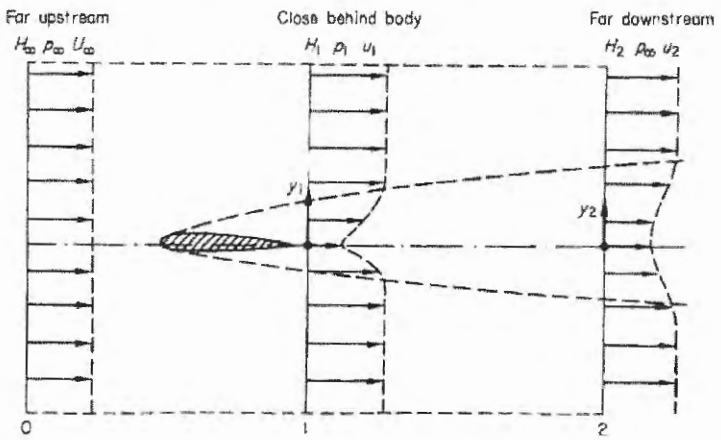

Source – Houghton and Carpenter (2003)

The wake characteristics, such as its size and mean velocity deficit are highly dependent on the boundary layer properties, right before the occurrence of separation. Therefore, in order to reduce the wake region, the boundary layer thickness must be kept as small as possible, and separation before the trailing edge must be completely avoided, since the growth rate at this region is even higher. Given the tendency of increased growth rate, when the boundary layer experiences an adverse pressure gradient, a flow control method of tangential blowing can be employed to introduce momentum in this low-speed region. By injecting a fluid with a velocity

equal or higher than the local free stream speed in the near-wall region, the boundary layer thickness is reduced by definition and the occurrence of separation is also postponed. The working mechanism of a tangential blowing is shown in Figure 45.

Figure 45 – Effect of tangential blowing on boundary layer velocity profile

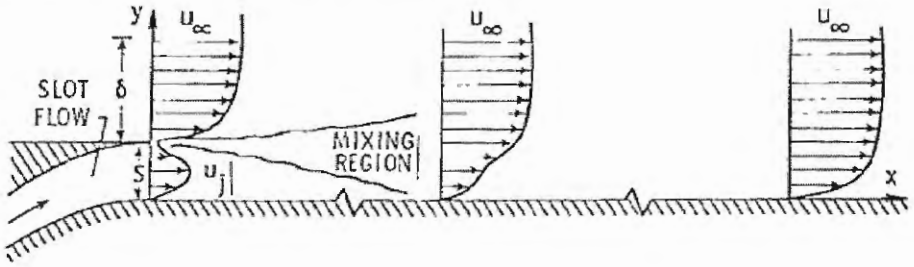

Source – Hefner and Bushnell (1990)

As shown in Figure 45, the blowing slot is positioned on the surface of the body and air is injected to the external flow, parallel to the wall. After the slot, both these flows will mix, and further downstream, the velocity profile returns to an "undisturbed" shape. The quality of the flow downstream of the slot will depend on a series of parameters, such as the jet velocity, the slot height, the lip thickness, the boundary layer profile before the mixing (Reynolds number and turbulence levels), and also important is the injection angle, relative to the local main stream direction (HEFNER; BUSHNELL, 1990). Another possibility of positioning the blowing slot could be at the trailing edge, to avoid further growth of the boundary layer, after the mixing in an adverse pressure gradient region. However, at this position, the full mixing between the jet and the external flow will tend to occur far downstream from the trailing edge.

2.3.2 Application of Pylon Blowing on Open Rotor Research

Given the possibility of eliminating, or at least reducing the intensity and size of the wake of a body, the blowing is a very interesting flow control technique for an open rotor in pusher configuration. By integrating a blowing system to the pylon, the aerodynamic and the aeroacoustic effects resultant from the interaction between the wake and the propeller inflow could be mitigated. One of the first attempts to assess the application of this solution was carried out by Shivashankara, Johnson and Cuthbertson (1990), and was already described in Section 1.5. After the cancellation of the ATP program, no more studies were carried out on this topic for a while. However, with the recent renewed interest in the open rotor technology for commercial application, the studies on pylon blowing have also resurfaced and there are now several groups developing this technology. In this section, the most important studies on the application of pylon blowing will be described.

At the latest stages of the ATP Program, there was also another important pylon blowing assessment, conducted by Gentry Jr., Booth Jr. and Takallu (1990) at NASA. Measurements of the pylon wake profile and the flow turbulence levels with and without the blowing were carried out. The pylon in the wind tunnel model was equipped with a blowing slot in the upper and lower surfaces, positioned at 80% of the chord. The model and the details of the blowing system are shown in Figure 46. It was also possible to change the span of the slot, reaching positions closer to the propeller hub (configs. 1 and 2) (GENTRY JR.; BOOTH JR.; TAKALLU, 1990).

Figure 46 – Wind tunnel model with propeller and pylon blowing system

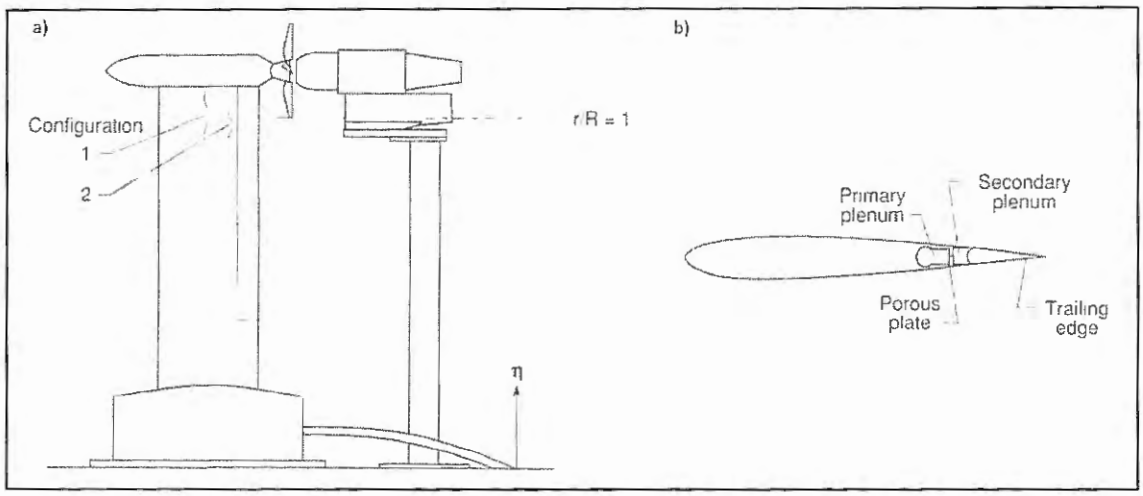

Source – Gentry Jr., Booth Jr. and Takallu (1990)

The wake total pressure measurements, shown in Figure 47, were carried out for blowing-off and -on configurations, with a rake positioned at the propeller plane. These measurements were conducted without the propeller, so it was not possible to assess the interaction effects on the flow around the pylon. Several spanwise stations were mapped and related to their respective blade stations. The results indicate that, for an optimum mass flow, the blowing was able to practically fill the entire wake region, especially near the propeller tip. Near the hub, there was still some velocity deficit, probably due to the presence of the nacelle and the occurrence of vortices at the junction with the pylon (GENTRY JR.; BOOTH JR.; TAKALLU, 1990).

The charts shown in Figure 48, performed with hot-wire, indicate a reduction in the wake turbulence, from 12% to 3% (for the $q_\infty = 30$ psf), for the case with the blowing on (GENTRY JR.; BOOTH JR.; TAKALLU, 1990). Despite no aeroacoustic measurements were conducted, those aerodynamic results would definitely translate into noise reduction, both for the tonal components (with the reduction of the wakes) and the broadband (with the reduction in turbulence).

Figure 47 – Pylon wake profiles at different blade radii stations

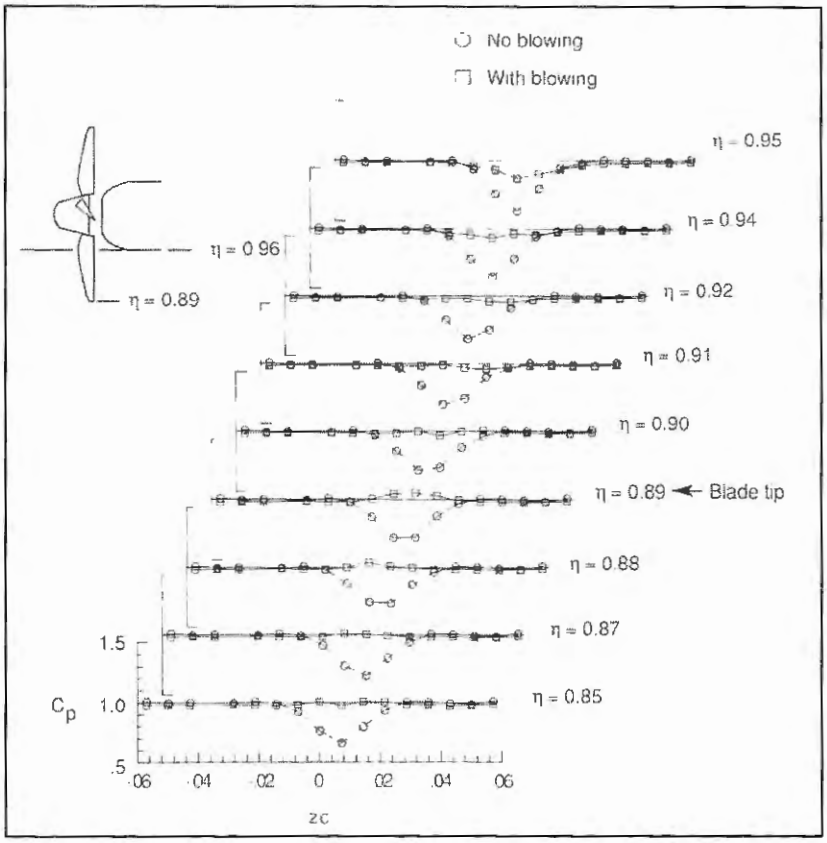

Source – Adapted from Gentry Jr., Booth Jr. and Takallu (1990)

Figure 48 – Turbulence measurements for pylon blowing on and off

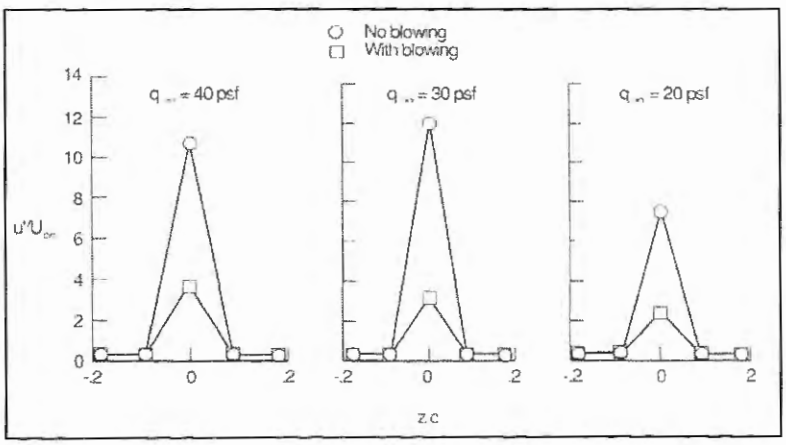

Source – Gentry Jr., Booth Jr. and Takallu (1990)

Ricouard et al. (2010) also evaluated the effects of pylon blowing on the noise characteristics of an open rotor model. The spectra for the optimum blowing configuration was added to the same ones shown in the previous section, for the installed configuration, as displayed in Figure 49.

Figure 49 – Noise spectra for isolated, installed and optimum blowing configurations

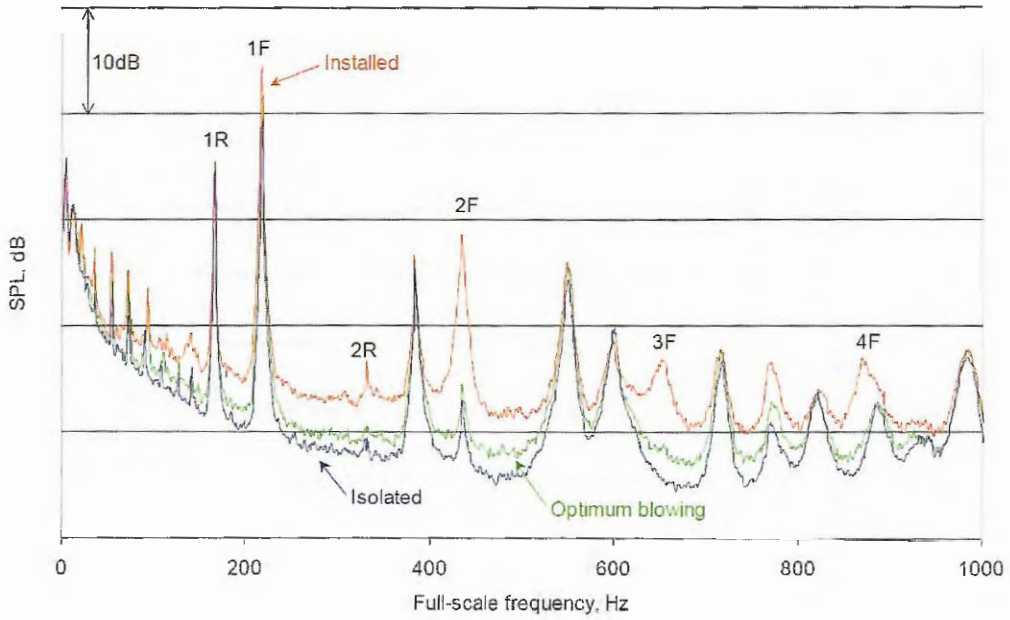

Source – Ricouard et al. (2010)

By comparing the spectra in Figure 49, it is possible to verify a significant noise reduction for the case with operating blowing (green curve), especially for the higher BPF harmonics. The noise levels for the tonal peaks have practically returned to the isolated condition. For the BPF, the noise reduction was not so large (~5 dB), and the blown configuration is placed halfway between the isolated and installed configuration. However, for the 2nd harmonic of the frontal rotor BPF, the blowing reduced almost entirely the 16 dB of increase due to the installation effects. The broadband noise was also largely reduced, most likely due to a reduction in the turbulence levels in the wake. The rotor-rotor interaction noise peaks were unaffected by the blowing, since they were already unaffected by the presence of the pylon wake (RICOUARD et al., 2010).

Another major test campaign, named Z08, was carried out by Airbus and the CleanSky Program partners to evaluate the installation effects and the potential benefits from pylon blowing. For this campaign, one model consisted in a pylon (equipped with blowing) with counterrotating propellers in the pusher configuration, in which both isolated and installed measurements could be performed. The other model was a full aircraft, with two aft-fuselage mounted open rotors, and the pylons also equipped with the blowing system, as shown in Figure 50. The spectra for the isolated and blown configurations is shown in Figure 51 (PAQUET et al., 2014).

Figure 50 – Z08 campaign wind tunnel models

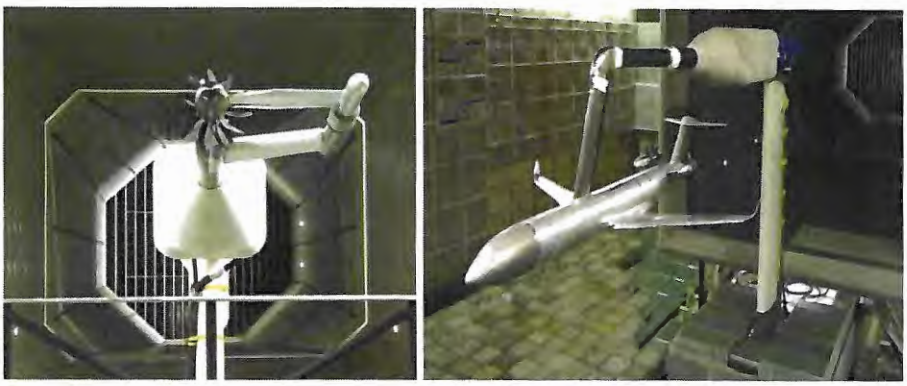

Source – Paquet et al. (2014)

Figure 51 – Noise levels comparison between installed and blown configurations

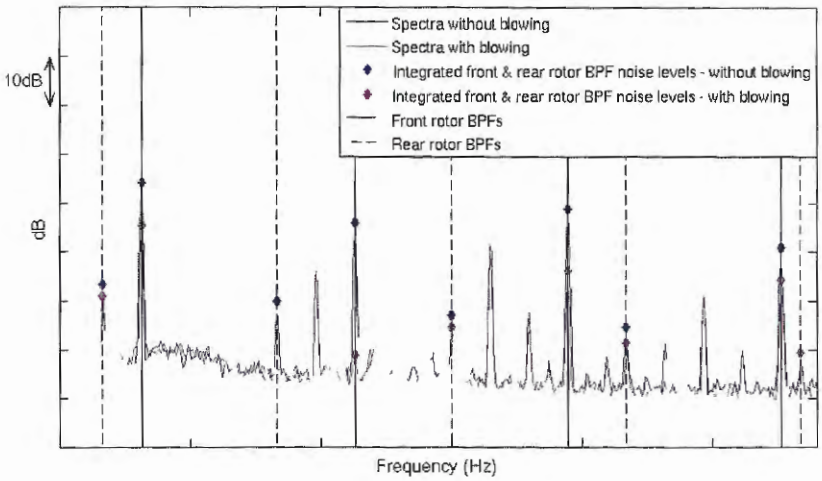

Source – Paquet et al. (2014)

By comparing the spectra in Figure 51, it is possible to verify a great noise reduction for the case with pylon blowing. For the BPF, it was estimated a reduction of almost 10 dB, but the largest difference was found in the second harmonic (approximately 25 dB), which is in accordance with the results obtained by Ricouard et al. (2010). However, since the isolated noise levels were not included in the analysis, it was not possible to conclude how effective the blowing was in eliminating the interaction noise. The rear rotor tones also showed some reduction and the rotor-rotor interaction tones remained unaltered. For the broadband noise, no visible changes were verified between the two cases (PAQUET et al., 2014).

Another assessment of the effects of pylon blowing on a pusher propeller aerodynamic and aeroacoustic properties was carried out by Sinnige (2013). Through wind tunnel tests, performance and aeroacoustic measurements were performed for the isolated, installed and blown configurations. The model consisted in a pylon mounted upstream of a single-rotation

propeller rig. The blowing system was integrated to the pylon model, with the exit slot positioned at the trailing edge. The inlet is located at the pylon root and there is an internal channel with variable cross-section and vanes to turn the flow towards the trailing edge. The model and the schematic of the blowing system are shown in Figure 52 (SINNIGE, 2013).

Figure 52 – Pylon-pusher propeller wind tunnel model and blowing system cross-section

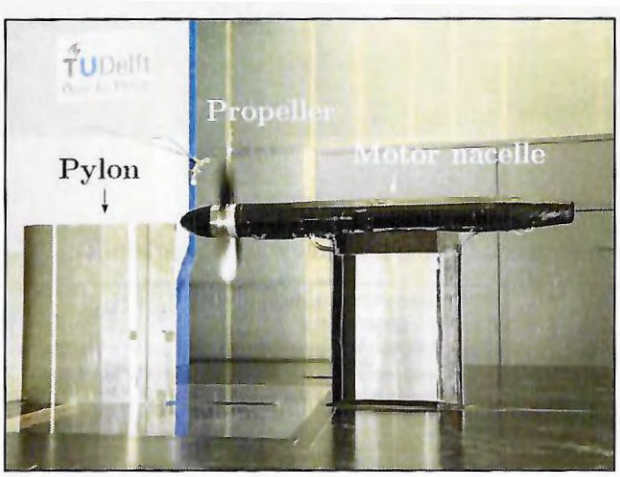

Source – Adapted from Veldhuis and Sinnige (2014)

The velocity profiles for the wake with different blowing rates were measured in order to verify the performance of the system, as shown in Figure 53. For a free stream speed of 19 m/s, at the maximum attainable mass flow, the velocity at the centerline (Y = 0) reached a maximum above the free stream value, with two minima left and right, and it is estimated that 60% of the integral wake velocity deficit was filled. According to the author, these minima occur because the blowing slot was positioned at the trailing edge (for a more straightforward integration), which most likely did not allow for a full mixing between the wake and the blowing, before the propeller plane was reached (SINNIGE, 2013).

Figure 53 – Unblown and blown wake measurements

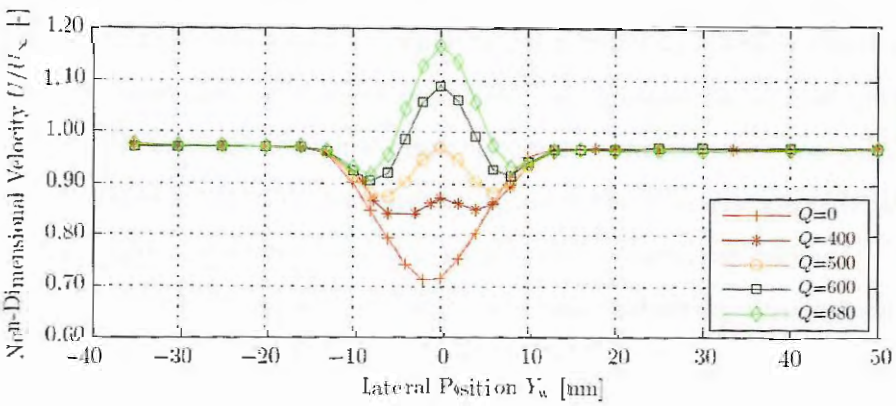

Source – Sinnige (2013)

The aeroacoustic results for the blown configuration are shown in the form of spectra, as displayed in Figure 54, and compared to the isolated and installed cases. The comparison of the sound pressure levels at the tonal peaks for the blown configurations is shown in Figure 55.

Figure 54 – Spectra for isolated, installed and blown configurations

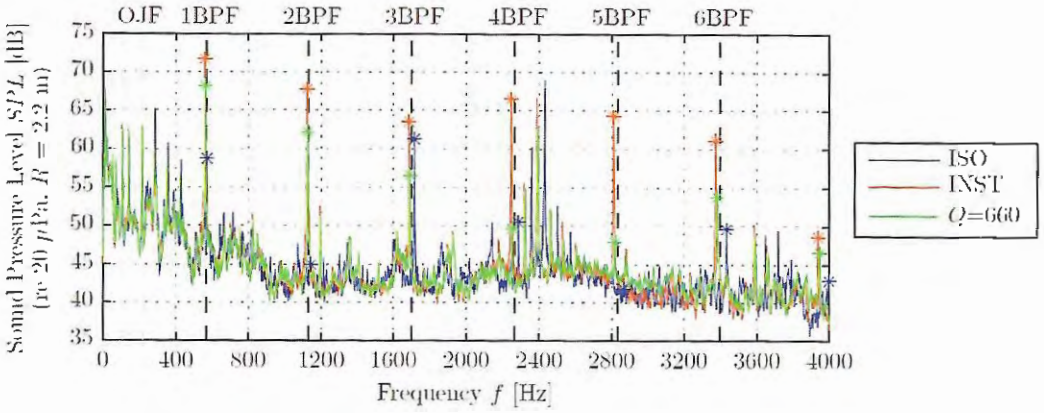

Source – Sinnige (2013)

Figure 55 – Difference in SPL for blown and installed configurations at the tonal peaks

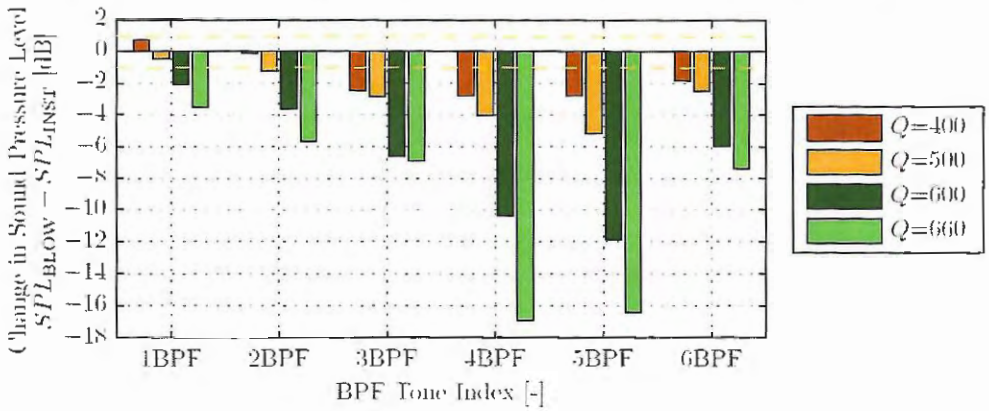

Source – Sinnige (2013)

The spectra in Figure 54 show an increase of almost 15 dB in sound pressure level at the blade passage frequency, from the isolated to the installed configuration. For the 2nd harmonic, the interaction noise was responsible for an increase of almost 25 dB. For the higher harmonics, the installed configuration also displayed much higher noise levels. The broadband levels, on the other hand, do not show visible changes for either configuration. By comparing the change in SPL for the tonal peaks with the blowing at the highest mass flow, reductions of approximately 4 dB were obtained for the BPF, and for the higher harmonics, the difference was even larger, reaching 17 dB, at the 4th harmonic. These results indicate the capabilities of blowing systems integrated to pylons to reduce the aerodynamic and aeroacoustic effects with a propeller in a pusher configuration (SINNIGE, 2013).

Sinnige (2013) also conducted aeroacoustic measurements for the propeller at different advance ratios. The obtained curves, shown in Figure 56, display the difference in noise levels between blown and installed configurations, for the first 3 BPF harmonics.

Figure 56 – Difference in SPL for blown and installed configurations at different advance ratios

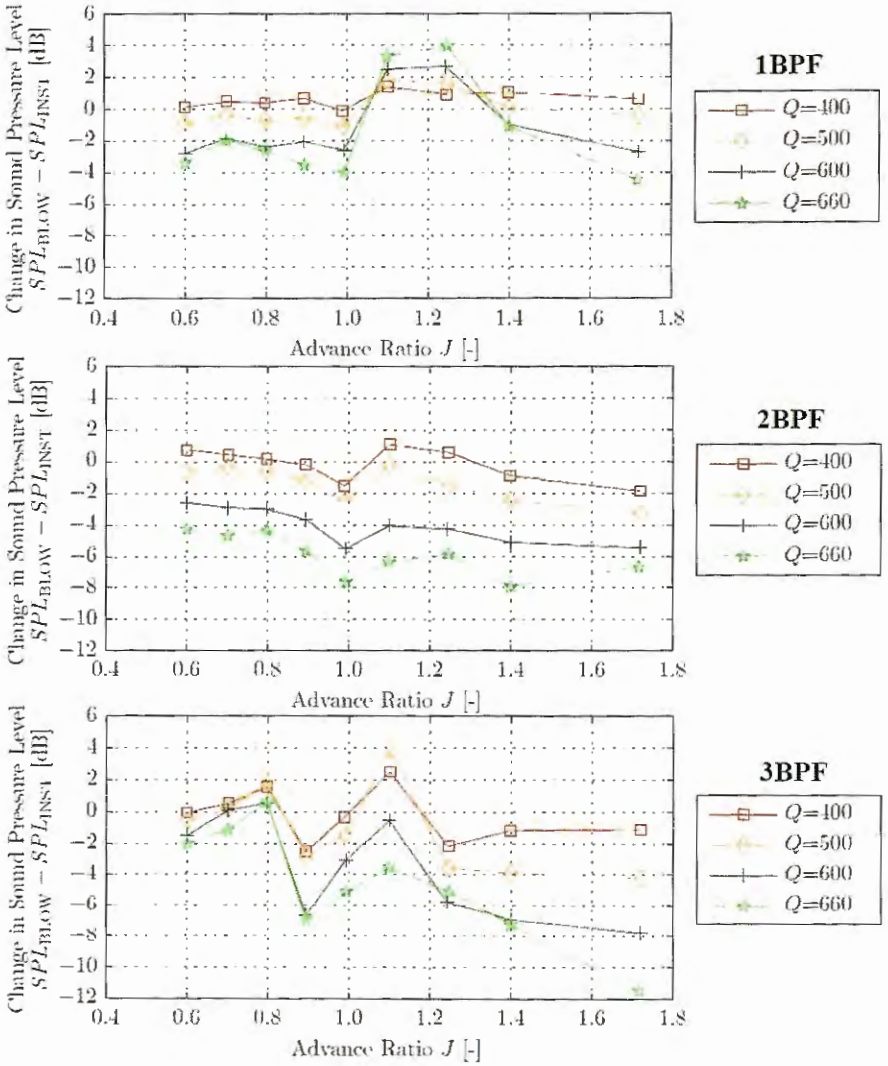

Source – Adapted from Sinnige (2013)

For higher advance ratios, large noise reductions were achieved at the BPF for the highest blowing mass flow. However, there are some advance ratios, where the blown configuration results in louder tones for the BPF, especially for higher blowing mass flows. This occurs in a region ($1.0 < J < 1.3$), where the change in SPL due to the installation effects is negative, likely due to the partial cancellation between the steady and unsteady loading noise emissions. When the blowing is operating, the installation effects are reduced and so is this cancellation between sound fields (SINNIGE, 2013).

The 2nd and 3rd harmonics of the BPF displayed decreased noise levels for the blown configuration, for almost all the tested advanced ratios. This occurs due to the strong effects of installation at those frequencies. Once again, there were some conditions where the blown configuration was louder than the installed one. Similarly as the BPF, the added noise due to installation at these advance ratios was negative or close to zero, indicating a cancellation of the steady loading noise by the unsteady component (SINNIGE, 2013).

3 EXPERIMENTAL SET-UP

3 EXPERIMENTAL SET-UP

This chapter describes the methodologies adopted in order to fulfill the objectives of this work. It contains the wind tunnel facilities that were used for the experiments as well as the models used in the tests, focusing on the three main configurations, and also the design of the blowing system, which will be described in details. The instruments and measurement techniques for each analysis, both aerodynamic and aeroacoustic are also included. Finally, the data post-processing techniques and the format of the results will be presented.

3.1 WIND TUNNEL FACILITY

The investigations and analyses performed in this work are all experimental. The nature of these analyses and the expected results require a low-speed facility, with a free stream speed in the range of 10 to 25 m/s in the working section. Therefore, the tests in this work were conducted at the LAE1 wind tunnel, at the Laboratory of Aerodynamics (LAE) from the Aeronautical Engineering Department of the São Carlos School of Engineering - University of São Paulo (EESC-USP). This facility is of the closed-circuit type, with a closed working section 3 m long, 1.30 m high and 1.70 m wide. It has an eight-bladed fan, driven by a 110 HP electric motor, with seven straighteners located downstream. The maximum speed in the working section is currently 40 m/s. Two mesh screens placed in the settling chamber promote turbulence levels of 0.25%. The wind tunnel circuit is displayed in Figure 57 (SANTANA; CARMO; CATALANO, 2014).

Figure 57 – Top view of the LAE1 wind tunnel

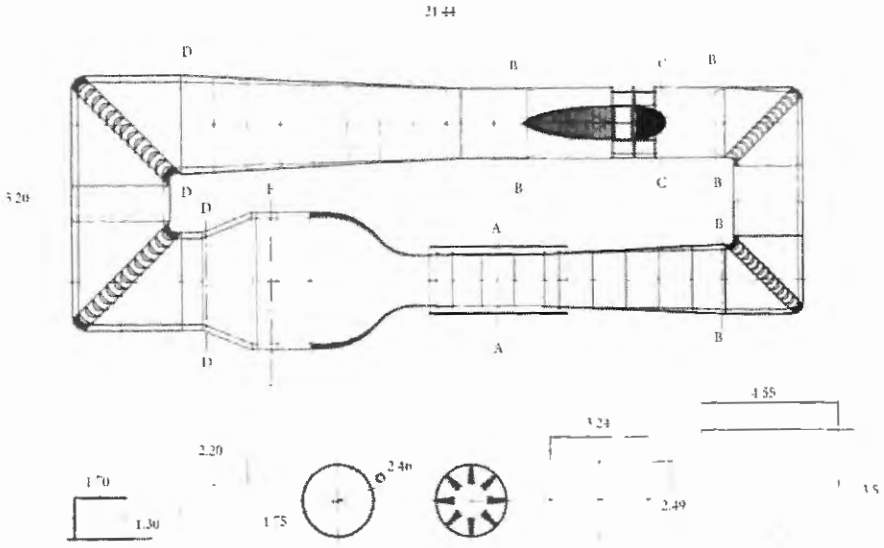

Source – Adapted from Santana, Carmo and Catalano (2014)

Originally, the LAE1 wind tunnel was built solely for aerodynamic tests. However, given the current worldwide focus on aircraft noise investigation and reduction, this facility underwent an update to allow for aeroacoustic measurements as well. The process was divided in two phases. The first one consisted in applying melamine foam on the walls between the corner vanes (A & B), for noise absorption, while the second one focused in putting polyurethane foam around the fan (C), with the same goal, and placing an acoustic baffle (D), between the first and second corner vanes, for the lower frequency noise reduction. In Figure 58, the regions with acoustic treatment are shown, as well as the reduction in background noise, after the two phases of the update (SANTANA; CARMO; CATALANO, 2014).

Figure 58 – LAE1 acoustic treatment and background noise reduction

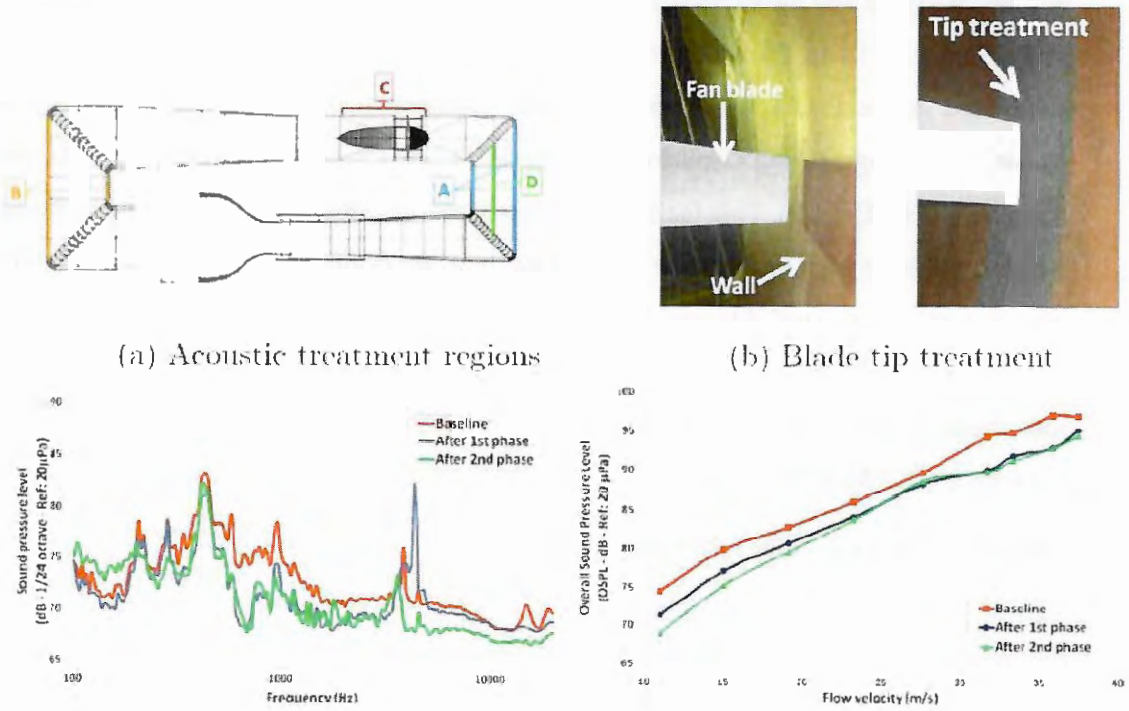

(a) Acoustic treatment regions

(b) Blade tip treatment

(c) Noise spectrum ($U = 37m/s$)

(d) Overall Sound Pressure Level

Source – Adapted from Santana, Carmo and Catalano (2014)

The modifications shown in Figure 58a and Figure 58b resulted in background noise reductions of 5 dB (overall sound pressure level), for different flow velocities. The acoustic treatment described above also had an effect on reducing flow turbulence. Measurements performed with a hot-wire anemometer indicated a reduction in turbulence levels from 0.25% to 0.21%, as shown in Figure 59 (SANTANA; CARMO; CATALANO, 2014).

Figure 59 – LAE1 turbulence levels reduction after the acoustic treatment

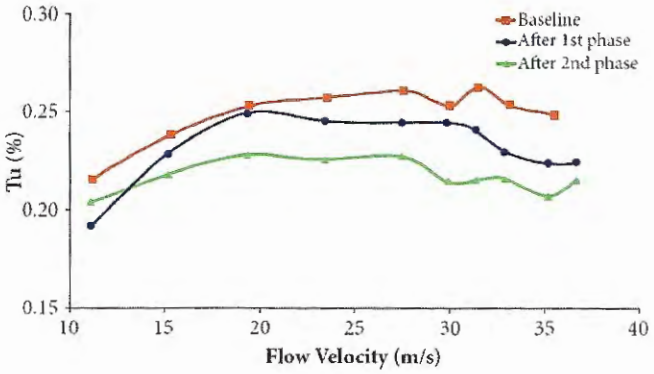

Source – Santana, Carmo and Catalano (2014)

3.2 WIND TUNNEL MODELS

The models used in the experimental measurements were divided in three different configurations, namely the isolated propeller, the installed propeller and the integrated pylon blowing. The same rig was used for all of them, and the particularities of each configuration were adapted to it. The rig was built from scratch, exclusively for this project.

3.2.1 Isolated Propeller Configuration

The isolated configuration was defined in order to get the aerodynamic and aeroacoustic noise results for the propeller alone, without interacting with any other body. Therefore, a tractor configuration was necessary for these tests. Two propellers were chosen: a 4-bladed Master Airscrew, built from wood and fiberglass, with a 16" diameter (0.41 m) and 6" pitch (0.15 m) and a 3-bladed, also from Master Airscrew, with a 16" diameter (0.41 m) and 8" pitch (0.2 m). Both propellers are shown in Figure 60.

Figure 60 – 3-Bladed 16" x 8" propeller and 4-Bladed 16" x 6" propeller

Source – Author

The 4-bladed propeller was built in the LAE from two 2-bladed ones, which were milled and glued together. Templates were used in order to ensure there would be no variations in the propeller diameter and angle of the blades. This 4-bladed propeller was selected for tests at low advance ratios and high thrust conditions, whereas the 3-bladed one was tested at higher advance ratios. Both propellers were also balanced statically and dynamically to avoid vibrations during the tests.

An electric motor, model GT5345-09 by EMAX, used was to rotate the propellers. This motor (Figure 61a) is equipped with 12 LiPo cells, with a 170 RPM/V ratio. It was controlled by an ESC (Electronic Speed Controller), model Turnigy Dlux (Figure 61b), with a maximum burst current of 120 A. The ESC was powered by a D.C. source, built in-house, with a maximum output voltage level of 20 V RMS. The propeller rotation was controlled through the throttle stick in a radio transmitter, model DX5e with a 2.4 GHz band and 5 channels. The receptor was connected to the ESC and was powered by a 6.6 V battery. With these components at hand, the rig could be designed and the first concept is shown in Figure 62.

Figure 61 – Electric motor and ESC for the propeller operation

Source – Author

Figure 62 – Dimensions for the isolated configuration wind tunnel model

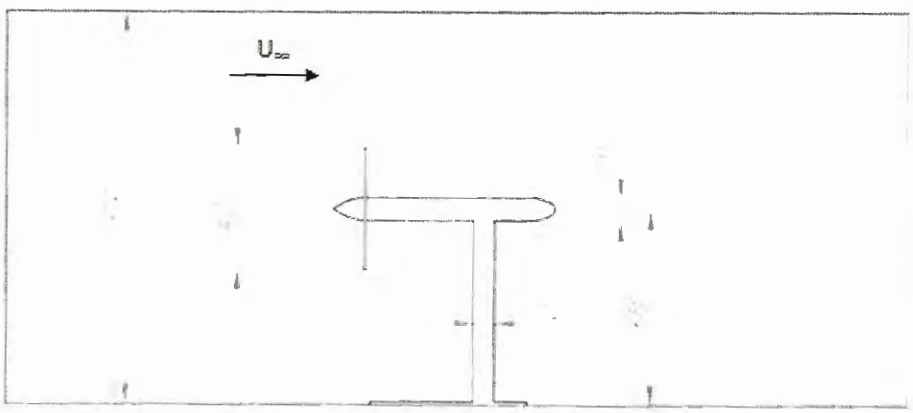

Source – Author

In this drawing, the rig is mounted in the working section of the wind tunnel. Aside from the propeller diameter, the only other constraint was the vertical position for the propeller axis, which needed to be 0.65 m, so it would be aligned with the center of the microphone array (Section 3.4.5), simplifying the postprocessing of the acoustic measurements. The components were then assembled and the resultant rig is shown in Figure 63. The main strut was designed with a streamlined shape, in order to avoid a wide wake or vortex shedding. A spinner was also attached to smooth the flow at the propeller hub. The ESC, its cables and the receiver were placed inside the nacelle, with the power source cables going through the strut as well, to avoid any undesirable flow interaction, especially in front of the propeller, when the model is changed to pusher configuration.

Figure 63 – Isolated configuration wind tunnel model

Source – Author

3.2.2 Installed Propeller Configuration

For the installed configuration, the idea was to utilize the same rig used for the isolated tests. The first necessary alteration was to change the propellers to a pusher configuration, which was done simply by turning the rig 180°, and also the propeller (relative to the motor shaft), so that its upper surface would be facing the oncoming flow. Then, the direction of the motor rotation needed to be reversed, which could be easily done by interchanging the ESC wires. Therefore, only the pylon was needed to complete this configuration. Initially, the only constraint was its span, which was limited by the nacelle and the platform at the bottom, to approximately 0.6 m. The chord was defined as 0.4 m, same as the propeller diameter, which

is the ratio regularly found in the literature. The distance between the trailing edge and the propeller plane would be equal to 0.3c, similarly as done by Block and Gentry Jr. (1986). The concept for the installed configuration is shown in Figure 64.

Figure 64 – Dimensions for the installed configuration wind tunnel model

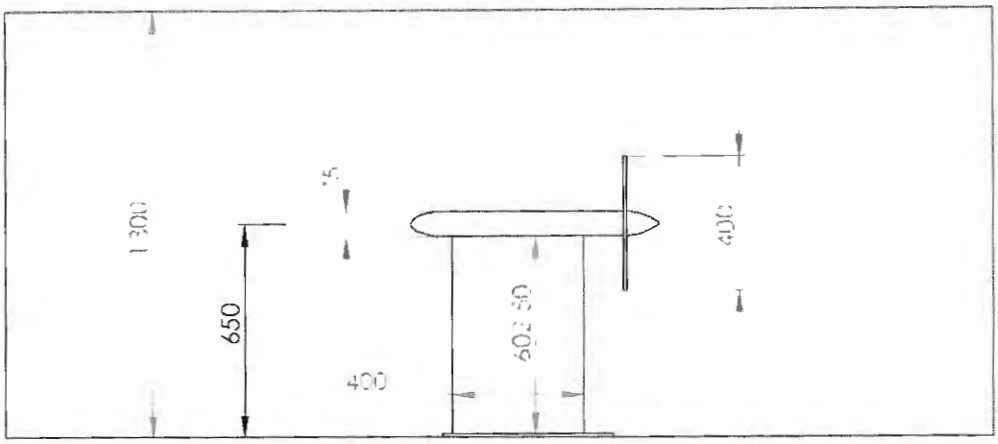

Source – Author

Then, the pylon profile should be defined. Initially, it was decided that a symmetric airfoil was to be chosen, so that the wake could also be symmetric for a zero angle of attack condition and also to simplify the blowing system, in order for the same internal duct geometry to be used for both the upper and lower surfaces. Another initial requirement was the profile thickness, defined as 12% of the chord, so that the adverse pressure gradient would not be so intense and to keep the boundary layer as thin as possible, especially near the blowing region. Lower thickness values were impractical due to structural weakness and less useable space inside the pylon to place the blowing ducts.

The initial idea was to conduct a comparative analysis between different airfoils with a 12% thickness, focusing on the boundary layer displacement thickness (δ^*) on three different chordwise positions (0.7c, 0.75c and 0.8c). This parameter would be ultimately related to the necessary blowing mass-flow and was thus chosen for this analysis. The selected airfoils were the NACA 0012, NACA 63012, EPPLER 297 and the WORTMANN FX71-120. This comparison was carried out using the software XFOIL, for a 2D panel method viscous analysis. The Reynolds Number was selected as 3.5×10^5, based on the pylon chord and the wind tunnel speed. The same input parameters were used for all the airfoils. Another important parameter to be set was the amplification factor (n_{crit}), defined as 6.3, to match the tunnel free stream turbulence of 0.21%. A fixed transition was also defined at 0.05c for both upper and lower sides. The calculations were performed for 0° and 10° of angle of attack. The results are shown in the plots in Figure 65.

Figure 65 – Boundary layer displacement thickness for different pylon profiles

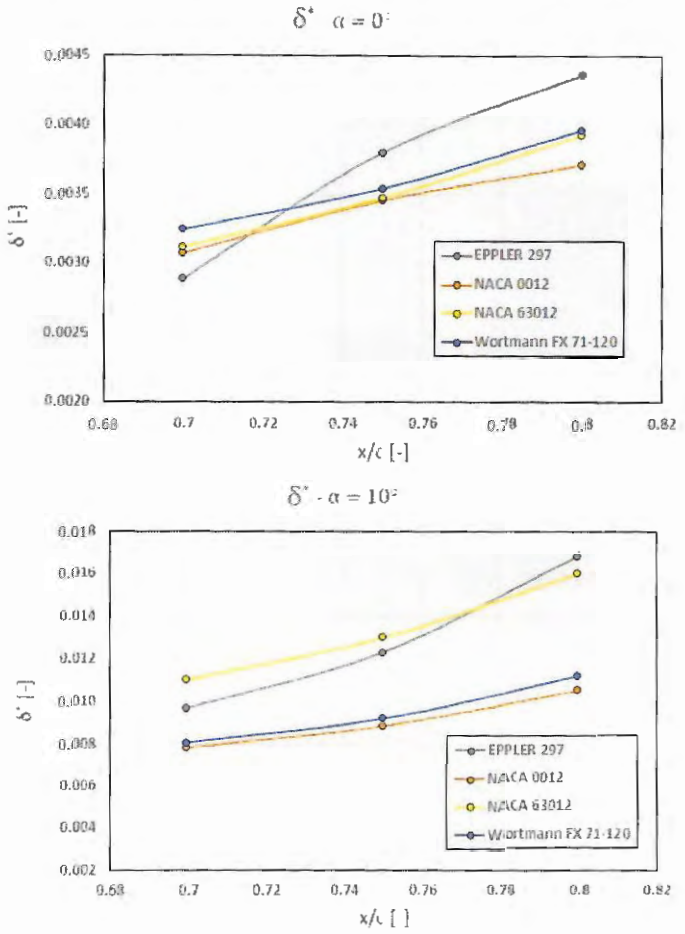

Source – Author

From the results, it can be verified that the airfoil with the lowest boundary layer displacement thickness, for $\alpha = 0°$ and $x/c = 0.7$, was the EPPLER 297. However, the boundary layer growth rate for this airfoil is high, and for the next chordwise position, it has the highest δ^* from all profiles. For the following chordwise positions the NACA 0012 provides the lowest results, same as all positions for $\alpha = 10°$. Therefore, the NACA 0012 was the chosen airfoil.

The aerodynamic results and the simplicity of this airfoil make it the best candidate for the pylon. Given that many similar wings with this profile have been built in the LAE, the construction process was not very complex. In order for the pylon to be assembled at the rig, the upper and lower surfaces, manufactured from wood, needed to be built separately, due to the presence of the support strut, and screwed together at the rig. The model also needed internal channels to fit the tubes used for surface pressure measurements (Section 3.4.3) which would go through the strut to the bottom of the model, to be attached to the pressure transducer. The resultant installed configuration is shown in Figure 66.

Figure 66 – Installed configurations with 3- and 4-bladed propellers

Source – Author

For some tests of the installed configuration, a tripping device was be used to induce boundary layer transition at a preselected region. This was be done in order to simulate a more realistic condition of boundary layer growth, increasing the similarity of the tests to a full-scale configuration. For that purpose, a zigzag adhesive strip was cut and placed in a position correspondent to 5% of the pylon chord, as shown in Figure 67. Thus, laminar separation and the formation of bubbles are no longer expected to occur. The effects of the addition of the trip were be investigated through both aerodynamic and aeroacoustic tests.

Figure 67 – Installed configurations with 3- and 4-bladed propellers

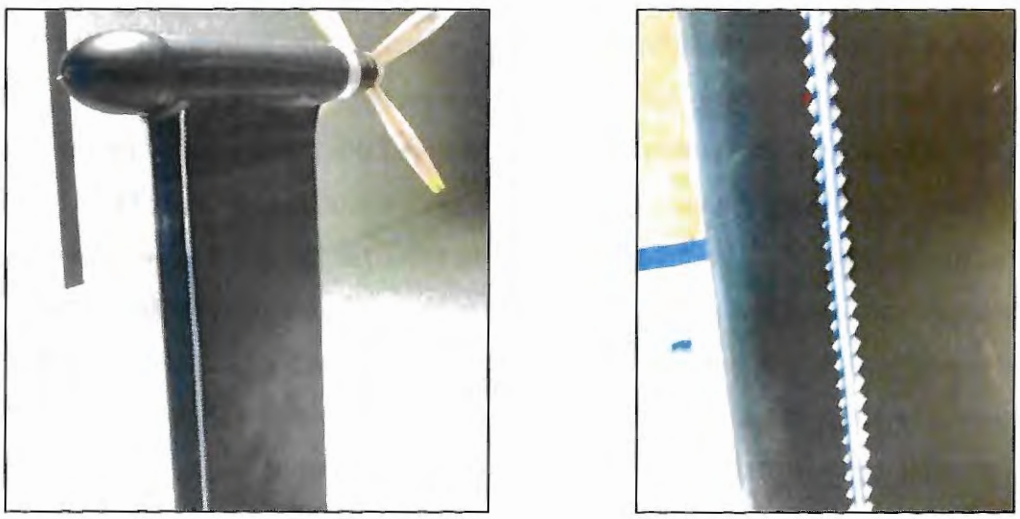

Source – Author

3.2.3 Blown Configuration

For the design of the blowing system, the only initial requirement was that it should be positioned on both upper and lower surfaces of the pylon. This was decided as so to ensure an enough mixing length between the jet and the external flow, as opposed to positioning the blowing slot at the trailing edge. The effect of the adverse pressure gradient on the remaining length before reaching the trailing edge will be counterbalanced by an increase in the jet velocity, with the objective to keep the boundary layer thickness to a minimum and consequently the wake, after the separation at the trailing edge.

Initially, it was thought to use the same values as Gentry Jr., Booth Jr. and Takallu (1990), and position the slot at 80% of the pylon chord. However, it was decided to move the slot upstream, to a position corresponding to 0.7c. This was done for three reasons: first, there would be a longer distance between the slot and the propeller, which would allow for a longer mixing length and the velocity profile of the wake would in turn be more uniform. Secondly, at this point, the boundary layer thickness would be smaller, also reducing the necessary blowing mass-flow. Finally, the profile itself is also thicker at this position, which allows more space for placing the system components with a lower risk of structural damage.

The dimensioning of the system started with the span of the blowing slot. Initially, the propeller radius, minus the region of the nacelle, was considered for this dimension. However, given the effect of the propeller to contract the upstream flow, the blowing slot span was increased by 10%. Larger spans, up to 25% of the propeller radius would be suggested, but this would require an increase in the mass flow, in order to have the same velocity at the slot. Since the air supply system conditions are a constraint, it was decided to keep this extra length as an intermediary value.

The slot height was defined based on the boundary layer characteristics at that specific point. The non-dimensional value for δ^* at 0.7c, for zero angle of attack, can be taken from the chart in Figure 65 as approximately 3.1×10^{-2}. By considering the pylon chord of 400 mm, the displacement thickness at that point will then be equal to 1.22 mm. Although the actual boundary layer thickness at that point would be larger, it was decided to keep the slot height to 2 mm, which is the minimum feasible value for manufacture purposes, in order to get the highest possible outflow velocity. Despite the relative thick boundary layer at this point, this blowing concept was based on giving the highest outflow velocity possible so the boundary layer growth downstream of this point would be kept small as possible.

Afterwards, it was necessary to define an air feeding system for this slot. The design of this system was based on the work of Croce (1998), who investigated the addition of mass to the wakes of a fixed and a rotating cylinder. In his work, this was carried out by positioning a secondary cylinder, with a much smaller diameter, downstream of the one that was the subject of the study. This mass addition cylinder had several holes of 1.5 mm throughout its span, so the blowing occurs at discrete positions and the mixing occurs in the wake. One of the ends was sealed, while the other was connected to the air supply system. This configuration is shown in Figure 68, and the actual cylinder with the holes is shown in Figure 69.

Figure 68 – Configuration for blowing in a cylinder wake

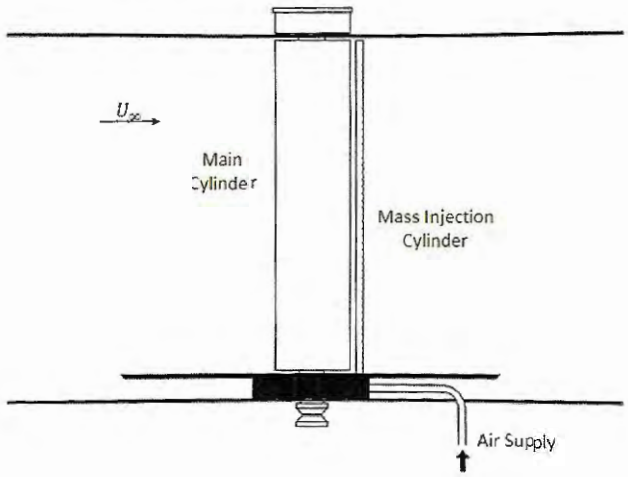

Source – Adapted from Croce (1998)

Figure 69 – Cylinder for mass injection with discrete blowing slots

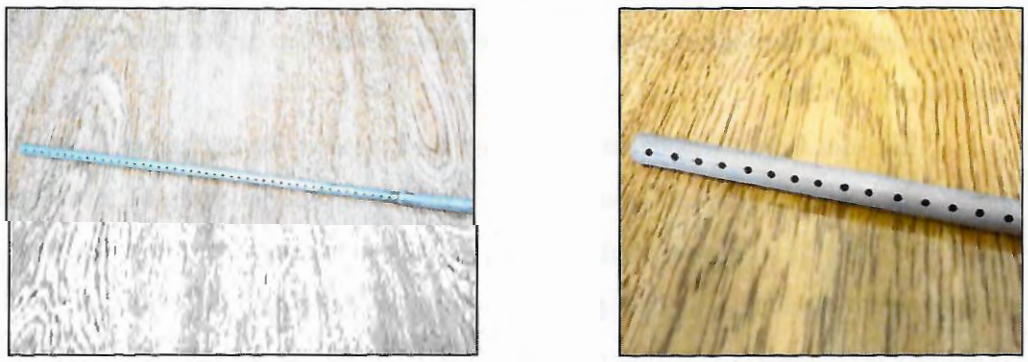

Source – Author

The results for the velocity profile in the cylinder wake with and without the blowing are shown in Figure 70. The blowing mass flow was set for the optimum condition as so to eliminate the velocity deficit and make the profile uniform. Very satisfactory results were achieved with this configuration and, despite the discrete mass injections from each slot, a good mixing occurs with the external flow. Therefore, this blowing concept was used as the basis for

the pylon system, where one of the main concerns was the uniformity of the flow upstream of the propeller.

Figure 70 – Velocity profile for the cylinder wake with and without blowing

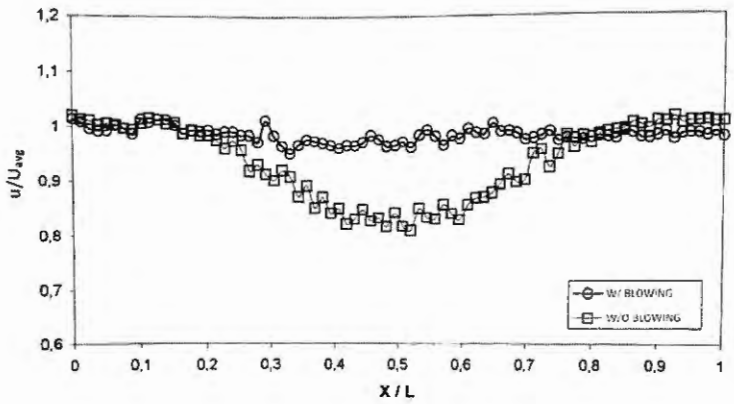

Source – Adapted from Croce (1998)

Another advantage of this system is the less need for internal space inside the pylon to fit the ducts and channels. Given the aspect ratio of the pylon, an internal geometry to turn the flow 90° smoothly from the inlet to the blowing slots would have to occupy almost the entire chord distance, even with the aid of turning vanes to guide the flow. This configuration would be expected to be more complex, and the outflow velocity might not have the expected characteristics. Therefore, this configuration was abandoned and the cylinder with holes was chosen as the air supply system.

For this cylinder with holes configuration to be applied at the pylon, there must be a path for the flow to leave the cylinder and reach the exit slot smoothly. This path must not be excessively long to avoid friction losses. Moreover, aiming to avoid any type of adverse pressure gradient, since the slot height was set as 2 mm, the cylinder holes were drilled with diameter of 2.4 mm, and the channel between them was designed with an always-contracting cross-section. These internal channels were also drawn symmetrically relative to the chord, so that the same mass flow would be delivered to both upper and lower surfaces. The cross-section of the blowing region on the pylon is shown in Figure 71.

Figure 71 – Shape of the pylon trailing edge with integrated blowing system

Source – Author

The air supply duct was built from a copper tube of 15 mm of diameter, with a row of holes for the blowing flow. These holes were drilled with the aid of a CNC machine, in order to assure correct placement and even spacing between them. The holes were drilled with a diameter of 2.4 mm, with a spacing of 4.4 mm between centers. In total, 44 holes were drilled to cover the entire span of the blown region. The cylinder with the holes is shown in Figure 74.

Figure 74 – Drilled cylinder for feeding air to the blowing slots

Source – Author

Finally, the air for the blowing was supplied from a compressor at the LAE with maximum nominal mass flow rate of 710 L/min. However, given the capacity of the compressor tank, this mass flow cannot be sustained for a long time. Therefore, the tests with blowing had to be conducted before the tank turned empty. The actual mass flow at the blowing will be smaller than this value, given the pressure losses throughout the circuit. The wind tunnel model equipped with the blowing system is shown in Figure 75. The fairings between the pylon and the nacelle had to be adapted for this configuration.

Figure 75 – Model in blown configuration with 4-bladed propeller

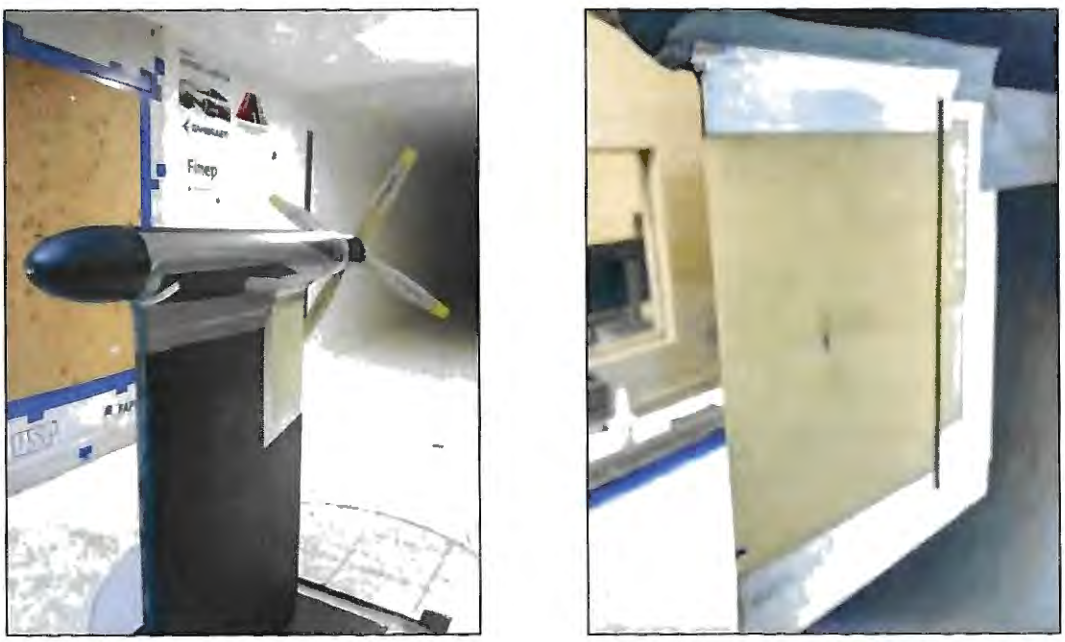

Source – Author

An issue with this configuration was found during preliminary tests of feeding air through the cylinder. The flow could not properly turn at the lower holes, and it tended to exit the cylinder only through the upper ones. This would result in a high non-uniformity in the blowing outflow, which means the wakes would not be properly filled and possibly no aeroacoustic benefits would be obtained. To fix this issue, small tubes were placed and glued inside the holes to better direct the flow outwards of the cylinder, perpendicular to each hole, as shown in Figure 76. Ideally, these tubes should have been longer outside of the cylinder, but given the limited space, they were trimmed at the cylinder surface. Although this is not an optimized solution, since these tubes will result in more pressure losses, it was found that the outflow uniformity had significantly improved, in comparison to the original results. The aerodynamic measurements for the blowing are shown in Section 4.3.

Figure 76 – Tubes inside the cylinder holes to direction the blowing outflow

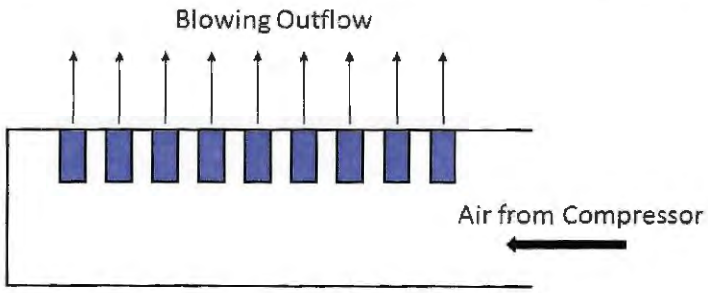

Source – Author

3.3 COORDINATES SYSTEMS

For the experimental campaign in this work, two different Cartesian coordinates systems were adopted. The first one places the origin at the intersection of the horizontal line, corresponding to the propeller axis, and the vertical line of the pylon leading edge, as shown in Figure 77. This one was used for all the aerodynamic measurements, including the forces, surface pressures and flowfield mapping tests. For the isolated case, the position of the origin is not relevant to data obtained, thus it will be actually used only for the installed and blown configurations. This coordinate system was chosen to facilitate the analysis of the surface pressures on the pylon, since $x = 0$ corresponds to the leading edge, as well as the hot-wire measurements, since the spanwise positions can be described as radial stations of the propeller blades.

Figure 77 – Coordinates systems for aerodynamic tests

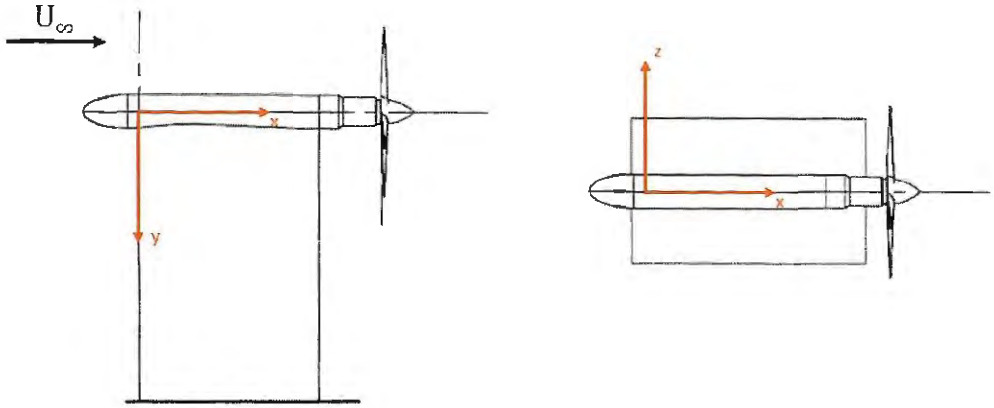

Source – Author

The aeroacoustic coordinates system is positioned at the intersection with the propeller plane and the propeller axis. This point is coincident with the center of the microphone array, so that the distance between the microphones to the noise source can be defined as half of the working section width, as shown in Figure 78.

Figure 78 – Coordinates systems for aeroacoustic tests

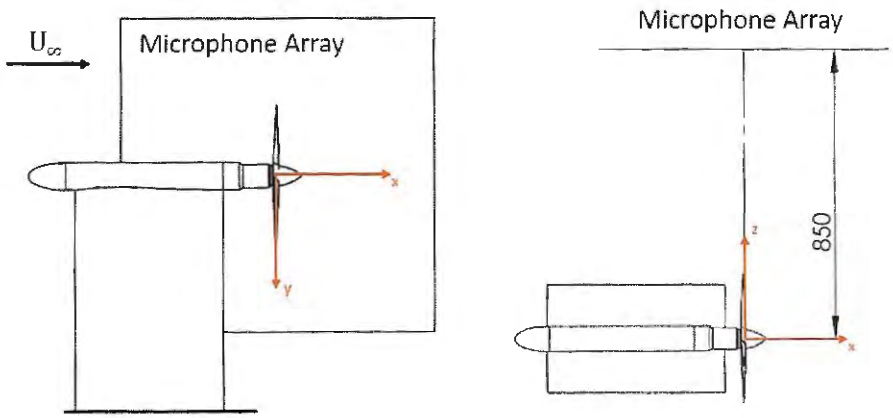

Source – Author

Two secondary coordinates systems were also included for the directivity and angle of attack aeroacoustic analyses. For the tests at different directivity angles, the model was moved forward and backwards, with the angle between the propeller plane and the array center defined as the directivity θ, as shown in Figure 79. When the propeller plane is aligned with the center of the array, this position corresponds to $\theta = 90°$. For the angle of attack, the positive α convention was different for when the propeller is mounted either in tractor or pusher positions, as shown in Figure 80. This was defined as such, since the direction of rotation was the opposite for the two positions.

Figure 79 – Convention for directivity aeroacoustic measurements

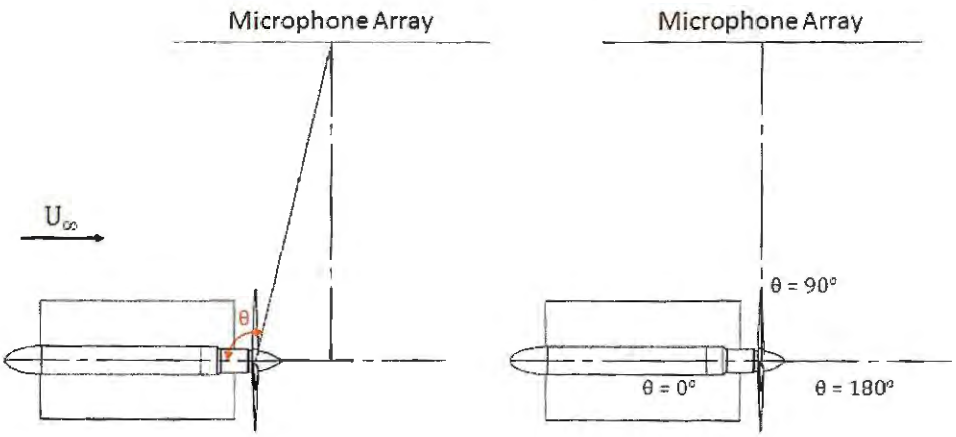

Source – Author

Figure 80 – Convention for angle of attack aeroacoustic measurements

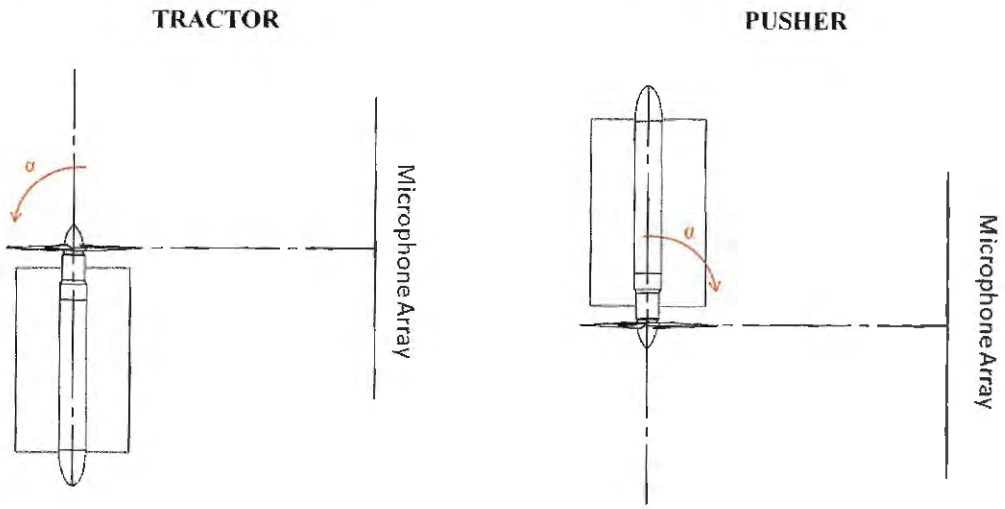

Source – Author

3.4 INSTRUMENTATION AND MEASUREMENT TECHNIQUES

In this section, the instruments and the techniques employed for the aerodynamic and aeroacoustic measurements will be described. Only the basic characteristics of the instruments will be stated in this section. For more information, refer to Appendix B of this work.

3.4.1 Measurements of Free Stream Conditions

Before the actual wind tunnel tests start, initial measurements related to the atmospheric and aerodynamic properties of the free stream need to be performed. These are required for the non-dimesionalization of parameters, in order to have an independence from the model scale.

They can also be used to correlate the obtained results with a specific flow condition (e.g. Mach number). One of these flow properties is the atmospheric pressure, which can be measured through a calibrated mercury barometer, with a precision of 1 mmHg.

Another important flow parameter is the temperature, for both aerodynamics and aeroacoustics, since it influences the flow Mach number (M), as shown in Equation 4. Since the tunnel is of the closed circuit type, it is expected that, during the execution of a test, the air temperature increases continuously until it stabilizes in a level different from the one at the start of the test. The longer the test lasts, the higher is the temperature variation inside the tunnel, which must be taken into account. The flow temperature measurements inside the tunnel are conducted with a thermocouple with a precision of 0.1 °C.

$$M = \frac{V}{\sqrt{\gamma RT}} \qquad \text{Equation 4}$$

Source – Houghton and Carpenter (2003)

In Equation 4, V represents the flow velocity, γ is the ratio of specific heats (equal to 1.4 for standard air conditions), T is temperature, and R is the universal gas constant, equal to 287 J/(kg.K), in S.I. units, for air. By having the local static pressure (p) and temperature, the air density (ρ) can be calculated through the Ideal Gas Law, as shown in Equation 5, also using the universal gas constant. The density value is used to calculate the dynamic pressure.

$$\rho = \frac{p}{RT} \qquad \text{Equation 5}$$

Source – Houghton and Carpenter (2003)

The last main free stream parameter to be measured is the dynamic pressure (q), which in turn is used to calculate the free stream speed (U_∞), for the local air density, as shown in Equation 6. This dynamic pressure can be measured through a differential micromanometer, which is connected to a Pitot-static probe, mounted inside of the working section. This probe measures both the total and the static pressure of the flow, and the pressure differential between them, the dynamic pressure, is then displayed by the micromanometer. The model used, with precision of 0.1 Pa, is described in Appendix B1.

$$U_\infty = \sqrt{\frac{2q}{\rho}} \qquad \text{Equation 6}$$

Source – Houghton and Carpenter (2003)

3.4.2 Measurements of Aerodynamic Forces

For the measurement of the aerodynamic forces acting on the model, a 3-component external balance was used, which was designed and built at the LAE. This balance has the capability of measuring aerodynamic loads in a single plane, which is usually chosen as the longitudinal plane, for the measurement of lift and drag forces and pitching moment. It is equipped with strain gauges fixed on aluminum plates (load cells), which will displace when the loads are transferred from the model to the balance where it is mounted. This displacement will change the strain gauge electric resistance and thus the current through it, for a given applied voltage.

The strain gauges are mounted in a Wheatstone bridge circuit, in order to facilitate the measurements, given the low order of variation in the resistance of these components. Starting with the bridge in the balanced condition, when a load is applied to the gauge, the resistance variation will unbalance the bridge, and the resultant voltage can be more easily measured. In the LAE1 external balance, full bridges configurations, in which all the four resistors in the Wheatstone bridge are changed to strain gauges, are used for each of the directions of measurement. The balance has a measurement precision of 0.7% for maximum loading, thus 1.0 N for lift force, 0.19 N for drag force, and 1 Nm for pitching moment (MAUNSELL, 1977). The aerodynamic balance is positioned beneath the working section of the wind tunnel and is shown in Figure 81.

Figure 81 – Aerodynamic balance at the LAE1 wind tunnel

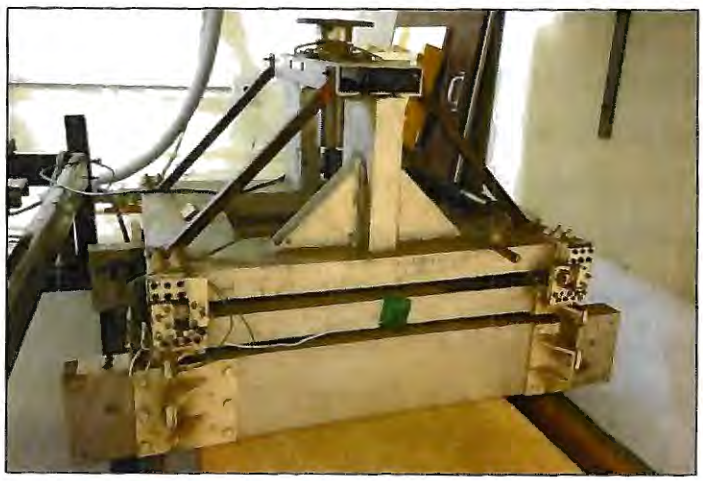

Source – Author

The voltage measurements from the strain gauges are then amplified through a HBM (*Hottinger Baldwin Messtechnik*) MGCPlus module, which allows for gains and filtering regulations. The HBM data is described in Appendix B2. The tests with the aerodynamic

balance were all conducted using a sampling frequency of 1000 Hz and measurement time of 5 seconds. Since the signal provided by the HBM has an electric nature, it must be converted to force units through a calibration curve. The calibration procedure is described in Appendix B2. The calibration constant is then embedded in the acquisition software, so the output is already in force units.

The angle of attack of the model is manually set, and thus a reference for positioning the model is needed, in this case, the working section walls were used. A good procedure for estimating the zero angle of attack of the model is measuring its lift force. Since the model is ideally symmetric (with possible minor variations during construction), the angle for which the lift is null is most likely the zero degree. Thus, if the lift curve is phased out from the origin, it can be offset of that angle. The model is mounted in a turntable, with a 0.5° precision. This turntable is controlled by a stepper motor, activated by a MATLAB® script, and a power screw that assures the precision of the angle of attack variation.

3.4.3 Measurements of Surface Pressures

Pressure measurements were conducted on the pylon surface with the aid of a Scanivalve™ pressure scanner, model ZOC33/64Px, as described in Appendix B3. The output from this instrument is a pressure differential, and thus, a reference of constant value must be used. For these tests, the static pressure in the tunnel working section was selected to facilitate the data post-processing. The Scanivalve™ used throughout this work has a full-scale range of ±20 inH_20 (0.72 psi) and the acquisition was performed with a sample rate of 5 kHz and 1000 samples per tapping.

In order to measure the pressure at the surface of the pylon, the model must be equipped with taps in the chordwise direction. Therefore, holes of 1.2 mm of diameter were drilled on the surface at specific points, both on the upper and lower sides of the pylon. For this work, a single row of pressure tappings was chosen, which was positioned at the spanwise station equivalent to 70% of the propeller radius (r/R = 0.70), as shown in Figure 82. Each side of the pylon has 21 tappings, making 42 on the total. The tappings coordinates are included in the Appendix A.

Tubes were then attached to those holes and connected to the Scanivalve™ for the pressure measurements. It is also necessary to connect the tubes from the static and total pressure of the free stream, carried out with the Pitot-static probe inside the tunnel. Thus, these parameters were also acquired and used for non-dimensionalization of the static pressure values on the pylon surface.

Figure 82 – Location of the pylon pressure tappings row

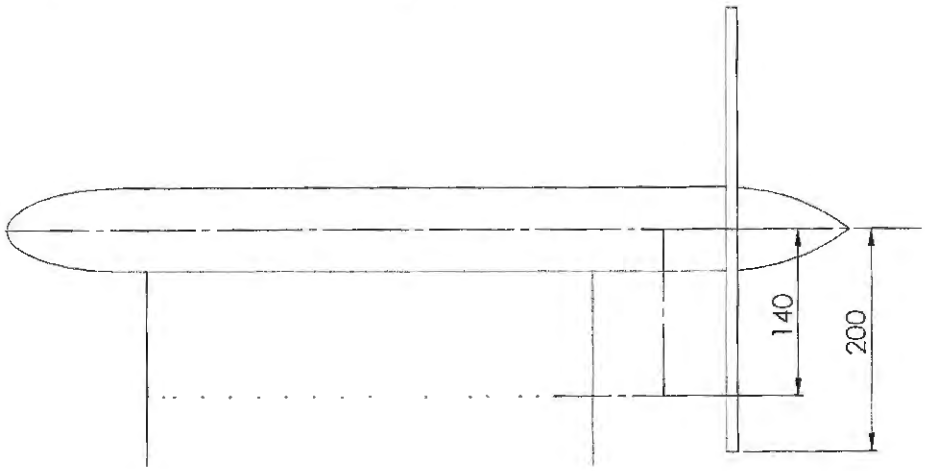

Source – Author

3.4.4 Measurements of the Flowfield Characteristics

Flowfield measurements were carried out to map the region downstream of the pylon trailing edge, in order to obtain the wake characteristics. For these tests, a hot-wire anemometer was used, which allows for the measurement of several flow parameters, such as mean velocities, flow angularities and turbulence levels, carried out with a very high precision and at very high frequencies. The probes are small wires, with diameter in the order of micrometers, attached to prongs. This technique is based on feeding current through the wire, which raises its temperature. For a given flow velocity, the heat exchange due to convection can be measured as voltage across the bridge, and correlated to this velocity through calibration charts (BARLOW; RAE JR.; POPE, 1999).

For the wake measurements, a Dual Sensor X-Shaped probe was chosen, wherein the wires are placed parallel to the probe axis. This was required due to the very limited space between the pylon and the propeller. With this configuration, the interference of the probe support structure in the flow can be the smallest possible. This probe was acquired from Dantec Dynamics™, and it is described in Appendix B4.

This hot-wire is of the Constant Temperature Anemometer (CTA) type. For this case, electronic circuits include a feedback differential amplifier to obtain a rapid variation in the heating current to compensate for instantaneous changes in the flow velocity and thus maintain the wire at a constant resistance and temperature, which is easier to use in incompressible flows. This way, the voltage changes at the bridge, necessary to modify the current, can be measured and the result will be proportional to the instantaneous flow velocity (BRUUN, 1995).

A Dantec™ StreamLine analog anemometer system was used with CTA modules for the measurements. The system is operated by the StreamWare Pro application software, which performs set-up, automatic probe calibration, and data acquisition, conversion and reduction. The data acquisition for the flowfield measurements was performed with a 1 kHz sampling rate, and 1024 samples were taken. In order to verify the time history of the hot-wire data, some measurements were conducted at higher frequencies, of 16 kHz, with 100000 samples. The calibration of the probes (both velocity magnitude and directions) was performed with an Automatic Calibrator, also from DANTEC™, and the calibration curve is shown in Appendix B4.

During the measurements, the probe is controlled by 3-axis traverse system, allowing it to move in all three orthogonal directions, if necessary. Thus, before the start of the experiment, a grid must be defined in which the acquisition will be performed for all defined points. This grid can be a line, a plane or a volume and can be refined to a precision of up to 12.5 μm or 6.5 μm (depending on the axis), according to the needs of the experiment.

The hot-wire measurements of the pylon wake were conducted for five spanwise stations, starting at r = 0.40R with a space of 40 mm between them. The following stations are then at 0.60R, 0.80R, 1.00R and 1.2R. The latter was chosen to verify if there was still an influence from the slipstream at this region, which is shortly after the blowing span. These stations are shown in Figure 83. The probe was set halfway between the pylon trailing edge and the propeller plane to avoid any contact with these components, which could damage the probe. The hot-wire probe placed downstream of the pylon trailing edge is shown in Figure 84.

Figure 83 – Spanwise stations for pylon wake measurements

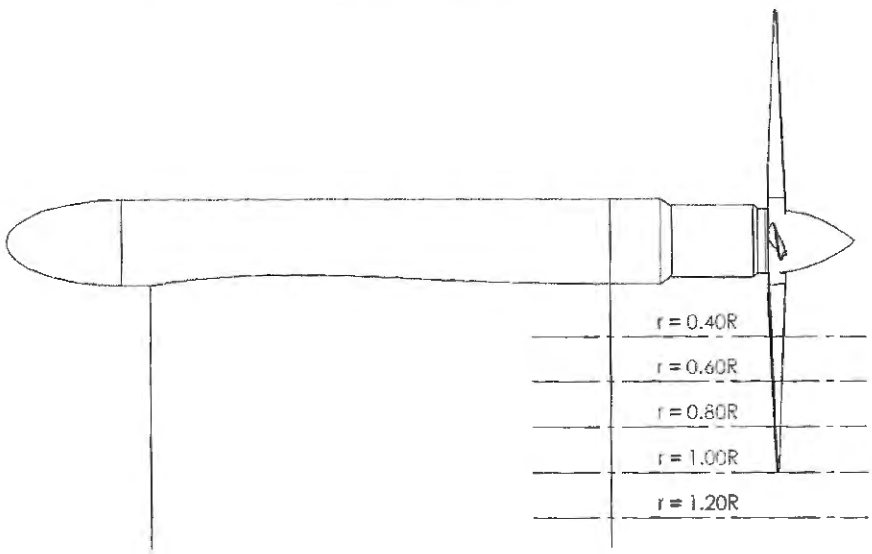

Source – Author

Figure 84 – Flow mapping between the pylon trailing edge and the propeller

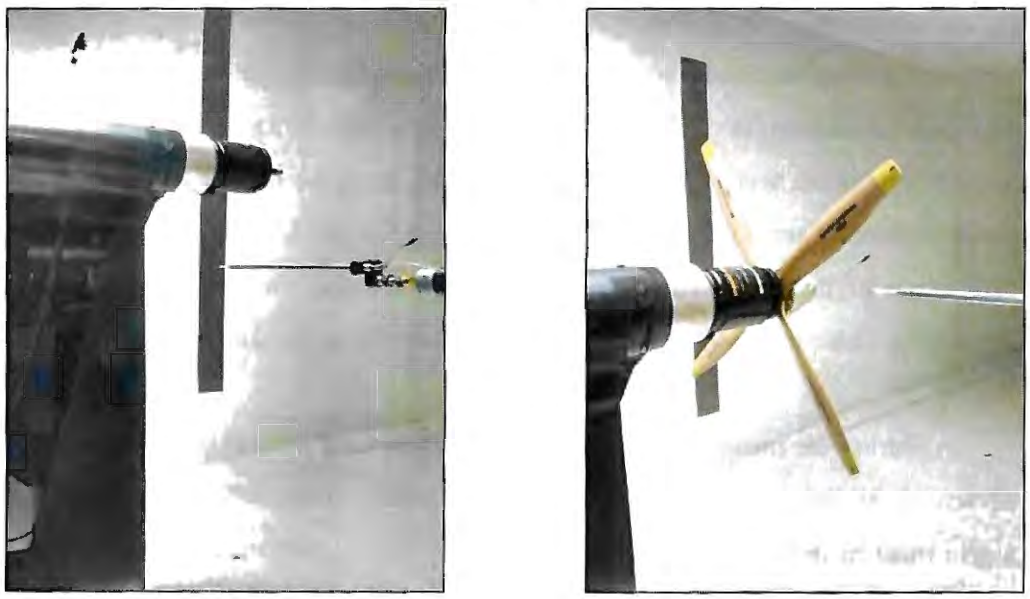

Source – Author

3.4.5 Aeroacoustic Measurements

For the aeroacoustic measurements, in-flow microphones were used to perform sound pressure acquisition, since the LAE1 wind tunnel is of the closed circuit type. An array of 61 microphones G.R.A.S. 46 *BD* is available for the aeroacoustic tests. This array is flush mounted on one of the working section walls. This array has a modified spiral geometry, in order to allow measurements at both low and high frequencies, with a diameter of approximately 0.85 m, as shown in Figure 85.

Figure 85 – Microphone array at LAE1

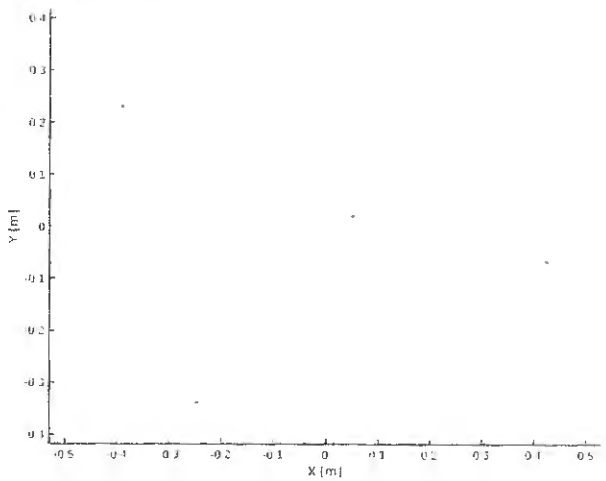

Source – Author

The beamwidth (main lobe width of the array response pattern at -3 dB of its peak value) and dynamic range (difference between the peak value for the main lobe and for the highest secondary lobe) this array is shown in Figure 86 (PAGANI JR., 2014).

Figure 86 – Beamwidth and dynamic range of the array

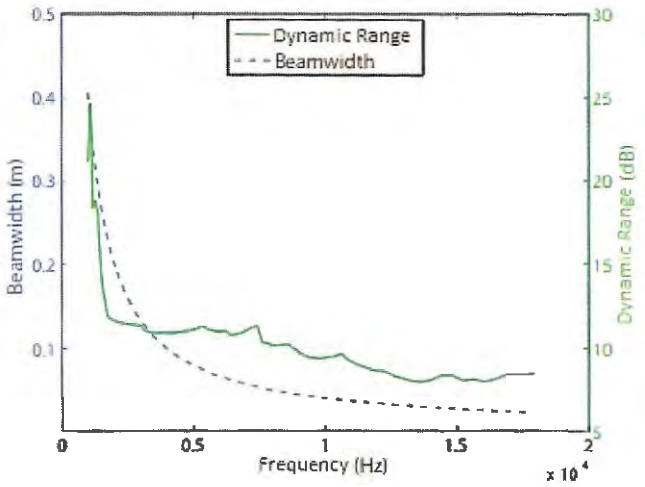

Source – Adapted from Pagani Jr. (2014)

The data acquisition is performed through a PXI system, composed by 4 NI PXIe-4496 (IEPE) with 16 channels each and capacity to hold 64 analog inputs simultaneously, with 24 bits resolution and maximum sample rate of 204.8 kS/s. MATLAB® codes developed at the LAE were used to acquire the signal from the microphones. A sample rate of 102.4 kHz and an acquisition time of 20 s were used. The conversion from the raw signals was already performed during acquisition, through the microphone calibration curves embedded in the MATLAB® codes.

3.5 DATA POST-PROCESSING AND PRESENTATION

The data acquired from the various instruments need to be post-processed, in order to provide the actual results of the analyses.

3.5.1 Aerodynamic Measurements

For the aerodynamic measurements of the isolated propeller, it is possible to measure only the thrust force, which will be plotted against the advance ratio (J), given by Equation 7. This parameter was altered by changing the wind tunnel speed (U_∞), while the propeller rotation (n) and diameter (D) were kept constant. However, variations in the wind tunnel flow speed also induced variations in the propeller rotation, which had to be taken into account in the advance ratio calculation. In order to get the net thrust force, the model drag was measured in

a prop-off condition, and the results used as offset for the prop-on results. The thrust was also non-dimensionalized to its respective coefficient, as shown in Equation 8.

$$J = \frac{U_\infty}{nD} \qquad \text{Equation 7}$$

$$C_T = \frac{T}{\rho n^2 D^4} \qquad \text{Equation 8}$$

Source – Houghton and Carpenter (2003)

The surface pressure data is obtained as a differential between the static pressure on the model (P_S) and a reference value (P_{ref}), set as the working section static pressure. This was done in order to calculate the pressure coefficient (Equation 9) and perform a non-dimensional analysis of this parameter. Thus, the pressure coefficient was calculated for each tapping on the model and then plotted versus its x-axis coordinate, as a percentage of the pylon chord. The dynamic pressure was obtained by plugging one port of the Scanivalve™ to the wind tunnel total pressure. Since it is already a differential measurement, the obtained result at that port was the dynamic pressure. The conversion of data to pressure units was automatically performed in the acquisition software.

$$C_P = \frac{P_S - P_{ref}}{q} \qquad \text{Equation 9}$$

Source – Houghton and Carpenter (2003)

For the flowfield measurements, the hot-wire started measuring at a distance of 35 mm of the trailing edge in the z-axis and measure 71 points (1 mm spacing) in this direction. For the blown configuration, only 35 points could be measured (2 mm spacing), before the blowing mass flow would start to decrease, given the tank capacity of the compressor. The local velocities u and v will be non-dimensionalized by the free stream speed, for each condition.

As described by the manufacturer, the Dual Sensor X-Shaped probe measures two velocity components in the xy-plane of the probe coordinate system, U_{1cal} and U_{2cal}, based on a previously performed calibration. These are used for the calculations in the wire coordinate system, using the yaw-factors (k_1 and k_2) and the angles between the wires and axes (α_1 and α_2), as described in Equation 10 and Equation 11 (DANTEC DYNAMICS, 2000). The default values provided by the manufacturer were used to calculate the velocities, also shown below.

$$U_{1cal}^2(1+k_1^2)\cos(90-\alpha_1) = k_1^2U_1^2 + U_2^2 \quad \text{Equation 10}$$

$$U_{2cal}^2(1+k_2^2)\cos(90-\alpha_2)^2 = U_1^2 + k_2^2U_2^2 \quad \text{Equation 11}$$

$$k_1^2 = 0.06\,;\ k_1^2 = 0.062\,;\alpha_1 = \alpha_2 = 45°$$

Source – Dantec Dynamics (2000)

Then, the velocities can be converted into probe coordinates, through Equation 12 and Equation 13.

$$U = U_1\cos\alpha_1 + U_2\cos\alpha_2 \quad \text{Equation 12}$$

$$V = U_1\sin\alpha_1 - U_2\sin\alpha_2 \quad \text{Equation 13}$$

Source – Dantec Dynamics (2000)

After the data is converted into *u* and *v* velocities, several calculations can be performed with it. An interesting parameter is the wake velocity deficit, which can be calculated through the integral of the wake profile at the measured region. This parameter gives an idea on the flow uniformity, which is also related to the unsteady blade loading and noise penalty in the installed configuration. Based on the non-dimensional wake profile, the velocity deficit can be calculated through Equation 14, where Z_{max} and Z_{min} are the boundaries of the measured domain.

$$I = \frac{1}{Z_{max} - Z_{min}}\int_{Zmin}^{Zmax}\left|\frac{u(z)}{U_\infty} - 1\right| dz \quad \text{Equation 14}$$

Source – Author

The hot-wire also allowed for the measurements of the spectra inside and outside of the wake flow, in a manner similar to the one performed by Horne & Soderman (1988). Through these spectra, it is possible to verify the disturbances caused by the propeller on the flow and compare the turbulence for those two regions. The results from these analyses can be correlated to the microphone acoustic measurements. The spectra were constructed through the application of the Welch's method on the time history data, measured by the hot-wire, with the post-processing parameters described in Table 2.

Table 2 – Parameters for hot-wire spectral analysis

Block size	8192
Block overlap	0.5
Window	Hanning

Source – Author

The Welch's method consists in estimating the power spectral density from the measurements through a fast Fourier transform. The process starts with the division of the time series data into overlapping (or not) segments, then computing a modified periodogram for each section and finally averaging them to obtain PSD estimates (WELCH, 1967). The data post-processing through the Welch's method was carried out through a MATLAB® routine. Given its relative simplicity and computational efficiency, this method was shown to provide fast and high quality results.

3.5.2 Aeroacoustic Measurements

The aeroacoustic measurements underwent two types of post-processing. The first one was also based on the Welch's method, and provided the results in terms of noise spectra in the frequency domain. The second one was based on phased array microphone measurements and beamforming techniques to plot the location of the noise sources and their respective strength.

Different types of spectra can be obtained from Welch's method. An average of the PSD levels from all microphones can be performed (auto-spectra), in order to avoid any effects from microphone positioning and distance to the noise sources. However, as will be presented in the next chapters, the wind tunnel background noise is relatively large in comparison to the model noise, at a specific frequency range. Therefore, in order to reduce the effects from the wall boundary layer, a cross-spectral analysis was conducted between the time series of a selected microphone and the remaining ones. The elements in the main diagonal of this cross-spectra matrix needed to be removed, since they represent the microphones self-noise spectra. The resultant PSD values were then averaged, and plotted against the frequency. The parameters used for this approach are included in Table 3.

Table 3 – Parameters for microphone spectral analysis

Source to microphone distance (m)	0.85
Block size	8192
Block overlap	0.5
Window	Hanning
Microphone ID for CSA	2

Source – Author

The selected microphone for the cross-spectral analysis was the one closest to center of the array (mic. #2), which is also closer to the propeller center. A block size of 8192 samples was chosen, with a 50% overlap. A source to microphone distance of 0.85 was selected, by

considering the center of the propeller as the origin, which was positioned at the center of the working section.

Besides the Welch's method for spectral analysis, a noise source localization was carried out through phased array measurements, which are processed using a technique known as beamforming. Through this process, a time series of simultaneously acquired data from the microphones is post-processed in order to determine the sources location and strength, based on a series of grid points in a plane (HORVATH, 2015). The output result is then a mapping of the sources distribution at specific frequencies, which allows for conclusions on the noise generation mechanisms and propagation.

The phased array for aeroacoustic measurements in hard-walled wind tunnels is also based on simultaneous time series acquisition of the pressure at the microphones. These series are then partitioned in blocks, an analysis frequency is selected and a digital filtering technique is used to compute a complex frequency-domain pressure amplitude for each block and each microphone. A series of frequencies are then processed to create a spectrum. In its simplest version, beamforming scales the microphone outputs by the elements of a steering vector and sums them, and consequently, the array will be steered to a specific point of the grid. For each of these points, the beamforming expression is calculated and plotted, which represents an estimate of the sum of the acoustic pressure-squared over each of the array microphones, caused by a source. The array cross-spectral matrix is also included in this calculation (MUELLER, 2002).

The beamforming code used in this work was developed at LAE1 by Pagani Jr. (2014). It uses a conventional beamforming method (variation of the sum-and-delay method). The sources distribution and strength will be plotted over a CAD drawing (instead of a photograph, as commonly used) of the model, in order to scale the grid properly and the regions of interest of the analysis. The grid dimensions for the beamforming analyses are included in Table 4, and they represent a vertical plane that is parallel to the microphone array and passes through the propeller axis.

Table 4 – Grid dimensions for beamforming analyses

Width [m]	0.8
Height [m]	1.3
Grid depth [m]	0.85

Source – Author

It is worth mentioning, however, that the application of regular beamforming for rotating propellers is not a trivial task. It has been previously done by Horvath, Envia and Podboy (2013) for the investigation of phased array measurements of the open rotor model shown in Figure 27, in order to locate the sources responsible for the noise radiation from this model. Similarly as was performed in this work, the examined plane is a vertical one parallel to the array and crossing the propellers axes.

The beamforming analyses at frequencies correspondent to the tonal peaks placed the sources either outboard of the blade tip or inboard of the blade root, within the hub, instead of along the span of the rotors, as was expected. According to the authors, those results are related to a radial station, at which the radiation efficiency is highest for any circumferential spinning mode, known as "Mach radius", denoted by z^* (HORVATH; ENVIA; PODBOY, 2013). This refers to a station that approaches the observer at sonic speed (M = 1), at some time in each propeller revolution. This station is a function of the axial and tip rotational Mach numbers (M_x and M_t, respectively) and the angle between the flight axis and the observer (θ), as given by Equation 15 (CRIGHTON; PARRY, 1992).

$$z^* = \frac{1 - M_x \cos(\theta)}{M_t \sin(\theta)} \qquad \text{Equation 15}$$

Source – Crighton and Parry (1992)

For the Mach radius calculations performed by Horvath, Envia and Podboy (2013), the θ angle was defined as 90°, which corresponds to the angle relative to the center of the array. From the beamforming maps, shown in Figure 87a and Figure 87b for the front rotor BPF tone and aft rotor BPF tone, respectively, it can be seen that location of the apparent noise source can be very well predicted by the Mach radius location (red line).

Figure 87 – Mach radius location at the beamforming maps

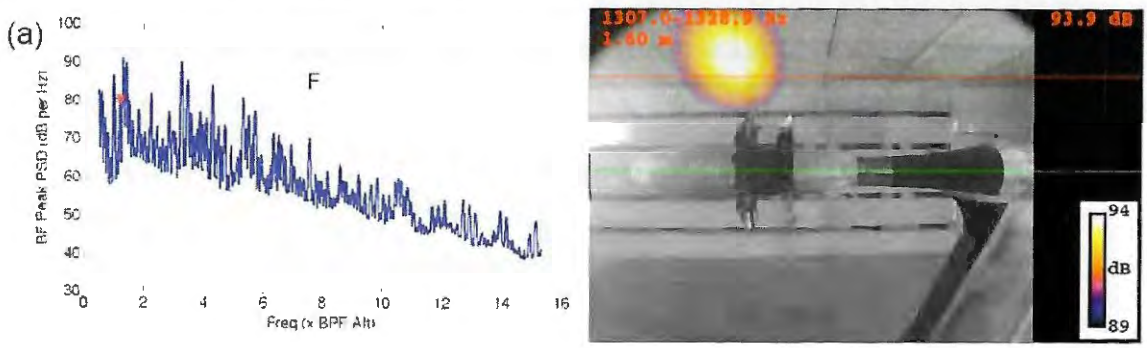

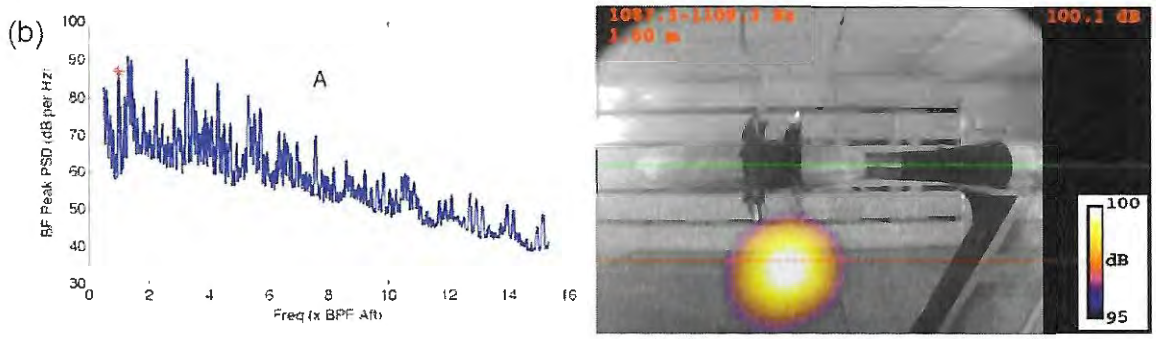

Source – Horvath, Envia and Podboy (2013)

According to the authors, the beamforming places the noise source at this apparent location (instead of at the blades), because of the spiraling nature of the wavefront propagating away from the rotors. In addition, the red line representing the Mach radius does not pass exactly through the center of the beamforming peak due to several factors. One of them is that the phased array (the observer) is not in the far field. Secondly, the Mach radius is calculated for the center of the array ($\theta = 90°$), but in reality each microphone location would correspond to different Mach radii due to the relative θ angle (HORVATH; ENVIA; PODBOY, 2013).

Similarly as was shown in Figure 12, phased array measurements were also conducted for the open rotor in pusher configuration. The beamforming map shown in Figure 88 places the noise source at the blades, instead of the Mach radius position. This occurs since the dominant noise generation mechanism for this case produces non-rotating noise sources, due to the stationary location of the pylon wake, and thus the wavefronts do not spiral as it occurs for the isolated case. Therefore, the Mach radius concept does not apply for this case (HORVATH; ENVIA; PODBOY, 2013).

Figure 88 – Beamforming map for installed open rotor

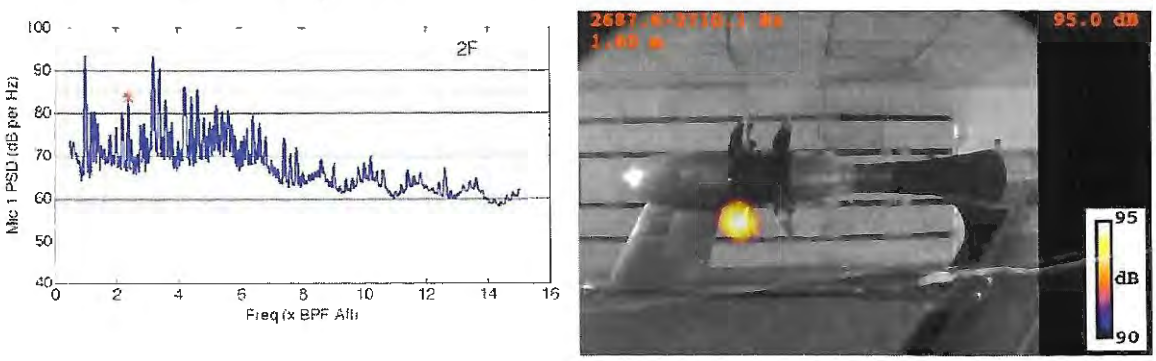

Source – Horvath, Envia and Podboy (2013)

3.6 ANALYSES AND PROCEDURES

In this section, the main goals for each of the aerodynamic and aeroacoustic analyses will be outlined. Each series of tests were conducted for the three model configurations, starting with the isolated, then the installed, and finally the blown configuration. The aeroacoustic tests were the same for all three, with the cross-spectral analysis through the Welch's method and the source localization through beamforming, as already described. The aerodynamic tests were not the same for all three, consisting in the propeller performance for the isolated case, the pylon surface pressure for the installed condition, and flowfield measurements for both installed and blown configurations. The wind tunnel tests conducted in this work are shown in Figure 89.

Figure 89 – Wind tunnel campaign breakdown

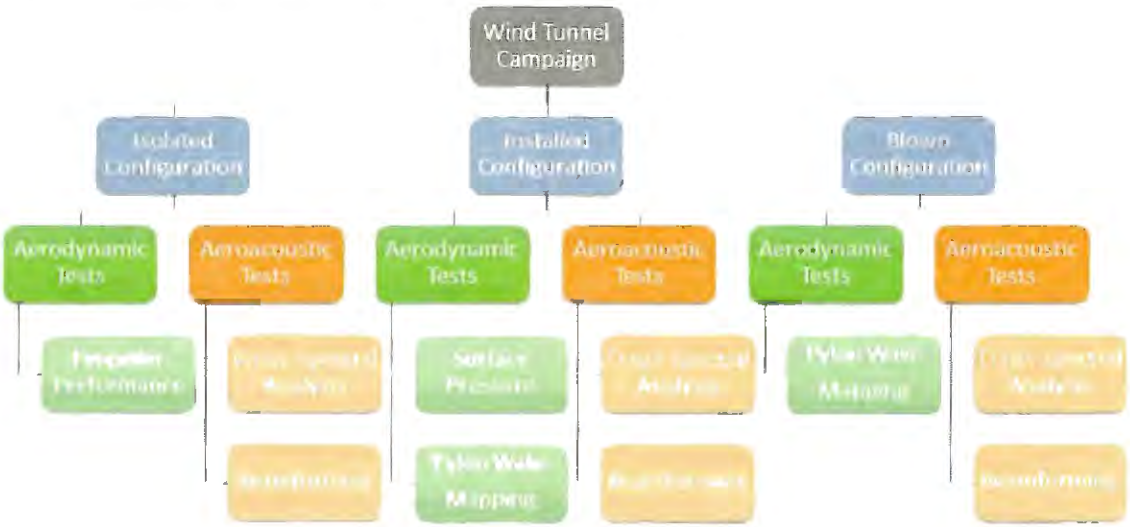

Source – Author

The balance was used for measurements of the aerodynamic forces only for the isolated configuration. Despite the effect of the pylon wake on the propeller loading, since it occurs only in a very small region, no visible changes on the propeller steady operating characteristics were expected to be measured with the balance. Therefore, these tests were carried out only to obtain the thrust coefficient curve for both 3- and 4-bladed propellers, at the isolated configuration. Since there was no available rotating balance for torque measurements, this parameter, as well as the propeller efficiency, could not be measured.

The pressure measurements on the surface of the pylon were carried out to assess the influence of the propeller inflow on the pylon, similarly as the worked performed by Catalano (1993), verifying possible changes in the boundary layer transition and/or separation regions. Ideally, the surface pressure would be measured for the blown configuration as well, but, given

the materials and manufacture of the blowing trailing edge, it was not possible to drill the taps and attach the tubes safely to this region, without risking structural damage.

The hot-wire anemometry tests allowed for an analysis of the pylon wake with and without blowing. Therefore, the effectiveness of the flow control system in reducing the velocity deficit on the wake was assessed. Different spanwise measurements were conducted, in order to evaluate the effect of the propeller inflow on the pylon wake profile. Spectra inside and outside of the wake were also measured with the hot-wire to verify the disturbances on the flow caused by the propeller and the pylon wake.

Finally, the acoustic spectra resultant from the cross-spectral analysis were compared for all three configurations. The effect of other parameters, such as the propeller angle of attack and directivity, were also assessed, as well as the advance ratio. The expected optimum result is for the blown configuration noise levels to be as close as possible to the isolated case, indicating that the flow control was effective in reducing the noise component caused by the installation effects. The source localization through beamforming allowed for an investigation on which noise generation mechanism (steady loading noise or asymmetric loading noise, for example) was dominant for a specific condition and frequency, which aided the conclusions on the aeroacoustic behavior of each configuration.

4 AERODYNAMIC RESULTS

4 AERODYNAMIC RESULTS

In this section, the results from the wind tunnel aerodynamic tests will be described, for each configuration. This includes the propellers thrust curves, pylon surface pressure distribution, and the flowfield mapping at different spanwise stations. For all the aerodynamic tests in this work, the propellers always operated at maximum rotational speed, and the advance ratio was controlled through the wind tunnel speed.

4.1 ISOLATED CONFIGURATION

For the isolated configuration, where the propeller is in the tractor position, the aerodynamic tests consisted in measuring the thrust force through the balance. Initially, the model was tested without propeller, in order to measure the rig drag variation with the free stream speed, which will offset the data obtained for the rotating propeller case. The drag force was measured for several velocities, starting from 10 m/s up to 27 m/s. The results were kept in voltage units, and are shown in Figure 90. The data was approximated through a 2nd order polynomial to simplify the subtraction from the thrust measurements.

Figure 90 – Rig drag force variation with flow speed

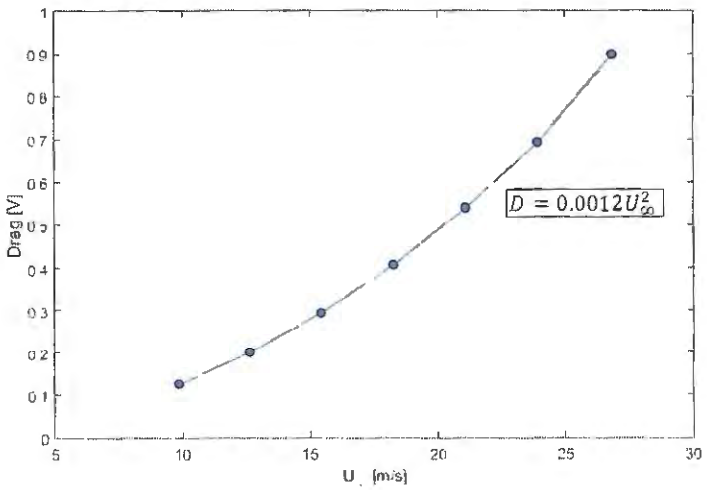

Source – Author

Then, the net thrust of each propeller could be obtained. The rotational speed of the propellers slightly increased for higher tunnel speeds, induced by the free stream. Therefore, the final RPM value was measured through a strobe. The analysis was performed in terms of advance ratio, in the conditions listed in Table 5. The tests were conducted for zero angle of attack. After the subtraction of the rig drag, the thrust was converted to force units through the calibration constant and then non-dimensionalized through Equation 8. The thrust coefficient curves for the 3-bladed and 4-bladed propellers are shown in Figure 91.

Table 5 – Flow and propeller operating conditions for thrust measurements

3-BLADED PROPELLER			4-BLADED PROPELLER		
U_∞ [m/s]	n [RPM]	J	U_∞ [m/s]	n [RPM]	J
7.6	4900	0.23	6.5	4900	0.19
9.8	5000	0.29	8.1	4900	0.24
12.1	5000	0.36	9.8	4950	0.29
14.4	5000	0.42	11.6	4950	0.35
16.7	5100	0.48	13.5	5000	0.40
19.1	5200	0.54	15.3	5100	0.44
21.5	5250	0.60	17.2	5200	0.49
23.9	5400	0.65	19.1	5300	0.53
26.3	5550	0.70	21.0	5400	0.57
28.7	5750	0.74	22.8	5500	0.61

Source – Author

Figure 91 – Thrust coefficient curves for the 3- and 4-bladed propellers with advance ratio

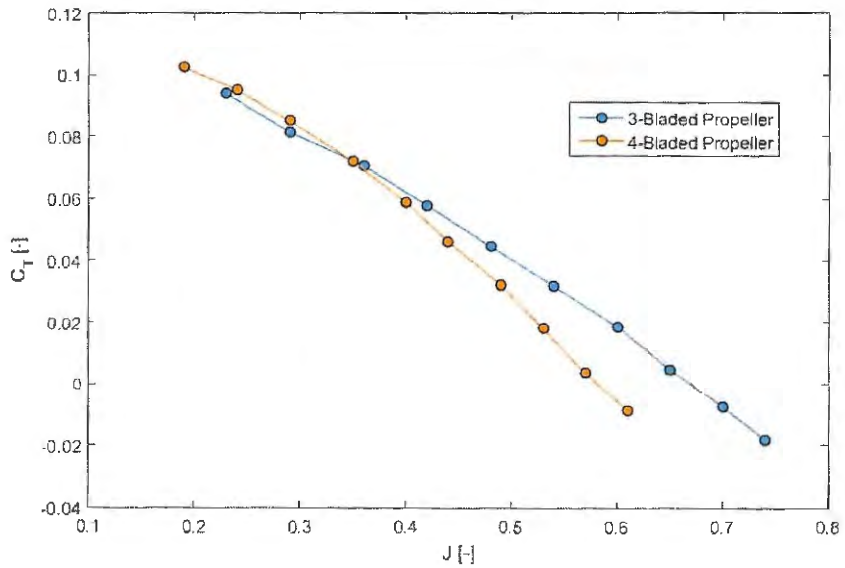

Source – Author

The curves shown in Figure 91 display a typical behavior for propellers, with decreasing thrust for increasing advance ratio. The 4-bladed propeller displayed slightly higher thrust levels for lower advance ratios (up to 0.35), given the relative smaller pitch, of 6". However, the thrust tends to decrease rapidly, reaching zero at approximately J = 0.58. This propeller is then better suited for take-off conditions, at low flight speeds. The 3-bladed propeller, with a higher pitch (8") started displaying negative thrust values for J = 0.67, and the curve slope is much smaller, allowing this configuration to be tested at higher flight speeds. Therefore, for the

following tests, the 4-bladed propeller will be investigated for lower flow speeds, reaching J = 0.40, while the 3-bladed propeller will be tested up to J = 0.60.

4.2 INSTALLED CONFIGURATION

4.2.1 Pylon Surface Pressure Distribution

The surface pressure measurements were carried out to investigate the effect of the propeller on the flow around the pylon, verifying the occurrence of boundary layer transition and separation and possible changes to the regions where these phenomena occur. The tests were conducted for different advance ratios and angles of attack. The Reynolds number for the tests is based on the pylon chord of 400 mm and the wind tunnel speed. These parameters are listed in Table 6, with the minimum and maximum Reynolds values tested.

Table 6 – Flow and propeller operating conditions for surface pressure measurements

α [°]	0 / 5 / 10 / 15
J (4-Bladed) [-]	0.30 / 0.40
J (3-Bladed) [-]	0.50 / 0.60
Reynolds Number [-]	$2.36 \times 10^5 - 4.85 \times 10^5$

Source – Author

Initially, an analysis of the effect of advance ratio will be performed. For all cases, the pressure distributions for a low angle of attack (5°) will be compared for the range of advance ratios tested. The results are shown in Figure 92, for the 4-bladed and 3-bladed propellers, respectively.

Figure 92 – Effect of 3- and 4-bladed propellers on pylon pressure distribution for α = 5°

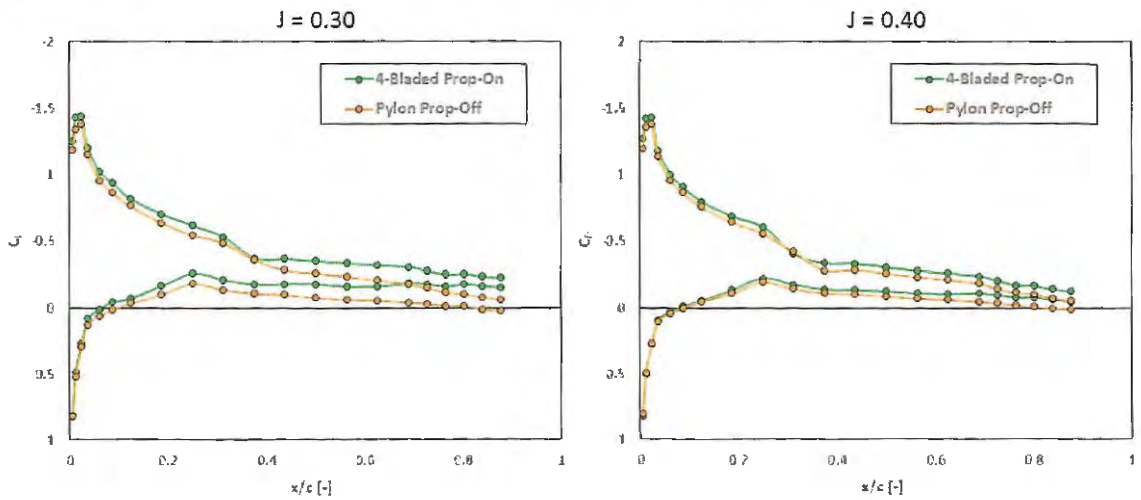

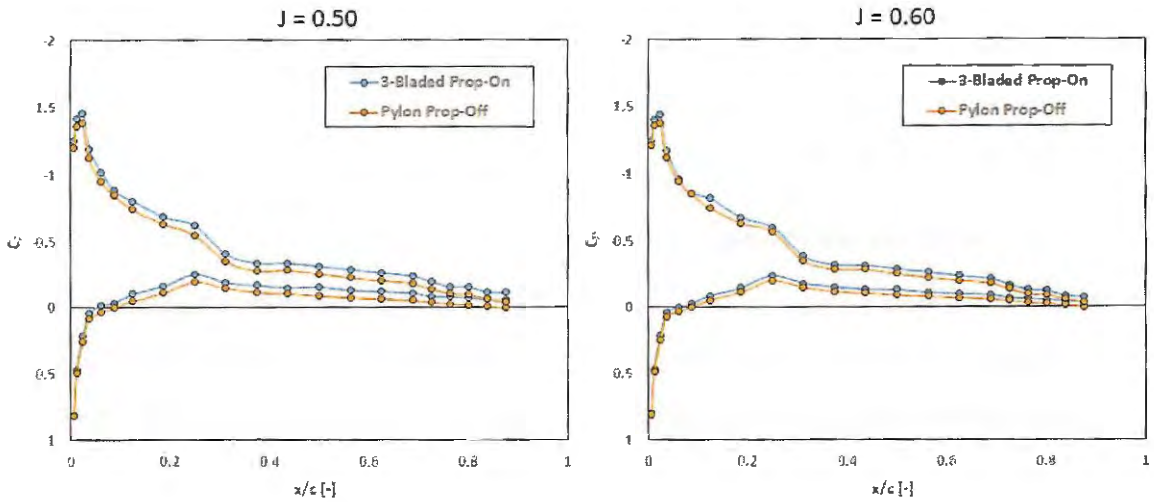

Source – Author

By comparing the pressure distribution curves for the prop-off and prop-on configurations, it can be verified that the rotating propeller has an effect of shifting the curves upwards, which means that the pressure on both upper and lower surfaces of the pylon become more negative. This effect had already been verified by Catalano (1993), and it occurs due to the induced velocities on the inflow slipstream by the propeller (V_{Px}), which tend to accelerate the flow around the pylon, thus increasing the suction. Since the propeller axis is on the same line as the pylon chord, the upward and downward components of V_{Pz} will cancel each other, so effect on the pylon upper and lower surfaces will be the same and so will the displacement of the curves, meaning that the net increase in lift will be zero.

Since this effect is caused by the inflow slipstream, it will be affected by the propeller operating conditions, namely the advance ratio. By comparing the curves, it is possible to conclude that the velocities induced on the flow around the pylon will be higher for smaller advance ratios. The largest difference between the prop-off and prop-on curves can be verified for the 4-bladed propeller at J = 0.30. At this condition, the propeller is generating a high thrust, as was shown in Figure 91. Therefore, for this increased thrust condition, the fluid acceleration downstream of the propeller must also be higher, and consequently the induced velocities on the flow. To compensate for this and satisfy the continuity, a larger contraction of the stream tube that passes through the propeller is necessary.

The induced velocities will tend to be higher at the trailing edge region, since it is closer to the propeller and the stream tube has a smaller cross-section. This can be verified for the J = 0.30 condition. This higher velocity at the trailing edge will translate into a reduction of the adverse pressure gradient and, consequently, the boundary layer growth rate will be smaller. With increasing advance ratio, the contraction rate of the stream tube is smaller, so the induced

velocity at the trailing edge will tend to be the same as the rest of the pylon. This can be seen for the curves of the 3-bladed propeller. For J = 0.50, there is still some displacement at the trailing edge. However, for the highest obtained advance ratio (J = 0.60), there is practically no induced velocity on the pylon, and the curves tend to almost overlap.

Changes in transition were not visible for lower angles of attack, most likely due to the insufficient number of pressure tappings on the pylon surface. The effect on boundary layer separation was also not visible, for these conditions. Surface pressure measurements were also conducted for a high angle of attack condition ($\alpha = 15°$), in order to assess the propeller effects for a much thicker boundary layer. The charts displayed in Figure 93 display the results for this condition, for different advance ratios.

Figure 93 – Effect of propellers on pylon pressure distribution for $\alpha = 15°$

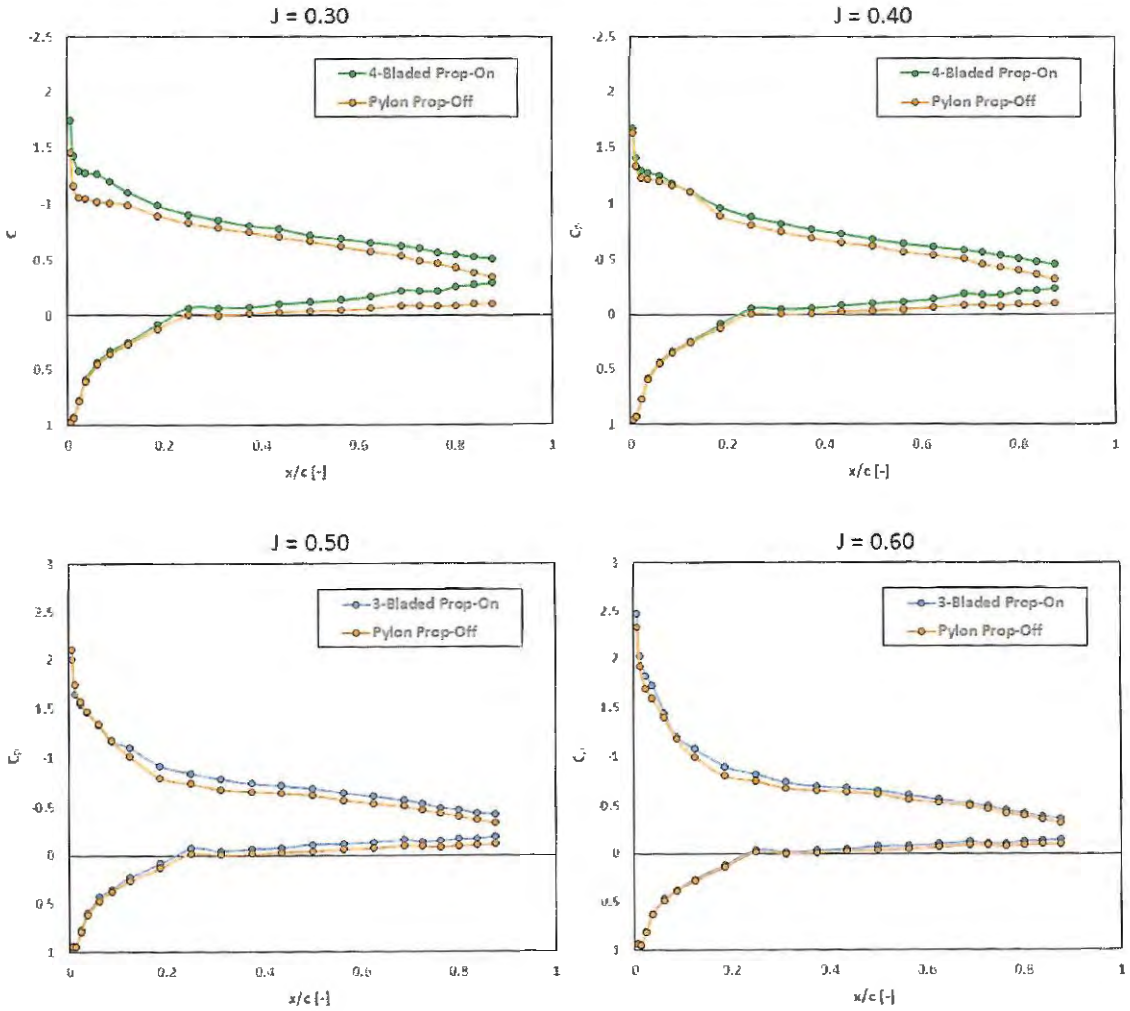

Source – Author

For the 4-bladed propeller curve, the highest increase in suction occurs at the trailing edge, similarly as the previous results, indicating a reduction in the adverse pressure gradient. This also occurs at the suction peak, and the laminar separation region right downstream. A visible change occurs at the reattachment point, which moves towards the leading edge for the prop-on configuration. This is in accordance with the results from Catalano (1993), in which, for high angles of attack, the transition tends to occur sooner for the case with rotating propeller. The boundary layer separation will probably be occurring at the trailing edge or at the region right upstream, without pressure tappings, given the high tridimensional characteristic of the pylon.

4.2.2 Pylon Wake Mapping

The pylon wake profiles were measured with a hot-wire anemometer, positioned halfway between the pylon trailing edge and the propeller plane. Several spanwise stations were mapped, in order to verify the effect of the propeller inflow at different blade radii. Two different advance ratios for each configuration were tested (0.3 and 0.4, for the 4-bladed propeller, and 0.5 and 0.6 for the 3-bladed propeller) in order to assess the effect of the propeller loading on the flow velocity distribution, similarly as was performed for the pylon pressure distribution. The configurations are compared in terms of velocity distribution, which was kept in dimensional units, in order to verify the overall increase in the local flow speed due to the propellers, similarly as was performed by Horne & Soderman (1988). The pylon wake profiles are shown below for a condition of zero angle of attack.

Figure 94 – Pylon wake profiles for prop-off configuration and 4-bladed propeller (J = 0.30)

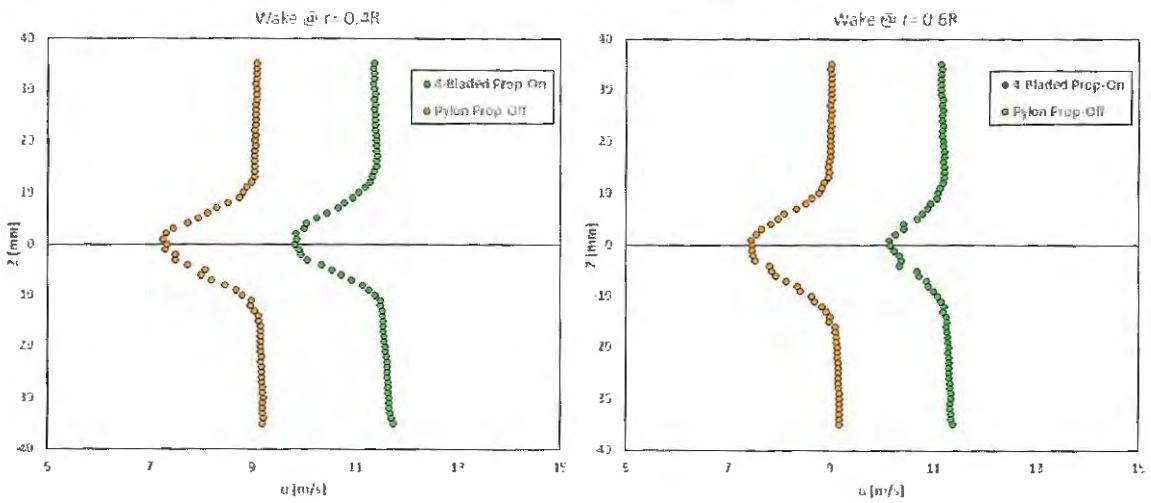

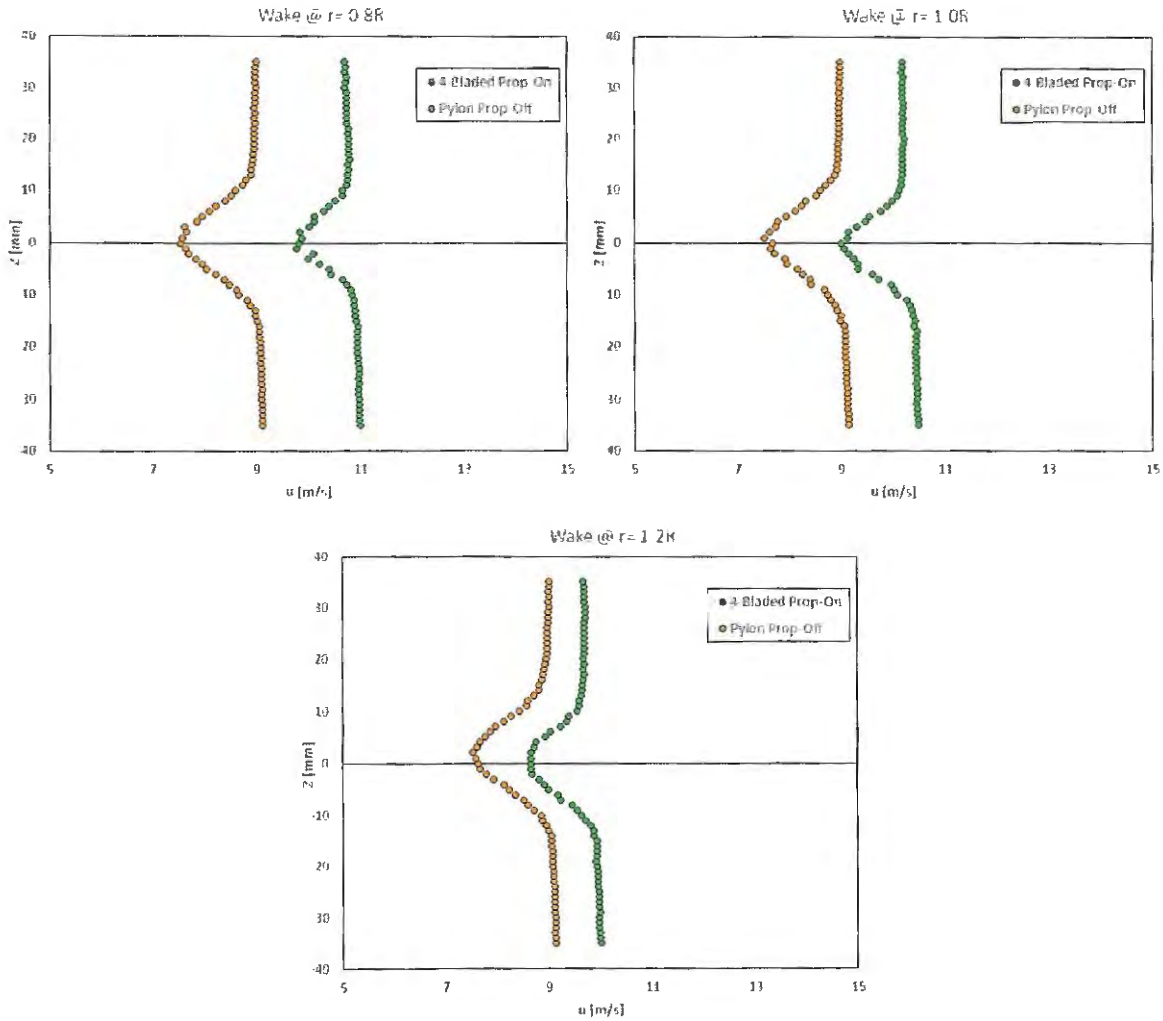

Source – Author

Figure 95 – Pylon wake profiles for prop-off configuration and 4-bladed propeller (J = 0.40)

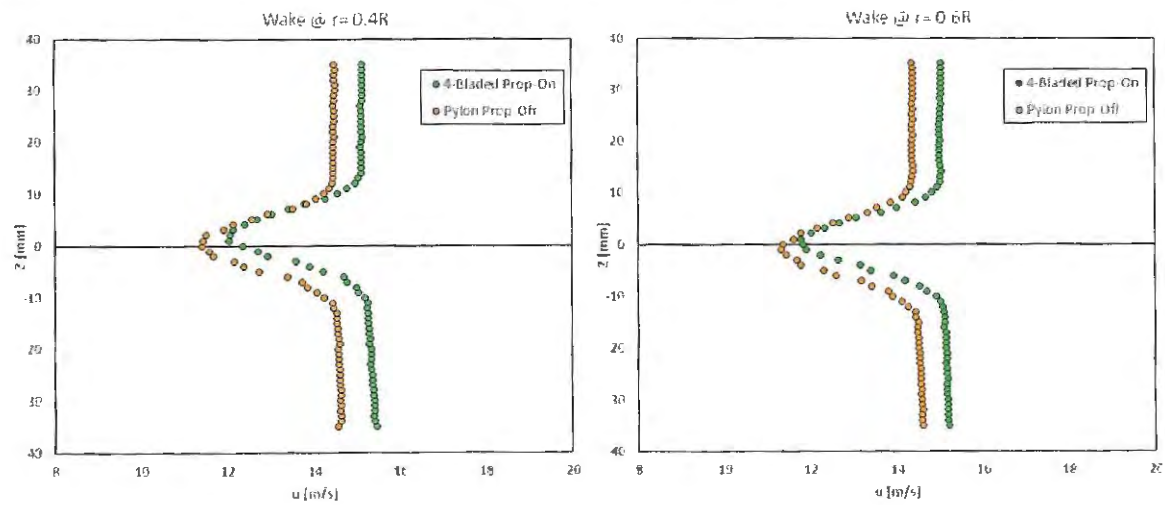

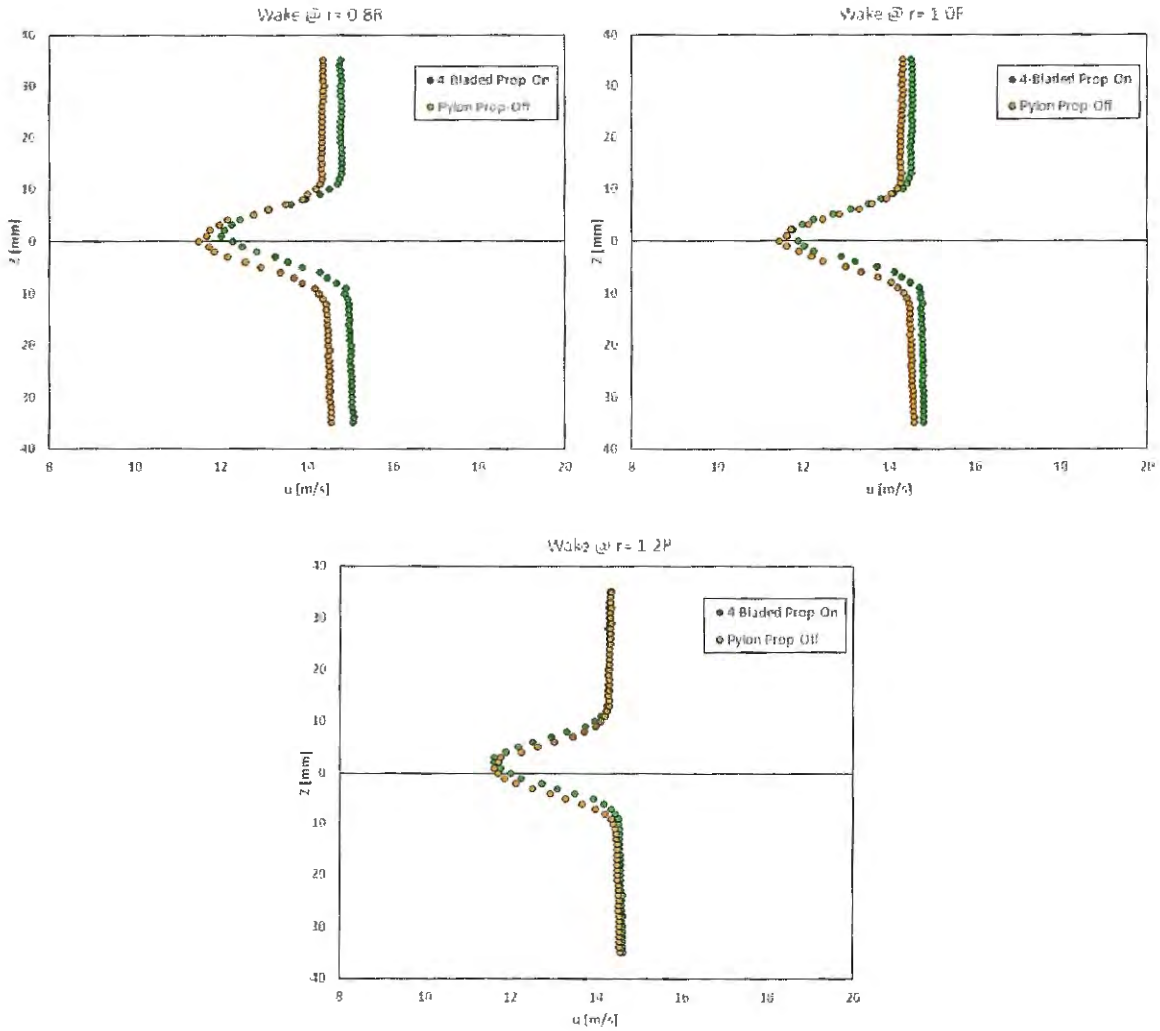

Source – Author

Figure 96 – Pylon wake profiles for prop-off configuration and 3-bladed propeller (J = 0.50)

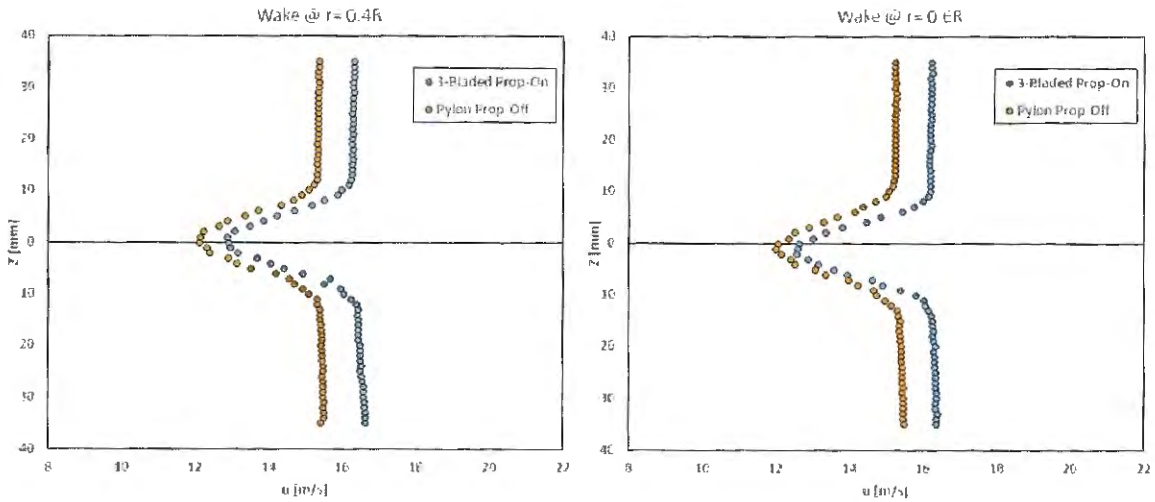

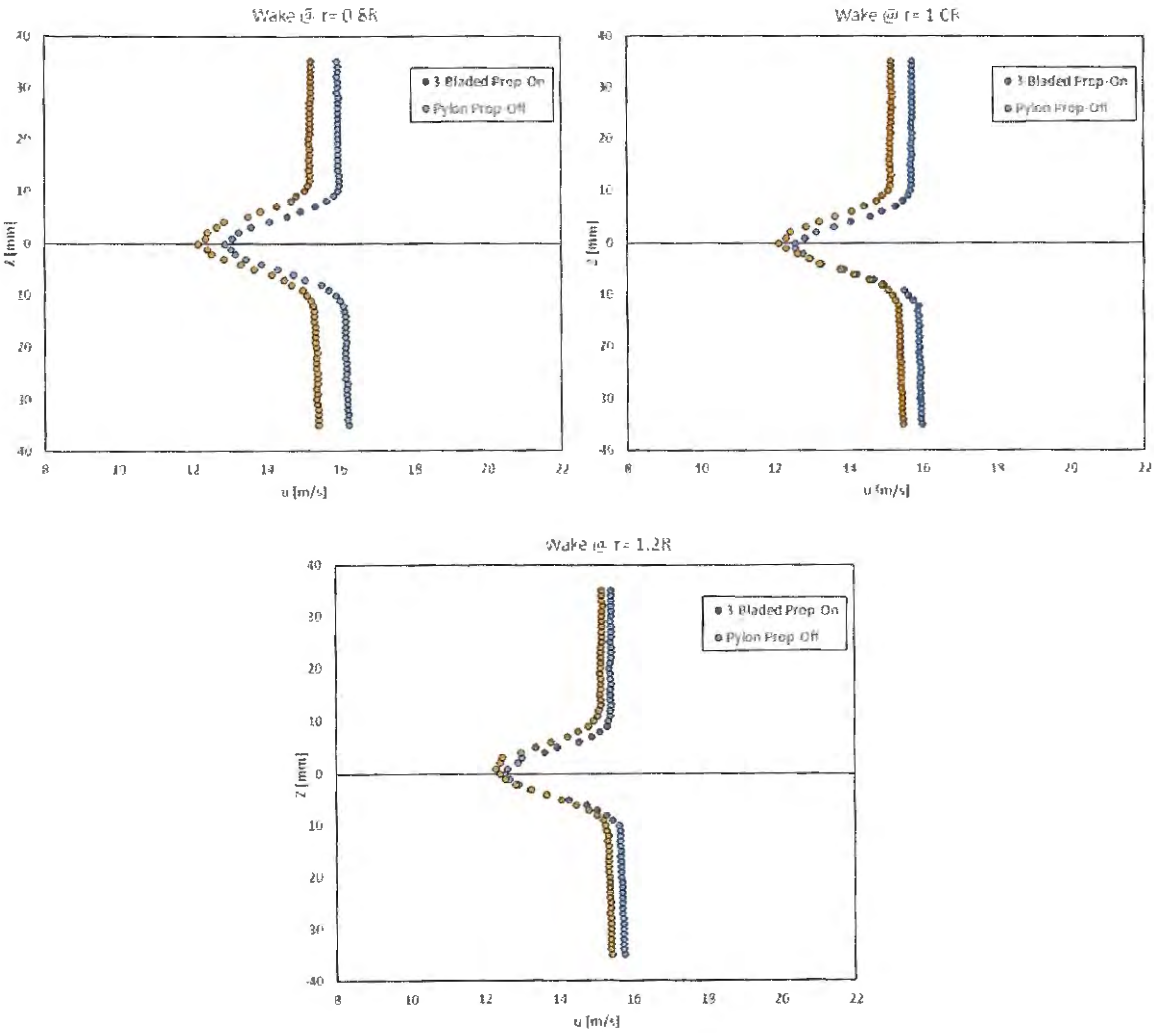

Source – Author

Figure 97 – Pylon wake profiles for prop-off configuration and 3-bladed propeller (J = 0.60)

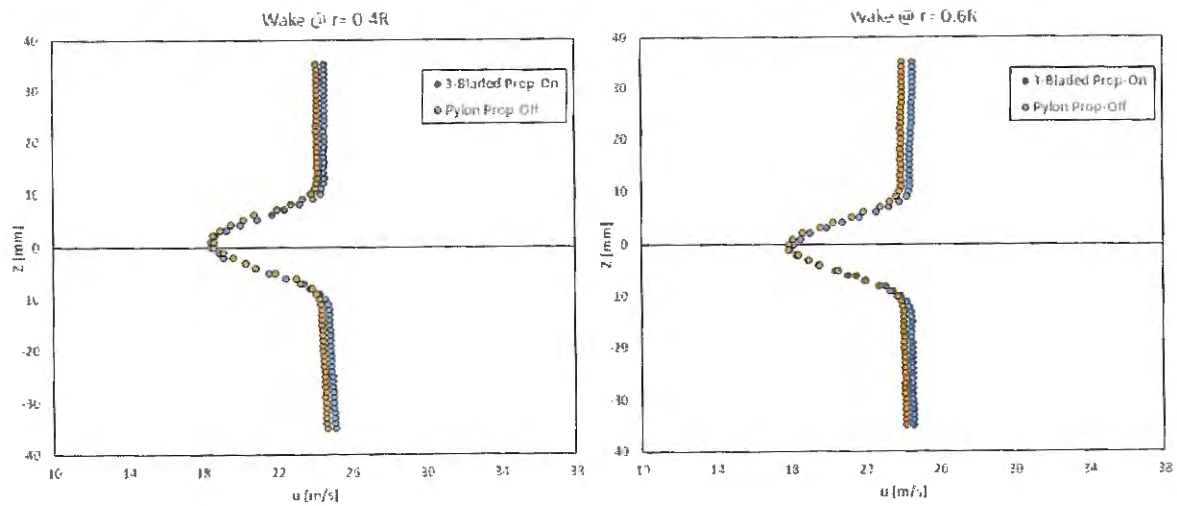

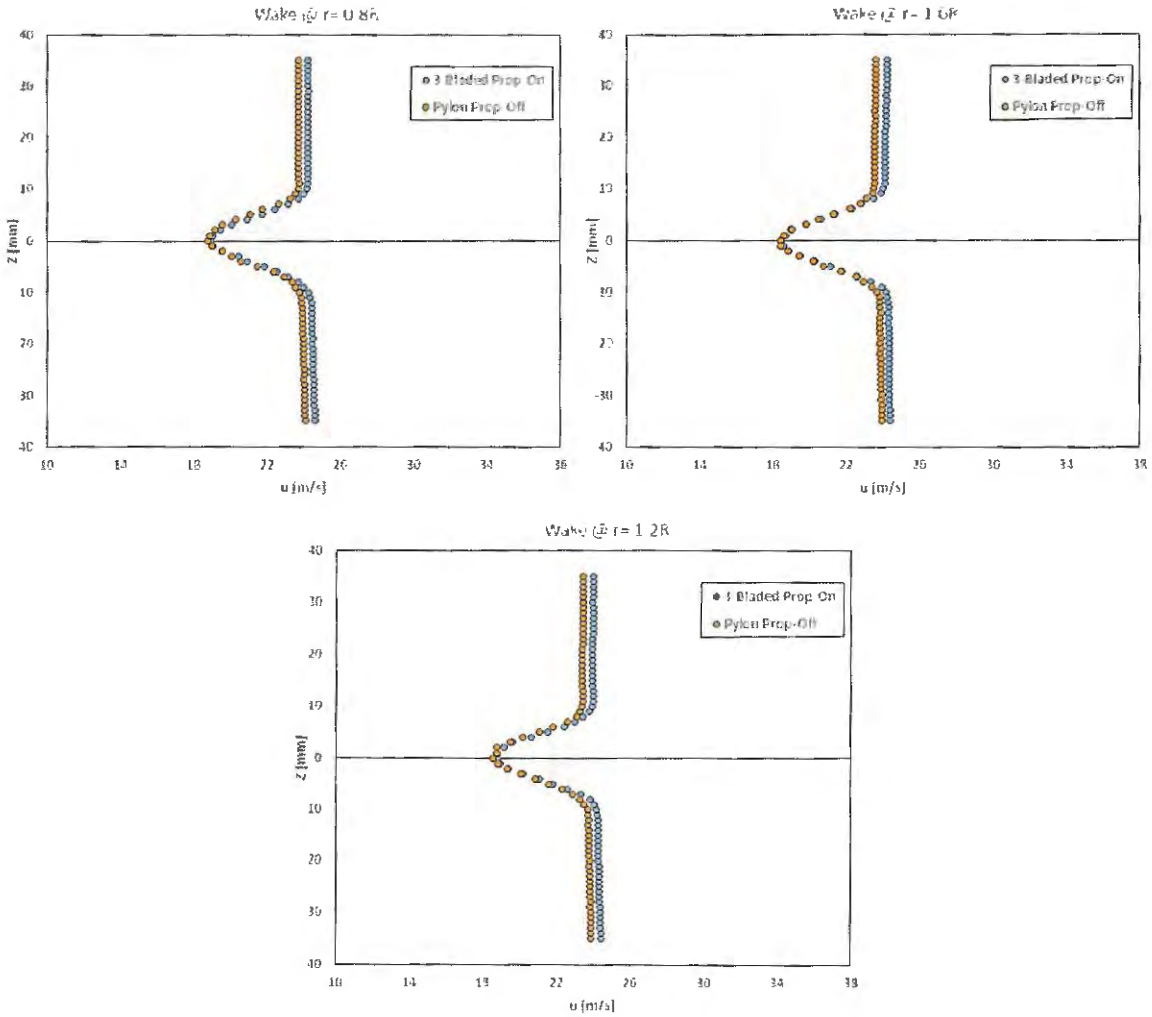

Source – Author

By comparing the wake profiles, it can be seen that the prop-on configuration accelerates the upstream flow for practically all positions and conditions measured. This effect is more expressive for the propeller at the lowest advance ratio (J = 0.30), which corresponds to the highest blade loading condition. Increases of more than 2 m/s to the local free stream speed were achieved at the position closest to the hub (r/R = 0.4). For increasing advance ratio, this flow acceleration still occurs, but to a lesser extent. This is in accordance with the pylon pressure distribution, which underwent the highest increase in suction for J = 0.30. Therefore, the phenomena to explain this effect is the same described in the previous section, related to the necessary flow acceleration to provide the given thrust value. Similarly as the pressure distribution, the conditions at the highest advance ratio, with almost no thrust being generated, provided the smallest increases in flow speed.

This effect is also more expressive near the blade hub, and the flow acceleration tends to decrease towards the blade tip. This trend occurs for all advance ratios, for both 3- and 4-

bladed propellers. For the 4-bladed at J = 0.40, as can be seen from Figure 95, the prop-on velocity profile becomes equal to the prop-off configuration at the r/R = 1.2 station. At this region, there is hardly any effect from the slipstream, which is likely to have a larger cross-section, for this condition.

For most of the profiles, the wake width and velocity deficit do not change for the prop-on configuration. The integral of the wake velocity deficit allows for conclusions on how the propeller affects the boundary layer behavior on the pylon. By calculating this integral, using Equation 14, it is possible to assess if the blade loading distribution affects the flow velocity profile at different pylon stations. The wake deficit for those stations, and at different advance ratios, are shown in Figure 98.

Figure 98 – Integral wake velocity deficit for prop-off, 3- and 4-bladed propellers

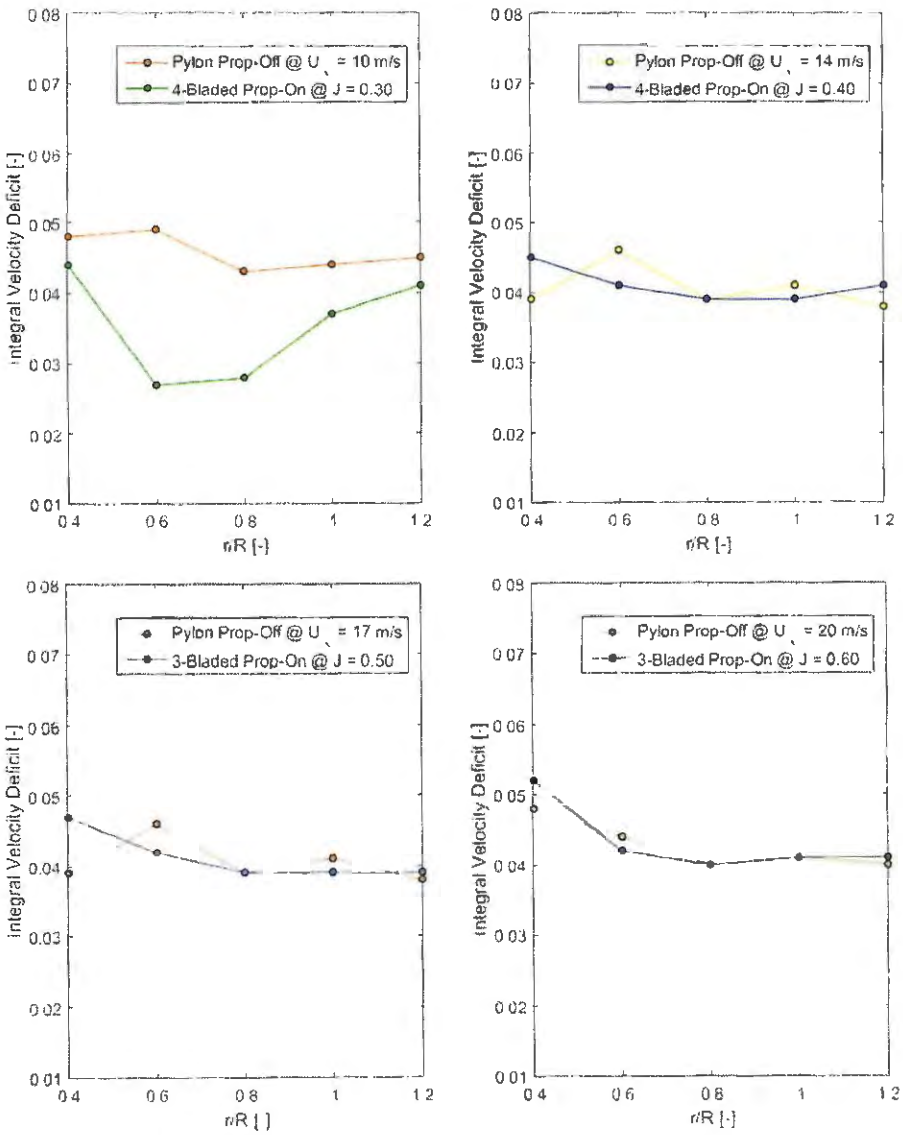

Source – Author

As shown in Figure 98, the lowest deficits were found for the r/R = 0.6 and r/R = 0.8 stations. This is compatible with the region of higher blade thrust, which tends to be maximum near the r/R = 0.70 station. This is again more expressive for the lower advance ratio (J = 0.30), which also coincides with increased blade loading. Near the blade tips, or for higher advance ratios, the curves tend to overlap. Therefore, the propeller also affects the wake by decreasing the velocity deficit, for some flow conditions.

In order to assess the effect of the advance ratio, a single wake was measured at the r/R = 0.8 for different flow speeds. This analysis focused on verifying the variation of the integral velocity deficit, for different blade loadings. This station was selected for the measurements, since it is closer to the point of maximum thrust on the blade. The variation percentage between the non-dimensional wake deficit for the prop-off and prop-on configurations, for different J values, are shown in Table 7.

Table 7 – Decrease percentage in the integral wake velocity deficit for different advance ratios

Configuration	J [-]	ΔInt. Vel. Deficit [%]
4-Bladed	0.30	31.6%
4-Bladed	0.35	10.7%
4-Bladed	0.40	6.9%
4-Bladed	0.45	-1.8%
3-Bladed	0.50	-0.8%
3-Bladed	0.55	0.4%
3-Bladed	0.60	-2.0%
3-Bladed	0.65	-3.1%

Source – Author

Similarly as the previous results, the non-dimensional wake velocity deficit turned to be smaller for the prop-on case on low advance ratio conditions. For J = 0.30, which is the condition with highest thrust, the velocity deficit decreased approximately 32%, due to the acceleration provided by the propeller to the flow around the pylon, especially near the trailing edge region. For increasing advance ratio of the 4-bladed propeller, this effect tends to be reduced and the prop-on velocity deficit approaches the prop-off configuration. For the 3-bladed propeller, there was no visible difference between the curves for any of the tested points, and the different is most likely in the variability of the measurements. This is compatible with the thrust curves obtained from the aerodynamic balance and the pylon pressure distribution.

The pylon wake profiles were also measured with a trip placed at 5% of the chord on the upper and lower surfaces, to force transition at this region. Since the turbulent boundary layer growth rate is much higher than the laminar, it is expected that, when separation occurs at the trailing edge, the wake present a higher velocity deficit, in comparison to the original results. The wake integral velocity deficit for the tripped case is compared with the natural transition configuration in Figure 99, for the different spanwise stations.

Figure 99 – Effect of pylon transition trip on the wake velocity deficit

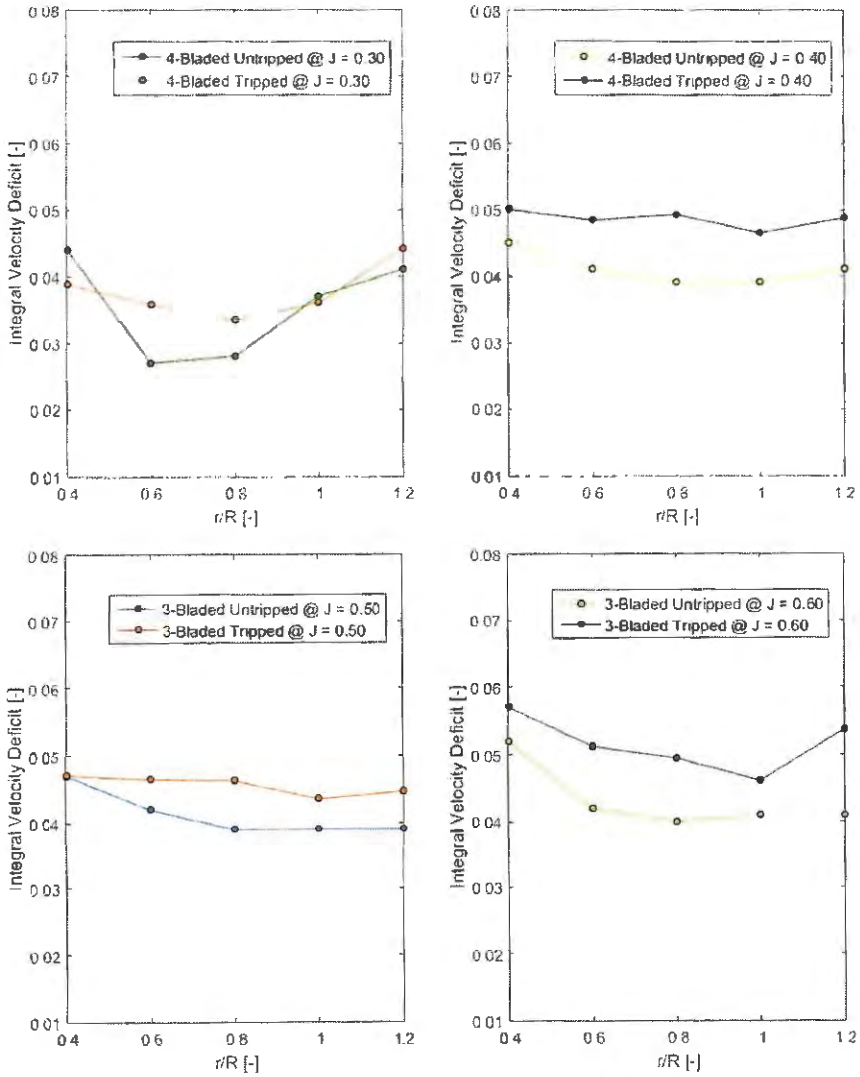

Source – Author

The wake integral velocity deficit increases for practically all points measured for the tripped pylon case. The most expressive difference occurs for the 4-bladed propeller at J = 0.30, especially near the point of maximum blade loading (r/R = 0.70), being approximately 35% higher for the tripped case. Some effect is also visible at this same station for the other tested advance ratios. This means that, for the untripped case, the propeller had an effect of delaying

transition, so that the boundary layer would remain laminar for a longer extent and thus have a lower growth rate. Since the trip forces the transition at a fixed region near the leading edge, the turbulent boundary layer, with a higher growth rate, will create a wake with higher velocity deficit, after separation at the trailing edge. This phenomenon is most likely happening for all the measured points, at all tested conditions.

The flow turbulence levels in the *x*-direction could also be measured with the hot-wire. The charts in Figure 100 display the percentage of turbulence in the flow, relative to the flow speed, for the prop-on configurations compared to the prop-off case, at different advance ratios. These turbulence levels were measured at the r/R = 0.8 station. Aside from a slight shift of the curve on the *z*-direction, for the 4-bladed results, the curves display the same turbulence levels for both prop-on and -off configurations. The increasing advance ratio, however, tends to reduce the maximum turbulence levels from approximately 9.5% to 7% at the center of the wake.

Figure 100 – Turbulence levels at the wake for 3- and 4-bladed propellers

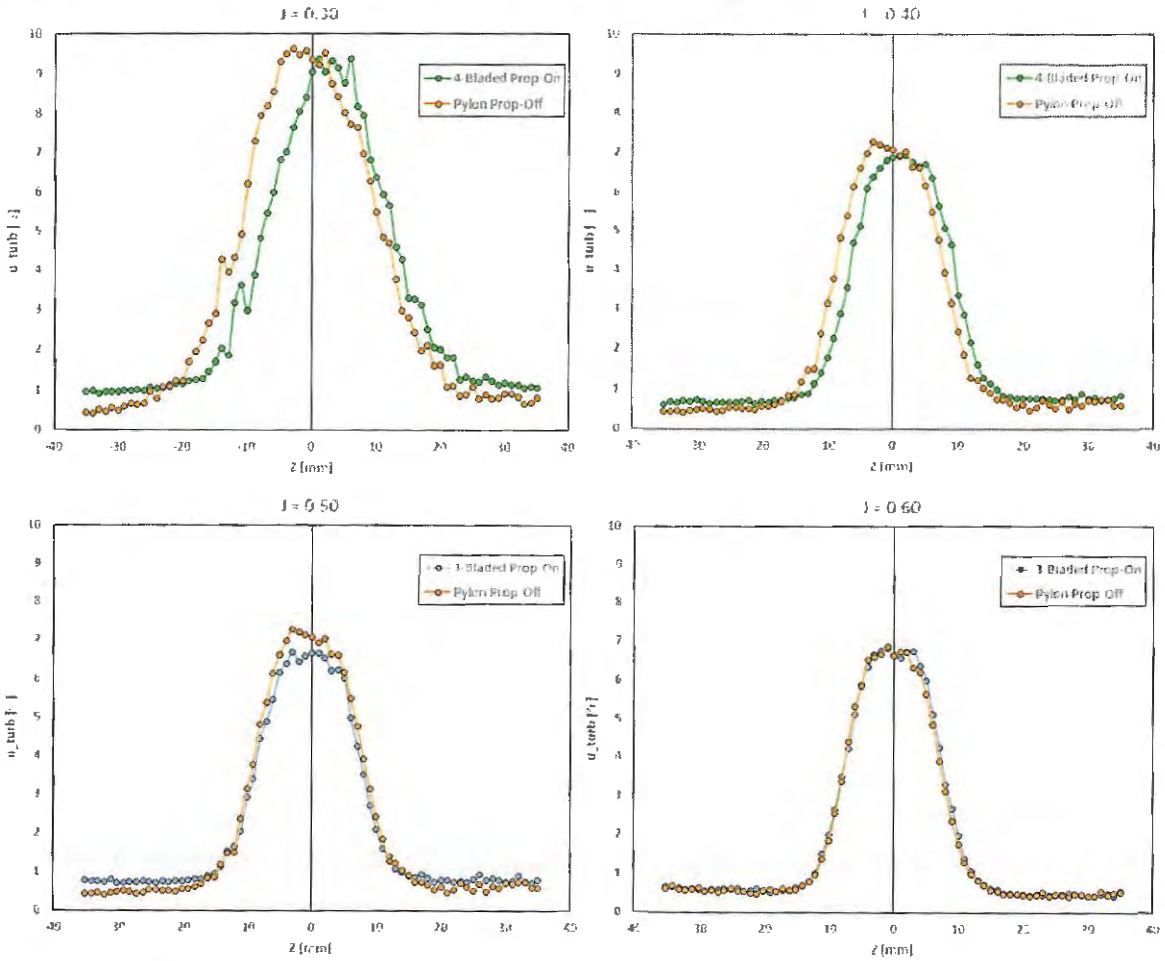

Source – Author

The data obtained from the hot-wire (time history) also allow for plotting the spectra of the flow disturbances with the frequency. Measurements were carried out at two points: one outside and another inside the wake (at the z = 0 position) at the r/R = 0.8 station. These spectra are shown in Figure 101 for the prop-off and in Figure 102 prop-on configurations.

Figure 101 – Flow spectra inside and outside of the wake with hot-wire for pylon prop-off configuration

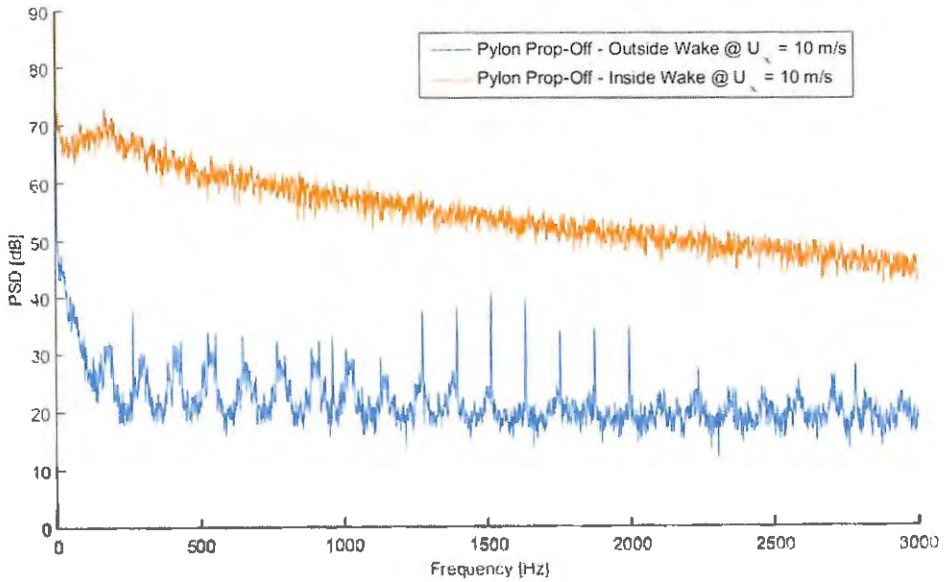

Source – Author

Figure 102 – Flow spectra inside and outside of the wake with hot-wire for 4- and 3-bladed propellers, at J = 0.30 and J = 0.50, respectively

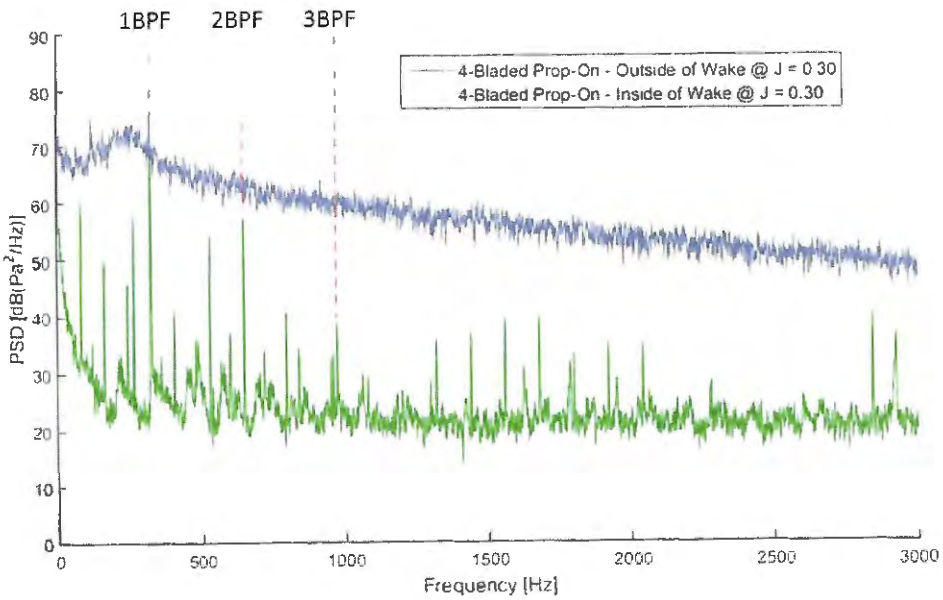

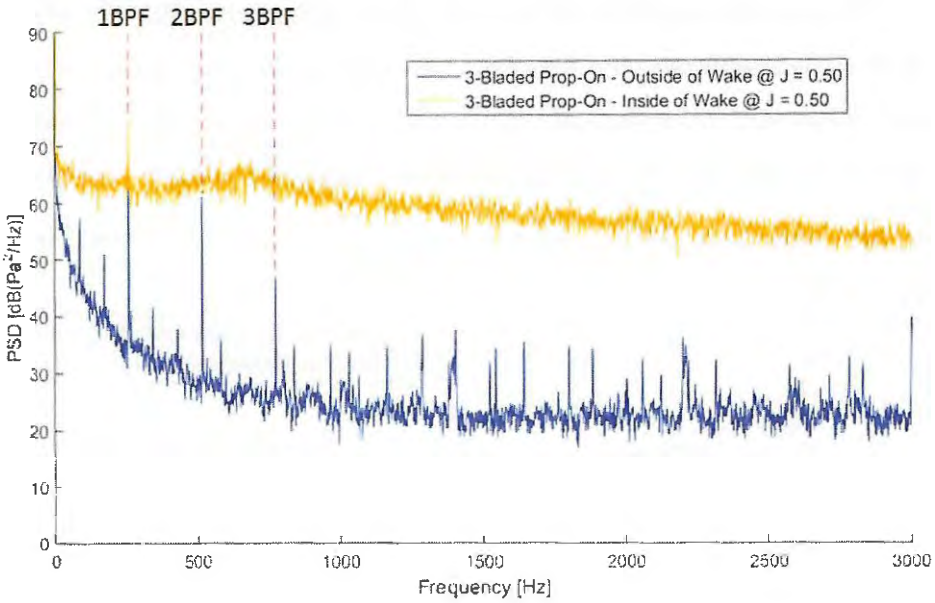

Source – Author

The spectra for the prop-off configuration showed the expected results, based on the ones obtained by Horne and Soderman (1988). Outside of the wake, the spectra displayed much lower values than inside of the wake, which is in accordance to the turbulence measurements from Figure 100. For the prop-on configurations, several peaks can be seen at the outside of the wake curves, which are then related to the blade passage frequency and harmonics. Based on the maximum rotation of the motor (5000 RPM) and the number of blades of each propeller, the expected and measured BPFs are shown in Table 8. The agreement between the values is very good, indicating a high measurement quality.

Table 8 – Expected and measured BPF for 3- and 4-bladed propellers with hot-wire

Configuration	Expected BPF [Hz]	Measured BPF [Hz]
4-Bladed	333.3	325.2
3-Bladed	250	257.8

Source – Author

The hot-wire was then able to capture the tones correspondent to the BPF and higher harmonics of both propellers outside of the wake. However, when the measurement is carried out inside of the wake, the high turbulence levels increase the broadband component, which buries most of the tones. Only the BPF peak remains visible, given the high power levels associated with this frequency, especially for the 3-bladed propeller. These spectra can be correlated with the microphone measurements, from Section 5, which show the tones at the BPF and harmonics and the broadband component for the installed configuration.

4.3 BLOWN CONFIGURATION

4.3.1 Pylon Wake Mapping

For the blown configuration, the same pylon spanwise stations were mapped as previously, and the results are compared with the installed case. The measurements for the two advance ratios of the 4-bladed propeller (J = 0.30 and J = 0.40) were successfully performed. However, before the tests for the 3-bladed propeller could be carried out, the hot-wire probe malfunctioned. Therefore, no aerodynamic measurements for the 3-bladed blown configuration could be performed. These wake measurements were carried out with a sample rate of 1 kHz and 512 samples, in order to avoid long measurements and variations on the blowing mass-flow. Therefore, it was also not possible to verify the spectra from the hot-wire time history, as was previously done for the installed configuration. In this section, since both tested configurations were prop-on, the results were non-dimensionalized by the free stream speed of each case, as shown in Figure 103 and Figure 104.

Figure 103 – Pylon wake profiles for installed and blown 4-bladed propeller (J = 0.30)

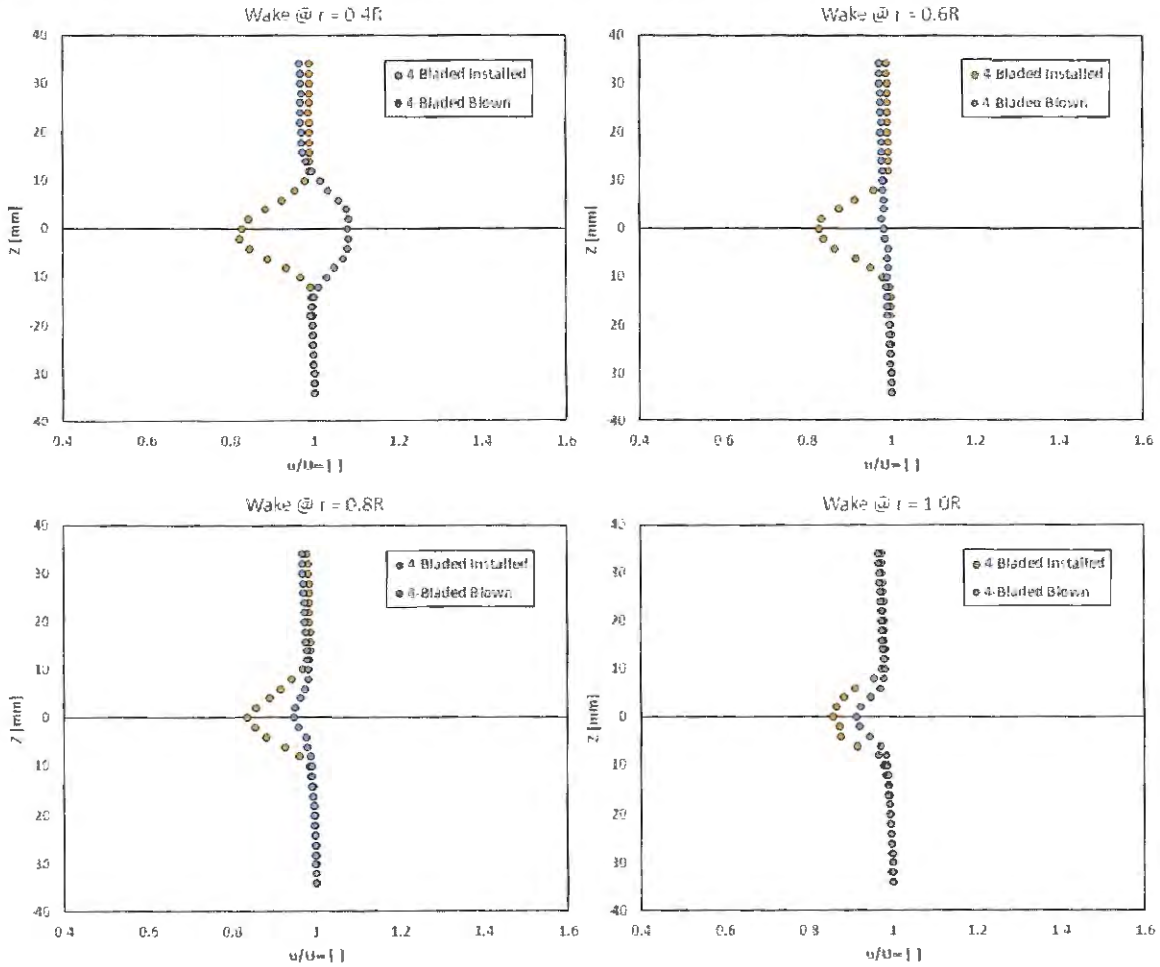

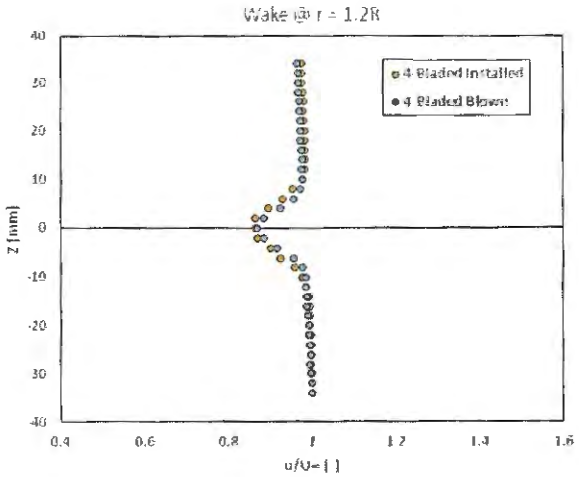

Source – Author

Figure 104 – Pylon wake profiles for installed and blown 4-bladed propeller (J = 0.40)

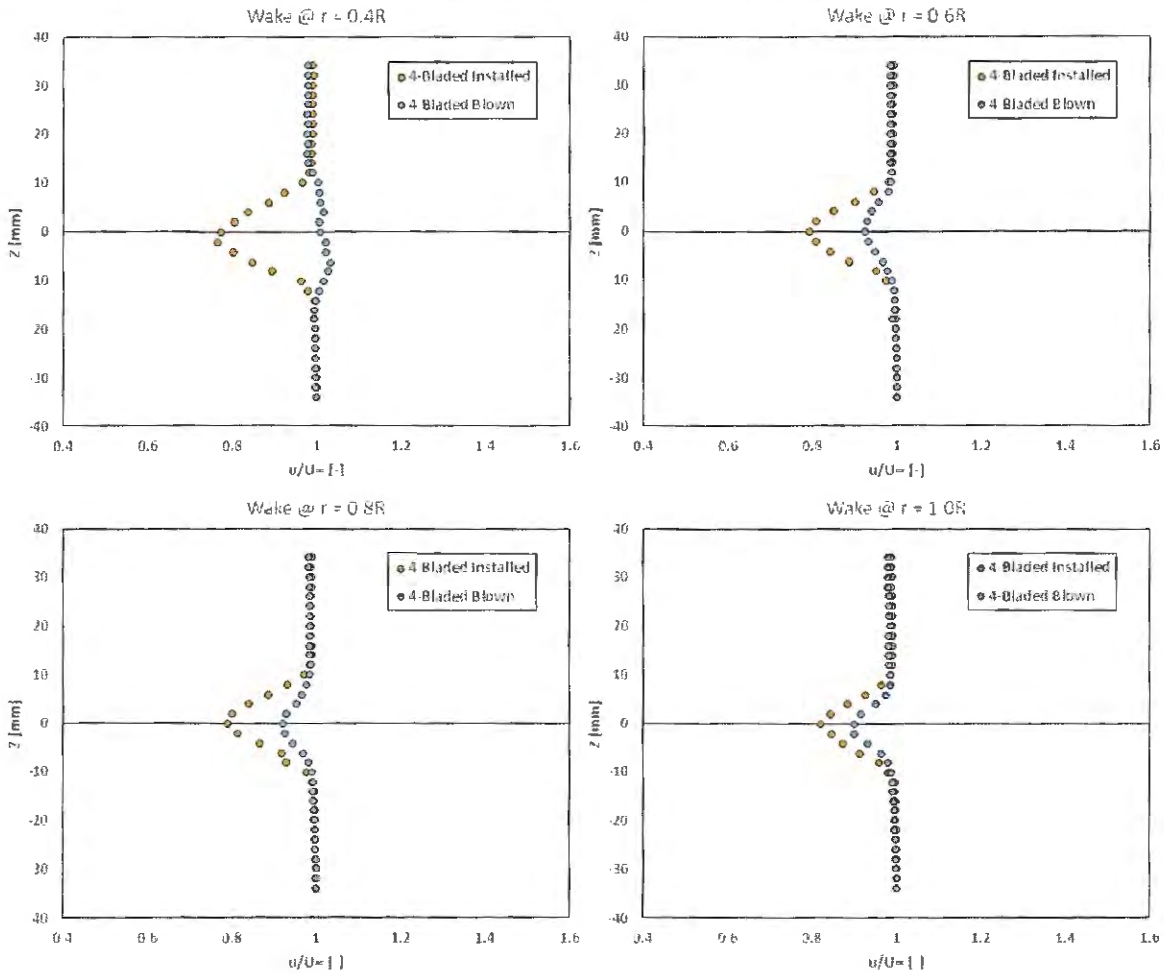

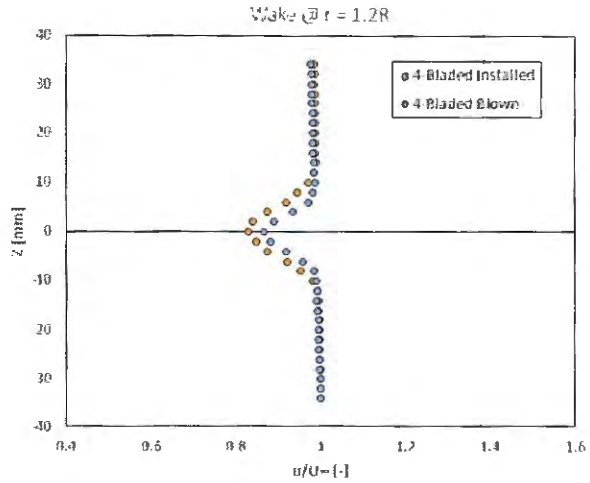

Source – Author

The wake profiles for the blown configuration indicate that the blowing outflow is not completely uniform in the spanwise direction. There is an increased velocity near the propeller hub, with an overshooting for the r = 0.4R station and progressive decrease of the local flow speed towards the tip. For the J = 0.30 condition, the optimum station, where the wake is completely filled and mostly uniform occurs for r = 0.6R, whereas for J = 0.40, this occurs between the r = 0.4R and the r = 0.6R station. This non-uniformity in the blowing outflow was caused by the inability of the flow inside the cylinder to turn 90° at the exit holes. Therefore, there was a velocity component in the *y*-axis, and the air tended to flow towards the hub region of the propeller. In order to try to correct this issue, small tubes were inserted inside each hole to try to direct the flow towards the *x*-axis, as was shown in Figure 76. For better results, the tubes should be longer outside the cylinder so that the flow would be purely horizontal. However, given the limited space in the internal ducts, and to avoid further pressure losses, the tubes were trimmed on the cylinder surface, and thus there was still a velocity component in the spanwise direction.

Despite this non-uniformity, the obtained results are still encouraging, in the sense that the wake intensity was reduced for most of the blade radii stations. As was previously mentioned, since the mass flow of the blown air could not be controlled, there should be a velocity where the best results in terms of propeller inflow uniformity and wake velocity deficit are obtained. The non-dimensional integral wake velocity deficit for the blowing-off and –on at the two tested advance ratio conditions are shown in Figure 105.

Figure 105 – Integral wake velocity deficit for installed and blown 4-bladed propeller

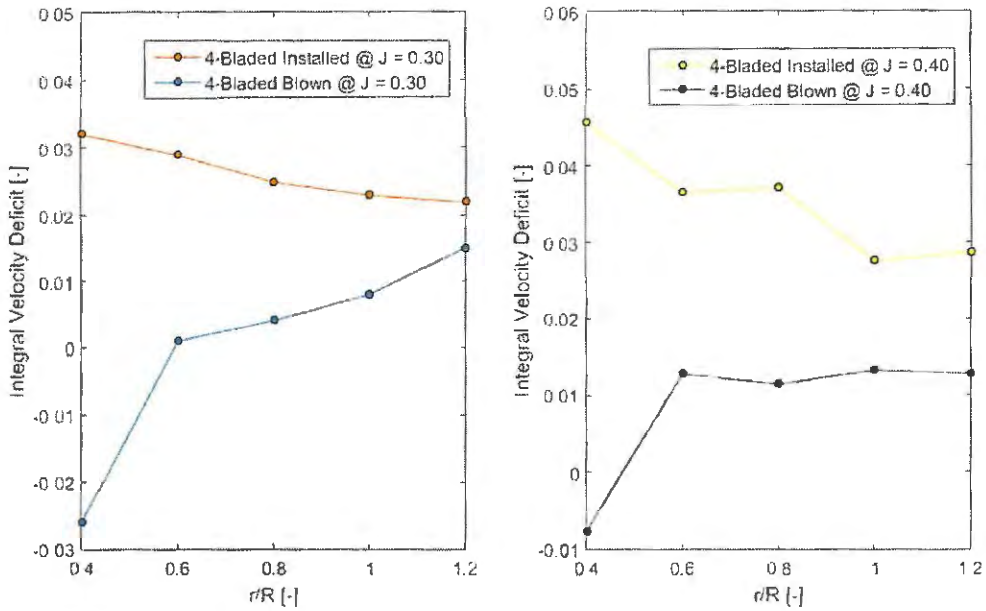

Source – Author

The integral of the wake velocity deficit allows for conclusions on the uniformity of the flow upstream of the propeller. As shown in Figure 103, for the J = 0.30 condition, there is some overshooting near the propeller hub, which tends to decrease towards the tip. At the r/R = 0.6 station, this deficit is nearly null, indicating this is the region where the flow is most uniform. Even after the propeller tip (r/R = 1.2), the velocity deficit for the blown configuration is also much lower than its installed counterpart. For the J = 0.40 condition, there is still a slight overshooting at the r/R = 0.4 station, and the station with zero velocity deficit should be close to this position (~r/R = 0.45), based on the trend shown in Figure 105. After the r/R = 0.6 station, the deficit tends to remain approximately constant, but with a value still much smaller than the installed configuration. Despite the wake not being eliminated for some of the stations, this deficit reduction shall still bring aerodynamic and aeroacoustic benefits, in comparison to the original installed case. Therefore, it is possible to conclude that the blowing is in fact reducing the flow non-uniformity at the wake, and thus will reduce the installation effects and noise penalty.

With the wake velocity profile measured at several stations, it is possible to create a flow map downstream of the pylon trailing edge to provide a better visualization on the differences between the installed and blown configurations, especially the reductions in the minimum velocity, at the center, as well as the wake width. The flow maps for the two tested advance ratios are shown in Figure 106 and Figure 107 with the propeller at the back for scale.

Figure 106 – Flow velocity contours for installed and blown configurations, respectively, at J = 0.30

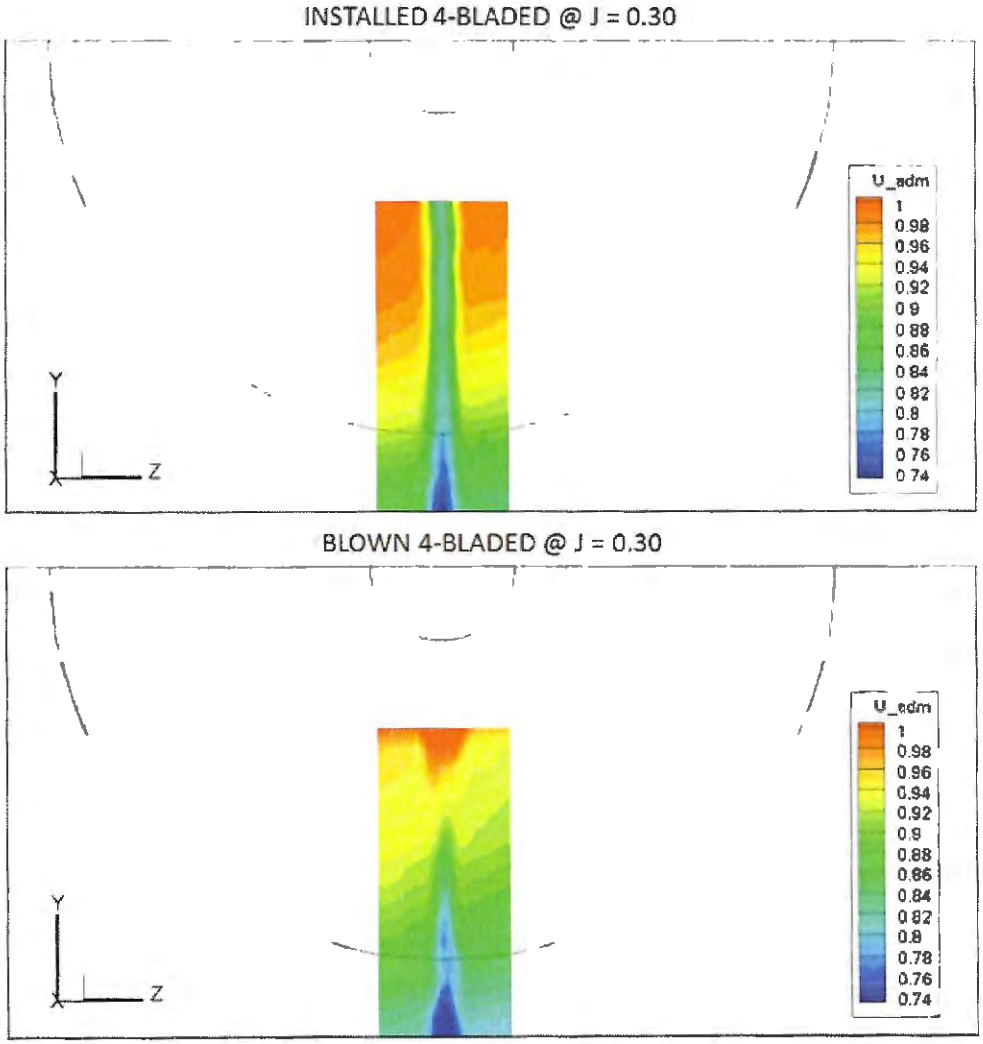

Source – Author

Figure 107 – Flow velocity contours for installed and blown configurations, respectively, at J = 0.40

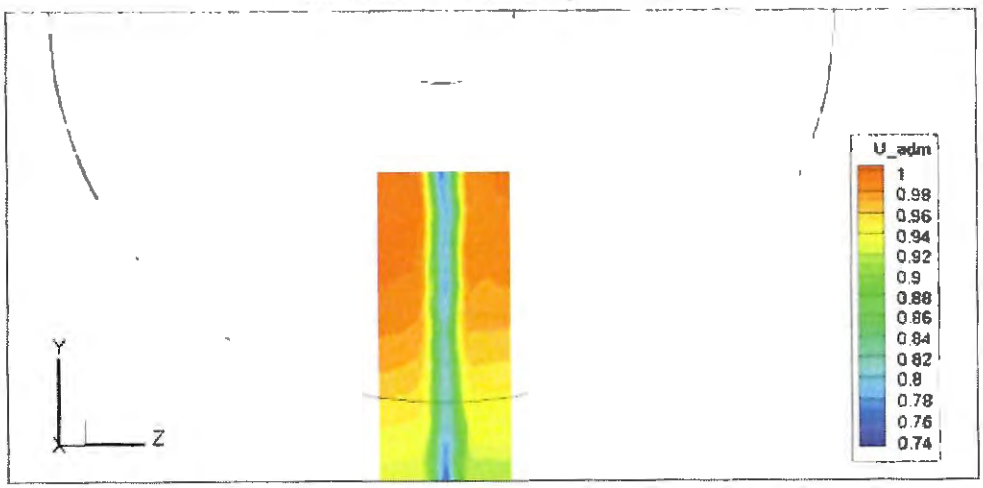

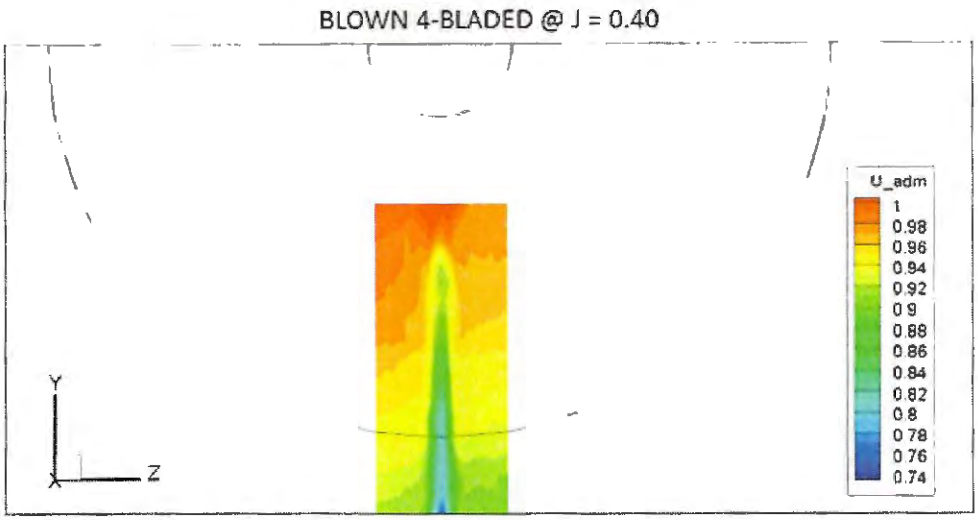

Source – Author

Despite some variation in the spanwise direction, for J = 0.30, the flow in the *z*-direction for the blown configuration was shown to be much more uniform than the installed one, without the occurrence of a visible wake for most of the propeller's span. For J = 0.40, a wake is visible for the blown configuration, but the velocities in this region are still much higher than the installed case.

The *x*-direction flow turbulence was also measured with the hot-wire. The charts in Figure 108 and Figure 109 display the percentage of turbulence in the flow for the installed and blown configurations, at the two tested advance ratios. Moreover, since the blowing presented some non-uniformity in the spanwise direction, the turbulence levels will be plotted for different blade radial stations.

Figure 108 – Turbulence levels at the wake for the installed and blown 4-bladed propeller at J = 0.30

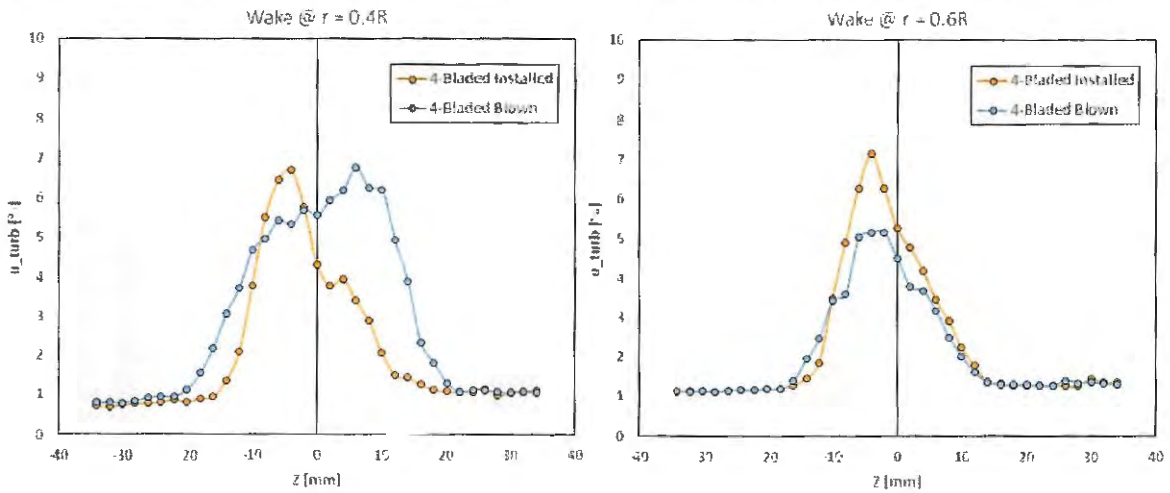

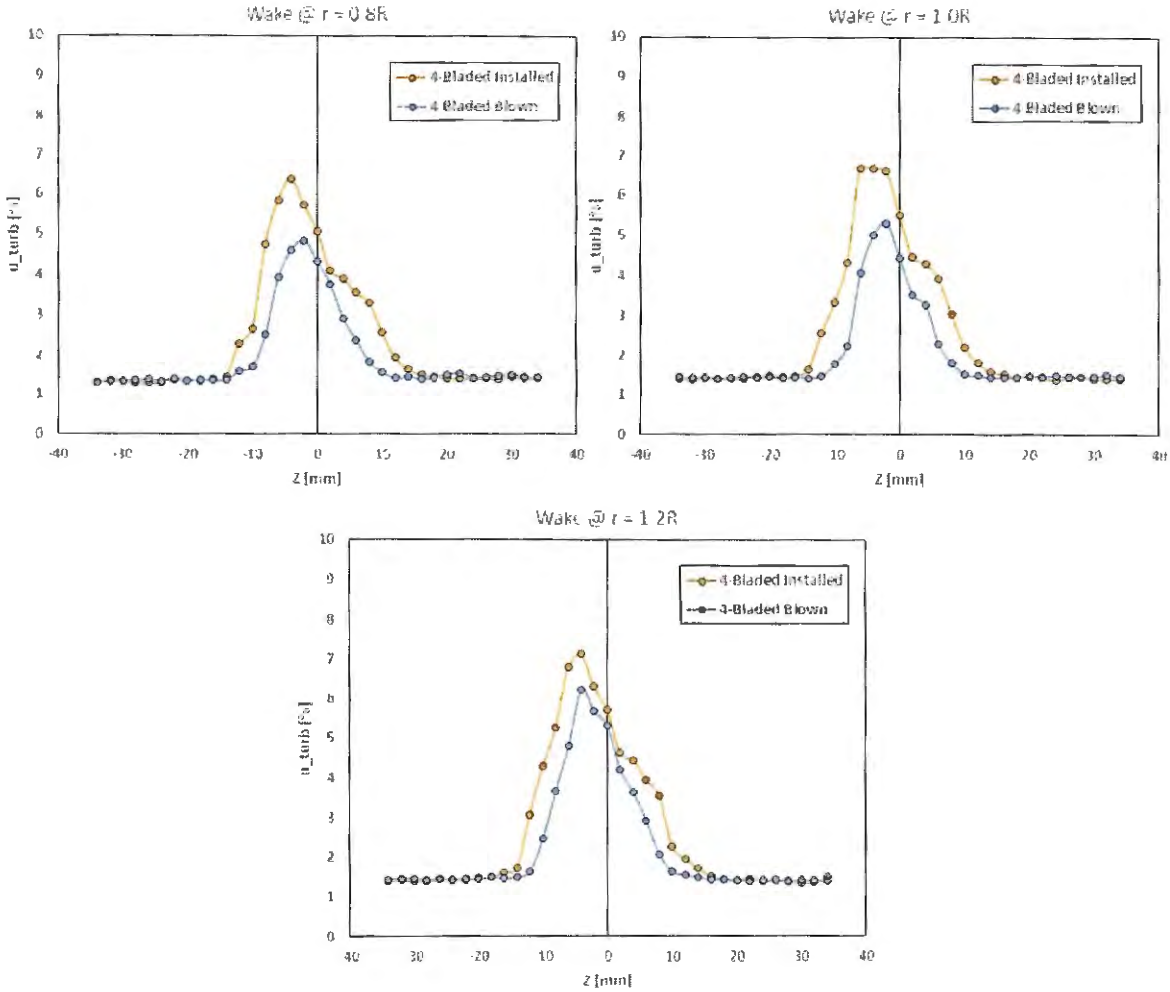

Source – Author

Figure 109 – Turbulence levels at the wake for the installed and blown 4-bladed propeller at J = 0.40

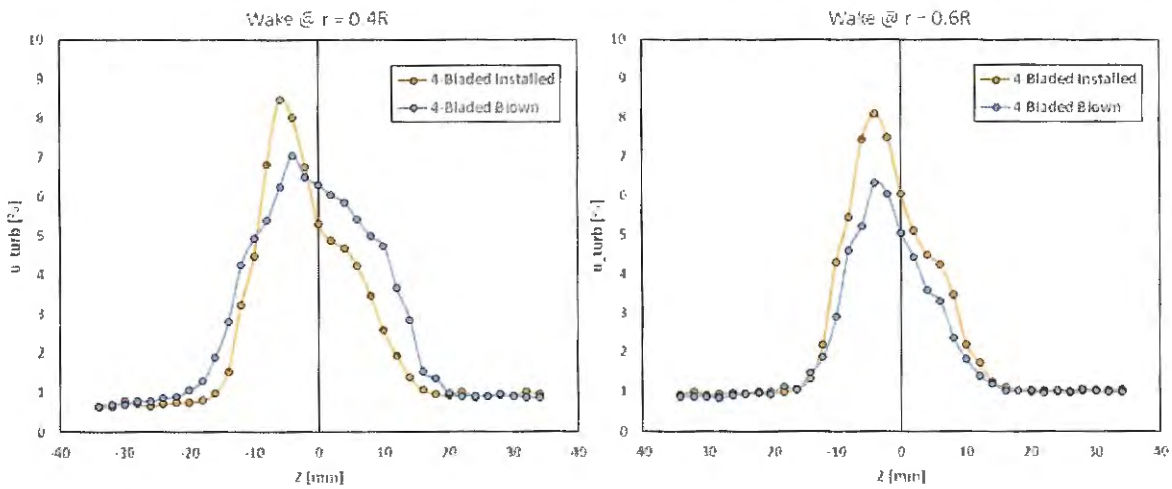

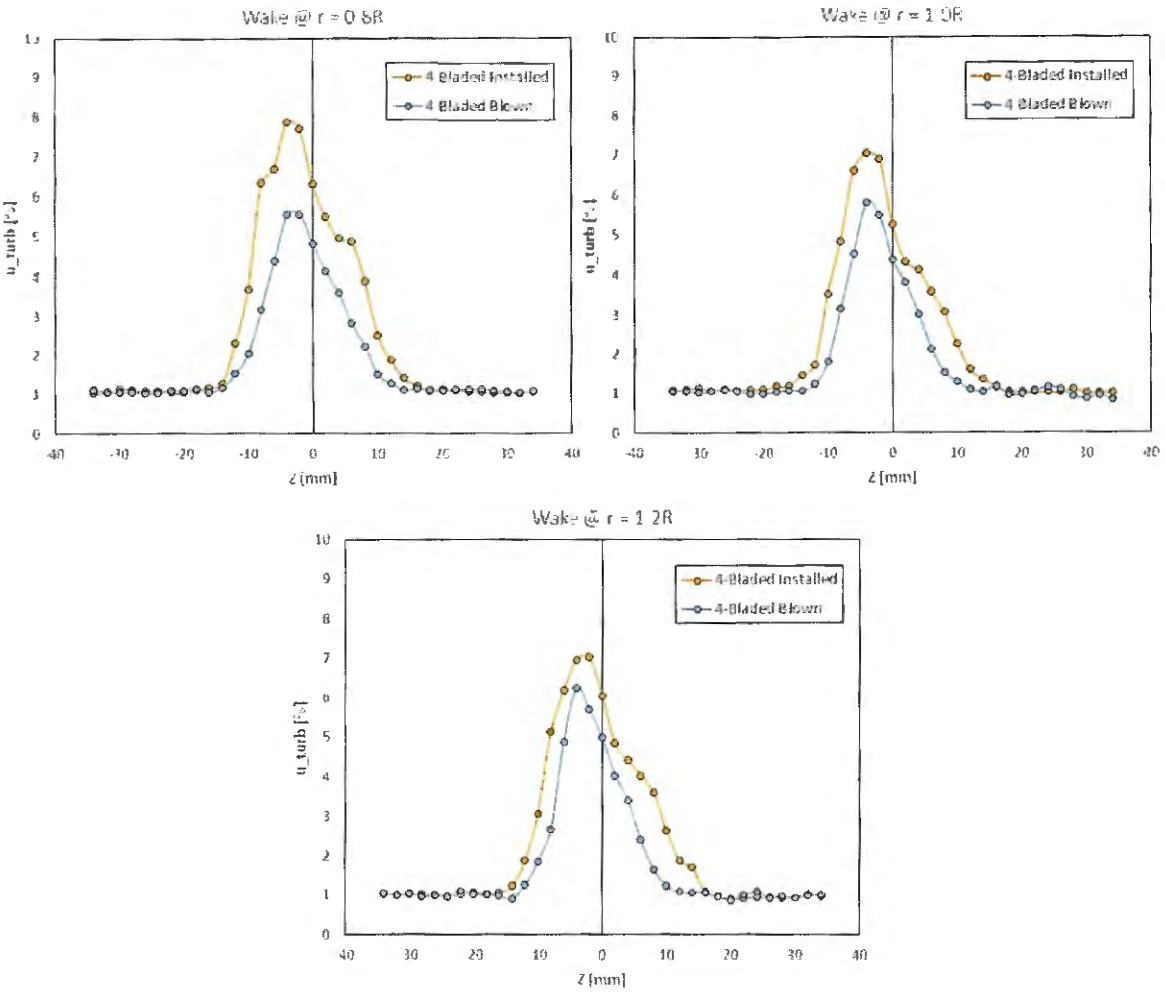

Source – Author

For the plots in Figure 108 and Figure 109, it is possible to verify a decrease in turbulence levels for the blown configuration, in comparison to the installed one. For the J = 0.30 condition, at the r/R = 0.6 station, the application of blowing reduces the turbulence from 7.2% to 5.2%, while for J = 0.40, the levels decrease from 8.1% to 6.3%. For the other stations (except the r/R = 0.4), similar results of reduced turbulence were obtained for the blowing-on configuration. Therefore, this should translate in a slight reduction in the propeller broadband noise, since the inflow turbulence is smaller. However, it is worth mentioning that this noise reduction was not obtained, due to the increased broadband noise caused by the blowing system itself, as will be shown in the next section. For the r/R = 0.4 station, the turbulence levels at J = 0.3 were higher for the blown configuration. This is most likely due to the high speeds at this region, caused by the blowing overshooting. For the higher advance ratio, there are still some points, where the turbulence is higher for the blown case, but the peak value is significantly lower.

5 AEROACOUSTIC RESULTS

5 AEROACOUSTIC RESULTS

5.1 BACKGROUND NOISE

Before the aeroacoustic measurements of the propellers, it is necessary to assess the background noise of the wind tunnel. Measurements for different flow velocities were carried out for the empty wind tunnel, matching the conditions for the aerodynamic tests, in order to get the PSD spectra from Welch's method, shown in Figure 110. Given the expected frequency range for the propellers BPF and harmonics, the spectra were limited in 3 kHz.

Figure 110 – Wind tunnel background noise spectra from Welch's method

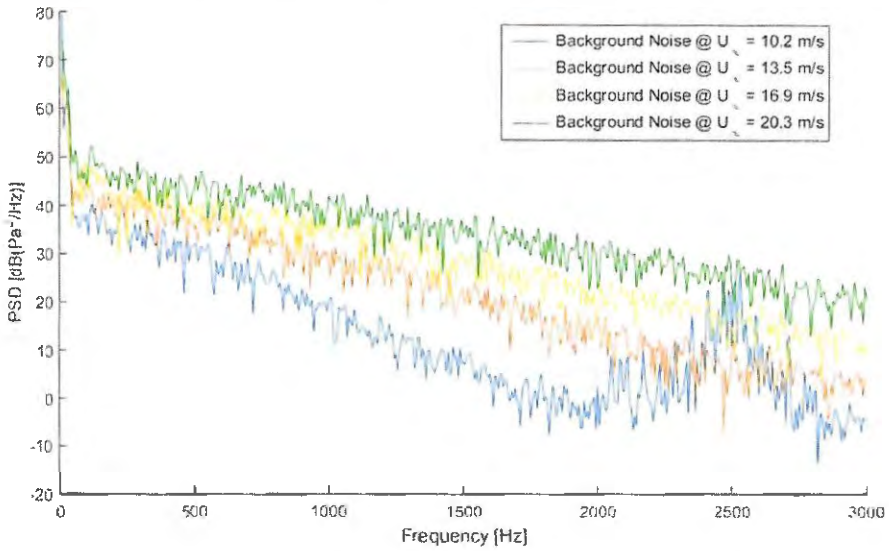

Source – Author

The background noise levels tend to display an almost linear decrease with increasing frequency, with exception for very low frequencies, below 100 Hz, where there are some tones likely related to the wind tunnel fan. As expected, higher noise levels are obtained with increasing the wind tunnel speed, and consequently, the Mach number. Despite being mostly of broadband nature, a region resembling a tone appeared for the lowest velocity, at a frequency of approximately 2.5 kHz. A further investigation was conducted through a beamforming analysis of the background noise, which yielded the integrated PSD spectra shown in Figure 111.

Measurements were conducted for a larger number of velocities. The tone at 2.5 kHz actually has a harmonic nature, given the presence of peaks at 5 kHz, 7.5 kHz and 10 kHz. However, for speeds higher than 12 m/s, the odd harmonics tend to disappear and only the even ones at 5 and 10 kHz remain. Since the frequencies where these tones occur do not change with speed and, given the region where they occur, it was believed that this noise is either generated

by the frequency inverter, which controls the rotation of the wind tunnel fan, or electric noise. For even higher velocities, these peaks become smaller and tend to be buried in the broadband noise.

Figure 111 – Wind tunnel background noise spectra from beamforming

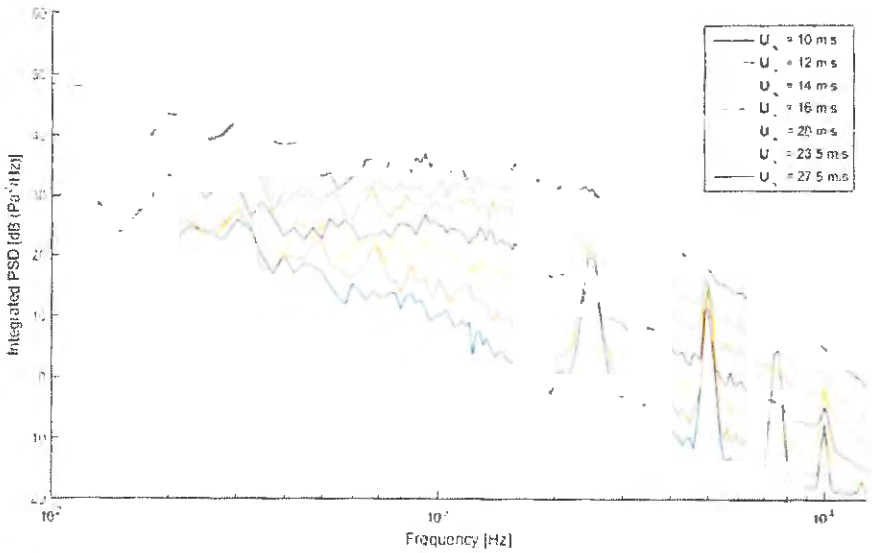

Source – Author

The first two mapping contours shown in Figure 112 display the results for the first tone (2.5 kHz), for U_∞ = 10 m/s and U_∞ = 12 m/s and the second row corresponds to the second harmonic (5 kHz) for U_∞ = 10 m/s and U_∞ = 16 m/s. The contours do not display any consistent source for these frequencies of interest, which indicates that those tones are related to side-lobes from outside sources. It is worth mentioning that, despite the presence of these tones, their sound pressure levels are relatively low and they should not affect the propeller noise spectra.

Figure 112 – Beamforming maps for background noise

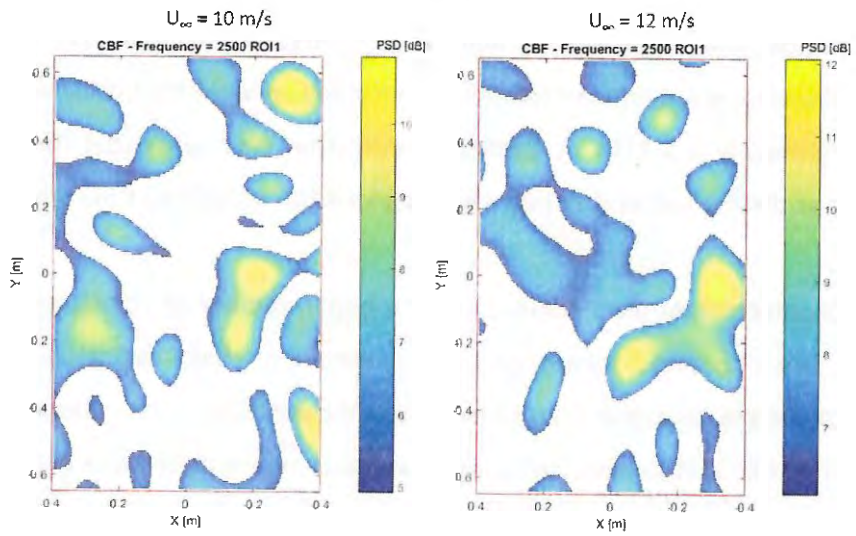

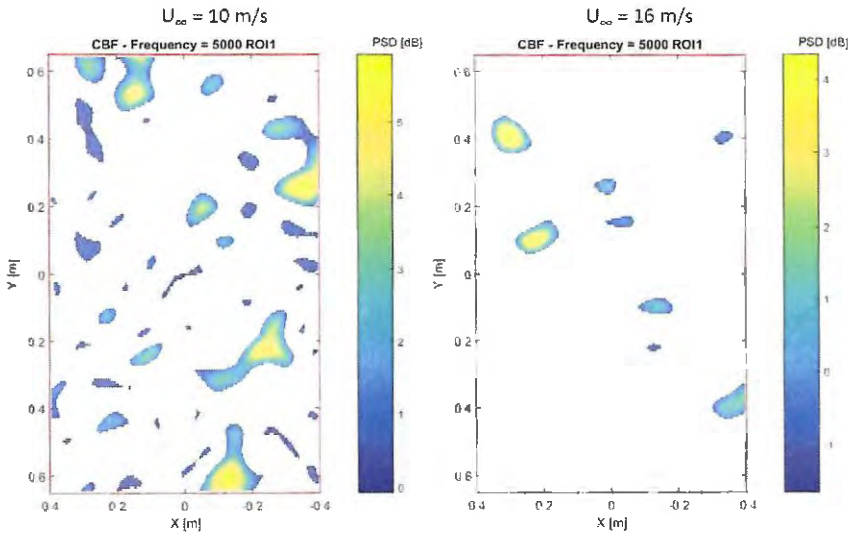

Source – Author

Aside from the wind tunnel, another unwanted noise source is the electric motor used for spinning the propeller. Measurements were conducted for the motor running at the nominal rotational speed for the prop-on cases (5000 RPM). Through the beamforming spectra shown in Figure 113, the frequencies of the motor tones can be verified. The highest peaks were found at 1200 Hz, 1475 Hz, 2400 Hz, and 2850 Hz, which are likely of harmonic nature. The beamforming contours for these frequencies (except the 1200 Hz, which is not very clear) confirm that the tones are in fact generated by the motor.

Figure 113 – Electric motor tones in the beamforming spectra and beamforming maps

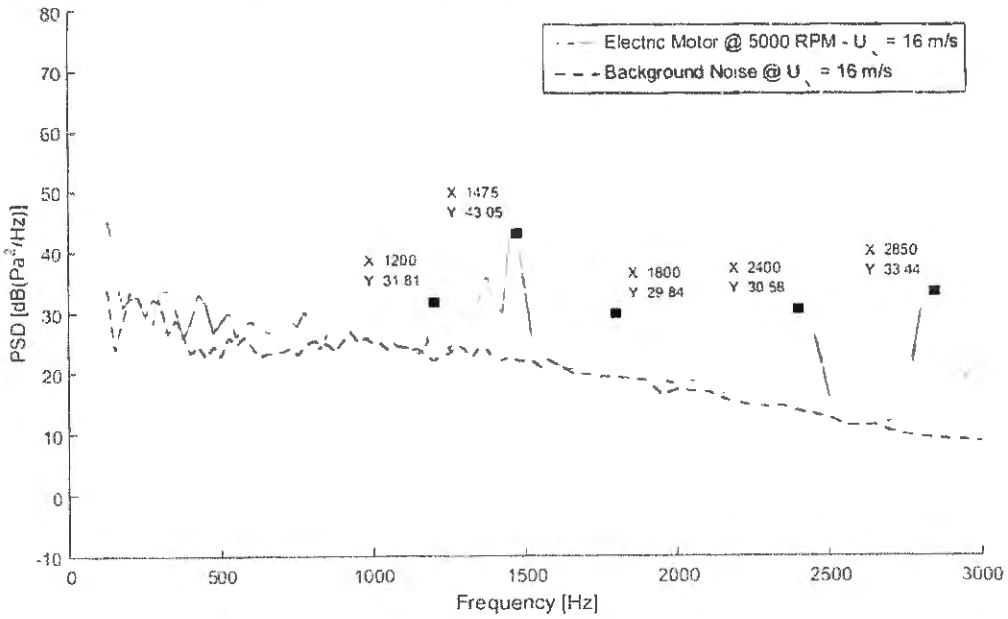

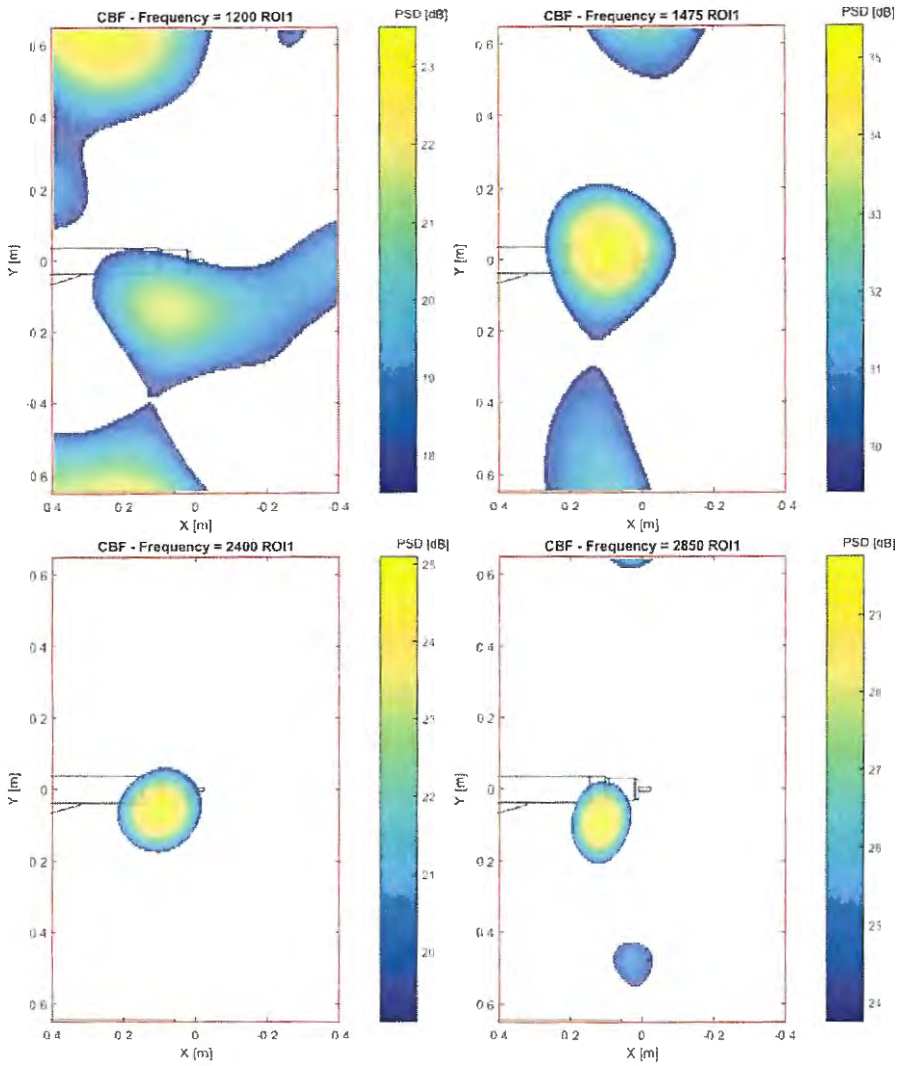

Source – Author

5.2 ISOLATED CONFIGURATION

The initial propeller aeroacoustic measurements were conducted at the isolated configuration. The propeller was placed in a tractor position, in order to avoid any influence with other components and only the self-noise generation mechanisms would occur. The data was obtained as noise spectra and source localization through beamforming. These results will be used for comparison with the other configurations in the following sections.

5.2.1 Isolated Propeller Spectra

In this section, the spectra for the 3- and 4-bladed propellers will be analyzed to assess the main characteristics of the emitted noise, focusing on the blade passage frequency tones and the broadband components, as shown in Figure 114. For both cases, the motor is running at

maximum rotational speed, of approximately 5000 RPM, which means the BPF for each propeller should be the same as shown in Table 8. The propellers were run at the same free-stream speed of 16 m/s. The wind tunnel background noise is also plotted as reference.

Figure 114 – Noise spectra for isolated 3- and 4-bladed propellers for U_∞ = 16 m/s

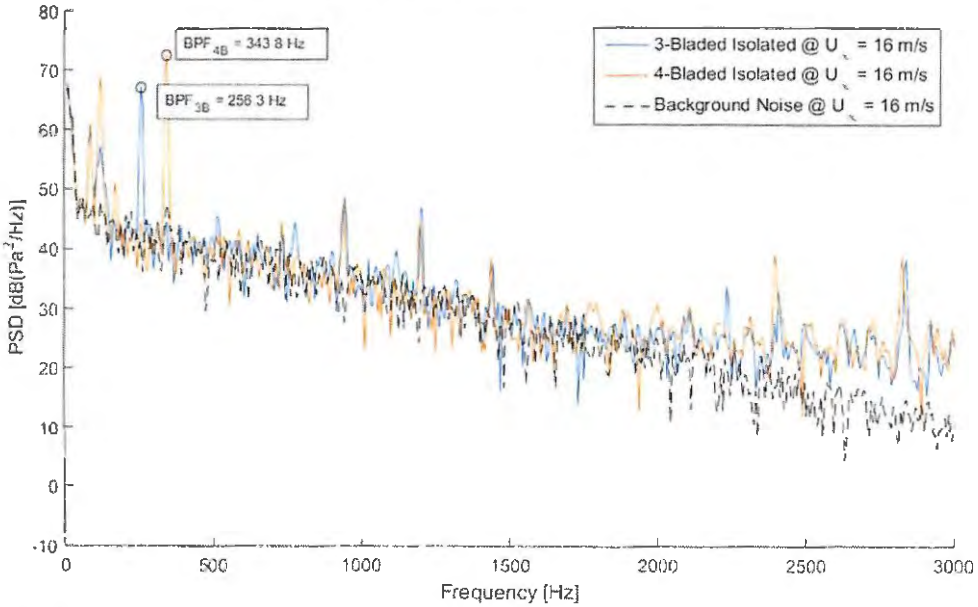

Source – Author

By comparing the spectra from Figure 114, it is possible to spot clearly the BPF peaks for each propeller, at the expected frequencies. The higher harmonics, with smaller power spectral density, are not so easily visible. Also, for low to medium frequency values (up to 2 kHz), the wind tunnel background noise is fairly high, so possible peaks and the broadband component for this range cannot be analyzed. After 2 kHz, the broadband noise becomes visible, and is likely higher for the 4-bladed, as better shown in the beamforming spectra in Figure 115. Some of the peaks presenting the same values for both configurations should be related to the electric motor, given the frequencies they occur. Some high level peaks are found for lower frequencies. One of them is related to the passage frequency of a single blade, and thus will be the same for both propellers (~85 Hz). The other one is probably related to interactions between the propeller and the rig, since it occurs at a fixed frequency for every case (~118 Hz). Given the absence of BPF subharmonics at the 4-bladed propeller spectra, it is likely that the blades have the same angles and there are no variations in the diameter for different directions.

The source localization through beamforming, shown in Figure 116, display the sources far away from the propeller blades. Therefore, either the beamforming is picking up the sound reflections on the wind tunnel walls, or it is positioning the sources at the Mach radius, which

was discussed in Section 3.5.2. Based on Equation 15, with the current operational conditions and also considering the observer at the center of the array ($\theta = 90°$), the Mach radius for the propellers will be positioned at 0.55 m from their axes (represented by the dashed lines in both figures). Given the proximity between the sources positions to the dashed lines, and the similarity between the results obtained from Horvath, Envia and Podboy (2013), it is likely that the beamforming is, in fact, positioning the sources at the apparent location, related to the Mach radius.

Figure 115 – Beamforming noise spectra for 3- and 4-bladed propellers for $U_\infty = 16$ m/s

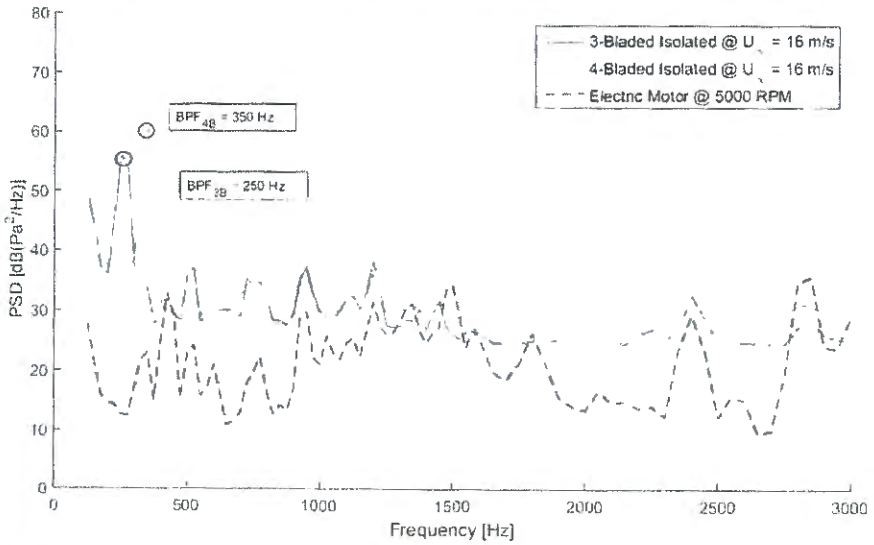

Source – Author

Figure 116 – Beamforming maps at the BPF of 3- and 4-bladed isolated propellers

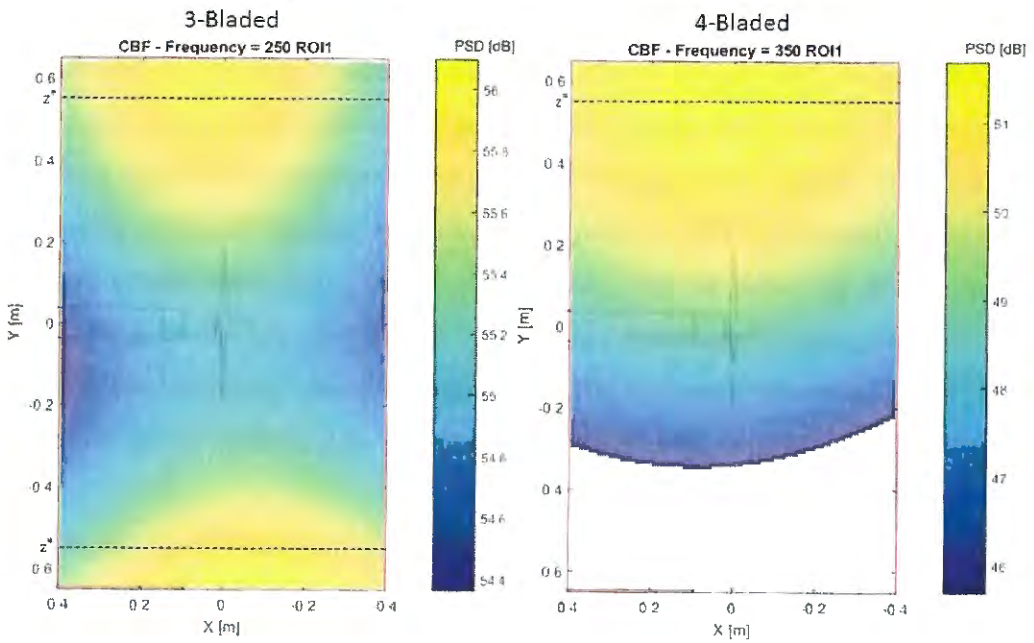

Source – Author

5.2.2 Advance Ratio Analysis

The effect of the advance ratio on the propellers aeroacoustic behavior was evaluated through two different approaches. For the first one, the rotation for the 4-bladed propeller was kept at the maximum level of 5000 RPM, and the free stream speed was changed, in order to obtain different values of *J*. The second approach was the opposite, so that the flow speed was kept constant and the propeller rotation was controlled to provide the desired advance ratio values. The results for the first approach are shown in Figure 117 and Table 9, with the difference in noise levels, relative to the J = 0.30 condition.

Figure 117 – Spectra for 4-bladed isolated propeller at different flow speeds

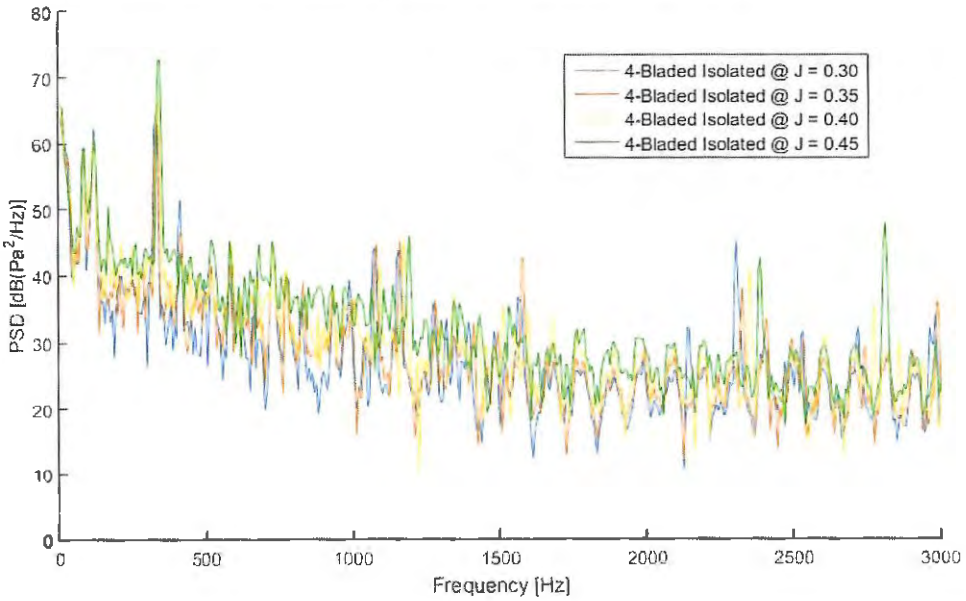

Source – Author

Table 9 – PSD for the 4-bladed isolated propeller BPF at different *J*

J [-]	BPF [Hz]	PSD_{BPF} [dB]	ΔPSD_{BPF} [dB]
0.30	331.3	65.25	-
0.35	331.3	65.37	0.12
0.40	337.5	67.84	2.6
0.45	343.8	72.75	7.5

Source – Author

Once again, only the BPF peak was easily distinguishable, while the higher harmonics do not display high power spectral density values. For the range of tested advance ratios, the PSD levels for the BPF tend to remain unaltered, except for the J = 0.45 condition (with a 7.5

dB increase), where the peak is slightly displaced to the left, indicating that the propeller rotational velocity was increased, likely induced by the free stream speed. For increasing velocity and consequently, increasing J, the thrust generated by the propeller would have to be smaller and so should the loading noise component. Given the obtained behavior, these noise levels are then likely related to a different generation mechanism other than the blades loading.

For the second approach, the results are shown in Figure 118. These spectra are related to the lowest and highest obtained advance ratios, of 0.32 and 0.45, for a free stream speed of 10 m/s. There is a visible difference between the power spectral densities for each case, especially for the tone at the blade passage frequency. Since the free stream speed was the same, the case with lower advance ratio had a higher rotational speed and, consequently, higher thrust. These are the expected results, considering the loading component as the main contributor to the overall noise.

Figure 118 – Spectra for 4-bladed isolated propeller for different rotational speeds

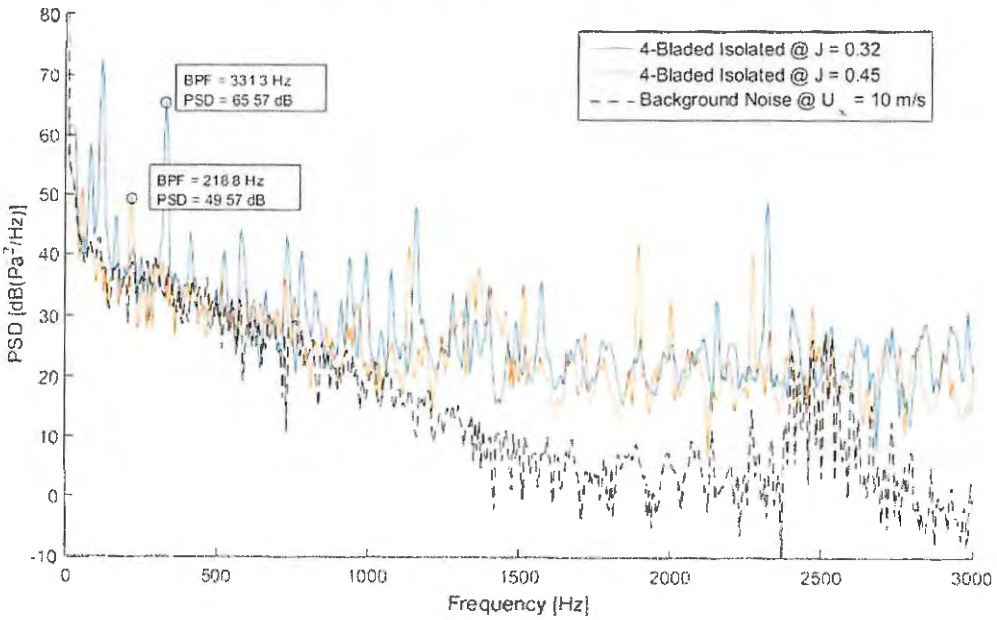

Source – Author

Aiming to investigate further the relation between the flow speed and the rotational speed to the noise levels, several other measurements were carried out, in which these parameters were changed. The chart in Figure 119 contains the sound pressure level for the blade passage frequency at four different flow speeds, in which the propeller rotation was used to control the advance ratio. For the U_∞ = 8 m/s and U_∞ = 12 m/s curves, a point of each one had to be removed, since excessive vibrations at those conditions lowered the quality of the aeroacoustic results.

Figure 119 – PSD variation with propeller RPM, for constant flow speeds (at the BPF of each condition)

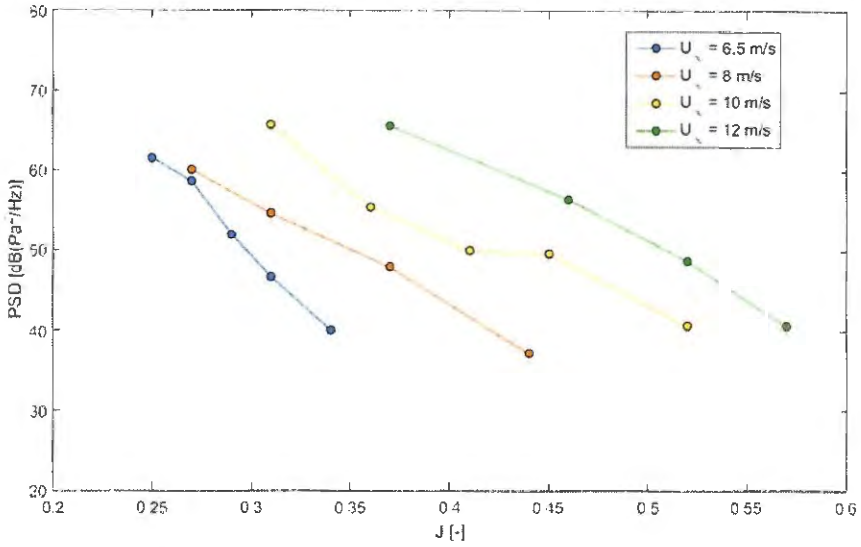

Source – Author

Considering the same tunnel speed, the propeller noise levels tend to decrease with increasing advance ratio. By increasing the free stream speed, the curves from Figure 119 tend to displace to the right. This means that for the same advance ratio, the condition with higher speed will also require a higher rotational velocity. With higher RPM, the propeller loading will also be higher and, consequently, the loading noise component at the blade passage frequency. However, if the velocity is increased, but the rotation is kept constant, there is not a considerable variation in the noise levels, as was shown in the first approach.

For lower advance ratios, at also low flow speeds, where the loading noise tend to be high in comparison to the background noise, it could be possible to see the BPF higher harmonics. The spectra shown in Figure 120 were obtained for a wind tunnel speed of 8 m/s, at the lowest advance ratio condition (4815 RPM). Each of the dashed red lines represent a harmonic of the blade passage frequency. The background noise at that speed was also plotted for reference.

From the spectra shown in Figure 120, the BPF and harmonics tones are clearly visible, up to the 4th one. After extracting the PSD values for each of those peaks, as shown in Table 10, it is possible to verify that the loudest tone occurs at the fundamental blade passage frequency of approximately 321 Hz, with 60 dB. Following, there is the third harmonic (962 Hz) with 48.6 dB, and finally the second (643 Hz) and fourth (1288 Hz) ones with 45 and 44.6 dB, respectively. The higher order harmonics were not distinguishable, since at those frequencies, the propeller broadband noise tends to be higher and then the tones end up buried. The beamforming maps for these four frequencies are shown in Figure 121.

Figure 120 – PSD levels for the BPF and higher harmonics at J = 0.27

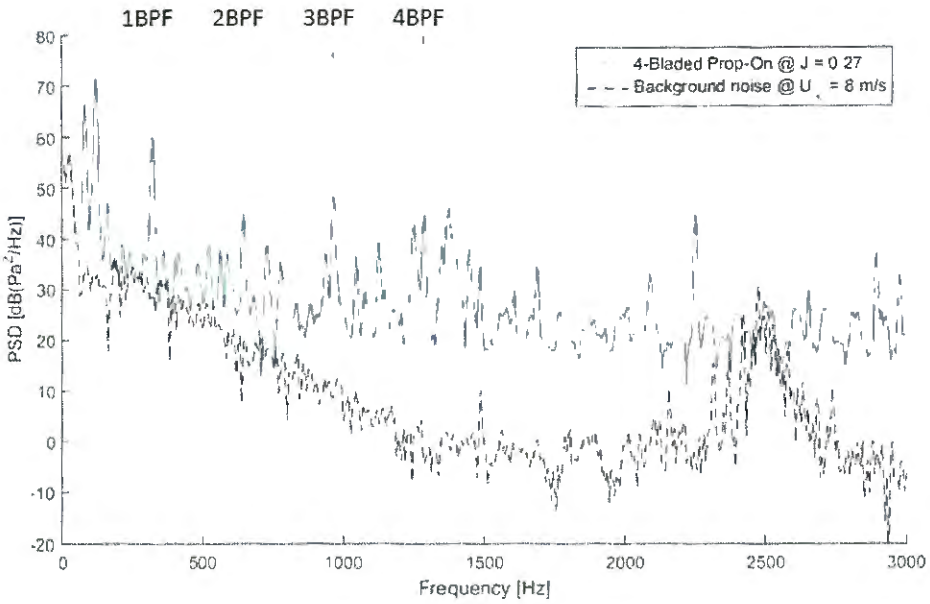

Source – Author

Table 10 – PSD for the 4-bladed propeller BPF and harmonics at J = 0.27

	1BPF (321 Hz)	2BPF (643 Hz)	3BPF (962 Hz)	4BPF (1288 Hz)
PSD [dB]	60.03	45	48.61	44.63

Source – Author

Figure 121 – Beamforming maps of the 4-bladed isolated propeller for four BPF harmonics

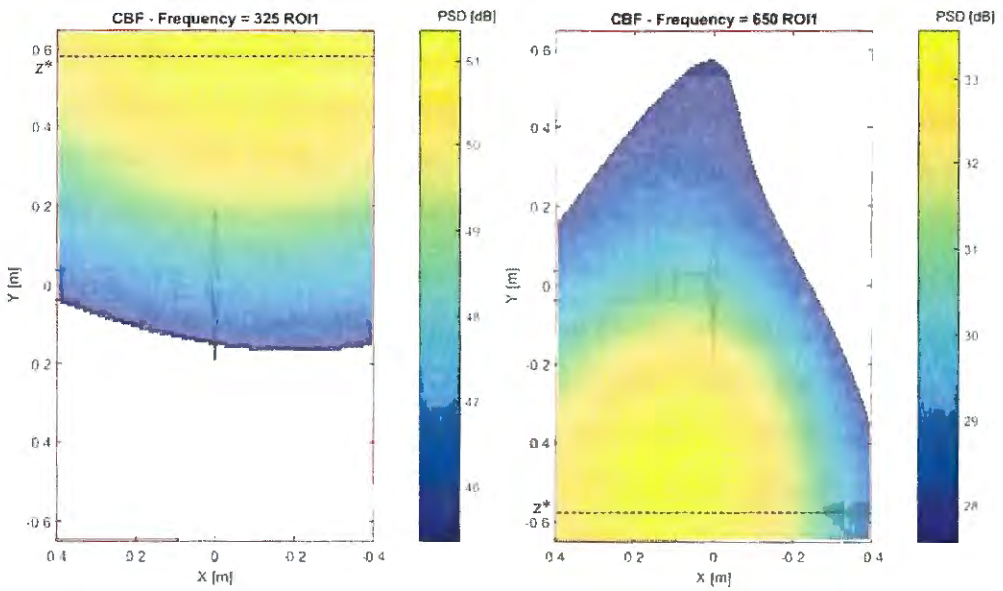

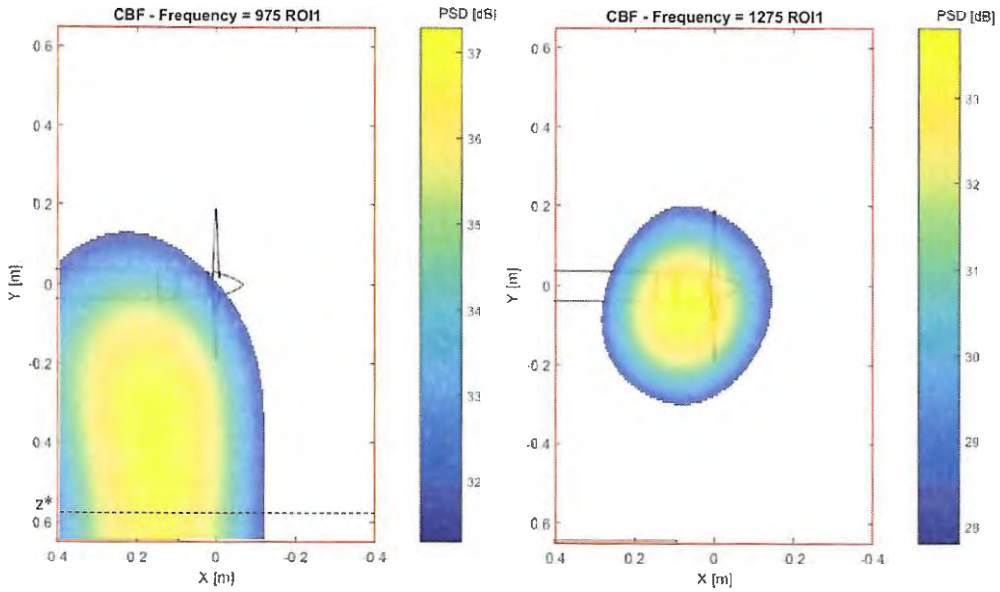

Source – Author

The beamforming once again places the noise source close to the wind tunnel walls, near the Mach radius position, for the blade passage frequency. For the second and third harmonics, the source is now placed in the lower side and moving towards the blades with increasing frequency. The proximity of the sources locations with the Mach radius line indicates that the beamforming is in fact placing the noise sources at an apparent location, due to high radiation efficiency. The beamforming for the fourth harmonic, given its proximity to one of the electric motor tones and the lower block length of this analysis, cannot properly separate both sources, thus it will be positioned closer to the motor.

5.2.3 Angle of Attack Analysis

An aeroacoustic analysis was carried out for the isolated 4-bladed propeller at different angles of attack, similarly as performed by Woodward (1987a). The convention for positive α was defined in Section 3.3, and it was selected based on the expected aeroacoustic results, as a consequence of the aerodynamic effects of angle of attack relative to the propeller axis, which is shown in Figure 122. For a positive angle of attack, the blades closer to the microphone array will experience a free stream speed U_∞, which can be decomposed into n', in the direction of the propeller rotation and U_e, as an effective free stream speed. This decomposition will result in an increase in effective RPM and a decrease in the perpendicular velocity vector magnitude, producing a local higher effective angle of attack (α_e) and, consequently, increased loading.

Figure 122 – Effect of the angle of attack on the propeller aerodynamic characteristics

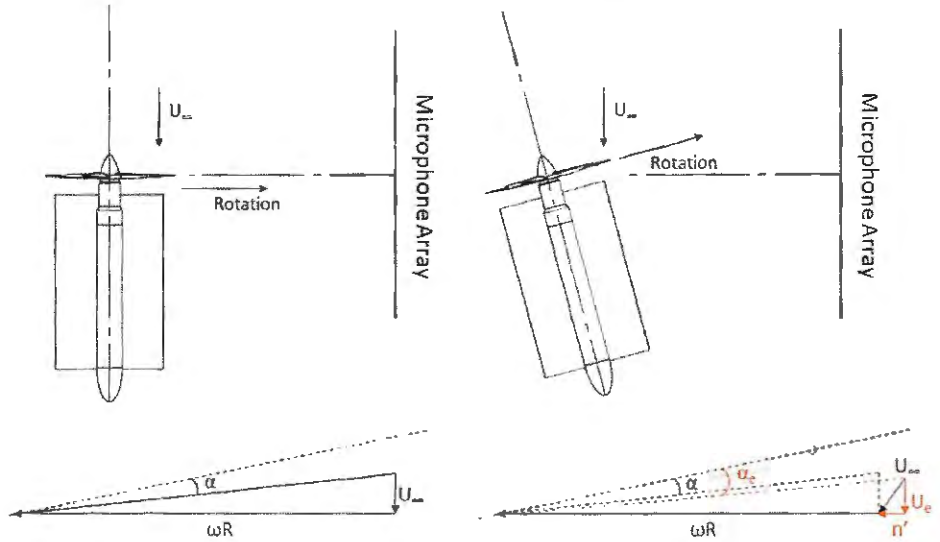

Source – Author

The opposite occurs for the blades furthest from the array, which experience a reduction in α and blade loading. Consequently, this unsteady loading during a single revolution will become a noise generation mechanism. For negative angles of attack, the blade closest to the array will experience the reduction in α and blade loading. Therefore, the aeroacoustic measurements should indicate increased loading noise, at the BPF tones, for positive angles of attacks. Two spectra were obtained for the highest and lowest angles of attack ($\alpha = \pm 15°$) and are shown in Figure 123, for a condition of J = 0.30, with the propeller at maximum rotation speed (~5000 RPM).

Figure 123 – 4-bladed isolated propeller spectra for $\alpha = \pm 15°$ at J = 0.30

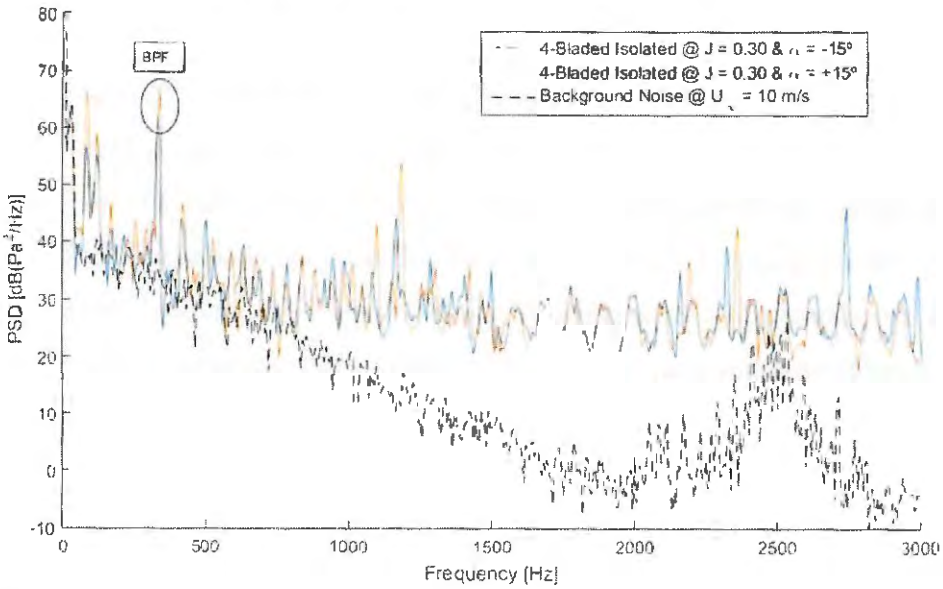

Source – Author

As seen from the spectra in Figure 123, the propeller at the positive angle of attack displayed higher noise levels than the one with negative angle of attack. This occurs because the blade with increased loading and higher noise is positioned closer to the array for the positive α. The chart in Figure 124 includes the PSD levels for the BPF at different angles of attack for two different advance ratios.

Figure 124 – PSD levels of the 4-bladed isolated propeller at the BPF, for different angles of attack and advance ratios

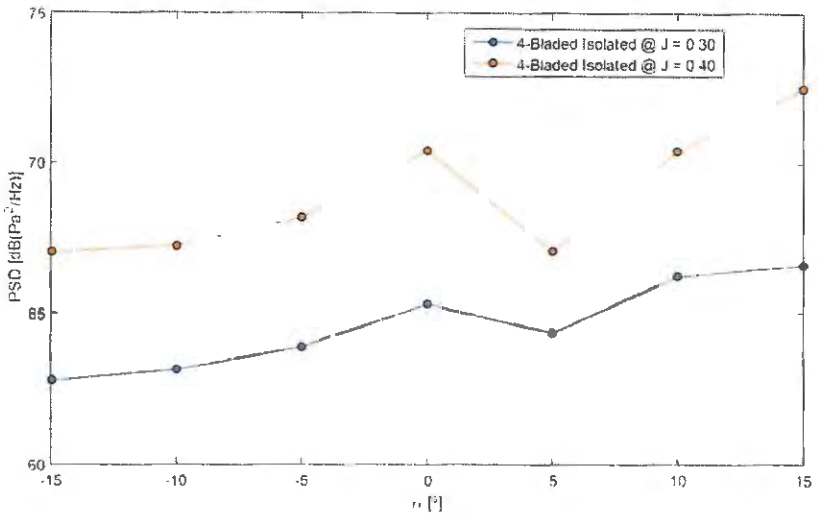

Source – Author

The noise levels at the blade passage frequency tend to increase for positive angles of attack, for both advance ratios tested. At J = 0.40, the noise levels are higher for all the angles, in comparison to J = 0.30. The maximum difference between the highest and lowest levels is 3.9 dB for J = 0.30, and 5.5 dB for J = 0.40. There was apparently a problem at +5°, where the points do not follow the trend, most likely due to vibrations in the structure, since it occurred for both velocities. These results are in accordance with the trends obtained by Woodward (1987a), in terms of noise level variations with propeller angle of attack.

5.2.4 Directivity Analysis

The directivity analysis for the isolated propeller was conducted at five different angular positions in respect to the center of the microphone array. Since the array is fixed on the wind tunnel wall, it was necessary to move the model forwards and backwards, in order to measure at specific directivity angles. The convention for the θ angle was defined in Section 3.3. Based on several works in the literature, the maximum noise levels tend to be located at the propeller plane ($\theta = 90°$) and decrease towards the axis. The spectra in Figure 125 display the noise levels for three different directivity angles at a condition of J = 0.30, with the propeller at maximum

rotation speed (~5000 RPM). The directivity curves for the 4-bladed and 3-bladed propellers are shown in Figure 126.

Figure 125 – 4-Bladed isolated propeller spectra for θ = 70°/90°/110° at J = 0.30

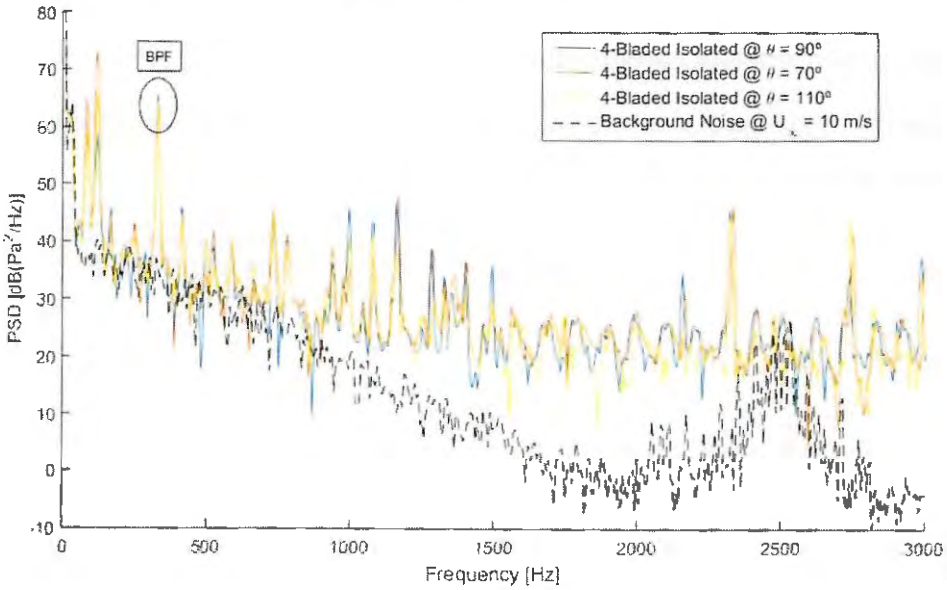

Source – Author

Figure 126 – Directivity curves for the BPF of the 4- and 3-bladed isolated propellers at J = 0.30 and J = 0.40

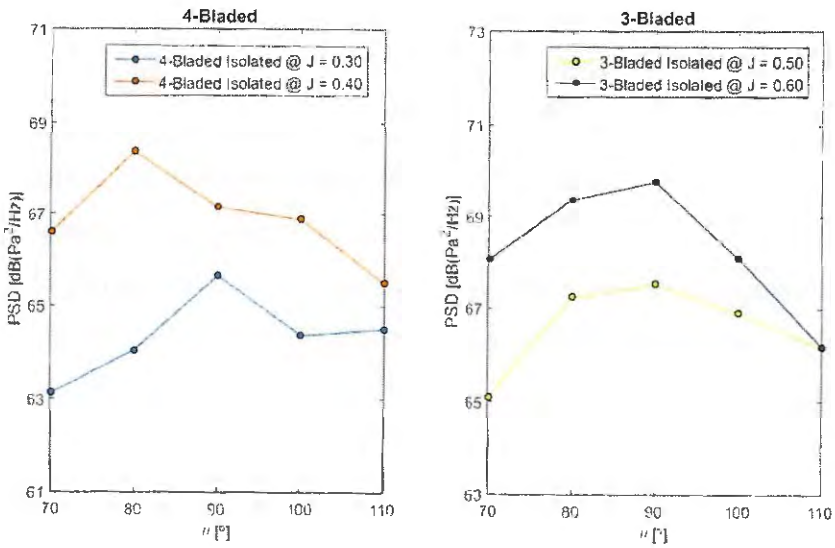

Source – Author

The power spectral density at the BPF was highest for the θ = 90° case, which corresponds to the propeller plane aligned with the center of the array. The difference between levels of this condition to the ones from the other directivity angles is rather small, but they are still higher than the variability for the isolated configuration (Appendix C1). The results for the

3-bladed propeller, at higher advance ratios, display a maximum at the propeller plane, giving results more similar to the ones obtained by Woodward (1987a), for example.

5.3 INSTALLED CONFIGURATION

The aeroacoustic tests for the installed configuration focused on evaluating the increase in the noise levels due to the interaction between the pylon wake and the propeller. Similar to the isolated case, several parameters will be investigated, such as the advance ratio, the angle of attack and the directivity. Beamforming analyses were also performed for sources localization.

5.3.1 Installed Propeller Spectra

In this section, the spectra for the 3- and 4-bladed propellers will be analyzed to assess the aeroacoustic effects of the presence of an upstream pylon, which is characteristic of a pusher configuration. By comparing the power spectral density between the installed and isolated cases, it is possible to quantify the effect of the unsteady blade loading on the propeller noise emissions. The spectra for the installed 3- and 4- bladed propellers are shown in Figure 127.

Figure 127 – Noise spectra for installed 3- and 4-bladed propellers at J = 0.45

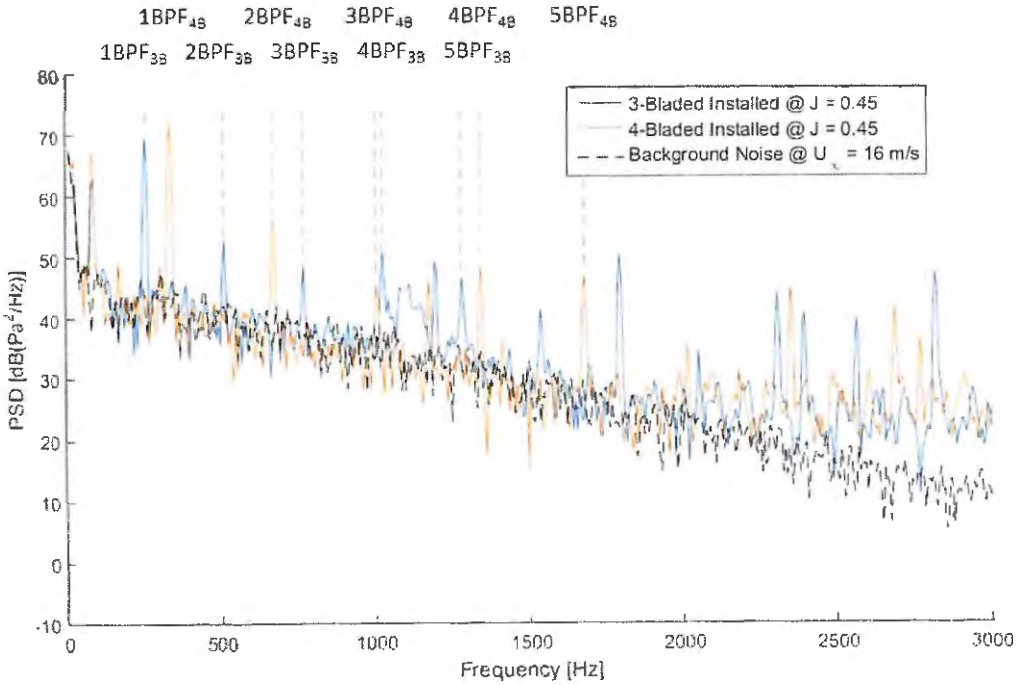

Source – Author

From Figure 127, it is possible to see an increased tonal content for the installed propellers spectra. For this configuration, not only the BPF, but also the higher harmonics tones

are clearly visible in the spectra. These tones are marked with the vertical dashed lines (blue for the 3-bladed propeller, and orange for the 4-bladed one), up to the 5th harmonic. There are other peaks with considerable power spectral density, such as the single blade passage frequency and the electric motor tones. The charts in Figure 128 contain both the installed and isolated spectra for the 3- and 4-bladed propellers, respectively. Table 11 displays the difference between the installed and isolated PSD levels for the tones up to the 5th harmonic for the 3- and 4-bladed propellers, respectively.

Figure 128 – Comparison between the noise levels of the isolated and installed 3- and 4-bladed propellers, respectively, for J = 0.45

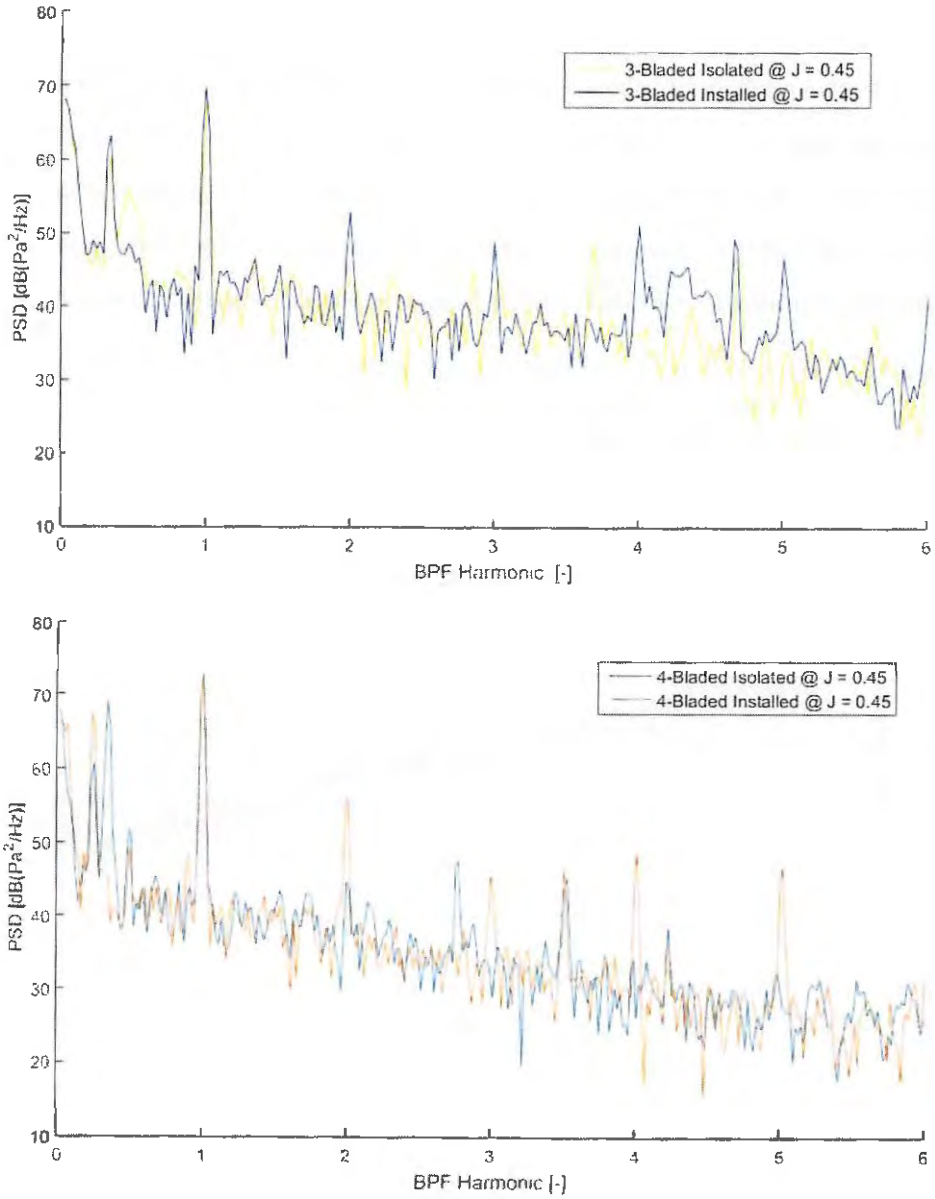

Source – Author

Table 11 – ΔPSD for the 3-bladed installed and isolated propeller at J = 0.45

	1BPF	2BPF	3BPF	4BPF	5BPF
ΔPSD_{3B} [dB]	2.1	8.6	3.8	13.8	12.5
ΔPSD_{4B} [dB]	-0.59	11.2	9.7	14.9	19.7

Source – Author

By comparing the isolated and installed configurations for both propellers, it is possible to see that the latter displays much higher noise levels for most of the propeller tones. For the fundamental blade passage frequency, there is a small variation in noise (2.1 dB for the 3-bladed and -0.59 dB for the 4-bladed), which could be considered inside the variability of the measurements, based on the results in Appendix C2. All other harmonics display a large increase in PSD levels. For the 4th and 5th harmonics of the 4-bladed propeller, the installation results in extra 15 to 20 dB, evidencing that in fact the higher harmonics are the ones most affected by the presence of the upstream pylon. The broadband component did not display any change, especially due to the high background noise levels up to 2 kHz.

For the beamforming maps shown in Figure 129 and Figure 130, the lower BPF harmonics still tend to position the noise sources far from the blades, similarly as the isolated configuration. This indicates a combination of both steady and unsteady loading on the blades. While the former tends to position the source at the Mach radius, the latter should position the source on the blades, since the unsteady loading is not a rotating noise generation mechanism, as opposed to the steady loading noise. For the higher harmonics, this is likely is case, since the tones were practically generated by the effect of the pylon wake and the sources are placed much closer to the blades.

Figure 129 – Beamforming maps of the 3-bladed installed propeller for five BPF harmonics

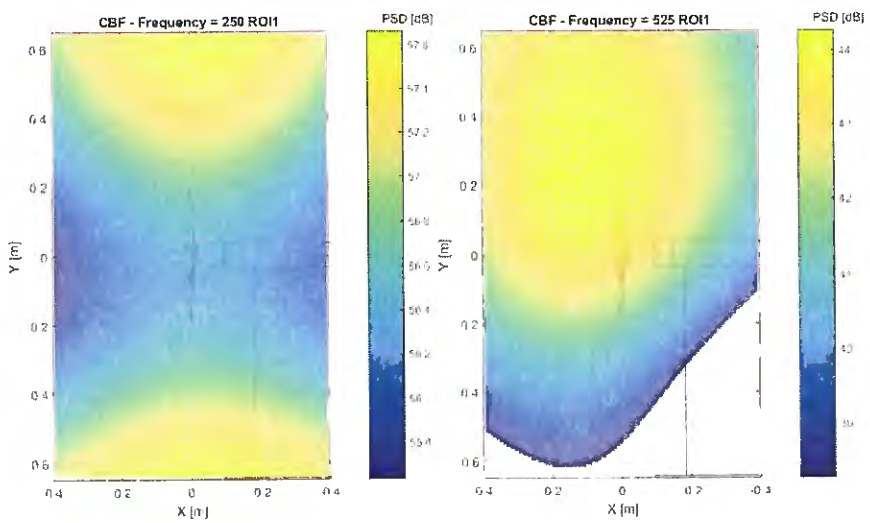

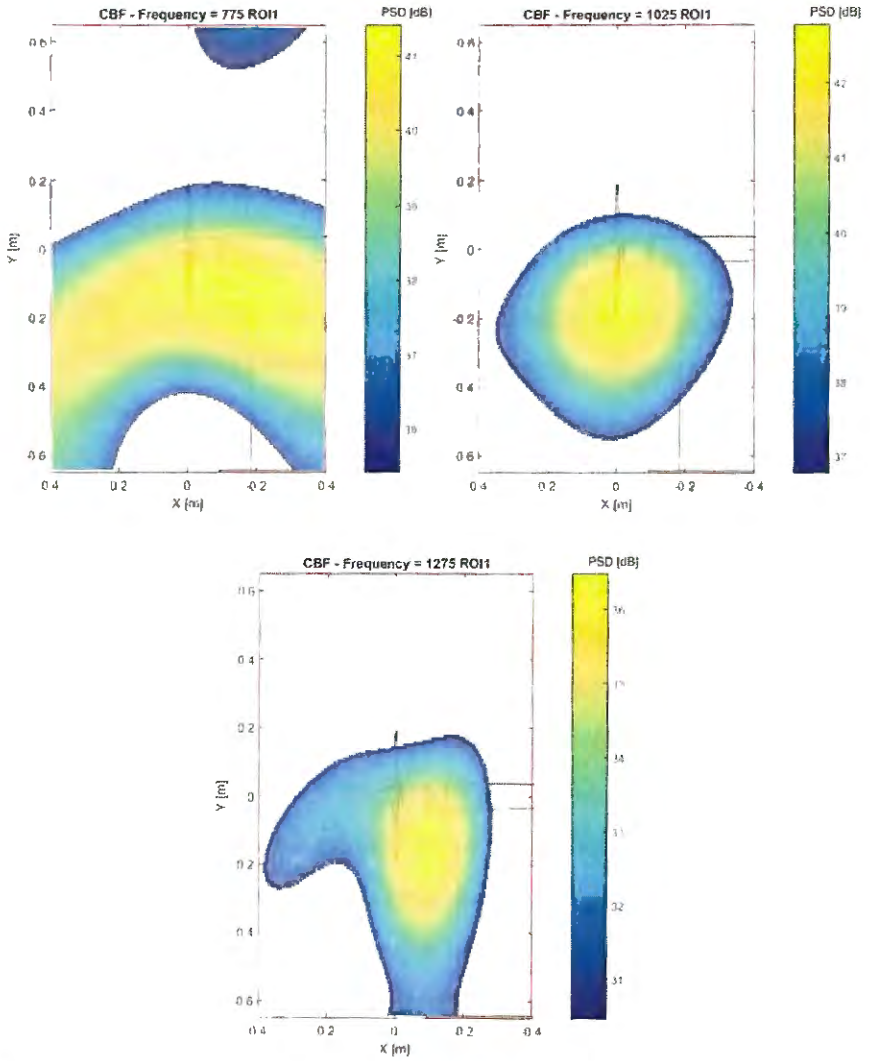

Source – Author

Figure 130 – Beamforming maps of the 4-bladed installed propeller for five BPF harmonics

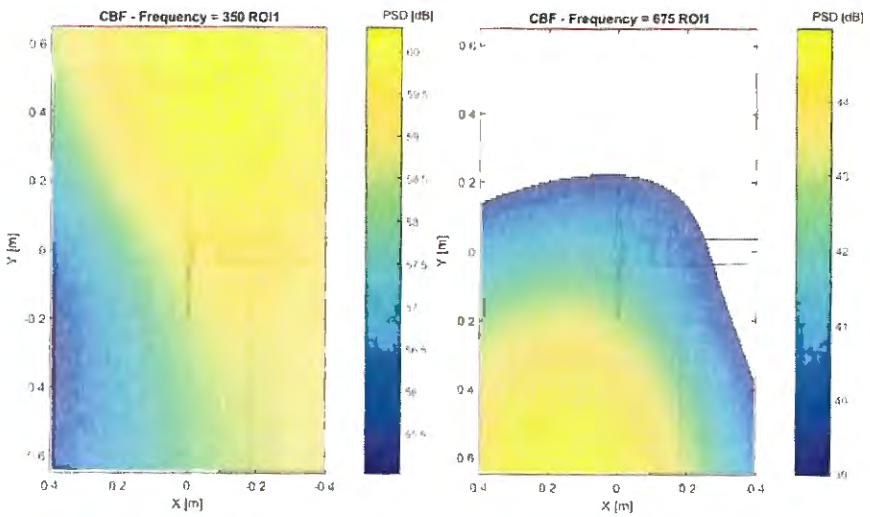

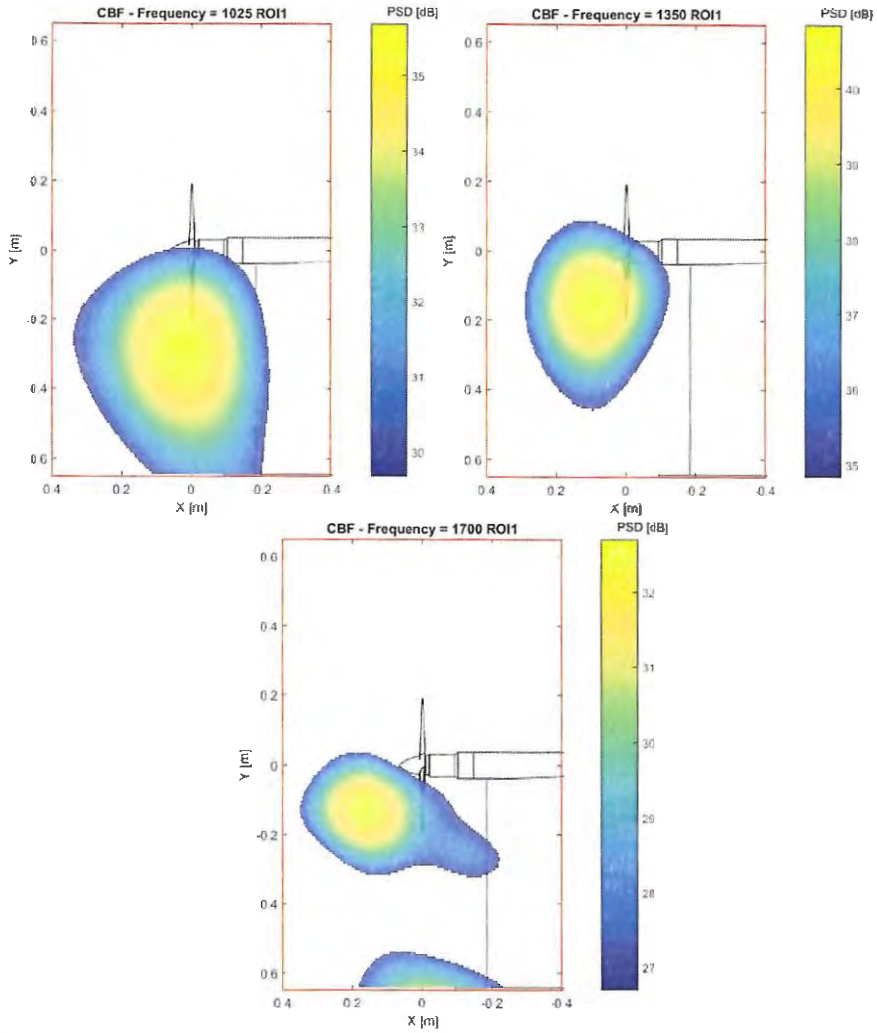

Source – Author

5.3.2 Advance Ratio Analysis

An analysis of the advance ratio on the propeller noise levels was also carried out for the installed configuration. The same two approaches applied for the isolated case were used. The aeroacoustic results for the first approach displayed in Figure 131 and Table 12, shown the same trend of increased noise levels for higher free stream speeds. For increasing advance ratio, the BPF peak displaces to the left, similarly to the isolated case, indicating that the free stream is inducing a rotational speed in the propeller. The relative increase in noise levels, compared to the isolated configuration, tends to be higher for the lowest advance ratio (J = 0.30). For the higher advance ratios, there is a slight noise decrease for the installed case, indicating that the unsteady loading does not play any role at this frequency or there could be some cancellation between the noise emissions from the steady and unsteady components.

Figure 131 – Spectra for 4-bladed installed propeller at different flow speeds

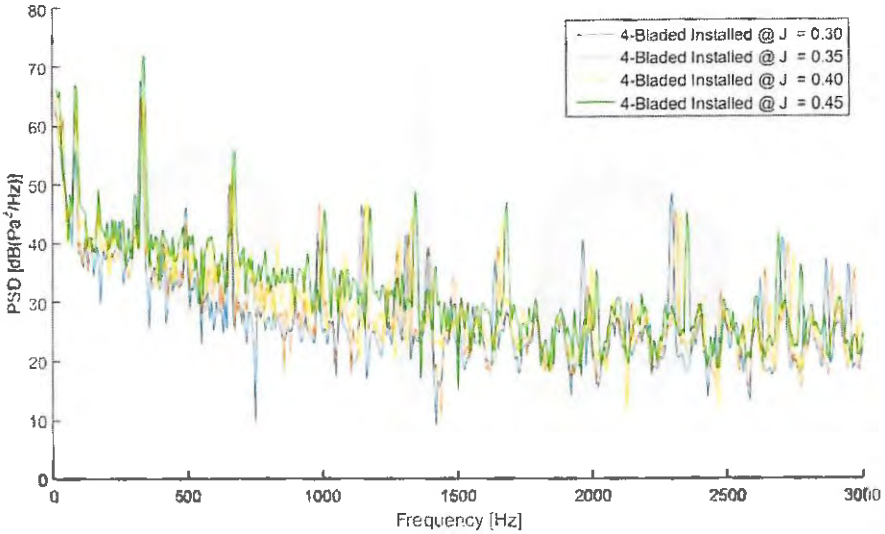

Source – Author

Table 12 – PSD for the 4-bladed installed propeller BPF at different flow speeds

J [-]	BPF [Hz]	PSD_{BPF} [dB]	$\Delta PSD_{INST-ISOL}$ [dB]
0.30	331.3	67.68	2.43
0.35	331.3	66.07	0.7
0.40	337.5	66.30	-1.54
0.45	343.8	72.10	-0.65

Source – Author

For the second approach, the results for each advance ratio will be compared with their respective isolated case data. The spectra were obtained for J = 0.32 and J = 0.45, for a free stream speed of 10 m/s, and are shown in Figure 132 and Figure 133, respectively. For the installed configuration at J = 0.32, the largest increases in noise were found for the 2nd, 4th and 5th BPF harmonic. The 1st harmonic remained unchanged, while the 3rd experienced a noise reduction. Given the high rotational speed for this condition, it is likely the radiation efficiency for the steady loading noise component is dominant for the BPF, while the unsteady loading is responsible for the noise levels at the other harmonics. At the 3rd, there could be a destructive interaction, resulting in cancellation of the sound fields. For J = 0.45, the background noise is fairly high, compromising the comparison of the 2nd and 3rd harmonics. The 1st, 4th and 5th harmonics, on the other hand display large noise increases due to the unsteady loading, as shown in Table 13.

Figure 132 – Isolated and installed 4-bladed propeller spectra for J = 0.32

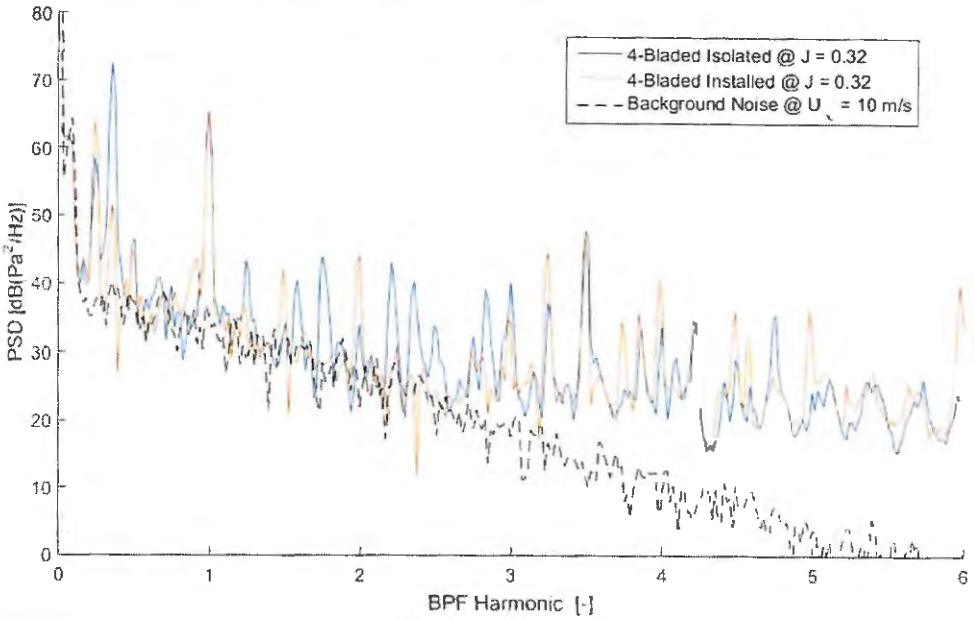

Source – Author

Figure 133 – Isolated and installed 4-bladed propeller spectra for J = 0.45

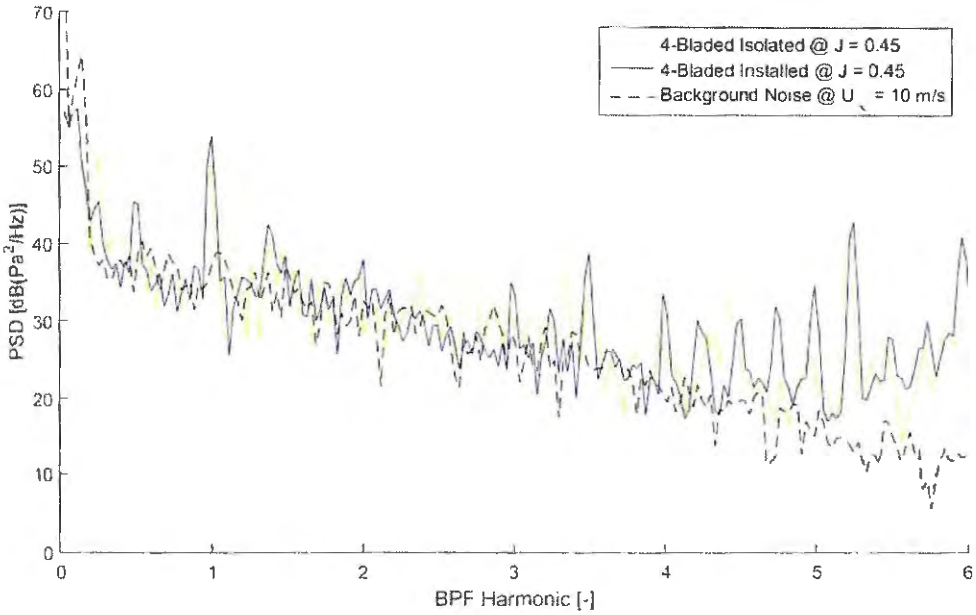

Source – Author

Table 13 – PSD increase for the 4-bladed installed propeller BPF at different rotational speeds

	1BPF	2BPF	3BPF	4BPF	5BPF
ΔPSD (J = 0.32) [dB]	0.1	10.2	-5.6	7.1	12.2
ΔPSD (J = 0.45) [dB]	4.4	1.8	3.0	5.3	8.9

Source – Author

5.3.3 Angle of Attack Analysis

The angle of attack analysis was carried out similar as for the isolated configuration. However, when the propeller was set in the pusher configuration, the rotation direction had to be reversed. Therefore, the convention for the positive angle of attack also had to be reversed, based on what was defined in Figure 80. The same phenomena that happened for the isolated case, of variations in the blade angle of attack, will also occur. The spectra shown in Figure 134 contains the noise levels for the installed configuration at ± 15° of angle of attack for a J = 0.30 condition.

Figure 134 – 4-bladed installed propeller spectra for $\alpha = \pm$ 15° at J = 0.30

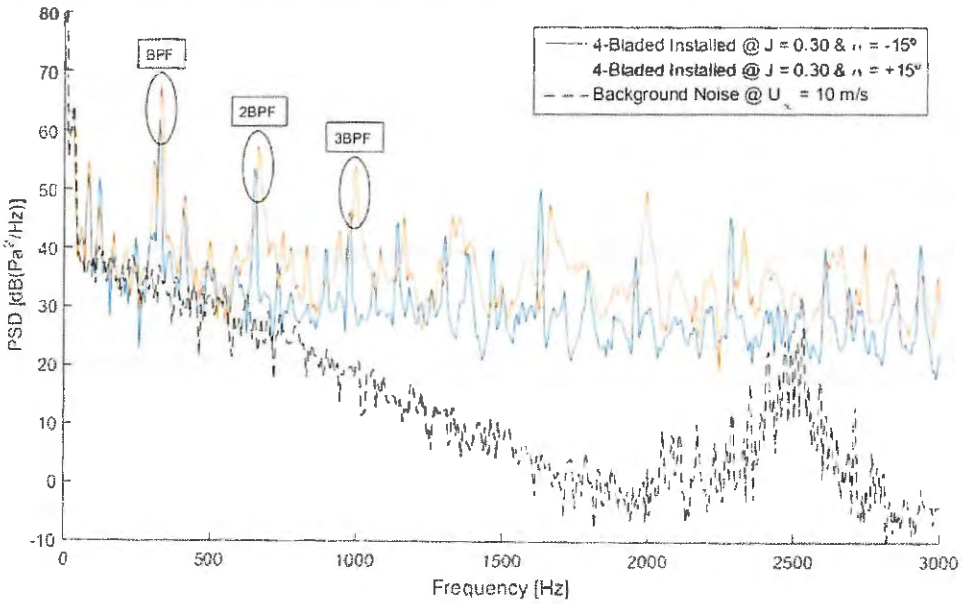

Source – Author

Once again, the propeller at the positive angle of attack displayed higher noise levels than the one with negative angle of attack. However, for the most negative angle of attack (-15°), which gave the smallest noise levels at the BPF for the isolated case, the pylon will also be at 15° of angle of attack. Since it was built based on a symmetrical airfoil, its wake intensity should be the same for a given angle, whether it is positive or negative. This will results in increased noise levels for the negative angles of attack. This behavior should also be more noticeable at the higher BPF harmonics, where the difference between the installed and isolated noise levels is higher. This is shown in Figure 135, for a J = 0.30 condition.

Figure 135 – PSD levels of the 4-bladed installed propeller for different angles of attack at J = 0.30

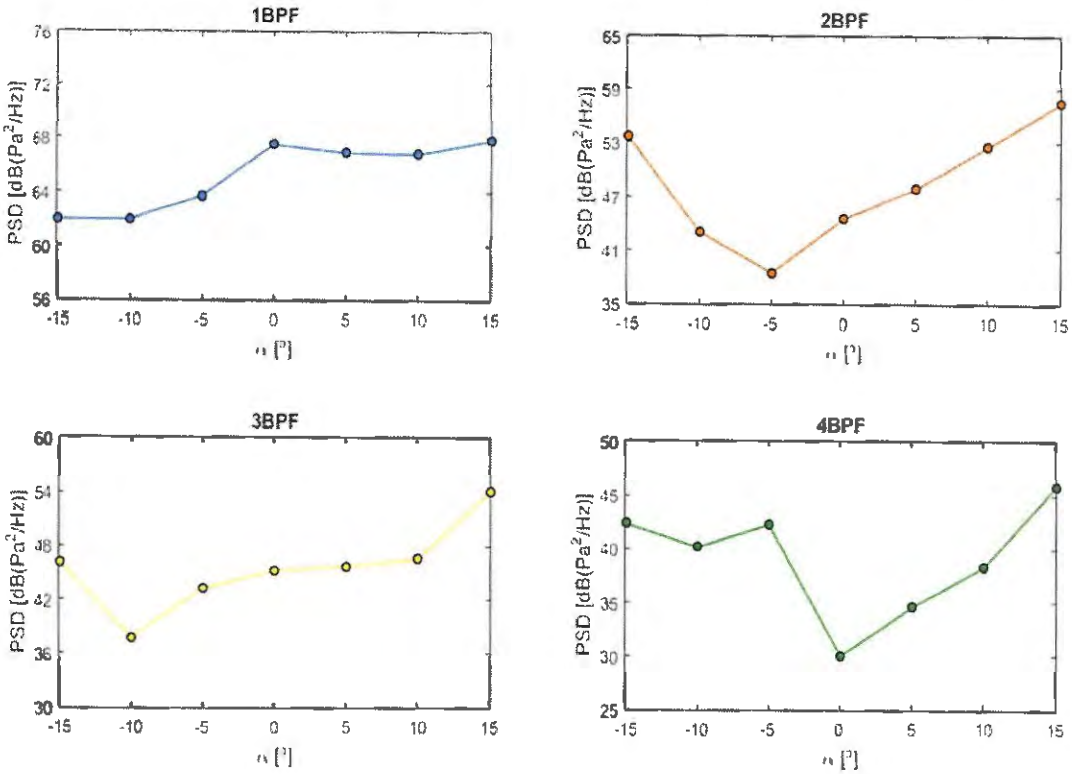

Source – Author

As shown in Figure 135, for the blade passage frequency, there is not a significant difference in noise levels for different angles of attack. This occurs because the steady loading noise component is dominant for this frequency. For the higher harmonics, the unsteady loading will be the major noise source. This is especially visible for the 2nd and 4th harmonics, where the noise levels for the negative angles of attack are similar to the positive ones, indicating that the effect of the pylon wake overcomes the effect of reduction in the effective propeller rotation, caused by the change in angle of attack.

5.3.4 Directivity Analysis

The directivity analysis for the installed propeller was conducted at the same five angular positions in respect to the center of the microphone array, as was done for the isolated case. The convention for the θ angle was the same as defined in Section 3.3. The spectra in display the noise levels for three different directivity angles at a condition of J = 0.30, with the propeller at maximum rotation speed (~5000 RPM). The power spectral density at the first four harmonics of the BPF, for different θ angles, are plotted for the 4- and 3-blade propellers in and, respectively.

Figure 136 – 4-bladed installed propeller spectra for θ = 70°/90°/110° at J = 0.30

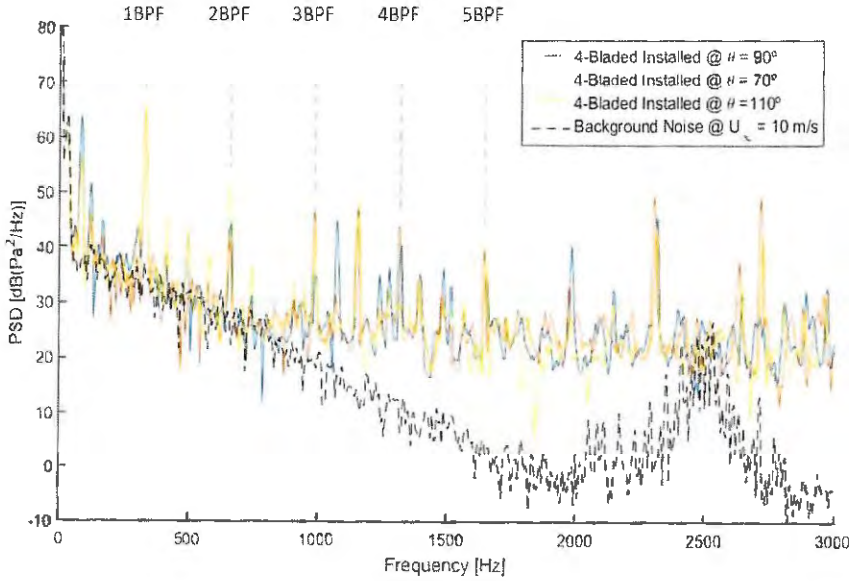

Source – Author

Figure 137 – Directivity curves for the installed 4-bladed propeller at J = 0.30

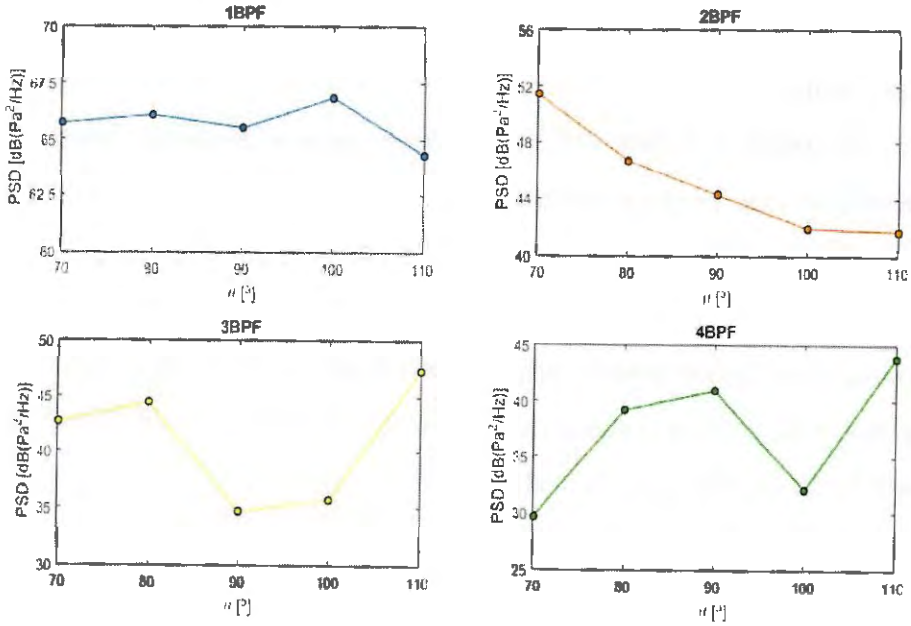

Source – Author

Figure 138 – Directivity curves for the installed 3-bladed propeller at J = 0.50

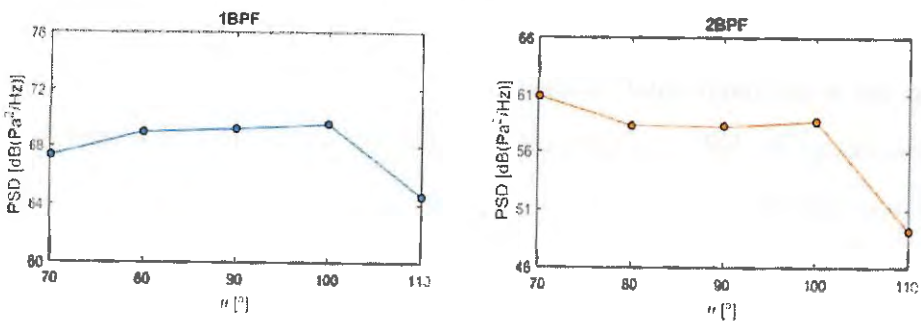

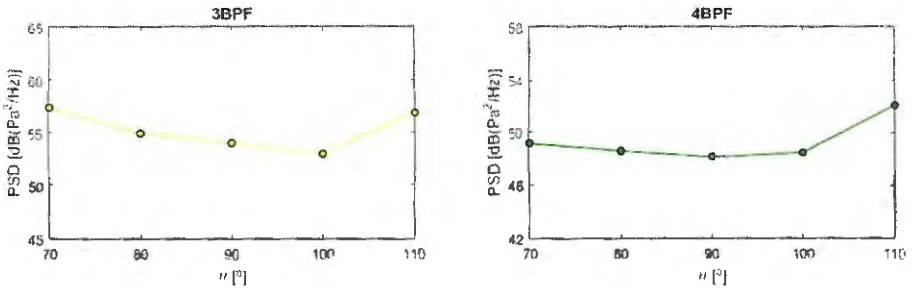

Source – Author

For the 1st harmonic of the BPF, the curve tends to remain flat for practically all directivity angles, which is in accordance with the results from the literature. As was described in Section 2.2.2, the largest installation noise penalties tend to occur towards the propeller axis. For the 2nd harmonic, there is a trend for increased noise in the upstream direction of the propeller plane. For the 3rd one, there is possibly a minimum at the propeller plane, while the noise increases towards the axis. Finally, for the 4th harmonic, the noise tends to go the opposite way as the 2nd and increase in the downstream direction of the propeller plane.

5.3.5 Tripped Pylon Analysis

Similar as was performed in the aerodynamics tests, aeroacoustic measurements were conducted for the pylon equipped with a zigzag transition trip. The spectra for the tripped and untripped pylon configurations are shown in Figure 139.

Figure 139 – Noise spectra for tripped and untripped installed 4-bladed

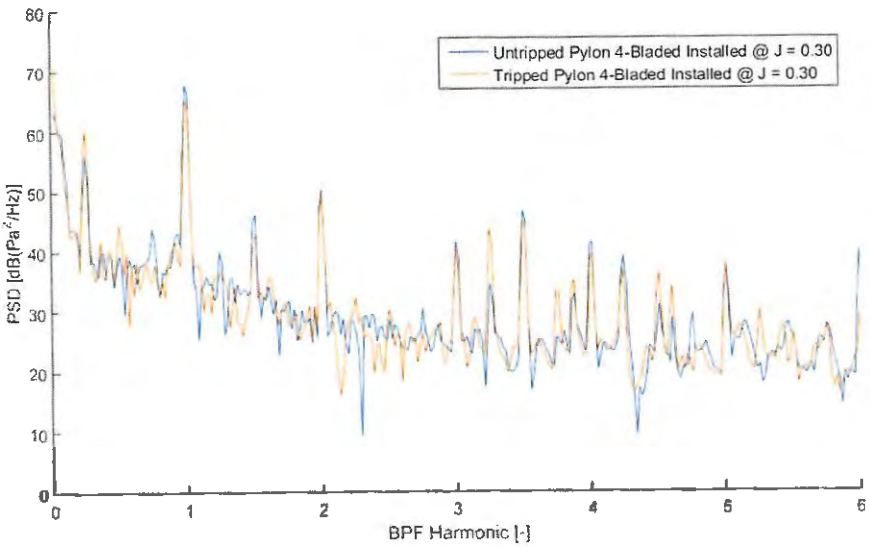

Source – Author

The wake profiles shown in Section 4.2.2 demonstrated an increased velocity deficit for the tripped pylon configuration. This effect should translate in increased noise levels, since the

unsteady loading component for the tripped case is likely to be higher. However, no significant changes were verified in the acoustic measurements. These results indicate that the trip effect falls inside the variability of the experiment (Appendix C2). For the BPF there was a slight noise decrease for the tripped configuration. This could be related to cancellation of sound fields from the steady and unsteady loading, which also happened in previous works, such as Sinnige (2013) for specific advance ratio conditions.

5.4 BLOWN CONFIGURATION

In this section, the results for the aeroacoustic tests of the blown configuration will be described. It is expected that the installation effects will be reduced, with consequent decrease in noise levels, especially at the BPF and harmonic tones. Given the assembly of the blowing system in the model and the components for the air supply system, it was not possible to conduct angle of attack or directivity analyses for the blown configuration. However, the noise spectra and source localization contours will be compared between the three model configurations, along with an advance ratio analysis.

5.4.1 Blown Propeller Spectra

The spectra for the 3- and 4-bladed propellers will be analyzed to assess the effect of the tangential blowing system on the aeroacoustic behavior of a pylon-pusher propeller configuration. By comparing the power spectral density between the blown, installed and isolated cases, it is possible to quantify the effect noise levels reductions due to the blowing system. The best expected result is that the noise levels return to those of the isolated configuration, and thus completely eliminating the installation effects. However, since it was not possible to control the blowing mass-flow, it is expected that the blowing will provide optimum results for a specific free stream speed, while for the other ones, the noise levels from the blown configuration should lie in between the installed and isolated configurations.

The spectra for the blown 3- and 4-bladed propellers shown in Figure 140 seems to display a lower tonal content then the installed configuration. The BPF tones still display high noise levels for the blown configuration, which was expected, since the added noise, generated from the unsteady loading, was not substantial at this frequency. The higher harmonics, however, which were more affected by the effects of the pylon wake, seem to be reduced, suggesting that the blowing will have a more significant effect for these frequencies. Another visible change for the blown spectra is the apparently high broadband noise over 2 kHz. This

added noise is related to the blowing outflow in the small holes on the cylinder, as will be shown in the next section.

Figure 140 – Noise spectra for blown 3- and 4-bladed propellers for U_∞ = 16 m/s

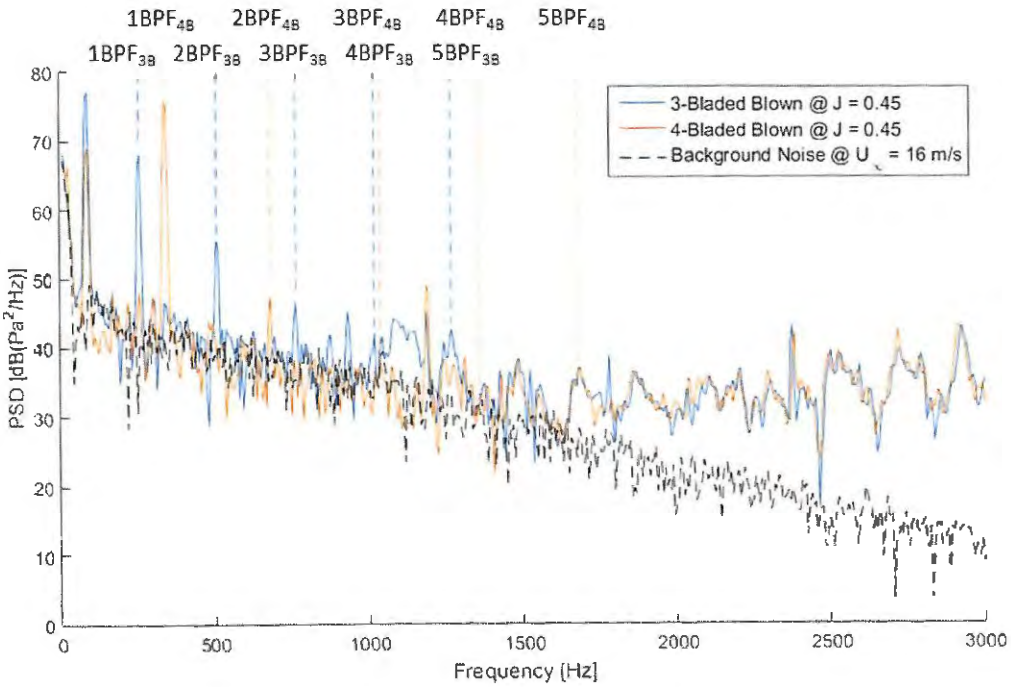

Source – Author

The charts in Figure 141 contain the spectra for the three tested configurations (isolated, installed and blown), with the 3- and 4-bladed propellers, respectively.

Figure 141 – Comparison between the noise levels of the isolated, installed and blown 3-bladed propeller for J = 0.45

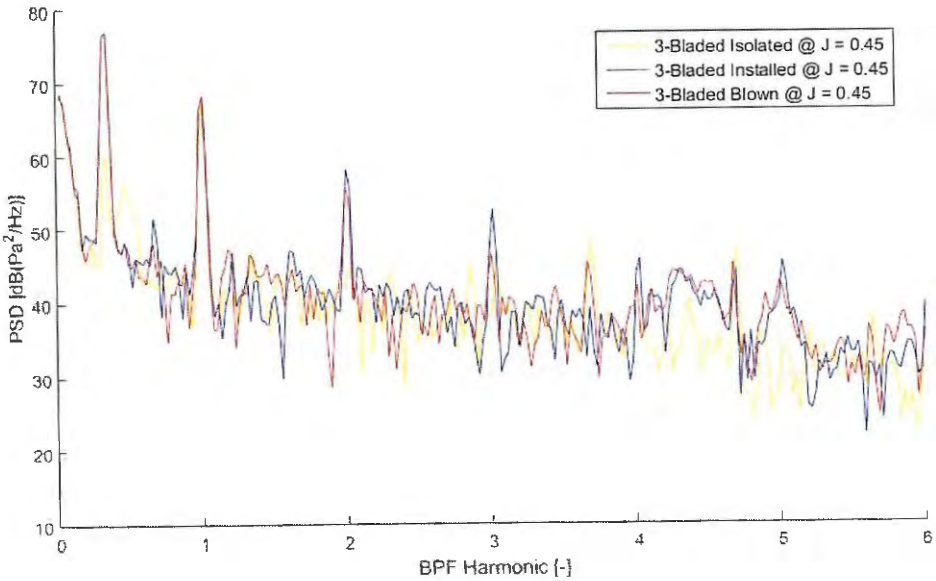

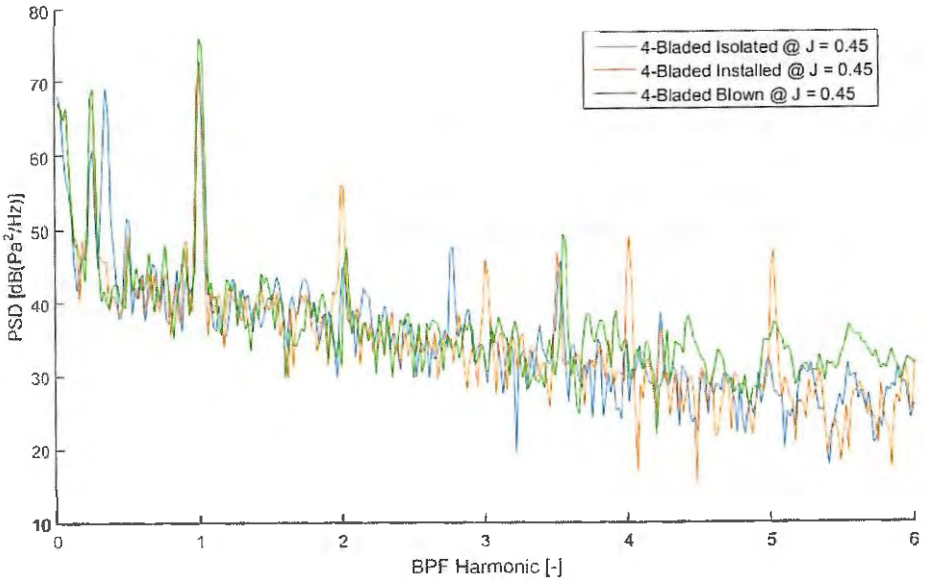

Source – Author

For these spectra, special attention is given to the tones at the first 5 harmonics of the BPF. Table 14 contains the difference between the installed and blown PSD levels, to assess quantitatively the effect of the pylon blowing. The difference in noise levels between the blown and isolated configurations is also plotted, in order to verify the difference between the actual and ideal noise levels with blowing.

Table 14 – Difference in noise levels between installed and blown; and blown and isolated configurations at J = 0.45

		1BPF	2BPF	3BPF	4BPF	5BPF
3-Bladed	**$\Delta PSD_{INST-BLWN}$ [dB]**	0.1	2.6	6.1	3.6	2.7
	$\Delta PSD_{BLWN-ISOL}$ [dB]	0.7	11.3	2.3	4.8	8.6
4-Bladed	**$\Delta PSD_{INST-BLWN}$ [dB]**	-3.8	8.5	9.0	15.4	9.7
	$\Delta PSD_{BLWN-ISOL}$ [dB]	3.2	2.7	0.7	-0.5	10

Source – Author

The aeroacoustic measurements for the blown configuration indicate noise reductions for all the verified tones, except for the BPF for the 4-bladed propeller. For the 3-bladed propeller, the most significant reduction occurred at the 3rd harmonic, with approximately 6 dB. The other frequencies had much smaller noise reductions, around 3 dB. For the 4-bladed propeller, the noise increase at the BPF is likely due to the mitigation of the installation effects, which in turn reduces the cancellation between the noise emissions from steady and unsteady loading, which was described in the previous section. This increased noise at the BPF was also

obtained by Sinnige (2013) for certain advance ratio conditions. For the 2nd harmonic, reductions of 8.5 dB were obtained for the blown configuration. For the higher harmonics, the results were even more positive, with reductions of 9 dB and 15.4 dB at the 3rd and 4th harmonics, respectively, which were completely eliminated. Finally, at the 5th harmonic, the tone was not eliminated, due to increased broadband noise from the blowing system, which will be described in the next section. Nonetheless, reductions of almost 10 dB were obtained. The beamforming maps of both propellers are shown in Figure 142 and Figure 143.

Figure 142 – Beamforming maps of the 3-bladed blown propeller for five BPF harmonics at J = 0.45

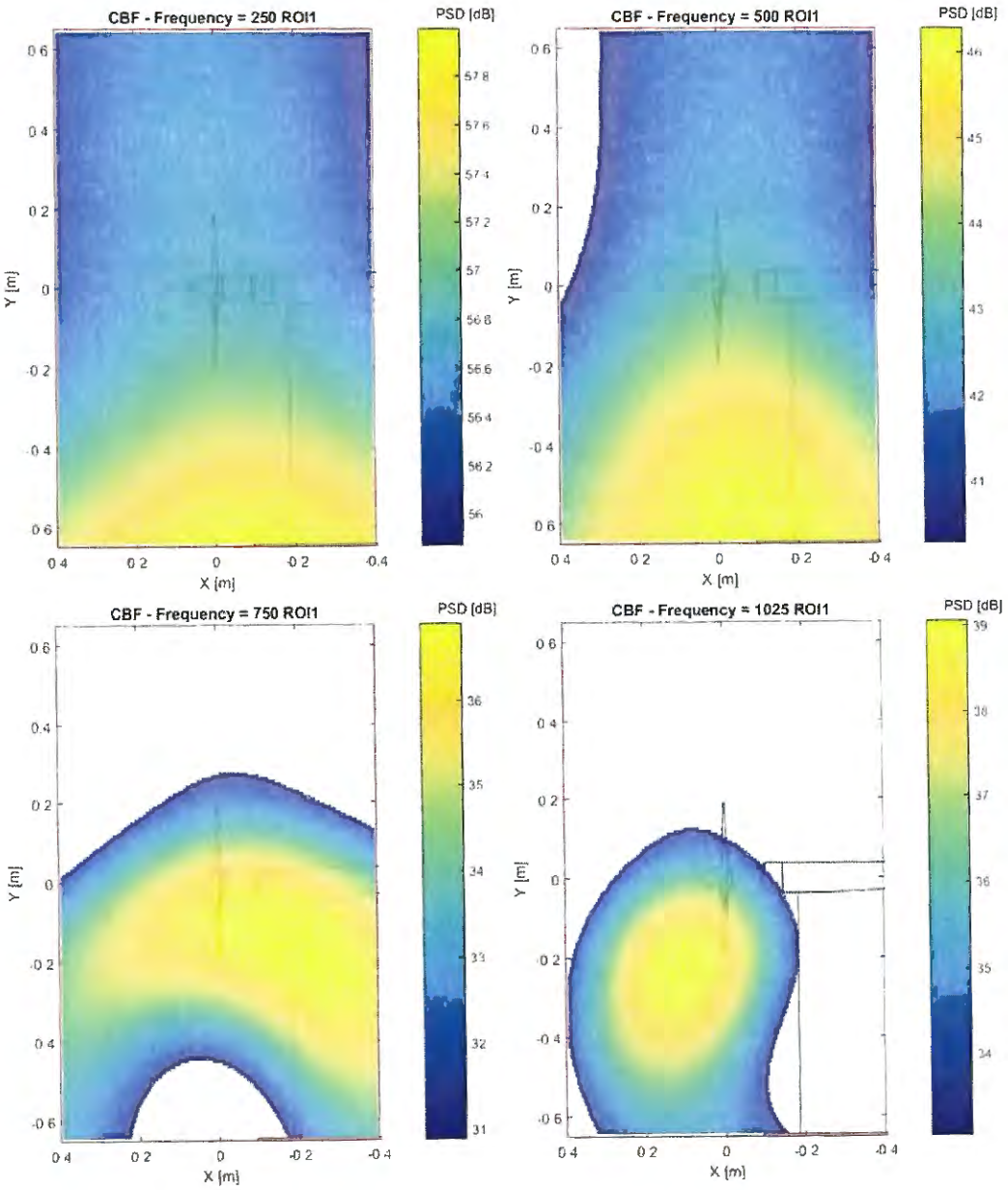

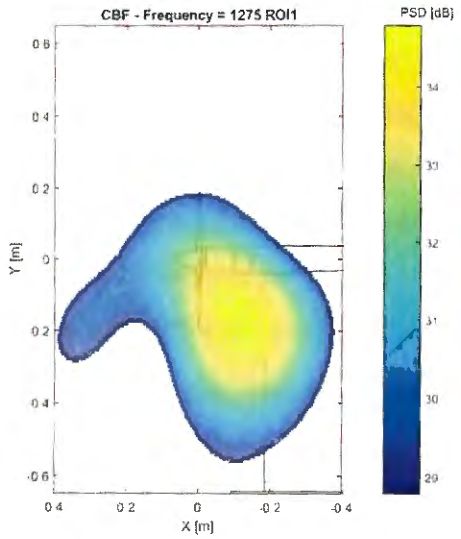

Source – Author

Figure 143 – Beamforming maps of the 3-bladed blown propeller for five BPF harmonics at J = 0.45

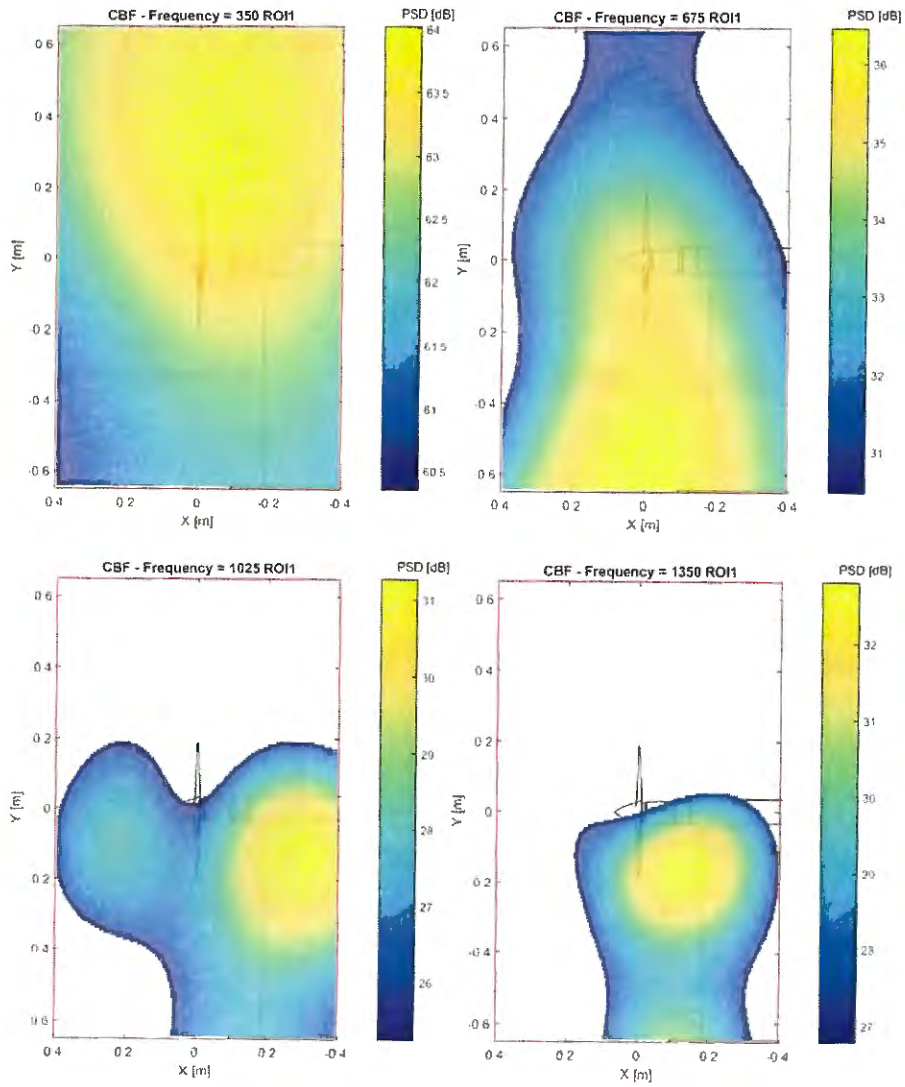

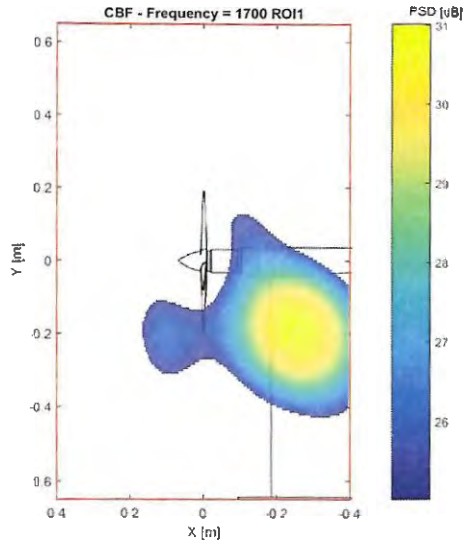

Source – Author

For the 3-bladed propeller, the 1st and 2nd BPF harmonics position the noise sources far from the blades, indicating the steady loading is dominant. For the higher harmonics, the sources are positioned in approximately the same places, as the installed configuration, but with a much smaller intensity, indicating the effect of the blowing. For the 4-bladed propeller, at the BPF, the source tended to move towards the blades, indicating an increase in the unsteady loading noise, which is likely to be no longer cancelling with the steady component. For the 2nd harmonic, the source is still positioned far from the blades, but with a smaller intensity for the blown configuration. For the following higher harmonics, with the largest noise reduction and elimination of the tones, the beamforming placed the dominant noise source at the blowing slot, indicating that the broadband noise generated by the system is dominant over the tones.

5.4.2 Blowing Noise Levels Analysis

From the blown configuration spectra shown in the previous sections, it was possible to verify an increased component of broadband noise, especially at higher frequencies. In order to verify if this noise was coming from the blowing system, aeroacoustic measurements were conducted for a prop-off case and the blowing system operating. The spectral results comparing blowing on and blowing off configurations are shown in Figure 144, and the beamforming maps in Figure 145.

Figure 144 – Beamforming noise spectra with and without blowing in prop-off configuration for U_∞ = 16 m/s

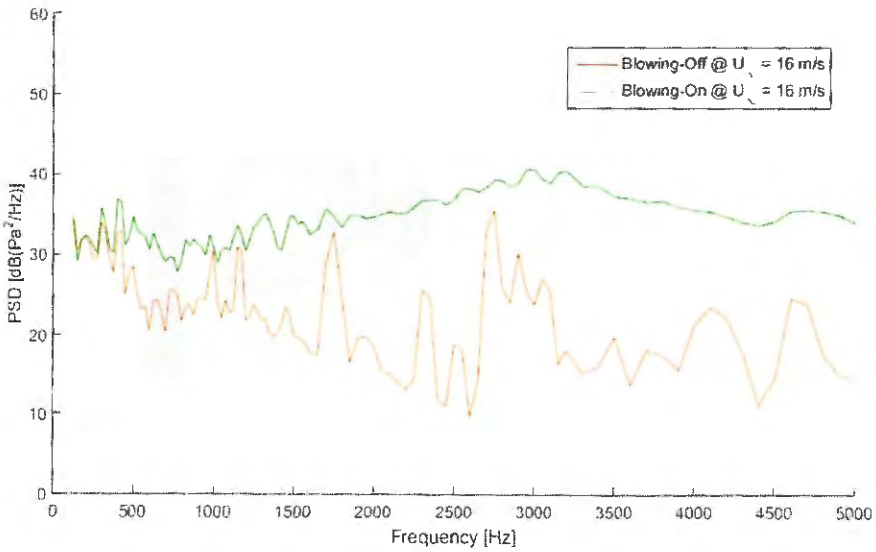

Source – Author

Figure 145 – Beamforming maps for blowing system in prop-off configuration

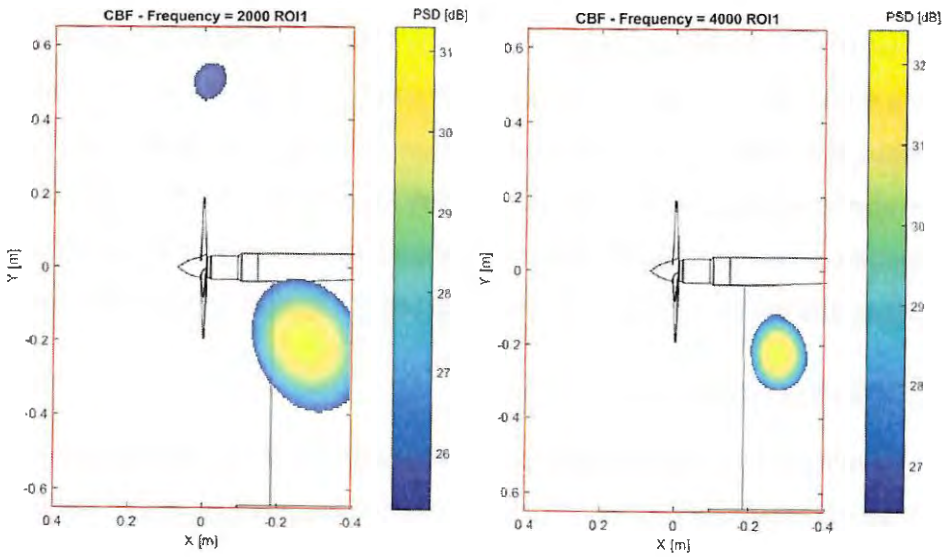

Source – Author

The beamforming spectra shown in Figure 144 show that there is a significant increase in broadband noise, when the blowing system is operating. This noise source occurs when the air leaves the small holes in the cylinder, which can also be confirmed with the source localization contours shown for two different frequencies in Figure 145. When the propeller own broadband noise is put into the chart, the difference for the blown configuration is much smaller, as shown in Figure 146.

Figure 146 – Beamforming noise spectra for 4-bladed propeller blown and installed configurations at J = 0.45

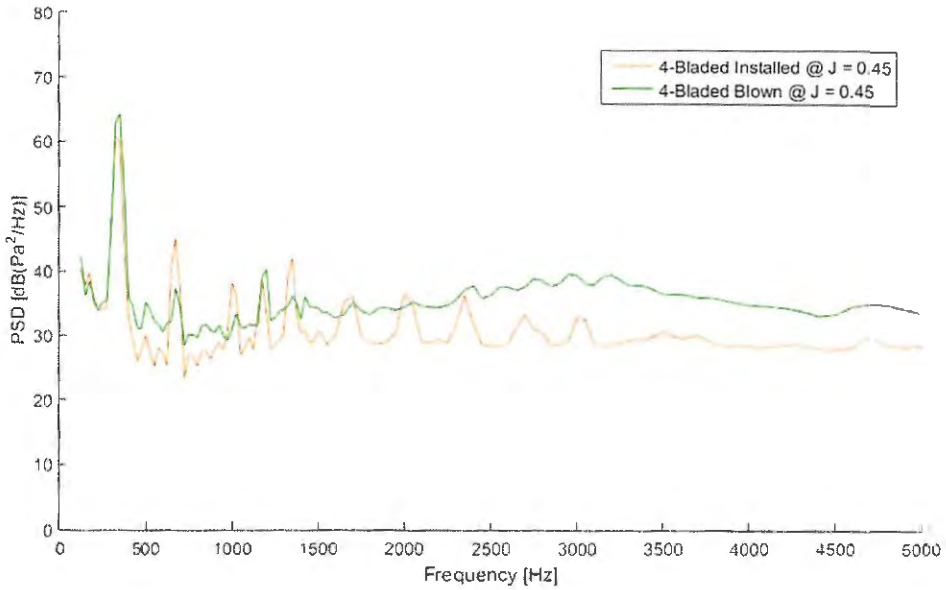

Source – Author

Moreover, since the source in the blowing system has a broadband characteristic, it should not be as problematic as the tones, in terms of annoyance. Therefore, despite this increase in broadband noise for higher frequencies, significant reduction in the tones was obtained with the blowing system, which still validates its use. This increase in broadband noise for higher frequencies also occurred for the tests conducted by Sinnige (2013), and given the similarities with the results obtained in this work, it is likely to be an intrinsic characteristic of this type of blowing configuration and should be addressed, if an optimization of the system would be carried out.

5.4.3 Advance Ratio Analysis

The advance ratio analysis for the blown configuration will allow for verifications on the flow speed, wherein the blowing system provides the optimum results in terms noise reduction. The difference in power spectral density between the blown and installed configurations for different advance ratios is shown in Figure 147 and Figure 148, for the 4- and 3-bladed propellers, respectively. For these curves, the rotational speed was kept at approximately 5000 RPM, and the advance ratio was controlled through the free stream speed.

Figure 147 – Difference in noise levels between installed and blown 4-bladed for different advance ratios

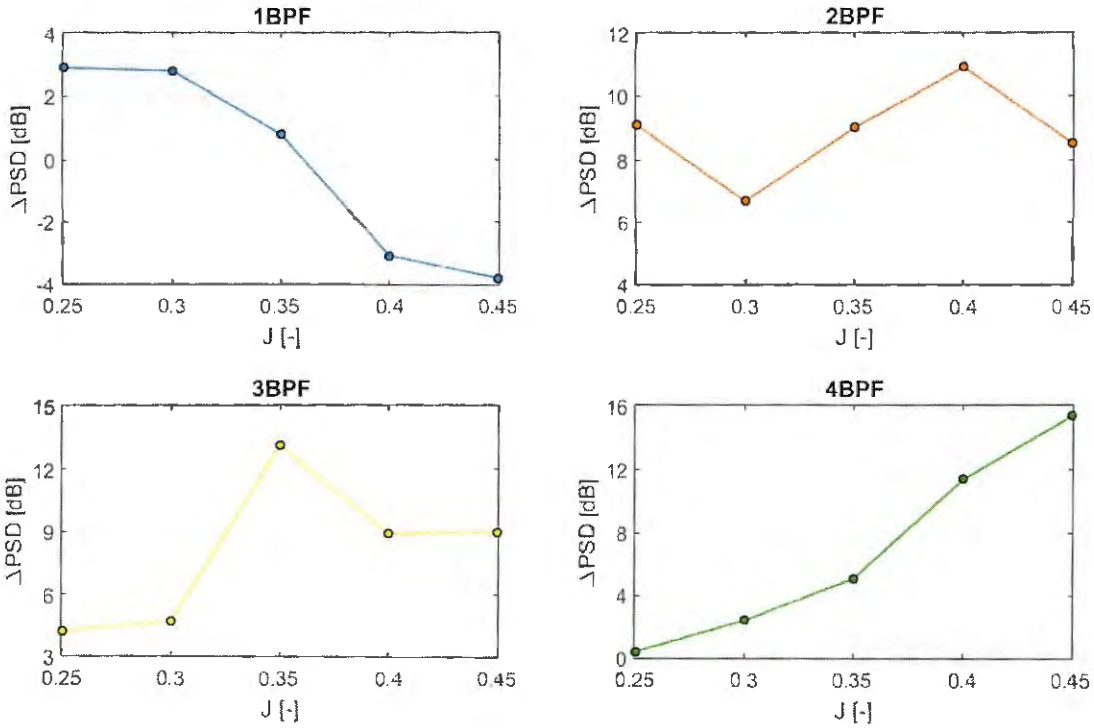

Source – Author

Figure 148 – Difference in noise levels between installed and blown 3-bladed for different advance ratios

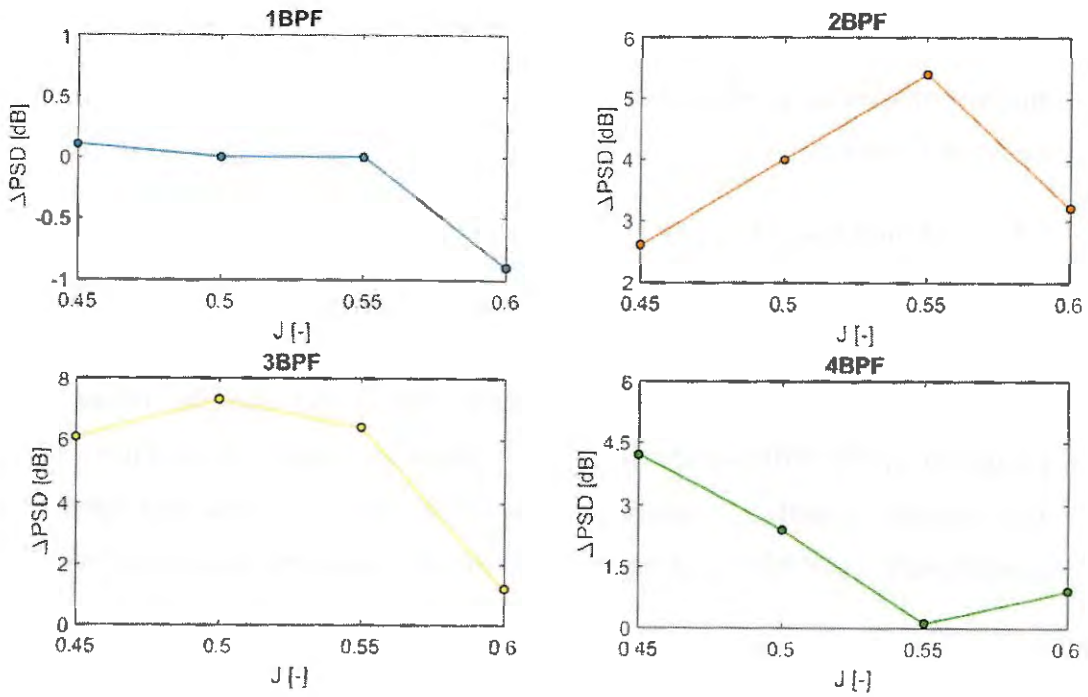

Source – Author

For the 4-bladed propeller, the results indicate small variations in the BPF with the application of blowing, with even increased noise for the higher advance ratios. Based on the results at the previous section, the noise generation for the BPF is dominated by the steady loading component, given the small difference between installed and isolated noise levels for this advance ratio condition. Therefore, it was not expected that the blowing would provide large noise reductions at this frequency. For the higher harmonics, however, significant reductions in the noise levels were obtained. For the 2nd harmonic, reductions of 11 dB occurred for J = 0.40, while for the 3rd and 4th harmonics, it reached approximately 13 dB at J = 0.35 and 15 dB at J = 0.45, respectively.

For the 3-bladed propeller, noise reductions for the blowing configuration were still obtained, but to a smaller extent, reaching close to 7 dB for the higher harmonics. These results indicate that the blowing system is working more efficiently for lower free stream speeds and, despite the isolated configurations noise levels were not attained for all of the tested conditions, significant reductions were obtained, especially at the higher harmonics, which are most affected by the installation effects.

The second approach of advance ratio analysis was also conducted for the blown configuration. The noise levels for different advance ratios (by changing the propeller rotational speed) are shown in Figure 149 and Figure 150, at free stream speeds of 10 m/s and 14 m/s, respectively.

Figure 149 – Difference in noise levels between installed and blown 4-bladed for different rotational speeds at $U_\infty = 10$ m/s

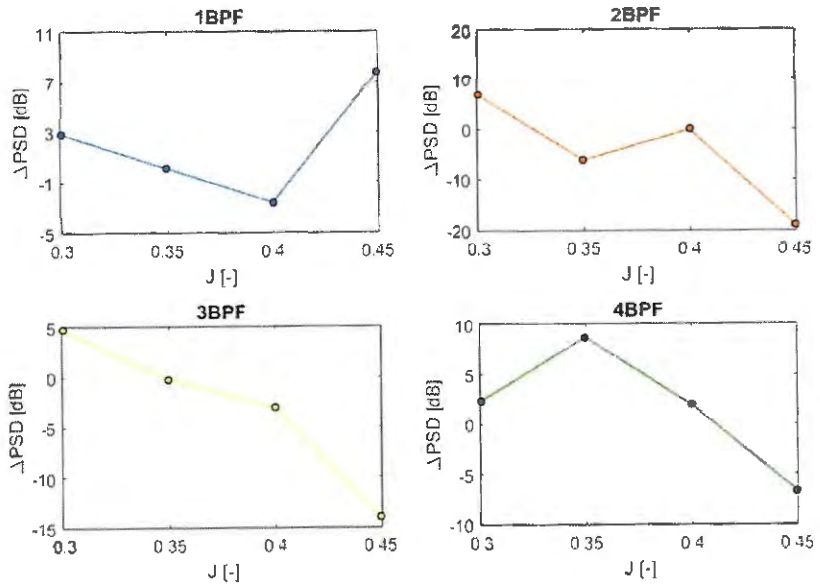

Source – Author

Figure 150 – Difference in noise levels between installed and blown 3-bladed for different rotational speeds at U_∞ = 14 m/s

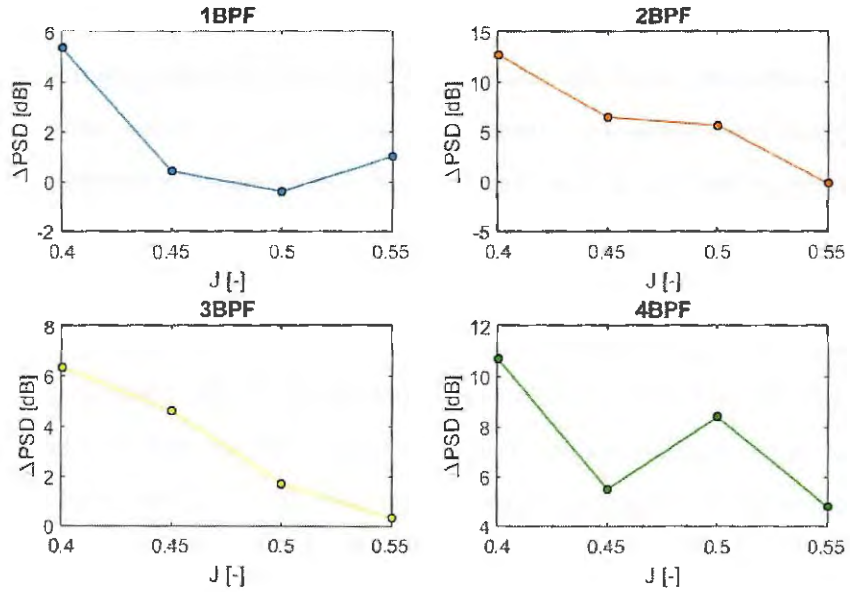

Source – Author

The results indicate that for increasing advance ratio (decreasing propeller rotational speed), the noise levels of the blown configuration tend to increase, up to the point where they are even higher than the installed case, which happened for the measurements at 10 m/s. At this free stream speed, only for J = 0.30, the blown configuration produced noise reductions. For J = 0.45, the noise increase reached 20 dB for the 2nd harmonic, and 15 dB for the 3rd one. For a higher free stream speed (14 m/s), the same trend was observed, but, for the highest tested advance ratio (J = 0.55), the difference between installed and blown noise levels was still positive. Therefore, the blowing does not work properly and it is worse for lower rotational speeds. One possible explanation is that for the lowest propeller rotation, the region where the blowing is overshooting is resulting in unsteady loadings and thus, generating noise. This is likely, since for the higher free stream speeds, the noise reductions were higher for all the harmonics, at all advance ratios.

6 CONCLUDING REMARKS

6 CONCLUDING REMARKS

6.1 CONCLUSIONS

The section contains the conclusions about the development of a blowing system for a propeller in pusher configuration, mounted with an upstream pylon. These conclusions are based on comparative analyses of aerodynamic and aeroacoustic measurements conducted in a wind tunnel. Also in this section, the objectives defined in Section 1.6 will be assessed, whether they were completely or partially fulfilled after the completion of this work.

The literature review on the topic allowed for a significant amount of information on propeller noise characteristics, installation effects, as well as the application of pylon blowing. The experiments performed in the past guided this work in terms of wind tunnel testing of the aerodynamics and aeroacoustics of propellers, in order to assure the best possible outcome. In addition, the results obtained in this work have been shown to agree consistently with the literature, demonstrating the validity of the experiments, as well as the conclusions drawn from them.

For the isolated configuration, the aerodynamic measurements consisted in obtaining the propellers thrust curve with advance ratio. These results were then used to define the conditions for the following tests, in terms of propeller rotational speed and free stream speed. The aeroacoustic measurements were able to capture only the BPF in the spectra, while the higher harmonics were buried in the background noise. Therefore, all the analyses for this configuration were conducted focusing on the BPF results. The beamforming maps showed results, which agree with the Mach radius concept, described in Section 3.5.2.

The advance ratio analysis, performed with two approaches, displayed unexpected results for the advance ratio variation with the flow speed. However, when the propeller rotational speed was changed, the noise levels showed to increase with also increasing propeller thrust. The angle of attack was defined as positive for the conditions where the propeller rotational speed was increased by the flow angle. The results showed that the propeller noise increases with also increasing angle of attack, which agrees well with the literature. The directivity analysis for the 3-bladed propeller showed the highest noise levels at the propeller plane. The difference in noise levels, however, is small but still higher than the variability of the experiment, given the repeatability analysis from Appendix C.

For the installed configuration, the surface pressure measurements on the pylon showed a region of increased suction near the trailing edge, caused by velocities induced by the

propeller. This effect is more pronounced for lower advance ratios, where the propeller is generating more thrust. This lower static pressure at the trailing edge tends to reduce the adverse pressure gradient, decreasing the boundary layer thickness and consequently the wake velocity deficit. This was confirmed through the flowfield mapping, conducted halfway between the pylon trailing edge and the propeller, using a hot-wire. The time history from this instrument also allowed the plotting of spectra inside and outside of the wake, which allowed for the verification of the BPF and higher harmonics. The BPF peak was also visible inside the wake, even with increased broadband component from the flow turbulence.

The aeroacoustic measurements displayed a large increase in tonal content for the installed configuration. Except for the BPF, where no significant changes were visible, the higher harmonics increased over 9 dB and some of them showed even 20 dB of added noise. These frequencies are strongly affected by the unsteady loading due to the impingement of the pylon wake on the propeller. The beamforming maps for those frequencies place the noise sources near the blades, indicating that the dominant noise generation mechanism is non-rotational, namely the unsteady loading.

The advance ratio analysis displayed similar results as the isolated configuration, however, for lower rotational speeds (higher J), the noise penalty for the BPF tended to increase, while for the higher harmonics, it seemed to slightly decrease. The angle of attack analysis displayed the expected trend for the BPF, similar as the isolated results. For some of the higher harmonics, the noise levels for negative angles of attack tend to be similar to the positive ones, most likely to the symmetrical behavior of the wake with this parameter. The directivity curves for the BPF displayed a flat behavior, consistent with the literature. The second harmonic tended to increase moving upstream of the propeller, while the third and fourth ones tended to increase downstream of the propeller. For the tripped pylon configuration, no significant changes with the baseline case were verified in the acoustic measurements.

The development of the blowing system was based on a configuration previously used for filling the wake of a cylinder, wherein a smaller cylinder, with holes on the surface, was positioned at the trailing edge of the main one. For this work, however, it was defined that the blowing slot would be positioned at the pylon upper and lower surfaces at 0.7c, to ensure better flow mixing. Therefore, the final concept consisted in the air exiting the cylinder through several holes, and passing through internal channels and reaching the pylon surface with sufficient speed. The blowing region in the pylon was manufactured with 3D printing, given the complexity of the geometry and for time and cost savings. The blowing massflow could not

be controlled, and thus the results in terms of noise reduction will not be optimum for all tested flow conditions.

The flowfield measurements for the blown configuration displayed a region of increased velocity (over the local free stream speed) near the propeller hub. This overshooting was caused by the inability of the flow to turn 90° in the holes, while exiting the cylinder. To improve this behavior, small tubes were placed inside the holes, which strongly improved the flow quality. There was still, nonetheless, some overshooting. Despite this slight non-uniformity, some of the stations displayed uniform profiles and the integral velocity deficits for all the measured positions were smaller for the blown configuration, indicating an effective operation of the blowing system. The application of blowing also reduced the turbulence levels at the wake, since the boundary layer thickness at separation was likely much smaller. Unfortunately, the hot-wire used for the measurements malfunctioned during the tests, so some of the measurements performed for the installed configuration could not be repeated for the blown case.

The aeroacoustic measurements for the blown configuration display much smaller tonal content. While the BPF was not largely affected, since the installation effects were not large for this frequency, the higher harmonics displayed significant noise reductions. For some frequencies, the noise levels of the isolated configuration were reached. The advance ratio analysis indicated that the best results with blowing were obtained for the 4-bladed propeller, around J = 0.40 to 0.45, which corresponds to a free stream speed of approximately 16 m/s. This blowing design was also responsible for increased broadband noise at higher frequencies, especially over 1.5 kHz. However, the large reductions in the noise levels for most of the tones are encouraging and indicate that the blowing is in fact effective in reducing the installation effects and is likely a potential solution for practical application in full-scale aircraft. More tests are still necessary though, in order to bring this technology to higher TRLs.

6.2 RECOMMENDATIONS FOR FUTURE WORKS

In this section, some recommendations for future works on pylon blowing and pusher propellers will be stated, based on several issues faced during the course of this work. These recommendations should be taken into account, in order to improve the quality of the analyses and, consequently, the obtained results.

One very significant issue, which restrained the conditions for the analyses, was the maximum obtainable propeller rotational speed. Higher RPMs would be better, in order to allow

larger free stream speeds to be tested, for a given advance ratio, which would also result in analyses for higher Mach numbers. Moreover, propellers with a higher number of blades, which are closer to an actual open rotor configuration, should also be evaluated. Finally, if it were possible to test counterrotating propellers, the results would turn out to be much more interesting and realistic.

The design of the blowing system could also be improved, in order to optimize the outflow in terms of uniformity in the spanwise direction. A more effective solution for turning the flow 90° while exiting the cylinder, with minimum pressure loss, should be investigated. If it were possible to make the outflow more uniform, certainly greater noise reductions would be achieved. The blowing mass-flow must also be controlled, so that the best results can be achieved for each tested condition. It is also desirable to eliminate or reduce the broadband noise produced by the blowing system, either by design modifications or by using noise-damping materials.

In terms of instrumentation, a rotational balance should be integrated to the model in order to determine the torque and efficiency curves of the propeller, to make the analysis more complete. A larger number of pressure tappings is also recommended, to provide better understandings of the propeller effect on the flow around the pylon. Pressure tappings in the blowing region should also be introduced. The use of hot-wire for the flow mapping was very effective, with very little disturbances to the flow. Measurements in more planes should also be carried out, in order to verify the flow progression and assess the mixing between the jet and the external flow. This is difficult, however, given the very limited space between the pylon and the propeller.

In terms of aeroacoustic analyses, it is recommended that measurements be conducted for lower background noise levels. For the higher speed tests, large background noise from the wind tunnel limited the analyses of this work, since it was highest for the frequency region of interest. The measurements from the phased array counterbalanced a little this effect, but it is recommended either to reduce the background noise or to use louder propellers to overcome this issue. Tests with a larger number of directivity angles are suggested, to obtain a larger number of results to confirm the trends. Angle of attack and directivity analyses for the blown configuration are also recommended.

BIBLIOGRAPHY

AIRBUS FLIGHT OPERATIONS SUPPORT & LINE ASSISTANCE. **Getting to grips with aircraft noise**. 2003. Available in:<http://dream-air.ru/new/pilotam/AircraftNoise-copy_2-.pdf>. Accessed: 24 Oct. 2016.

BARLOW, J. B.; RAE JR., W. H.; POPE, A. **Low-speed wind tunnel testing**. 3rd ed. Hoboken: Wiley-Interscience, 1999.

BERTON, J. J. **Empennage noise shielding benefits for an open rotor transport**. Cleveland: NASA, 2012. (NASA/TM—2012-217218).

BLAKE, W. K. **Mechanics of flow-induced sound and vibration**. Orlando: Academic Press, 1986. v.2: Complex flow-structure interactions.

BLOCK, P. J. W. **Experimental study of the effects of installation on single- and counter-rotation propeller noise**. Hampton: NASA, 1986. (NASA TP-2541).

BLOCK, P. J. W.; GENTRY JR., G. L. **Directivity and trends of noise generated by a propeller in a wake**. Hampton: NASA, 1986. (NASA TP-2609).

BLYTHE, A. A.; SMITH, P. Prospects and problems of advanced open rotors for commercial aircraft. In: JOINT PROPULSION CONFERENCE, 21., Monterey, 1985. **Proceedings...** Reston: AIAA/SAE/ASME/ASEE, 1985.

BRUUN, H. H. **Hot-wire anemometry:** principles and signal analysis. Oxford: Oxford Science, 1995.

CATALANO, F. M. **The Effect of a high thrust pusher propeller on the flow over a straight wing**. 1993. Thesis (PhD) - Cranfield Institute of Technology, Cranfield University, Cranfield, 1993.

CRIGHTON, D. G.; PARRY, A. B. Higher approximations in the asymptotic theory of propeller noise. **AIAA Journal**, v.30, n.12, p.3023-3039, Jan. 1992.

CROCE, J. A. G. **eDeterminação do efeito da injeção de massa na esteira de um cilindro rotativo**. 1998. 104p. Dissertação (Mestrado) - Escola de Engenharia de São Carlos, Universidade de São Paulo, São Carlos, 1998.

DANTEC DYNAMICS. **StreamLine(R)/StreamWare(R) installation & user's guide**. Skovlunde, 2000. v.3.

DANTEC DYNAMICS™. **StreamLine pro anemometer system:** CTA system for turbulence investigations. Available in: <http://www.dantecdynamics.com/docs/products-and-services/fluid-mechanics/cta/PI119_StreamLine_Pro_Anemometer_System.pdf>. Accessed: 10 Feb. 2017.

DEPITRE, A. Session2: EPNdB metric - why is it used in aircraft noise certification? How is it calculated? In: NOISE CERTIFICATION WORKSHOP, 2006, Bangkok.

DICKSON, N. ICAO noise standards. In: ICAO SYMPOSIUM ON AVIATION AND CLIMATE CHANGE, "DESTINATION GREEN", 2013, Montréal. **Proceedings...** [S.l.:s.n.], 2013.

ELLIOTT, D. M. **Initial investigation of the acoustics of a counter-rotating open rotor model with historical baseline blades in a low-speed wind tunnel**. Cleveland: NASA, 2012. (NASA/TM—2012-217258).

ENVIA, E. **NASA** open rotor noise research. In: CEAS-ASC WORKSHOP, 14./SCIENTIFIC WORKSHOP OF X-3-NOISE AEROACOUSTICS OF HIGH-SPEED AIRCREAFT PROPELLERS AND OPEN ROTORS, 5., 2010, Warsaw. **Proceedings...** Warsaw: Institute of Aviation, 2010.

ENVIA, E. Contra-rotating open rotor tone noise prediction. In: AIAA/CAES AEROACOUSTICS CONFERENCE, 20., 2014, Atlanta. **Proceedings...** Belgium: Council of European Aerospace Societies; Reston: AIAA, 2014.

FFOWCS-WILLIAMS, J. E.; HAWKINGS, D. L. Theory relating to the noise of rotating machinery. **Journal of Sound and Vibration**, London, v.10, n.1, p.10-21, 1969.

GAD-EL-HAK, M. **Flow control:** passive, active and reactive flow management. Cambridge: Cambridge University Press, 2000.

GENTRY JR., G. L.; BOOTH JR., E. R.; TAKALLU, M. A. **Effect of pylon wake with and without pylon blowing on propeller thrust**. Hampton: NASA, 1990. (NASA TM-4162).

G.R.A.S. SOUND & VIBRATION. G.R.A.S. **46BD 1/4" CCP pressure standard microphone set**: specifications. Available in:<http://www.gras.dk/46bd.html>. Accessed: 11 Feb. 2017.

GUYNN, M. D. et al. Initial assessment of open rotor propulsion applied to an advanced single-aisle aircraft. In: AIAA AVIATION TECHNOLOGY, INTEGRATION, AND OPERATIONS (ATIO) CONFERENCE, 11., 2011, Virginia Beach. **Proceedings...** Reston: AIAA, 2011.

HANSON, D. B. Noise of counter-rotation propellers. **Journal of Aircraft**, Windsor Locks, v.22, n.7, p.609-617, 1985.

HEFNER, J. N.; BUSHNELL, D. M. **Viscous drag reduction in boundary layers**. Hampton: American Institute of Aeronautics and Astronautics, 1990. v.123.

HENDRICKS, E. S. et al. **Updated assessment of an open rotor airplane using an advanced blade design**. Cleveland: NASA, 2013. (NASA/TM—2013-218074).

HOFF, G. E. **Experimental performance and acoustic investigation of modern, counterrotating blade concepts**. Cincinnati: GE Aircraft Engines; NASA, 1990. (NASA Contractor Report 185158).

HORNE, W. C.; SODERMAN, P. T. **Flow-field survey of an empennage wake interacting with a pusher propeller**. Moffett Field: NASA, 1988. (NASA TM-101003).

HORVATH, C. Beamforming investigation of dominant counter-rotating open rotor tonal and broadband noise sources. **AIAA Journal**, Budapest, Hungary, v.53, n.6, p.1602-1611, 2015.

HORVATH, C.; ENVIA, E.; PODBOY, G. G. **Limitations of phased array beamforming in open rotor noise source imaging**. Cleveland: NASA, 2013. (NASA TM2013-217902).

HOUGHTON, E. L.; CARPENTER, P. W. **Aerodynamics for engineering students**. 5th ed. Burlington: Butterworth-Heinemann, 2003.

IATA ECONOMIC BRIEFING. **Airline fuel and labour cost share**. [S.l.]: IATA, 2010.

INTERNATIONAL CIVIL AVIATION ORGANIZATION. Available in:<http://www.icao.int/Newsroom/Pages/New-ICAO-Aircraft-CO2-Standard-One-Step-Closer-To-Final-Adoption.aspx>. Accessed: 20 Aug. 2016.

INTERNATIONAL COUNCIL ON CLEAN TRANSPORTATION. Available in:<http://www.theicct.org/sites/default/files/publications/ICCT-ICAO_policy-update_feb2016.pdf>. Accessed: 20 Aug. 2016.

KNOWLES, K. Importance of broadband noise for advanced turboprops. **Journal of Aircraft**, Shrivenham, v.24, n.6, p.386-391, June 1987.

MANN, S. A. E.; STUART, C. A. **Advanced propulsion through the 1990s an airframers view**. In: JOINT PROPULSION CONFERENCE, 21., Monterey, 1985. **Proceedings...** Reston: AIAA/SAE/ASME/ASEE, 1985.

MARTE, J. E.; KURTZ, D. W. **A Review of aerodynamic noise from propellers, rotors and lift fans**. Pasadena: California Institute of Technology; NASA, 1970. (NASA TR 32-7462).

MAUNSELL, M. G. **Desenvolvimento, construção e ensaios de uma balança aerodinâmica**. 1977. Dissertação (Mestrado) - Escola de Engenharia de São Carlos, universidade de São Paulo, São Carlos, 1977.

MCALPINE, A.; KINGAN, M. J. Far-field sound radiation due to an installed open rotor. **International Journal of Aeroacoustics**, Southampton, v.11, n.2, p.213-245, 2012.

METZGER, F. B. **A Review of propeller noise prediction methodology 1919-1994**. Simsbury: NASA, 1995. (NASA Contractor Report 198156).

HOFF, G. E. **Experimental performance and acoustic investigation of modern, counterrotating blade concepts**. Cincinnati: GE Aircraft Engines; NASA, 1990. (NASA Contractor Report 185158).

HORNE, W. C.; SODERMAN, P. T. **Flow-field survey of an empennage wake interacting with a pusher propeller**. Moffett Field: NASA, 1988. (NASA TM-101003).

HORVATH, C. Beamforming investigation of dominant counter-rotating open rotor tonal and broadband noise sources. **AIAA Journal**, Budapest, Hungary, v.53, n.6, p.1602-1611, 2015.

HORVATH, C.; ENVIA, E.; PODBOY, G. G. **Limitations of phased array beamforming in open rotor noise source imaging**. Cleveland: NASA, 2013. (NASA TM2013-217902).

HOUGHTON, E. L.; CARPENTER, P. W. **Aerodynamics for engineering students**. 5thed. Burlington: Butterworth-Heinemann, 2003.

IATA ECONOMIC BRIEFING. **Airline fuel and labour cost share**. [S.l.]: IATA, 2010.

INTERNATIONAL CIVIL AVIATION ORGANIZATION. Available in:<http://www.icao.int/Newsroom/Pages/New-ICAO-Aircraft-CO2-Standard-One-Step-Closer-To-Final-Adoption.aspx>. Accessed: 20 Aug. 2016.

INTERNATIONAL COUNCIL ON CLEAN TRANSPORTATION. Available in:<http://www.theicct.org/sites/default/files/publications/ICCT-ICAO_policy-update_feb2016.pdf>. Accessed: 20 Aug. 2016.

KNOWLES, K. Importance of broadband noise for advanced turboprops. **Journal of Aircraft**, Shrivenham, v.24, n.6, p.386-391, June 1987.

MANN, S. A. E.; STUART, C. A. **Advanced propulsion through the 1990s an airframers view**. In: JOINT PROPULSION CONFERENCE, 21., Monterey, 1985. **Proceedings...** Reston: AIAA/SAE/ASME/ASEE, 1985.

MARTE, J. E.; KURTZ, D. W. **A Review of aerodynamic noise from propellers, rotors and lift fans**. Pasadena: California Institute of Technology; NASA, 1970. (NASA TR 32-7462).

MAUNSELL, M. G. **Desenvolvimento, construção e ensaios de uma balança aerodinâmica**. 1977. Dissertação (Mestrado) - Escola de Engenharia de São Carlos, universidade de São Paulo, São Carlos, 1977.

MCALPINE, A.; KINGAN, M. J. Far-field sound radiation due to an installed open rotor. **International Journal of Aeroacoustics**, Southampton, v.11, n.2, p.213-245, 2012.

METZGER, F. B. **A Review of propeller noise prediction methodology 1919-1994**. Simsbury: NASA, 1995. (NASA Contractor Report 198156).

MONGEAU, L. Noise technology goals: summary of the conclusions of the second CAEP noise technology independent expert panel (IEP2). In: ICAO SYMPOSIUM ON AVIATION AND CLIMATE CHANGE, "DESTINATION GREEN", 2013, Montréal. **Proceedings...** [S.l.:s.n.], 2013.

MUELLER, T. J. **Aeroacoustic measurements**. Berlin: Springer-Verlag, 2002.

NODÉ-LANGLOIS, T. et al. Prediction of contra-rotating open rotor broadband noise in isolated and installed configurations. In: AIAA/CAES AEROACOUSTICS CONFERENCE, 20., 2014, Atlanta. **Proceedings...** Belgium: Council of European Aerospace Societies; Reston: AIAA, 2014.

PAGANI JÚNIOR, C. C. **Mapeamento de fontes aeroacústicas de um eslate em túnel de vento de seção fechada utilizando beam-forming com deconvolução DAMAS**. 2014. 215p. Tese (Doutorado) - Escola de Engenharia de São Carlos, Universidade de São Paulo, São Carlos, 2014.

PAQUET, C. et al. Z08: low-speed aero-acoustic experimental characterization of open rotor installation on aircraft. In: AIAA/CAES AEROACOUSTICS CONFERENCE, 20., 2014, Atlanta. **Proceedings...** Belgium: Council of European Aerospace Societies; Reston: AIAA, 2014.

PARRY, A. B.; KINGAN, M.; TESTER, B. J. Relative importance of open rotor tone and broadband noise sources. In: AIAA/CEAS AEROACOUSTICS CONFERENCE, 17., 2011, Portland. **Proceedings...** Reston: AIAA, 2011.

PRATT & WHITNEY PUREPOWER ENGINE FAMILY SPECS CHART. 2012. Available in:<https://www.pw.utc.com/Content/PurePowerPW1000G_Engine/pdf/B-1-1_PurePowerEngineFamily_SpecsChart.pdf>. Accessed: 28 Aug. 2016.

REVELL, J. D.; TULLIS, R. H. **Fuel conservation merits of advanced turboprop transport aircraft**. Burbank: Lockheed-California, 1977. (NASA-CR-152096).

RICOUARD, J. et al. Installation effects on contra-rotating open rotor noise. In: AIAA/CEAS AEROACOUSTICS CONFERENCE, 16., 2010, Stockholm. **Proceedings...** Reston: AIAA, 2010.

SANTANA, L. D.; CARMO, M.; CATALANO, F. M. The Update of an aerodynamic wind-tunnel for aeroacoustics testing. **Journal of Aerospace Technology and Management**, São José dos Campos, v.6, n.2, p.111-118, 2014.

SCANIVALVE CORPORATION. **Model ZOC33 electronic pressure scanning module data sheet no.G480**. Liberty Lake. Available in:<http://scanivalve.com/media/4265/zoc33_1305.pdf>. Accessed: 10 Feb. 2017.

SCHLICHTING, H. **Boundary-layer theory**. 7thed. New York: McGraw-Hill, 1979.

SHIVASHANKARA, B.; JOHNSON, D.; CUTHBERTSON, R. Installation Effection on Counter Rotation Propeller Noise. In: AEROACOUSTICS CONFERENCE, 13., 1990, Tallahassee. **Proceedings...** Reston: AIAA, 1990.

SINNIGE, T. **The Effects of pylon blowing on pusher propeller performance and noise emissions:** an experimental and numerical study. 2013. 240p. Dissertation (MSc) - Faculty of Aerospace Engineering, Delft University of Technology, Delft, 2013.

STACK, J. et al. **Investigation of the NACA 4-(3)(08)-03 and NACA 4-(3)(08)-045 two-blade propellers at forward mach numbers to 0.725 to determine the effects of compressibility and solidity on performance**. Washington: NACA, 1950. (NACA-TR-999).

STUERMER, A.; YIN, J. Aerodynamic and aeroacoustic installation effects for pusher-configuration cror propulsion systems. In: AIAA APPLIED AERODYNAMICS CONFERENCE, 28., 2010, Chicago. **Proceedings...** Reston: AIAA, 2010.

SUSTAINABLE SKIES. Available in:<http://sustainableskies.org/quiet-may-be-the-new-black/>. Accessed: 19 Sept. 2016.

TRENDS IN THERMAL AND PROPULSIVE EFFICIENCY. Available in:<http://web.mit.edu/16.unified/www/FALL/thermodynamics/notes/node84.html>. Accessed in: 28 Aug. 2016.

VAN ZANTE, D. E. et al. Progress in open rotor propulsors: the FAA/GE/NASA open rotor test campaign. **The Aeronautical Journal**, London, v.118, n.1208, p.1181-1213, Oct. 2014.

VELDHUIS, L. L. M.; SINNIGE, T. The Effect of pylon trailing edge blowing on the performance and noise production of a propeller. In: CONGRESS OF THE INTERNATIONAL COUNCIL OF THE AERONAUTICAL SCIENCES, 29., 2014, St.Petersburg. Proceedings... Bonn: ICAS, 2014.

WELCH, P. D. The Use of fast fourier transform for the estimation of power spectra: a method based on time averaging over short, modified periodograms. **IEEE Transactions on Audio and Electroacoustics**, v.AU-15, n.2, p.70-73, June 1967.

WHITLOW JR., J. B.; SIEVERS, G. K. **Fuel savings potential of the NASA advanced turboprop program**. Washington: NASA, 1984. (NASA Technical Memorandum, 83736).

WOODWARD, R. P. **Measured noise of a scale model high speed propeller at simulated takeoff/approach conditions**. Washington: NASA, 1987a. (NASA Technical Memorandum 88920).

WOODWARD, R. P. **Noise of a model high speed counterrotation propeller at simulated takeoff/approach conditions (F7/A7)**. Washington: NASA, 1987b. (NASA Technical Memorandum 100206).

WRIGHT, S. E. Sound radiation from a lifting rotor generated by asymmetric disk loading. **Journal of Sound and Vibration**, Southampton, v.9, n.2, p.223-240, 1969.

APPENDIX A – COORDINATES FOR THE PYLON PRESSURE TAPPINGS

This section contains the coordinates for the pressure tappings on the upper surface of the NACA 0012 pylon. The same coordinates were used for the tappings on the lower surface.

Table 15 – Coordinates of pylon pressure tappings

Tap #	x [mm]	x/c [-]	y [mm]	y/c [-]
1	3	0.008	5.9	0.0148
2	5	0.013	7.6	0.0189
3	10	0.025	10.5	0.0261
4	15	0.038	12.5	0.0314
5	25	0.063	15.6	0.0390
6	35	0.088	17.8	0.0446
7	50	0.125	20.2	0.0506
8	75	0.188	22.6	0.0566
9	100	0.250	23.8	0.0594
10	125	0.313	24.0	0.0600
11	150	0.375	23.5	0.0589
12	175	0.438	22.6	0.0564
13	200	0.500	21.2	0.0529
14	225	0.563	19.4	0.0486
15	250	0.625	17.4	0.0435
16	275	0.688	15.1	0.0378
17	290	0.725	13.7	0.0342
18	305	0.763	12.1	0.0303
19	320	0.800	10.5	0.0262
20	335	0.838	8.8	0.0220
21	350	0.875	7.0	0.0175

Source – Author

APPENDIX B – INSTRUMENTATION AND CALIBRATION

This appendix contains information and pictures of the instrumentation used for the wind tunnel tests carried out throughout this work. All the data were taken from the information provided by the manufacturers.

B1 FREE STREAM MEASUREMENTS

Some properties of the free stream are necessary for the post-processing of results. Some of them are static and total pressure of the flow in the working section of the wind tunnel. These parameters are measured with a Pitot-static probe, placed on one of the working section walls, as shown in Figure 151a. This probe is connected to a micromanometer (DP-CALC 8702), which measures those two pressure components, as shown in Figure 151b. The digital output from the micromanometer is the difference between the two measured pressures, which is equivalent to the dynamic pressure. With the local air density, it is possible to calculate the free stream speed. The micromanometer is also equipped with an Ethernet port, which allows the data acquisition software to store this parameter.

Figure 151 – a) Pitot-static probe in the wind tunnel b) Micromanometer for dynamic pressure calculation from total and static pressure measurements

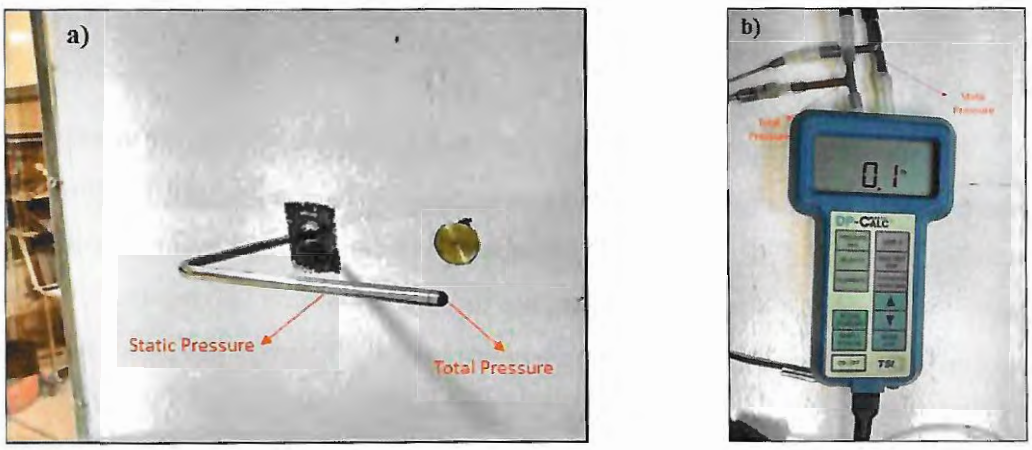

Source – Author

B2 AERODYNAMIC FORCES MEASUREMENTS

The aerodynamic forces are measured through a 3-component balance (Figure 81), based on strain gauges placed in full bridge, for each direction of measurement. The voltage

measured from each bridge is obtained through a HBM (*Hottinger Baldwin Messtechnik*) MGCPlus module, which allows for gains and filtering regulations, as shown in Figure 152.

Figure 152 –HBM MGCPlus used for the acquisition of aerodynamic forces

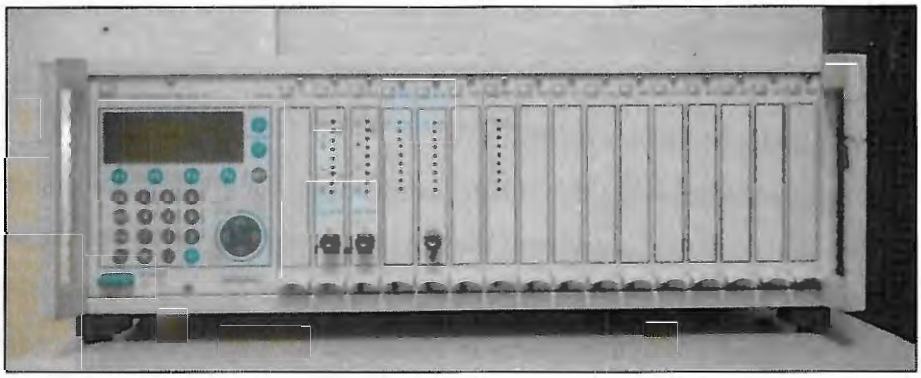

Source – Author

The values displayed in the HBM are in voltage units. Therefore, a calibration curve is necessary to convert the data into force units. The calibration is performed through pulleys, cables and dead weights. The weights are progressively attached to the balance and the signal is measured for each condition and plotted against the total weight applied. At the end, there should be a line crossing the origin, and its angular coefficient is the multiplication factor for converting from Volts to Newtons, for example.

B3 SURFACE PRESSURE MEASUREMENTS

The pressure measurements were performed with the aid of a Scanivalve™ pressure scanner, model ZOC33/64Px, as shown in Figure 153. This instrument has the capability of measuring up to 64 points (inputs) simultaneously and converting them to high-level electronic signals. Each group of 8 pressure sensors has its own calibration valving and multiplexer. The model used throughout this work has a full-scale range of ±20 inH_20 (0.72 psi), with an accuracy of 0.15% of this value, or 0.003 inH_20. The acquisition is performed with a sample rate of 5 kHz. A DSMCPM (Control Pressure Model), which contains 3 solenoid valves, distributes 65 psi to the ZOC pressure scanner calibration valves, placing them in operate, calibrate or purge modes (SCANIVALVE CORPORATION).

Figure 153 – Scanivalve™ pressure scanner, model ZOC33/64Px

Source – Scanivalve Corporation

B4 FLOWFIELD MEASUREMENTS

For the wake measurements, a Dual Sensor X-Shaped probe was chosen, wherein the wires are placed parallel to the probe axis, which was necessary given the space constraints. This probe is shown in Figure 154. The DANTEC™ StreamLine analog anemometer system with CTA modules for the measurements is shown in Figure 155.

Figure 154 – Hot-wire dual sensor x-shaped probe

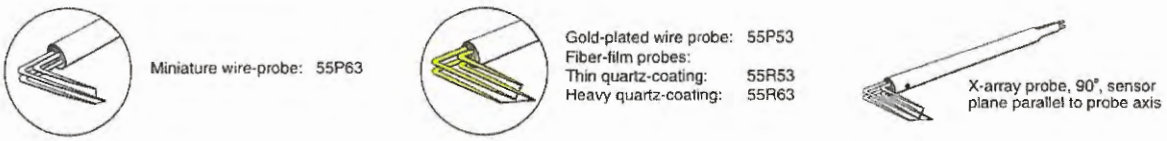

Source – Dantec Dynamics

Figure 155 – CTA modules for hot-wire acquisiton

Source – Author

A 3-axes traverse was used to move the probe precisely in two directions for the flow mapping, as shown in Figure 156.

Figure 156 – Traverse for flow mapping with hot-wire

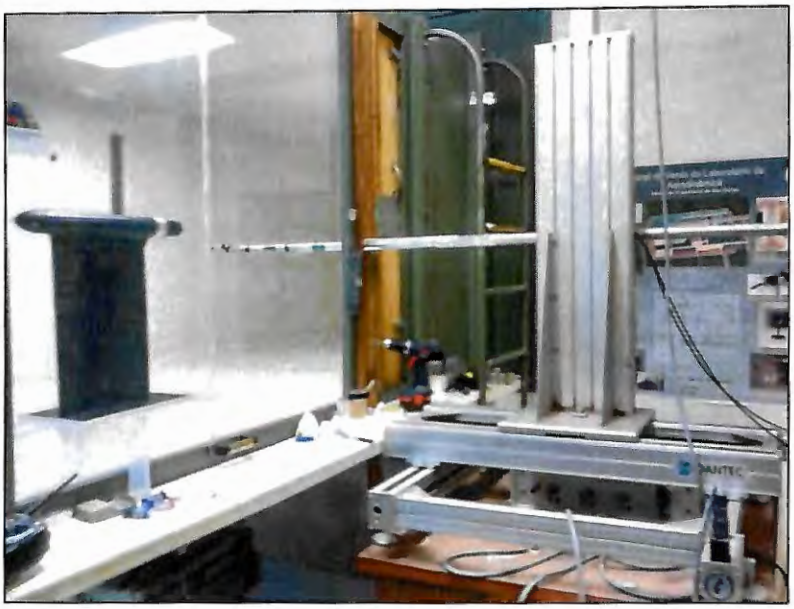

Source – Author

The calibration of the hot wire was performed with an automatic calibrator, also from Dantec, as shown in Figure 157. The calibration curve for this probe is shown in Figure 158.

Figure 157 – Calibration of the hot-wire probe

Source – Author

Figure 158 – Hot-wire calibration curves

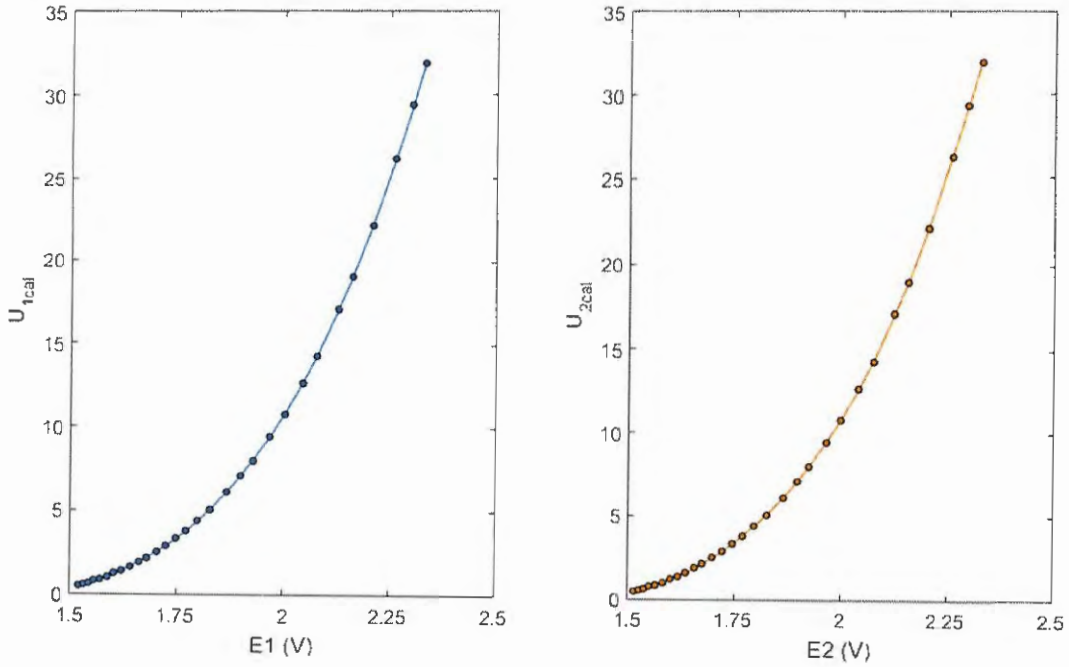

Source – Author

B5 AEROACOUSTIC MEASUREMENTS

An array of 61 microphones G.R.A.S. 46 *BD*, which combine a pressure transducer (*40 BD*) and a pre-amplifier (*26 CB*), was available for the aeroacoustic measurements. The microphones are able to operate with a flat response from 10 Hz to 25 kHz (with a 1 dB loss), or from 4 Hz to 70 kHz (2 dB loss) (G.R.A.S. SOUND & VIBRATION). The type of microphones used is shown in Figure 159.

Figure 159 – Microphone G.R.A.S. 46 *BD*

Source – G.R.A.S. Sound & Vibration

APPENDIX C – VARIABILITY OF THE AEROACOUSTIC MEASUREMENTS

This appendix contains information on a variability analysis conducted for the aeroacoustic measurements. The analyses were performed for both isolated and installed configurations in order to verify how much the noise levels for these cases change for non-consecutive measurements.

C1 ISOLATED CONFIGURATION

The spectra for two different non-consecutive aeroacoustic measurements is show in Figure 160, for the 4-bladed propeller at J = 0.30, and for the 3-bladed propeller at J = 0.50, both in the isolated configuration.

Figure 160 – Repeatability measurements for isolated 4-bladed propeller at J = 0.30, and 3-bladed propeller at J = 0.50

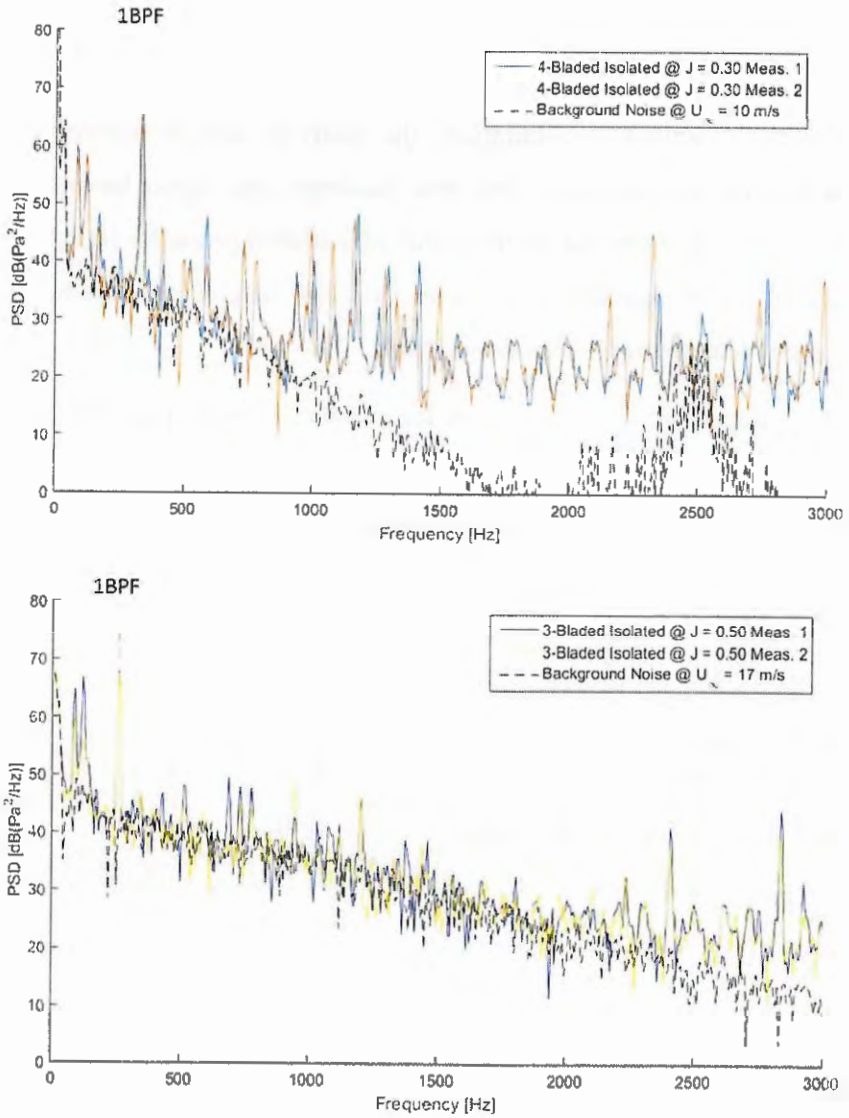

Source – Author

For the isolated configuration, the BPF levels will be compared, since this frequency is the focus of the analysis for this configuration. The tones that are more visibly different are related to the electric motor and are not the focus of this study. The levels for the two measurements of each propeller are shown in Table 16. For both propellers, the sound pressure levels at BPF changed up to 0.38 dB. This indicates a high precision for the tone at this frequency.

Table 16 – PSD for the non-consecutive measurements for the BPF of the 4- and 3-bladed isolated propellers

	Meas. 1 [dB]	Meas. 2 [dB]	ΔPSD [dB]
BPF_{4B}	65.29	65.65	0.36
BPF_{3B}	67.90	67.52	0.38

Source – Author

C2 INSTALLED CONFIGURATION

For the installed configuration, the analysis will be carried out similarly as was performed for the isolated case. This time, however, the higher harmonics (up to the 5th) will also be evaluated. The spectra for the installed 4-bladed propeller (at J = 0.30) and the installed 3-bladed (at J = 0.50) are shown in Figure 161. The difference between the noise levels for the tones of each measurement is shown in Table 17.

Figure 161 – Repeatability measurements for installed 4-bladed propeller at J = 0.30, and 3-bladed propeller at J = 0.50

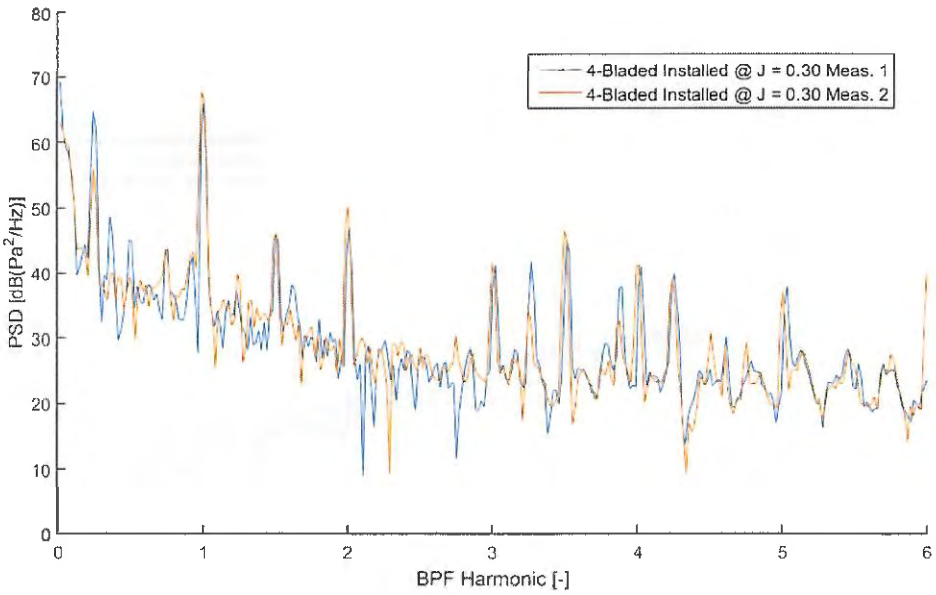

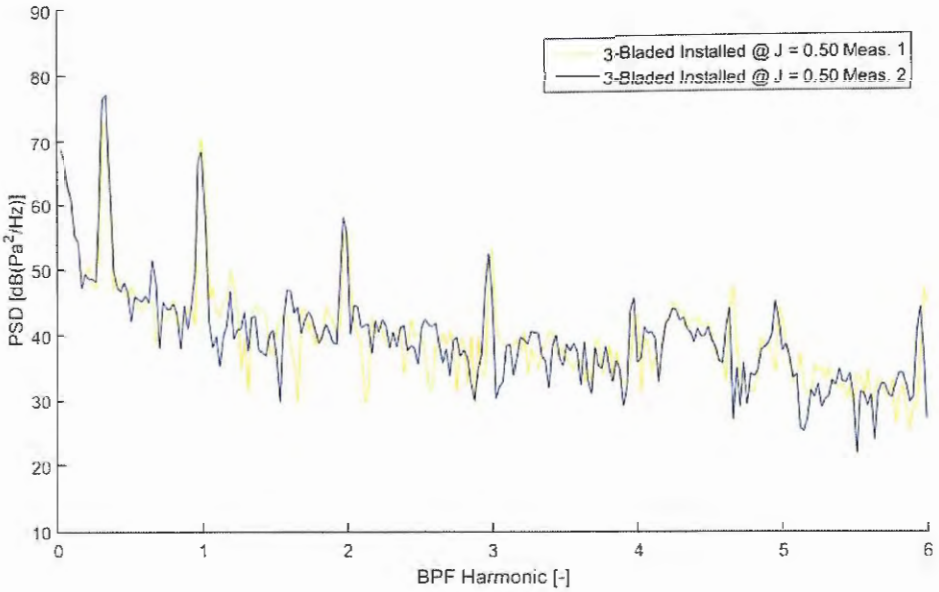

Source – Author

Table 17 – ΔPSD for the non-consecutive measurements for the BPF of the 4- and 3-bladed installed propellers

	ΔPSD_{1BPF} [dB]	ΔPSD_{2BPF} [dB]	ΔPSD_{3PF} [dB]	ΔPSD_{4BPF} [dB]	ΔPSD_{5BPF} [dB]
4-Bladed	1.72	3.06	0.25	0.30	0.68
3-Bladed	2.25	1.45	0.62	2.45	0.83

Source – Author

The two measurements conducted for the installed 4- and 3-bladed propellers indicate that the maximum variability of the acoustic measurements for this condition is 3 dB, which was obtained for the 2nd harmonic of the 4-bladed propeller. The average difference, however, for other frequencies is about 1 dB, or even less. Therefore, even for higher frequencies, the variability of the results is still small, which indicates a high reliability on the measured data for variations over 3 dB.